

# Coexistence and Structure of Deformed Shapes Near the $Z=82$ Closed Shell

by

Gregory John Lane

A thesis submitted for the degree of  
Doctor of Philosophy  
at The Australian National University

May, 1995

# Preface

This work describes an investigation of high spin states in  $^{183}\text{Hg}$ ,  $^{185}\text{Tl}$  and  $^{187}\text{Tl}$ , a project suggested by Prof. G.D. Dracoulis. The spectroscopic measurements were performed at the Department of Nuclear Physics at the Australian National University using the 14UD Pelletron and the CAESAR array. Successful running of the experiments relied upon help from Prof. G.D. Dracoulis, Dr. A.P. Byrne, Dr. A.E. Stuchbery, Dr. P.M. Walker, Dr. T. Kibédi, Dr. A.M. Baxter, Dr. P.H. Regan, Mr. S.S. Anderssen and Mr. P.M. Davidson. The experimental analysis and interpretation was carried out by the author using computer codes developed by different people over many years, and with the help of many invaluable suggestions from Prof. G.D. Dracoulis and Dr. A.P. Byrne. The equilibrium deformation and microscopic configuration calculations presented in Chapter 7 play an essential role in analysing the microscopic proton configuration of the prolate-deformed thallium and mercury isotopes. These calculations were performed by Dr. J.A. Sheikh and Prof. W. Nazarewicz.

Some of the data presented in this thesis were collected in an experiment performed at Argonne National Laboratory by Dr A.M. Baxter, Prof. G.D. Dracoulis and Dr A.P. Byrne, together with their collaborators at Argonne.

The original research project for this thesis was to have involved the Particle Detector Ball (PDB), a device consisting of fourteen plastic scintillator detectors. It is designed to measure the light charged particles emitted in compound nucleus decay and thus identify the evaporation residues. Although substantial effort was put into developing the device, it was not necessary for the (HI,xn) reactions studied in this thesis, and no details will be reported here.

Parts of the work presented in this thesis have been or will be published in the following articles:

- **Deformed  $i_{13/2}$  Bands and Prolate-oblate Shape Coexistence in  $^{185}\text{Tl}$  and  $^{187}\text{Tl}$ .**

G.J. Lane, G.D. Dracoulis, A.P. Byrne, P.M. Walker, A.M. Baxter, R.G.

Henry, D. Nisius, C.N. Davids, T. Lauritsen, H. Penttilä, D.J. Henderson, J.A. Sheikh and W. Nazarewicz, Phys. Lett. **B324** (1994) 14-19.

- **Shape Coexistence in  $^{185}\text{Tl}$  and  $^{187}\text{Tl}$  - Investigation of the Deformed Minima.**

G.J. Lane, G.D. Dracoulis, A.P. Byrne, P.M. Walker, A.M. Baxter, J.A. Sheikh and W. Nazarewicz, Nucl. Phys. **A586** (1995) 316-350.

- **Prolate-Oblate Shape Coexistence in  $^{183}\text{Hg}$ .**

G.J. Lane, G.D. Dracoulis, A.P. Byrne, S.S. Anderssen, P.M. Davidson, B. Fabricius, T. Kibédi, A.E. Stuchbery and A.M. Baxter, Nucl. Phys. **A**, in press.

No part of this thesis has been submitted for a degree at any other university.

Greg Lane  
May, 1995

# Acknowledgements

The last five years (including honours) have been a fantastic time and I would like to thank both George Dracoulis for letting me work in the Department and also the Australian Government and the Research School for providing me with an APRA scholarship and a Graduate Assistantship.

I could not have asked for any more assistance from my supervisors, Aidan Byrne, George Dracoulis and Andrew Stuchbery, who were absolutely magnificent both in and outside of working hours. (Aidan makes the best cakes in any hemisphere and George and Andrew throw mean parties!) In particular, Aidan and George were a source of much help and academic inspiration, besides also providing a comprehensive proof-reading service. I'm grateful for all their efforts. The rest of the GAMMA crew, past and present, are a great bunch, and have made studying what most of my old school friends would call dry and boring, in fact extremely interesting! My thanks also go to the technical and engineering staff in the Department, who, under the able leadership of David Weissner, have made the 14UD the most reliable machine in the known universe, despite all of our earnest attempts to stuff it up.

Javid Sheikh and Witek Nazarewicz deserve a special round of applause for their comprehensive calculations which illustrate exactly what the protons are up to in the thallium and mercury isotopes. I would also like to thank Allan, George, Aidan and their collaborators at Argonne, for allowing me to use the mass-gated  $\gamma$ -ray data from their  $^{186}\text{Pb}$  experiments with the Fragment Mass Analyzer.

On the personal side there are many people I should thank individually, however, space is limited and I can only mention a few of the names and activities responsible for the departmental social scene. Life just wouldn't be the same without lunchtime table tennis and its somewhat malleable rules and regulations (new blood!), and the darkroom with its traditional amber fluid (Reschs Pilsener for the uninitiated). I will make special mention of the old gang of students, Roy, Steve and Paul, we've finally all finished, and honorary member, Clyde,

who still has a bit to go. I would also like to thank Paddy and Nanda, our less than “model-worker” postdocs for their “she’ll be right messages” and for being a part of (especially Paddy), the “let’s go crowd.” (Let’s play golf, let’s play table tennis, let’s go to uni house, let’s go to Delicateating, let’s go to the pub, let’s have a barbie, let’s do some bloody work!) The above might make it seem like I never did any work. That, of course, is blatantly untrue. The real reason I took four and a bit years to finish “isn’t my fault”, and has nothing to do with Jodie. Thanks for absolutely everything Jodie.

In the last few days before submitting my thesis I suffered the misfortune of having to move house, and, while moving the bookcase, I happened to come across a pile of old letters. Reading them has reminded me once again (as if I could forget!), just how important Mum, Dad, my sister Toni and my Uncle David, have all been in getting me to where I am today. This thesis is as much yours as it is mine, and I hope I’ve made you proud.

# Abstract

This thesis reports the observation of high-spin states in the odd-neutron isotope,  $^{183}\text{Hg}$ , and the odd-proton isotopes,  $^{185}\text{Tl}$  and  $^{187}\text{Tl}$ , using the methods of  $\gamma$ -ray spectroscopy. The properties of these and other odd-mass mercury and thallium isotopes are used to investigate the structure of the prolate and oblate shape-coexisting states in the neutron-deficient mercury region.

Gamma-ray transitions in the thallium isotopes were assigned via X-ray coincidences, supported by mass selected  $\gamma$ -ray spectra obtained with a recoil mass spectrometer. Rotational bands associated with both prolate and oblate shape were observed. The bandheads of the proposed oblate  $\frac{13}{2}^+[606]$  states are isomeric, with meanlives of  $12\pm 2$  ns in  $^{185}\text{Tl}$  and  $1.0\pm 0.2$  ns in  $^{187}\text{Tl}$ . Prolate deformed  $i_{13/2}$  bands were observed in both nuclei, while in  $^{187}\text{Tl}$ , bands due to  $h_{9/2}$  and  $f_{7/2}$  protons coupled to the prolate shape were also assigned. A prolate  $h_{9/2}$  band was tentatively assigned in  $^{185}\text{Tl}$ .

Equilibrium deformation calculations for intrinsic states in a range of thallium nuclei are presented. Experimental trends with mass number are reproduced, but absolute excitation energies, and energy differences between the prolate and oblate states are not, continuing the persistent discrepancy between theory and experiment in the mercury region. Theoretical calculations of intruder orbital occupation probabilities show a correlation between prolate deformation and population of the  $h_{9/2}$  and  $f_{7/2}$  orbitals, in particular of the  $\frac{1}{2}^- [541]$  orbital from the  $h_{9/2}$  proton shell. They also show that blocking of the  $\frac{1}{2}^- [541]$  orbital significantly suppresses the prolate deformation. However, the experimental observation of the prolate rotation-aligned bands at low excitation energy implies that the development of prolate deformed minima in the odd-mass nuclei is not blocked by the odd proton occupying the  $h_{9/2}$ ,  $f_{7/2}$  or  $i_{13/2}$  orbitals. The implication is that the microscopic proton configuration of the prolate-deformed mercury and thallium nuclei is more collective, and is formed from a mixture of low- $\Omega$  proton intruder excitations.

Gamma-ray transitions in  $^{183}\text{Hg}$  were identified via X-ray coincidences. Prolate deformed bands associated with the  $\frac{1}{2}^-$  [521],  $\frac{7}{2}^-$  [514] and mixed  $i_{13/2}$  states were observed, while the presence of an oblate  $\frac{13}{2}^+$  state was inferred. The energies of the shape coexisting states due to the  $i_{13/2}$  neutron in  $^{183}\text{Hg}$ ,  $^{185}\text{Hg}$  and  $^{187}\text{Hg}$ , as well as the intra- and inter-band E2 transition strengths, are investigated within a two-band mixing model. The B(E2) ratios for transitions within and between the coexisting  $i_{13/2}$  neutron bands are not consistent with the assumption of prolate and oblate deformations, a problem previously noted in the even-mass isotopes. Possible explanations are briefly discussed. Systematics of the prolate-oblate energy differences provide evidence for a lowering of the prolate well relative to the oblate well by  $\sim 350$  keV in the odd-mass isotopes as compared to the even-mass isotopes. This may be a blocking effect due to the different densities of neutron orbitals at prolate and oblate deformations.

# Contents

<b>1</b>	<b>Introduction</b>	<b>1</b>
1.1	The Nuclear Shape . . . . .	2
1.2	Even-Mass Mercury and Lead Isotopes . . . . .	3
1.3	Odd-Mass Mercury and Thallium Isotopes . . . . .	6
1.3.1	Mercury isotopes . . . . .	6
1.3.2	Thallium isotopes . . . . .	8
1.4	Scope of the Current Work . . . . .	9
<b>2</b>	<b>Theoretical Background</b>	<b>11</b>
2.1	Shape Parameters . . . . .	11
2.2	Collective Rotation . . . . .	12
2.3	Nilsson Model . . . . .	14
2.4	The Pairing Interaction . . . . .	16
2.5	Particle-Rotor Model . . . . .	17
2.6	Cranked Shell Model . . . . .	21
2.7	“Signatures” of Shape Coexistence . . . . .	23
<b>3</b>	<b>Methods of <math>\gamma</math>-ray Spectroscopy</b>	<b>25</b>
3.1	Heavy Ion Fusion Reactions . . . . .	25
3.1.1	Statistical model calculations . . . . .	27
3.1.2	Nucleus identification . . . . .	29
3.2	Gamma-Ray Detectors . . . . .	30
3.2.1	Compton suppression . . . . .	31
3.3	The CAESAR Detector Array . . . . .	32
3.3.1	Compton suppression . . . . .	34
3.3.2	Coincidence logic . . . . .	34
3.3.3	Gamma-ray detection times . . . . .	34
3.3.4	Data acquisition . . . . .	35
3.3.5	Off-line analysis . . . . .	36



3.3.6	Lifetime analysis . . . . .	37
3.4	Angular Distributions . . . . .	38
3.5	Angular Correlations and DCO ratios . . . . .	39
3.6	Internal Conversion . . . . .	42
<b>4</b>	<b>Analysis and Results</b>	<b>43</b>
4.1	Analysis and Results for $^{187}\text{Tl}$ . . . . .	43
4.2	Level Scheme for $^{187}\text{Tl}$ . . . . .	50
4.2.1	Other spectroscopic studies . . . . .	52
4.2.2	Band 6. . . . .	52
4.2.3	Bands 3 and 5. . . . .	56
4.2.4	Bands 1 and 2. . . . .	57
4.2.5	Band 4 . . . . .	59
4.2.6	Other transitions. . . . .	61
4.2.7	Isomeric states. . . . .	61
4.3	Analysis and Results for $^{185}\text{Tl}$ . . . . .	64
4.4	Level Scheme for $^{185}\text{Tl}$ . . . . .	66
4.4.1	Bands 2, 3 and 4. . . . .	66
4.4.2	Band 1 . . . . .	69
4.4.3	Other transitions . . . . .	70
4.4.4	Isomeric states . . . . .	70
4.5	Analysis and results for $^{183}\text{Hg}$ . . . . .	72
4.6	Level scheme for $^{183}\text{Hg}$ . . . . .	74
4.6.1	Other spectroscopic studies . . . . .	74
4.6.2	$\frac{1}{2}^-$ [521] band . . . . .	77
4.6.3	$\frac{7}{2}^-$ [514] band . . . . .	80
4.6.4	Positive parity states . . . . .	80
4.6.5	Comparison with other work . . . . .	82
<b>5</b>	<b><math>^{185}\text{Tl}</math> and <math>^{187}\text{Tl}</math>: Configuration Assignments</b>	<b>86</b>
5.1	Expected Structures . . . . .	86
5.2	Band Properties . . . . .	88
5.2.1	In-band decay properties . . . . .	88
5.2.2	Aligned angular momenta . . . . .	89
5.3	Band Assignments and Intrinsic States . . . . .	91
5.3.1	$\frac{9}{2}^-$ [505] states, oblate deformation . . . . .	91
5.3.2	$\frac{13}{2}^+$ [606] states, oblate deformation . . . . .	92

5.3.3	$\frac{1}{2}^+[660]$ states, prolate deformation . . . . .	92
5.3.4	$\frac{3}{2}^-[532]$ and $\frac{1}{2}^-[530]$ states, prolate deformation . . . . .	93
5.3.5	$\frac{11}{2}^-[505]$ state, weak prolate deformation . . . . .	94
5.4	Nilsson Parameters . . . . .	94
<b>6</b>	<b><math>^{183}\text{Hg}</math>: Configuration Assignments</b>	<b>96</b>
6.1	Expected Structures . . . . .	96
6.2	Comparison with N=103 Isotones . . . . .	98
6.3	In-band Decay Properties . . . . .	99
6.3.1	$\frac{7}{2}^-[514]$ and mixed $i_{13/2}$ neutron bands . . . . .	99
6.3.2	$\frac{1}{2}^-[521]$ band . . . . .	100
6.4	Band crossings and Aligned Angular Momenta . . . . .	102
6.4.1	Shape changes in the $i_{13/2}$ bands . . . . .	102
6.4.2	$\frac{1}{2}^-[521]$ and $\frac{7}{2}^-[514]$ bands . . . . .	104
6.4.3	S-band crossing . . . . .	104
<b>7</b>	<b>Proton Configurations of the Core Nuclei</b>	<b>107</b>
7.1	Equilibrium Deformation Calculations . . . . .	107
7.2	Intrinsic State Energies . . . . .	111
7.3	Occupation Number Calculations . . . . .	113
7.4	Microscopic Structure of the Mercury Cores. . . . .	116
7.5	Absence of the $h_{9/2}$ Decoupled Band in $^{189}\text{Tl}$ . . . . .	117
7.6	Prolate-Oblate Energy Differences . . . . .	118
<b>8</b>	<b>Odd-Mass Mercury Isotopes</b>	<b>121</b>
8.1	Band-Mixing Analysis of the State Energies . . . . .	121
8.1.1	$^{187}\text{Hg}$ . . . . .	124
8.1.2	$^{185}\text{Hg}$ . . . . .	125
8.1.3	$^{183}\text{Hg}$ . . . . .	126
8.1.4	Mixed wavefunctions . . . . .	126
8.2	Band-Mixing Analysis of the B(E2) Branching Ratios . . . . .	128
8.2.1	$^{187}\text{Hg}$ . . . . .	130
8.2.2	$^{185}\text{Hg}$ . . . . .	133
8.2.3	$^{183}\text{Hg}$ . . . . .	133
8.3	Signs of the Deformations . . . . .	133
8.4	Prolate-Oblate Energy Differences . . . . .	135

<b>9 Summary and Conclusions</b>	<b>139</b>
9.1 The Odd Nucleon as a Structural Probe . . . . .	140
9.2 Conclusions . . . . .	142
<b>Appendices</b>	<b>144</b>
<b>A In-band Decay Properties</b>	<b>144</b>
<b>B Band-mixing</b>	<b>146</b>
B.1 VMI Model for the State Energies . . . . .	146
B.2 Two-State Mixing . . . . .	147
B.3 Calculating $B(E2)$ Strengths . . . . .	150
<b>References</b>	<b>153</b>

# List of Figures

1.1	Potential energy surface and calculated rotational band energies for $^{184}\text{Hg}$ . . . . .	3
1.2	Systematics of the rotational bands built upon the oblate ground states and prolate excited states in the even-mass mercury isotopes. . . . .	4
1.3	Changes in the square of the nuclear radius for the mercury isotopes measured using laser spectroscopy. . . . .	7
1.4	Systematics of the rotational bands built upon the oblate intruder states in the odd-mass thallium isotopes. . . . .	9
2.1	Angular momentum coupling in the rotational wave function. . . . .	13
2.2	Coupling of the single-particle angular momentum for deformation and rotation alignment. . . . .	19
2.3	Comparison between energy levels in a deformation-aligned and a rotation-aligned band. . . . .	20
2.4	Quasiparticle Routhians in the Cranked Shell Model . . . . .	23
3.1	Heavy ion fusion reaction . . . . .	26
3.2	Statistical model calculations . . . . .	28
3.3	Detection efficiencies for HPGe and LEPS detectors . . . . .	31
3.4	Geometry of the CAESAR array . . . . .	32
3.5	CAESAR electronics . . . . .	33
3.6	Typical time difference spectrum . . . . .	36
3.7	Theoretical DCO ratio for a mixed dipole/quadrupole transition . . . . .	41
4.1	Comparison of the total projections of the $\gamma - \gamma$ coincidence matrices for the bombardments used at the ANU to make $^{187}\text{Tl}$ and $^{185}\text{Tl}$ . . . . .	45
4.2	Spectrum of $\gamma$ -rays in coincidence with mass-187 residues. . . . .	47
4.3	Selected DCO ratios and angular distributions for transitions in $^{187}\text{Tl}$ . . . . .	48

4.4	Level scheme for $^{187}\text{Tl}$ . . . . .	51
4.5	Projections of the $\gamma-\gamma$ and $\gamma$ -LEPS coincidence matrices showing the 392.8/394.1 keV doublet. . . . .	53
4.6	Coincidence spectra for the unfolded 392.8/394.1 keV doublet and the 366.3 keV transitions from the yrast cascade in $^{187}\text{Tl}$ . . . . .	55
4.7	Coincidence spectra for the 268.3 and 716.2 keV transitions in $^{187}\text{Tl}$	57
4.8	Coincidence spectra for transitions associated with the decoupled bands 1 and 2 in $^{187}\text{Tl}$ . . . . .	58
4.9	Coincidence spectra for transitions associated with band 4 in $^{187}\text{Tl}$	60
4.10	Time centroid shifts for the yrast cascade in $^{187}\text{Tl}$ . . . . .	62
4.11	Spectrum of $\gamma$ -rays in coincidence with mass-185 residues. . . . .	65
4.12	Level scheme for $^{185}\text{Tl}$ . . . . .	67
4.13	Coincidence spectra for transitions in the yrast cascade in $^{185}\text{Tl}$ . .	68
4.14	Coincidence spectra for transitions from band 1 in $^{185}\text{Tl}$ . . . . .	69
4.15	Time spectra for transitions in $^{185}\text{Tl}$ , $^{186}\text{Hg}$ and $^{155}\text{Gd}$ . . . . .	71
4.16	Selected DCO ratios and angular distributions for transitions in $^{183}\text{Hg}$ . . . . .	75
4.17	Level scheme for $^{183}\text{Hg}$ . . . . .	76
4.18	Level scheme for $^{183}\text{Hg}$ obtained in previous $\alpha$ -decay work . . . . .	77
4.19	Coincidence spectra for the $\frac{1}{2}^-$ [521] band in $^{183}\text{Hg}$ . . . . .	78
4.20	Low-energy region of the coincidence spectrum for the 376.0 keV transition in $^{183}\text{Hg}$ . . . . .	79
4.21	Coincidence spectra for the $\frac{7}{2}^-$ [514] band in $^{183}\text{Hg}$ . . . . .	80
4.22	Coincidence spectra for the mixed $i_{13/2}$ neutron band in $^{183}\text{Hg}$ . . .	81
4.23	Summed coincidence spectra for the unfavoured signature of the $\frac{1}{2}^-$ [521] band in $^{183}\text{Hg}$ . . . . .	84
5.1	Nilsson scheme for protons . . . . .	87
5.2	Alignments for the positive parity sequences in $^{185}\text{Tl}$ , $^{187}\text{Tl}$ and their even-even neighbours. . . . .	90
5.3	Alignments for the decoupled bands in $^{185}\text{Tl}$ , $^{187}\text{Tl}$ and their isotones, $^{183}\text{Au}$ and $^{185}\text{Au}$ . . . . .	91
6.1	Nilsson scheme for neutrons. . . . .	97
6.2	Magnetic moments in $^{183}\text{Hg}$ from in-band decay properties. . . . .	101
6.3	Aligned angular momenta for the rotational bands in $^{183}\text{Hg}$ , $^{185}\text{Hg}$ and $^{181}\text{Pt}$ . . . . .	103

7.1	Theoretical excitation energies of intruder states in the odd-mass thallium nuclei. . . . .	109
7.2	Theoretical deformations of intruder states in the odd-mass thallium nuclei. . . . .	110
7.3	Comparison between theoretical and experimental excitation energies for the intrinsic states in the odd-mass thallium isotopes. . .	112
7.4	Occupation numbers of the high- $j$ intruder orbitals for various intrinsic states in the odd-mass thallium and even-mass mercury isotopes. . . . .	114
7.5	Prolate-oblate energy differences for the odd-mass thallium and even-mass mercury isotopes. . . . .	119
8.1	Partial level schemes showing the coexisting $i_{13/2}$ neutron bands in $^{183}\text{Hg}$ , $^{185}\text{Hg}$ and $^{187}\text{Hg}$ . . . . .	123
8.2	Energies of states in the $i_{13/2}$ bands in $^{183}\text{Hg}$ , $^{185}\text{Hg}$ and $^{187}\text{Hg}$ with a nominal rotor energy subtracted. . . . .	127
8.3	Effect of mixing on the $i_{13/2}$ bands in $^{187}\text{Hg}$ . . . . .	131
8.4	Deduced value of the interaction matrix element as a function of the ratio of the quadrupole moments for the coexisting $i_{13/2}$ bands in $^{187}\text{Hg}$ . . . . .	132
8.5	Prolate-oblate energy differences for the mercury isotopes. . . . .	137
B.1	Mixing of two levels . . . . .	148
B.2	Schematic picture of the mixing of two rotational bands showing the unperturbed and perturbed wavefunctions. . . . .	150

# List of Tables

3.1	Theoretical DCO ratios for the CAESAR array . . . . .	40
4.1	Summary of experiments performed for this thesis . . . . .	44
4.2	Transitions assigned to $^{187}\text{Tl}$ . . . . .	49
4.2	continued . . . . .	50
4.3	Unfolded coincidence intensities for the yrast cascade in $^{187}\text{Tl}$ . .	54
4.4	Transitions assigned to $^{185}\text{Tl}$ . . . . .	65
4.5	Transitions assigned to $^{183}\text{Hg}$ . . . . .	72
4.5	continued . . . . .	73
5.1	Magnetic moments determined from crossover/cascade branching ratios in $^{187}\text{Tl}$ . . . . .	89
5.2	Energies of prolate intrinsic states in $^{187}\text{Tl}$ relative to the prolate $h_{9/2}$ state . . . . .	95
6.1	In-band decay properties for $^{183}\text{Hg}$ . . . . .	99
6.2	Experimental $g_K$ values deduced for $\frac{1}{2}^- [521]$ bands in the $A = 180$ region . . . . .	102
6.3	S-band crossing frequencies in the mercury isotopes . . . . .	105
7.1	Calculated deformations and excitation energies for some of the low-lying states in $^{185}\text{Tl}$ and $^{187}\text{Tl}$ . . . . .	108
7.2	VMI parameters used to fit the aligned bands in $^{185}\text{Tl}$ , $^{187}\text{Tl}$ and $^{189}\text{Tl}$ . . . . .	111
7.3	Calculated deformations of the prolate minima for the even-mass mercury isotopes and occupation probabilities for the intruder or- bitals . . . . .	115
8.1	VMI parameters used to fit the coexisting $i_{13/2}$ neutron bands in $^{183}\text{Hg}$ , $^{185}\text{Hg}$ and $^{187}\text{Hg}$ . . . . .	124
8.2	Mixed wavefunctions for states in $^{187}\text{Hg}$ . . . . .	128

8.3	Experimental B(E2) ratios for the odd-mass mercury isotopes . .	129
8.4	Predicted deformations and quadrupole moments for the coexisting $i_{13/2}$ bands in $^{183}\text{Hg}$ , $^{185}\text{Hg}$ and $^{187}\text{Hg}$ . . . . .	129
8.5	Mixing matrix elements deduced from the B(E2) ratios. . . . .	130
8.6	Comparison of experimental B(E2) branching ratios in $^{188}\text{Hg}$ with theoretical predictions . . . . .	134



# Chapter 1

## Introduction

The nucleus is a unique system in nature, consisting of a relatively small number of interacting fermions. One of the consequences of the finite number of particles is that in different regimes of excitation energy and spin, and for nuclei with different numbers of protons and neutrons, the nucleons within the nucleus can behave in a variety of ways. For example, one extreme model description considers the nucleons to move independently within a central potential with a strong spin-orbit force. The quantised energy levels exhibit large shell gaps, so that there are especially stable nucleon configurations for nuclei with particular numbers of protons or neutrons. The excited states in these *magic* nuclei (and their near neighbours) can be described in terms of excitations of individual nucleons between the energy levels.

On the other hand, the nucleons in nuclei far from closed shells often show a collective behaviour, and the nucleus may be described by a model which considers it to be a macroscopic object which can deform and vibrate or rotate. The excited states in a rotational nucleus are separated in energy according to the quantum mechanical analogue of a classical rotor, and the nucleus can be characterised by a moment-of-inertia,  $\mathfrak{I}$ , which is related to its deformation.

An important feature of nuclear spectroscopy is that the pattern of the energy levels provides a clue as to the behaviour of the nucleons and the model description which is appropriate, and hence the structure, and sometimes even the shape, of the nucleus. In terms of the models just discussed, an irregular behaviour with spin for the energy levels is a signature for spherical shape, while levels spaced in energy according to  $E_I = \frac{\hbar^2}{2\mathfrak{I}} I(I+1)$  are a signature for a deformed rotational nucleus.

## 1.1 The Nuclear Shape

The shape of the nucleus is intimately related to the density of single particle levels. In an axially deformed nucleus with symmetry axis,  $z$ , the single particle levels may be labelled by the angular momentum projection,  $j_z = \Omega$ . Orbitals with high- $\Omega$  have an oblate density distribution and are favoured in energy if the nucleus is oblate deformed, while at prolate deformation the low- $\Omega$  orbitals are favoured. Thus, in a deformed nucleus, the familiar spherical shell gaps disappear, and the densities of the single particle levels change with deformation. The calculation of the single particle levels in a deformed potential is discussed in more detail in §2.3.

The many methods of calculating the shape, or mean field, of the nucleus have recently been reviewed by Åberg *et al.* [Åbe90]. The most common calculations are of the Nilsson-Strutinsky type [Str67, Bra72] where the binding energy of the nucleus is given by a sum between the liquid drop energy, which always favours a spherical shape at zero spin, and the shell correction energy, which favours deformations which give a low level density at the Fermi surface. Since the level densities vary as a function of deformation for a given nucleus, it is possible for the binding energy as a function of deformation, or potential energy surface, to exhibit minima at two or more deformations. When these minima are separated by potential barriers, it is possible for the nucleus to take on the shape appropriate for each of the minima, and it is said to exhibit shape coexistence. The question as to whether or not there is a potential barrier is non-trivial. It does appear that quite shallow minima, or even flat spots in the potential energy surface, can result in stable deformed shapes. This is often because the flatter region or shallow minimum in the potential is due to the existence of a different microscopic configuration which is favoured in energy at that deformation. It is then possible to talk about a barrier in “configuration-space.” Examples of such minima are discussed in the next section with regard to the lead isotopes.

The neutron-deficient mercury isotopes are amongst the best known examples of shape coexistence, exhibiting structures built upon an impressive range of spherical, oblate and prolate shapes (see Ref. [Woo92] and references therein). A similar range of nuclear shapes occur in the neighbouring thallium isotopes. This thesis will concentrate on the lighter mercury and thallium isotopes with  $A < 190$ , which exhibit collective structures built upon both weakly oblate and more deformed prolate shapes. The rest of this chapter describes the current state of experimental and theoretical knowledge regarding the shape coexisting

states in these and neighbouring nuclei, beginning with the even-mass cases.

## 1.2 Even-Mass Mercury and Lead Isotopes

Potential energy surface calculations for the the even-mass mercury isotopes with  $A < 190$  show both a weakly deformed oblate minimum at  $\beta_2 \approx -0.15$  and a normally deformed prolate minimum at  $\beta_2 \approx +0.25$  (see for example, Refs. [Dic74, Kol75, Fra75, Ben87, Naz93]). Figure 1.1 shows an example for  $^{184}\text{Hg}$  together with the calculated rotational band energies [Fra75]. Two  $K = 0$  bands are predicted, with the excited band from the larger deformation having a larger moment-of-inertia. Experimental studies have actually identified two low-lying collective bands built upon  $K = 0^+$  states in all the even-mass nuclei from  $^{182}\text{Hg}$  to  $^{190}\text{Hg}$ , as shown in Figure 1.2. (The  $0_i^+$  and  $2_g^+$  states in  $^{180}\text{Hg}$  are not known.) The spacing of the energy levels in the excited bands is compressed compared to the ground state bands, and  $\gamma$ -ray spectroscopy measurements of the lifetimes of excited states in  $^{184}\text{Hg}$  [Rud73] and  $^{186}\text{Hg}$  [Pro74], have shown that this is due to

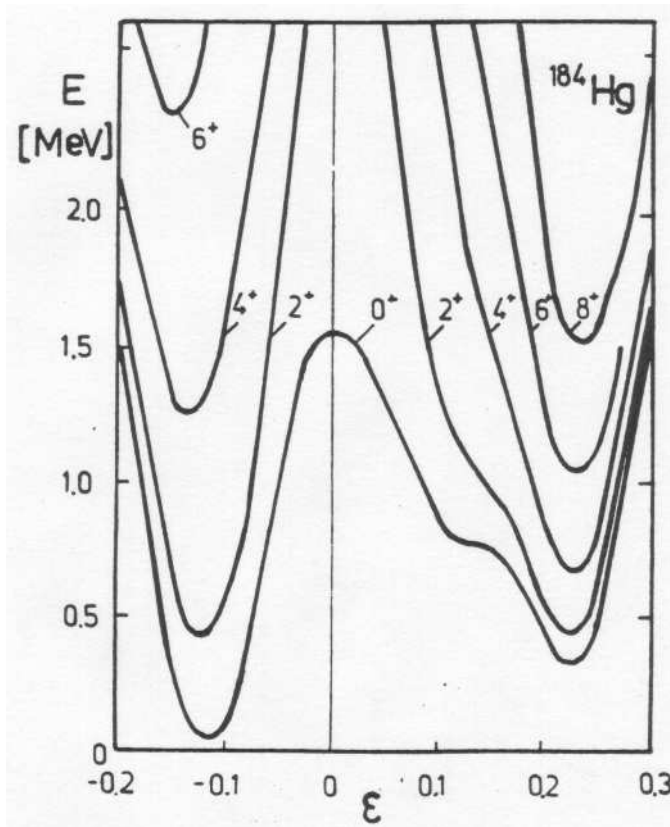


Figure 1.1: Potential energy surface and calculated rotational band energies for  $^{184}\text{Hg}$ . (Figure taken from Frauendorf and Pashkevich [Fra75].)

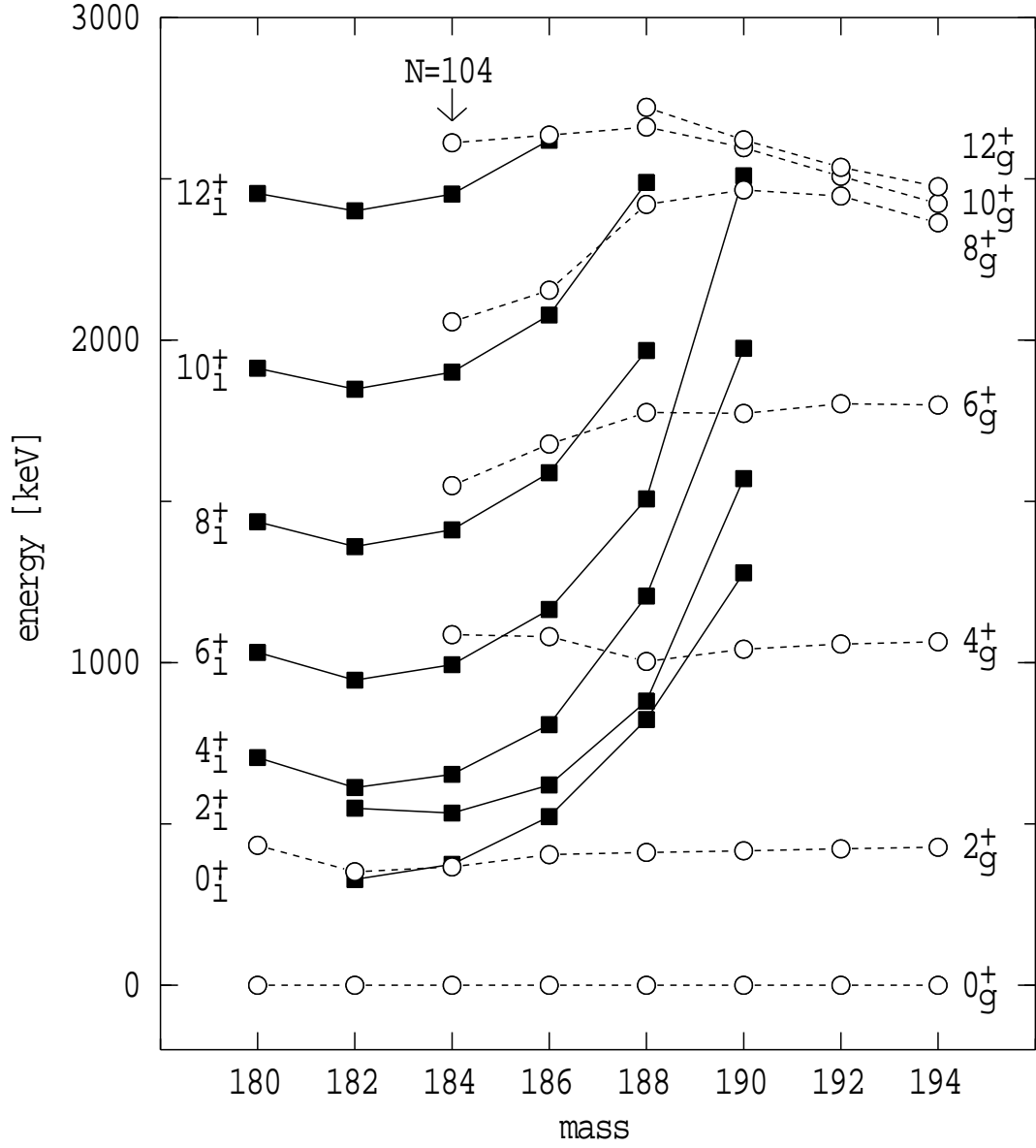


Figure 1.2: Systematics of the rotational bands built upon the oblate ground states and prolate  $0_i^+$  intruder states in the even-mass mercury isotopes. States in the ground band are shown as open circles, while filled squares indicate states in the intruder band. Note the fall and rise of the  $0_i^+$  state as the neutron number passes through  $N \approx 104$ . (Data are taken from:  $^{180}\text{Hg}$  [Dra88],  $^{182}\text{Hg}$  [Ma84, Bin94, Wau94],  $^{184}\text{Hg}$  [Ma86, Col76],  $^{186}\text{Hg}$  [Por92, Ma93, Ham75],  $^{188}\text{Hg}$  [Han88, Ham75, Col84],  $^{190}\text{Hg}$  [Hüb86, Bea94, Kor91, Del94],  $^{192}\text{Hg}$  [Hüb86],  $^{194}\text{Hg}$  [Hüb86]. Note that Delaroche *et al.* argue that the excited band built upon the  $0_2^+$  state in  $^{190}\text{Hg}$  is actually a  $\beta$ -vibrational band, not a rotational band [Del94].)

different deformations, with the magnitudes of the deformations for the excited and ground state bands being  $|\beta_2| \approx 0.25$  and  $|\beta_2| \approx 0.15$  respectively. The two bands can be naturally associated with the prolate and oblate minima predicted in the potential energy surface calculations.

It appears to be a general feature that nuclei near closed shells exhibit deformed “intruder” states, formed by  $n$ -particle –  $n$ -hole (np-nh) excitations across the shell gap into “intruder” orbitals [Hey83, Woo92]. In this context, the term “intruder” is used to describe the strongly sloping low- $\Omega$  and high- $\Omega$  orbitals which at spherical shape are above (or below) the shell gap, but approach the Fermi surface when the magnitude of the deformation is increased. For the mercury isotopes (with  $Z = 80$ ), the  $\frac{1}{2}^-$ [541] orbital from the  $h_{9/2}$  proton shell intrudes from above the  $Z = 82$  shell gap at prolate deformation. A two-proton excitation into this orbital can result in the nucleus being deformed, indeed Bengtsson *et al.* [Ben87] report a large  $(\pi h_{9/2})^2$  component in the prolate minimum of their potential energy surface calculations. Furthermore, in many even-mass nuclei near the  $Z = 20$ ,  $Z = 50$  and  $Z = 82$  closed shells, there is ample evidence that  $0_2^+$  states are strongly populated in proton-pair transfer reactions, suggesting that these “intruder” states are due to proton two particle – two hole (2p-2h) excitations (see Ref.[Woo92] and references therein).

Evidence for shape coexistence has also been presented for the neighbouring even-mass platinum and osmium nuclei (see Ref. [Dra94] and references therein). Shape coexisting states are even observed in the neutron-deficient lead isotopes which have a closed proton shell. The calculations for the lead isotopes all predict a spherical ground state [May77, Dup84, Ben89, Naz93]. There is also a flat region in the potential energy surface at a weak oblate deformation of  $\beta_2 \approx -0.15$ , associated with a two-proton excitation into the  $\frac{9}{2}^-$ [505] orbital. The different configuration between this excitation and the ground state results in the flat part of the potential giving rise to stable oblate deformation [Ben89], and excited  $0_2^+$  states associated with this “minimum” have been observed in the isotopes  $^{190}\text{Pb}$  to  $^{200}\text{Pb}$  [Dup84, Dup85, Dup87]. There is also evidence for a collective band structure built upon the  $0_2^+$  state in  $^{196}\text{Pb}$  [Pen87]. The calculations for the lead isotopes with  $A \leq 188$  also show distinct minima at a prolate deformation of  $\beta_2 \approx 0.25$ , and collective rotational bands believed to be built upon this minimum have recently been observed in  $^{186}\text{Pb}$  [Hee93, Bax93] and  $^{188}\text{Pb}$  [Hee93]. (The  $0^+$  states associated with the prolate bands are yet to be observed, and as yet there is no evidence for the oblate states which are predicted to persist in these lighter

nuclei.) As in the mercury isotopes, the prolate minimum is associated with proton excitations into the strongly sloping  $\frac{1}{2}^- [541]$  orbitals [Ben89].

### 1.3 Odd-Mass Mercury and Thallium Isotopes

Shape coexistence in odd-mass nuclei is complicated by the presence of the odd nucleon. At the various minima in the potential the Fermi level will lie amongst different sets of orbitals, possibly giving rise to intrinsic excitations with different spins and parities, unlike the even-mass nuclei where  $K^\pi = 0^+$  states are always observed. Furthermore, even if the same orbitals are available at each shape, the different deformations may still give rise to collective motions which result in different level structures. (Details of the collective structures associated with the odd nucleon coupled to a deformed core will be addressed in Chapter 2.) Finally, the presence of the odd-particle may actually affect the potential well, either through its driving of the deformation itself, or by blocking of some component of the microscopic core configuration. The latter scenario raises the possibility of the odd nucleon in an odd-mass nucleus being used to probe the microscopic configuration of the even-even core.

The deformed states in the even-mass mercury and lead isotopes have been associated with proton excitations across the closed shell. Thus the different proton structures of the prolate and oblate states are expected to be the cause of the different deformations, and studies of the intervening odd-proton thallium isotopes might provide details of the particular orbitals responsible for the formation of the deformed cores. In contrast, studies of the neighbouring odd-neutron mercury and lead isotopes are only likely to provide limited information about the microscopic structure of the cores. The next two subsections address what is currently known about the odd-mass mercury and thallium isotopes.

#### 1.3.1 Mercury isotopes

Figure 1.3 shows the results of atomic spectroscopy measurements performed on both stable and radioactive mercury isotopes. The shifts of the electronic energy levels can be related to the change in the square of the nuclear charge radius,  $\delta \langle r^2 \rangle$ . The straight line shows the expected change in  $\delta \langle r^2 \rangle$  if the lighter nuclei were simply to decrease in volume and remain spherical. The excess above this line is interpreted as being due to the onset of a weak oblate deformation. In 1972, Bonn *et al.* [Bon72] observed a large increase in  $\delta \langle r^2 \rangle$  for the ground

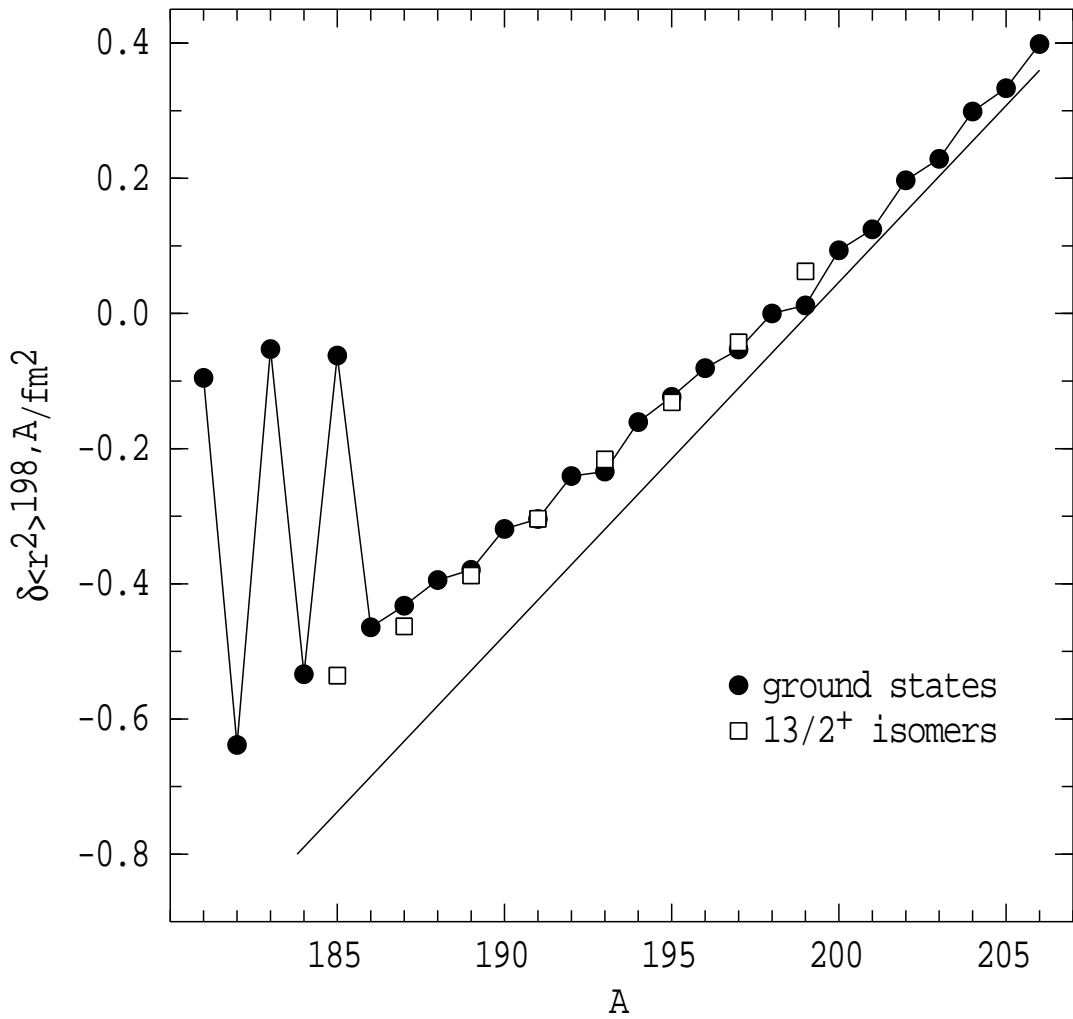


Figure 1.3: Changes in the square of the nuclear radius as deduced from laser spectroscopy on the mercury isotopes, with  $^{198}\text{Hg}$  taken as reference. Results are given for the ground states, and also for the  $\frac{13}{2}^+$  isomers which occur in the odd-mass isotopes. Note that the ground states do not all have the same configuration and hence have various spins and parities. (Data obtained and figure adapted from Ulm *et al.* [Ulm86].)

state of  $^{185}\text{Hg}$ , indicating an abrupt change in the nuclear shape<sup>1</sup>. Hyperfine structure measurements of the spin and magnetic moment of the ground state in  $^{185}\text{Hg}$  [Bon76] showed that it could be associated with the  $\frac{1}{2}^- [521]$  Nilsson state expected to be near the Fermi surface at a prolate deformation of  $\beta_2 \approx 0.25$ . Later measurements on the ground states of  $^{183}\text{Hg}$  and  $^{181}\text{Hg}$  produced similar results and conclusions.

Coexistence between two different shapes in  $^{185}\text{Hg}$  was first confirmed by laser measurements [Dab79], when a much smaller charge radius was deduced for the

<sup>1</sup>This was actually the first evidence for well-deformed shapes in the mercury region and provided the impetus for investigations of the even-mass isotopes.

low-lying  $\frac{13}{2}^+$  isomer compared to that of the  $\frac{1}{2}^-$  ground state (see Figure 1.3). (The  $\frac{13}{2}^+$  isomer in  $^{185}\text{Hg}$  and heavier odd-mass mercury isotopes is associated with an  $i_{13/2}$  neutron coupled to a weakly-oblate deformation. An equivalent isomer has not been observed in the lighter mercury isotopes.) It is only recently that in-beam  $\gamma$ -ray spectroscopy identified the collective bands built upon the  $\frac{1}{2}^- [521]$  ground state and the  $\frac{13}{2}^+$  isomer in  $^{185}\text{Hg}$  [Han88a]. The ground state band has a level structure like that expected for a prolate deformed  $\frac{1}{2}^- [521]$  band, while the positive parity states above the  $\frac{13}{2}^+$  isomer can be interpreted as excitations formed from the coupling of the  $i_{13/2}$  neutrons to both prolate and oblate cores. A similar interpretation can be applied to the states observed above the  $\frac{13}{2}^+$  isomer in  $^{187}\text{Hg}$  [Han88].

### 1.3.2 Thallium isotopes

The odd-mass thallium isotopes have  $Z = 81$  and may be considered as a proton particle or hole coupled to the even-even mercury or lead isotopes. The ground states have spin and parity  $\frac{1}{2}^+$ , formed from the  $s_{1/2}$  proton hole near sphericity. The neutron-deficient thallium isotopes also exhibit a low-lying isomer with spin and parity  $\frac{9}{2}^-$ , which is due to the  $\frac{9}{2}^- [505]$  state intruding from above the  $Z = 82$  shell gap at oblate deformation. (The oblate nature of the  $\frac{9}{2}^- [505]$  states has been confirmed by laser spectroscopy [Bou85].) Figure 1.4 shows that the energy of this intruder state minimises near the middle of the neutron shell just like the  $0_2^+$  state in the even-mass mercury isotopes. A similar behaviour is also observed for the  $\frac{13}{2}^+$  state (which is due to the  $\frac{13}{2}^+ [606]$  intruder orbital at oblate shape), although it has not yet been observed to a low enough mass number to define a minimum.

Recently, Porquet *et al.* [Por91] observed a rotational band in  $^{189}\text{Tl}$ , interpreted as being due to the  $i_{13/2}$  proton coupled to the prolate  $^{188}\text{Hg}$  core, the first evidence for prolate deformation in the thallium isotopes. They did not observe a prolate rotational band due to the  $h_{9/2}$  proton, even though the  $h_{9/2}$  orbitals lie lower in energy than the  $i_{13/2}$  orbitals at a prolate deformation of  $\beta_2 \approx 0.25$ . They interpreted this to mean that population of the  $h_{9/2}$  proton orbitals in the odd-mass nucleus blocks the  $(\pi h_{9/2})^2$  component in the prolate mercury core, thereby either raising the prolate  $h_{9/2}$  band in energy or blocking the prolate shape altogether. They did observe rotational bands due to *both* the  $i_{13/2}$  and  $h_{9/2}$  protons at *oblate* deformation.



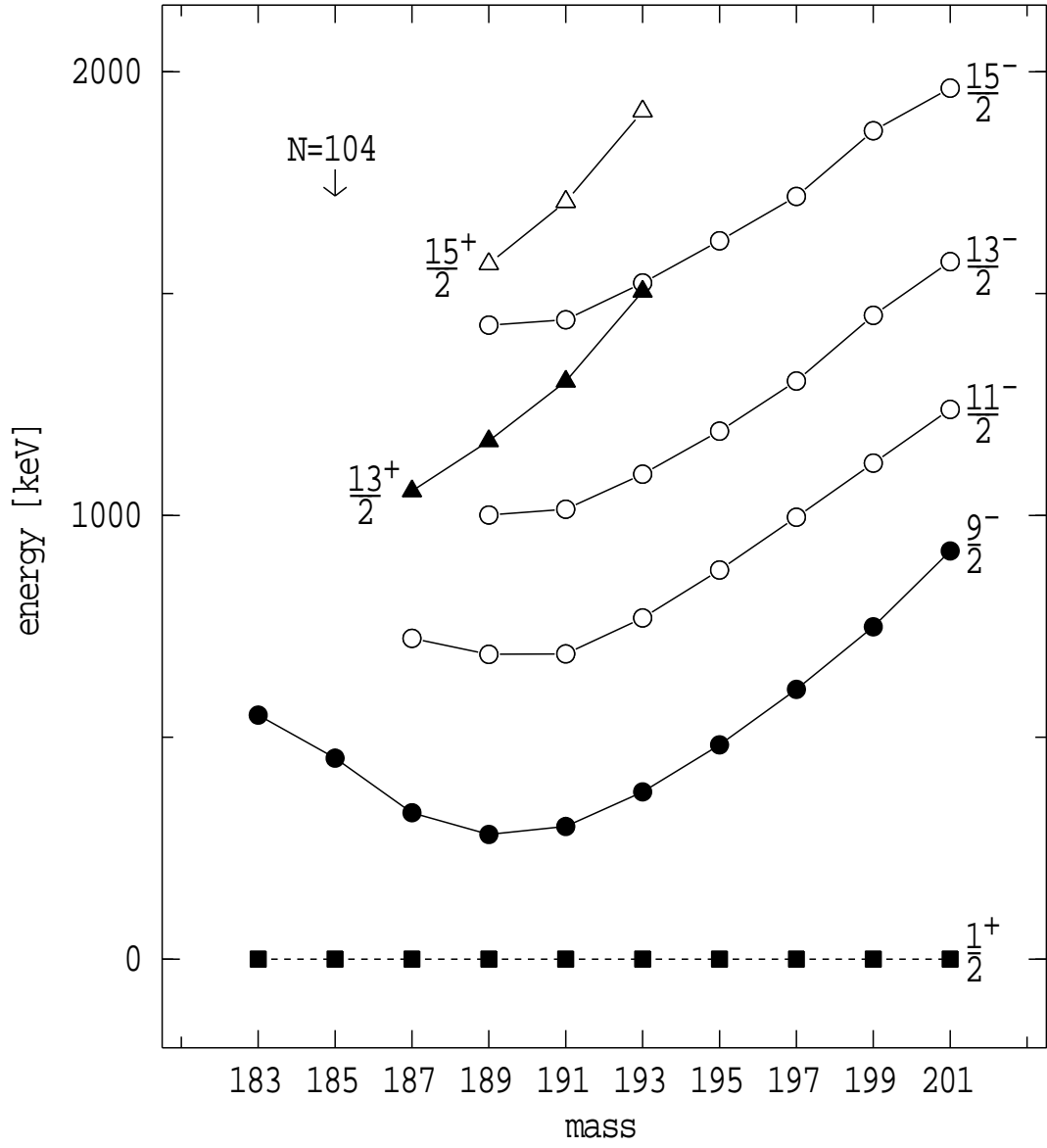


Figure 1.4: Systematics of the rotational bands built upon the oblate intruder states in the odd-mass thallium isotopes. Circles indicate states in the  $\frac{9}{2}^- [505]$  band, triangles indicate states in the  $\frac{13}{2}^+ [606]$  band. Filled symbols are used for the band-heads. Compare the rise and fall in energy of the  $\frac{9}{2}^-$  isomeric state with that seen for the  $0_2^+$  state in the mercury isotopes in Figure 1.2. (Data are taken from Refs. [Hey83, Rev95, Por91, Rev92, New74]. Note also that the absolute excitation energies of the  $\frac{9}{2}^-$  isomers in  $^{183}\text{Tl}$ ,  $^{187}\text{Tl}$ ,  $^{189}\text{Tl}$ ,  $^{191}\text{Tl}$  and  $^{193}\text{Tl}$  are not known precisely and have been variously estimated to within  $\pm 7$  to  $\pm 30$  keV. Further details may be found in Ref. [Hey83] and references therein.)

## 1.4 Scope of the Current Work

The various models which have been proposed to describe the shape coexisting states in near closed shell nuclei all suggest, in one fashion or another, that the coexisting states are due to particle-hole excitations across the closed shell into

strongly sloping intruder orbitals. In the  $Z \leq 82$  region, strongly sloping low- $\Omega$  orbitals from the  $h_{9/2}$ ,  $i_{13/2}$  and  $f_{7/2}$  proton shells all cross the Fermi surface at  $\beta_2 \approx 0.25$ , and occupation of these orbitals can be expected to favour a prolate deformation. The recent theoretical calculations by Nazarewicz [Naz93], have suggested that the prolate shape in the mercury and lead nuclei is associated with 4p-4h proton configurations rather than the  $(\pi h_{9/2})^2$  excitations detailed earlier. The current work seeks to identify the particular proton orbitals responsible for the prolate deformation by investigation of the odd-mass thallium isotopes. Studies of odd-mass mercury nuclei are also performed so as to ascertain whether or not particular neutron orbitals are important in stabilising the prolate shape.

This thesis reports the observation of high spin states in the most neutron-deficient odd-mass mercury and thallium isotopes yet studied in-beam,  $^{183}\text{Hg}$ ,  $^{185}\text{Tl}$  and  $^{187}\text{Tl}$ . At the beginning of this work, only very limited information from decay studies was available for  $^{183}\text{Hg}$  and  $^{185}\text{Tl}$ , and  $\gamma$ -rays had to be assigned to these nuclei *ab initio*. Some decay and preliminary in-beam results were available for  $^{187}\text{Tl}$ , and a few of the low-spin transitions in the level scheme were already known. During the course of this work, parallel and independent studies of  $^{187}\text{Tl}$  [Rev94] and  $^{183}\text{Hg}$  [Bin93, Shi95] were also reported.

The next chapter provides the theoretical background for the description of the rotational structures which can occur in odd-mass nuclei, finishing with details on the level structures which are “signatures” for shape coexistence. The experimental methods are described in Chapter 3, followed by the analysis and results chapter where the deduced level schemes are presented. The subsequent two chapters give evidence to support the assigned configurations. Chapter 7 presents the results of calculations of the equilibrium deformations, excitation energies and microscopic proton configurations for intrinsic states in the thallium nuclei. The results are used in conjunction with the experimental observations to deduce the proton structure of the even-even cores. Chapter 8 concentrates on the odd-mass mercury isotopes and presents the results of band-mixing calculations. These are used to investigate both the mixing matrix elements between the coexisting states and the E2 transition strengths. Finally, Chapter 9 summarises the results and presents the conclusions of this work.

# Chapter 2

## Theoretical Background

To investigate shape coexistence it is necessary to understand how the observed level structures can provide knowledge of the shape of the nucleus. This chapter gives a brief account of the theory of nuclear rotation, with special attention paid to the types of rotational bands which can occur. The last section indicates the particular band structures that would be “signatures” of shape-coexistence in odd-mass thallium and mercury nuclei.

### 2.1 Shape Parameters

The nuclear shape is often parameterised by an expansion of the radius,  $R$ , in terms of the spherical harmonics,

$$R = R(\theta, \phi) = C(\beta_{\lambda\mu})R_0 \left( 1 + \sum_{\lambda\mu} \beta_{\lambda\mu} Y_{\lambda\mu}(\theta, \phi) \right) \quad (2.1)$$

where  $C(\beta_{\lambda\mu})$  is a volume conservation factor, reflecting the fact that the nucleus is incompressible. This expansion is much simpler for a nucleus axially symmetric about the  $z$ -axis, as all but the  $\mu = 0$  terms vanish, thus defining the  $\beta_i = \beta_{\lambda 0}$  coordinates used in the calculations presented in Chapter 7.

For a nucleus with quadrupole ( $\lambda = 2$ ) deformation it is possible to rotate the coordinate system to obtain transformed coordinates,  $\tilde{\beta}_{\lambda\mu}$ , which satisfy  $\tilde{\beta}_{2-\mu} = \tilde{\beta}_{2\mu}$ , with  $\tilde{\beta}_{2\pm 1} = 0$ . The rotated coordinates may be again transformed according to

$$\tilde{\beta}_{20} = \beta \cos \gamma \quad (2.2)$$

$$\tilde{\beta}_{22} = \frac{1}{\sqrt{2}} \beta \sin \gamma \quad (2.3)$$

thus defining new coordinates  $(\beta, \gamma)$  in which the nucleus is axially symmetric whenever  $\gamma = n \times 60^\circ$  and is triaxial whenever  $\gamma$  is not a multiple of  $60^\circ$ . This triaxial parameterisation can also be generalised to the situation where  $\lambda = 4$  and other multipoles are used.

Another system often used is the  $(\epsilon_2, \epsilon_4)$  coordinates, which are related to the changes in the fundamental frequencies of a deformed harmonic oscillator and are discussed in §2.3 on the Nilsson model. A transformation between deformation coordinates is often required so as to compare the results of different calculations. The transformation between the  $(\beta_2, \beta_4)$  and  $(\epsilon_2, \epsilon_4)$  coordinates is given by

$$\epsilon_2 \approx 0.944\beta_2 - 0.122\beta_2^2 + 0.154\beta_2\beta_4 - 0.199\beta_4^2 \quad (2.4)$$

$$\epsilon_4 \approx -0.852\beta_4 + 0.141\beta_4^2 + 0.122\beta_2\beta_4 + 0.295\beta_2^2 \quad (2.5)$$

$$\beta_2 \approx 1.058\epsilon_2 + 0.141\epsilon_2^2 + 0.170\epsilon_2\epsilon_4 + 0.317\epsilon_4^2 \quad (2.6)$$

$$\beta_4 \approx -1.169\epsilon_4 + 0.234\epsilon_4^2 - 0.235\epsilon_2\epsilon_4 + 0.445\epsilon_2^2 \quad (2.7)$$

The  $(\beta_2, \beta_4) \rightarrow (\epsilon_2, \epsilon_4)$  transformation is taken from Ref. [Ben89a] and is valid for  $-0.2 \leq \beta_2 \leq 0.4$  and  $-0.05 \leq \beta_4 \leq 0.15$ . For large  $\epsilon_2$  and negative  $\epsilon_4$ , large  $\beta_6$  and  $\beta_8$  terms may be needed. The inverse transformation was deduced from a least squares fit to data points obtained using the forward transformation, and is valid in the approximate region  $-0.2 \leq \epsilon_2 \leq 0.36$  and  $-0.1 \leq \epsilon_4 \leq 0.1$ .

## 2.2 Collective Rotation

The variables required to describe a rotating nucleus are the Euler angles which characterise the orientation,  $\omega = (\phi, \theta, \psi)$ , and the intrinsic variables which describe the internal (particle) degrees of freedom,  $q$ . Under the adiabatic condition where the frequency of the internal motion of nucleons is much higher than the frequency of collective rotation, the collective and single-particle motions are separable and the total nuclear wavefunction may be considered as a product of the intrinsic wavefunction and the rotational wavefunction.

The angular momentum due to rotation,  $R$ , and the intrinsic angular momentum due to particle motion,  $j$ , couple together to give the total angular momentum,  $I$ , as shown in Figure 2.1. Two coordinate systems are defined in this figure, the intrinsic system  $(x', y', z')$  and the lab-fixed system  $(x, y, z)$ . The operators  $I_z$  and  $I_{z'}$  operate in different coordinates and commute with each

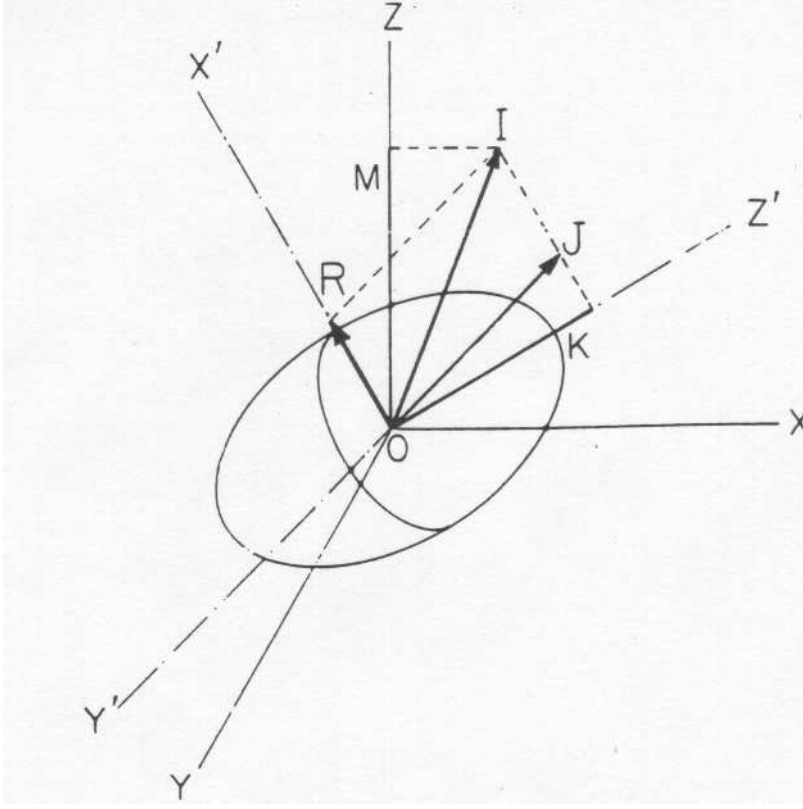


Figure 2.1: Angular momentum coupling for an axially symmetric nucleus. (Figure taken from Ejiri and de Voigt [Eji89].)

other, hence  $I_z = M$  and  $I_{z'} = K$  are both conserved. (Note also that Figure 2.1 describes a nucleus axially symmetric about the  $z'$ -axis so that  $I_{z'} = j_{z'}$ .)

For an axially symmetric system, the nuclear wavefunction is given by [Boh75]

$$\Psi_{IKM} = \sqrt{\frac{2I+1}{16\pi^2}} \left( \Phi_K(q) \mathcal{D}_{MK}^I(\omega) + (-1)^{I+K} \Phi_{\bar{K}}(q) \mathcal{D}_{M-K}^I(\omega) \right) \quad (2.8)$$

where  $\Phi_K(q)$  is the intrinsic wavefunction with  $j_{z'} = K$  and  $\mathcal{D}_{MK}^I(\omega)$  are the wavefunctions of the symmetric top.  $\Phi_{\bar{K}}(q)$  denotes the intrinsic wavefunction with  $j_{z'} = -K$ , obtained by rotating the intrinsic coordinate system through an angle  $\pi$  around an axis perpendicular to the symmetry axis. For a particular intrinsic state,  $\Phi_K(q)$ , a rotational band consisting of states with angular momentum  $I \geq K$  can be formed. In the special case of  $K = 0$ , since  $K = \bar{K}$ , the rotational band only contains either odd or even values of  $I$  [Boh75].

The quantity  $(-1)^{I+K}$  in equation (2.8) is known as the signature and changes sign for alternating spin values. This separates the states in a rotational band into two sequences with  $I = K, K+2, \dots$  and  $I = K+1, K+3, \dots$  respectively. The signature is more commonly denoted by the quantum number,  $\alpha$ , defined by

$$\begin{aligned} \alpha &= I \bmod 2 \\ &= \begin{cases} 0 & \text{for } I = 0, 2, 4, \dots \\ 1 & \text{for } I = 1, 3, 5, \dots \\ \frac{1}{2} & \text{for } I = \frac{1}{2}, \frac{5}{2}, \frac{9}{2}, \dots \\ -\frac{1}{2} & \text{for } I = \frac{3}{2}, \frac{7}{2}, \frac{11}{2}, \dots \end{cases} \end{aligned} \quad (2.9)$$

## 2.3 Nilsson Model

To characterise the intrinsic wavefunction,  $\Phi_K(q)$ , it is necessary to consider what happens to the single particle orbits in a deformed nucleus. The first comprehensive deformed shell model calculations were performed by Nilsson [Nil55] using a spheroidal oscillator potential

$$V = \frac{m}{2}(\omega_{\perp}^2(x'^2 + y'^2) + \omega_{z'}^2 z'^2) \quad (2.10)$$

It is instructive to introduce the deformation parameter,  $\epsilon_2$ , by

$$\omega_{z'} = \omega_0(\epsilon_2)(1 - \frac{2}{3}\epsilon_2) \quad (2.11)$$

$$\omega_{\perp} = \omega_0(\epsilon_2)(1 + \frac{1}{3}\epsilon_2) \quad (2.12)$$

The oscillator frequency,  $\omega_0$ , is defined by the condition of constant volume,

$$\omega_{z'}\omega_{\perp}^2 = \overset{o}{\omega}_{p/n}^3 \quad (2.13)$$

and it is usual to choose  $\hbar \overset{o}{\omega}_0 = 41A^{-1/3}$  MeV, with,

$$\overset{o}{\omega}_p = \overset{o}{\omega}_0 \left(1 + \frac{N - Z}{3A}\right) \quad (2.14)$$

$$\overset{o}{\omega}_n = \overset{o}{\omega}_0 \left(1 - \frac{N - Z}{3A}\right) \quad (2.15)$$

so as to give the correct nuclear radius for protons and neutrons [Nil69].

In terms of  $\epsilon_2$ , the quadrupole part of the potential is approximately proportional to  $\epsilon_2 r^2 P_2(\cos \theta)$ . This term has non-zero matrix elements between shells differing by  $\Delta N = 2$ , however, these can be removed by a transformation to the stretched coordinates  $(\xi, \eta, \zeta) = \sqrt{m\omega_{\perp}/\hbar} (x', y', z')$  [Nil69].

Because the harmonic oscillator potential has infinite walls, the different orbital angular momentum states are degenerate. In a more realistic finite well, the

high angular momentum states are more bound, an effect artificially introduced to the oscillator potential by the addition of a term proportional to  $l^2$ . After also including a spin-orbit force, as well as a hexadecapole deformation coordinate,  $\epsilon_4$ , the Nilsson potential in stretched coordinates is [Nil69]

$$V = \frac{1}{2}\hbar\omega_0(\epsilon_2, \epsilon_4)\rho^2\left[1 - \frac{2}{3}\epsilon_2 P_2(\cos\theta_t) + 2\epsilon_4 P_4(\cos\theta_t)\right] - 2\kappa\hbar\omega_0[l_{t.s} - \mu(l_t^2 - \langle l_t^2 \rangle)] \quad (2.16)$$

Here  $\langle l_t^2 \rangle$  describes the orbital angular momentum averaged over all states in a major shell,  $N$ . The parameters  $\kappa$  and  $\mu$  describe the strengths of the spin-orbit and potential flattening terms, and are different for each major shell and for protons and neutrons. A “Universal” set of values chosen to reproduce energy levels in a wide range of nuclei may be found in Ref. [Ben85]. (See however, §5.4.)

In the limit of large quadrupole deformation, the  $l.s$ ,  $l^2$  and  $\epsilon_4 P_4(\cos\theta_t)$  terms may be neglected, in which case the Hamiltonian is diagonal in  $l$ ,  $l_{z'}$ ,  $j$  and  $j_{z'}$ . The eigenfunctions may be labelled by the “asymptotic” quantum numbers,  $[Nn_z\Lambda]$ , where  $N$  is the total number of oscillator quanta,  $n_z$  is the number of oscillator quanta along the  $z'$ -axis, and  $\Lambda$  is the projection  $l_{z'}$ .

For smaller deformations, the Hamiltonian is no longer diagonal in  $j$ , however, the projection  $j_{z'}$ , denoted by  $\Omega$ , is still a good quantum number. The states are labelled by the asymptotic quantum numbers together with  $\Omega$  and the parity,  $\pi$ , i.e.  $\Omega^\pi[Nn_z\Lambda]$ . The energy eigenvalues obtained with this potential as a function of quadrupole deformation (Nilsson diagrams) are plotted in Figure 5.1 for protons (p87) and Figure 6.1 for neutrons (p97).

As the deformation increases, certain levels with the same  $\Omega^\pi$  and from the same shell come closer in energy, interact and eventually repel one another while exchanging character. A level which originates from one spherical state at zero deformation can have a completely different nature at large deformation. For example, the  $\frac{5}{2}^- [512]$  orbital in Figure 6.1, has asymptotic quantum numbers indicating it originates from the  $f_{7/2}$  spherical state, although at zero deformation it leaves the  $h_{9/2}$  multiplet. This is due to the level “crossing” at  $\epsilon_2 \approx 0.1$  between the  $\frac{5}{2}^- [512]$  and  $\frac{5}{2}^- [523]$  states.

The Nilsson states may be expressed as a linear combination of the spherical states with good  $j$ ,

$$\Phi_\Omega(q) = \sum_{jl} C_{jl}^\Omega |Nlj\Omega\rangle \quad (2.17)$$

A tabulation of the coefficients  $C_{jl}^\Omega$  as a function of deformation may be found in the paper by Chi [Chi66]. This expansion can be used to evaluate Coriolis matrix elements connecting single particle states (see §2.5), as well as the magnetic moments of single particle states (see Appendix A).

Although most Nilsson states have mixed- $j$ , some states are reasonably pure. For example, in Figure 6.1 (p97) it can be seen that the  $i_{13/2}$ ,  $N = 6$  neutron orbitals with positive parity, have been lowered by the spin-orbit interaction to lie in the midst of the  $N = 5$  negative parity orbitals, with which they do not interact. The  $i_{13/2}$  orbitals are referred to as unique parity states and are essentially pure  $j = \frac{13}{2}$ , at least for moderate deformations.

## 2.4 The Pairing Interaction

Evidence for the existence of a strong monopole pairing between like nucleons comes from observations such as the differences in mass between odd and even nuclei and the existence of an energy gap between the ground state of an even-even nucleus and its excited intrinsic states.

The pairing force is a short-range, attractive force which tends to couple nucleons into time-reversed orbits so there is maximum spatial overlap between them. Thus, the pairing forces can be considered to scatter pairs of particles between the different single particle states, always producing and destroying pairs of particles in time-reversed orbits. The single particle Hamiltonian with pairing is

$$H = H_p + \Delta(P^+ + P) - \lambda N \quad (2.18)$$

where  $H_p$  is the single-particle Hamiltonian and  $P^+$  and  $P$  create and destroy pairs of particles in time-reversed orbits. This Hamiltonian does not conserve the number of nucleons exactly, however, the inclusion of the Lagrange multiplier term,  $-\lambda N$ , allows the reproduction (on average) of the nucleon number,  $N$ , by suitable choice of the Fermi energy,  $\lambda$ .

In the presence of pairing, the experimentally observed spectrum of single particle states is not given by the Nilsson energies, but is instead given by the quasiparticle energies,

$$E_{qp} = \sqrt{(\epsilon_K - \lambda)^2 + \Delta^2} \quad (2.19)$$



The pairing produces a gap in the energy spectrum of width  $2\Delta$  around the Fermi level. This pairgap is responsible for the absence of 2-quasiparticle excited states just above the ground state in even-even nuclei as well as for the odd-even mass differences. Thus the parameter,  $\Delta$ , in equations (2.18) and (2.19), may be estimated from the odd-even mass differences [Möl92].

Under the influence of pairing, the single particle levels obtained from  $H_p$  are no longer occupied by integral numbers of particles, but are instead occupied by fractions of pairs of particles, with the occupation probability,  $V_K^2$ , given by

$$V_K^2 = \frac{1}{2} \left( 1 - \frac{\epsilon_K - \lambda}{\sqrt{(\epsilon_K - \lambda)^2 + \Delta^2}} \right) \quad (2.20)$$

Note that single particle levels far below the Fermi surface are fully occupied,  $V_K^2 \approx 1$ , those far above not occupied,  $V_K^2 \approx 0$ , while those near the Fermi surface have partial occupation, with  $V_K^2 \approx \frac{1}{2}$ . The Fermi energy,  $\lambda$ , is chosen to satisfy  $\sum_K 2V_K^2 = N$ , where  $N$  is the number of nucleons. The probability of the single particle levels being empty of a pair is  $U_K^2 = 1 - V_K^2$ . (Note that an alternative definition of  $V_K^2$  is used in Chapter 7, where the occupation probability is in terms of particles, not pairs of particles, and ranges between 0 and 2.)

## 2.5 Particle-Rotor Model

The Hamiltonian for collective rotation may be expressed as  $\frac{\hbar^2}{2\mathfrak{I}}R^2$ , where  $\mathfrak{I}$  is the nuclear moment-of-inertia, so that the total nuclear Hamiltonian is

$$H = H_p + \frac{\hbar^2}{2\mathfrak{I}}R^2 \quad (2.21)$$

The single-particle Hamiltonian,  $H_p$ , may be obtained, for example, from the Nilsson model. The coupling between the core angular momentum,  $R$ , and the single particle angular momentum,  $j$ , can be written as  $R = I - j$ , and is illustrated in Figure 2.1. The figure shows an axially symmetric nucleus for which the projection of the total angular momentum,  $I_{z'} = K$ , is equal to the projection of the single particle angular momentum,  $j_{z'}$ , denoted by  $\Omega$  in the Nilsson model.

Writing  $R^2 = I^2 + j^2 - 2I \cdot j$ , equation (2.21) can be expanded to give

$$H = H_p + \frac{\hbar^2}{2\mathfrak{I}}(I(I+1) - K^2) + \frac{\hbar^2}{2\mathfrak{I}}(\langle j^2 \rangle - \Omega^2) - 2\frac{\hbar^2}{2\mathfrak{I}}(I_{x'}j_{x'} + I_{y'}j_{y'}) \quad (2.22)$$

The second term is the energy of a rotor with  $I_{z'} = K$ . The third term, called the recoil term, only depends on the single particle degrees of freedom and is often either ignored or absorbed into  $H_p$ . The final term, called the Coriolis term, contains both Coriolis and centrifugal effects and can be rearranged to give

$$H_c = -2\frac{\hbar^2}{2\mathfrak{I}}(I_{x'}j_{x'} + I_{y'}j_{y'}) = -\frac{\hbar^2}{2\mathfrak{I}}(I_+j_- + I_-j_+) \quad (2.23)$$

The Coriolis term obviously connects states differing by  $\Delta K = 1$ . It is also diagonal for  $K = \frac{1}{2}$  states because the rotational wavefunction given in equation (2.8) contain both  $K$  and  $-K$  components. The matrix elements of  $H_c$  are

$$\langle I, K \pm 1 | H_c | I, K \rangle = -\frac{\hbar^2}{2\mathfrak{I}} \sqrt{(I \mp K)(I \pm K + 1)} \langle K \pm 1 | j_{\pm} | K \rangle \quad (2.24)$$

where the matrix element  $\langle K \pm 1 | j_{\pm} | K \rangle$  can be obtained from the Nilsson state expansion given in equation (2.17), with the result

$$\langle K \pm 1 | j_{\pm} | K \rangle = \sum_j C_{jl}^K C_{jl}^{K \pm 1} \sqrt{(j \mp K)(j \pm K + 1)} \quad (2.25)$$

$$\langle K = \frac{1}{2} | j_{\pm} | K = \frac{1}{2} \rangle = \sum_j C_{jl}^{\frac{1}{2}} C_{jl}^{\frac{1}{2}'} (-1)^{j-\frac{1}{2}} (j + \frac{1}{2}) \quad (2.26)$$

Due to pairing correlations these Coriolis matrix elements should be multiplied by the factor  $U_K U_{K \pm 1} + V_K V_{K \pm 1}$  [Boh75].

Depending on the relative magnitudes of the Coriolis and rotor terms in equation (2.22), different rotational level structures can occur. Coriolis effects are smallest for orbitals with low  $j$  and high  $\Omega$ , so that when the Fermi level is near the high- $\Omega$  orbitals,  $K$  is a good quantum number and the angular momentum of the particle is coupled to the deformation axis as shown in Figure 2.2. The rotational energies are approximately given by

$$E_I \approx E_K + \frac{\hbar^2}{2\mathfrak{I}}(I(I+1) - K^2) \quad (2.27)$$

where  $E_K$  is the energy of the intrinsic state with  $j_{z'} = K$ , upon which the band is built.

Orbitals with large  $j$  and small  $\Omega$  experience large Coriolis effects. It is of interest to first diagonalise the Hamiltonian in a space consisting of just one  $\Omega = \frac{1}{2}$  orbital. The rotational energy is given by [Boh75]

$$E_I = E_{K=1/2} + \frac{\hbar^2}{2\mathfrak{I}} \left( I(I+1) + a(-1)^{I+1/2}(I+1/2) \right) \quad (2.28)$$

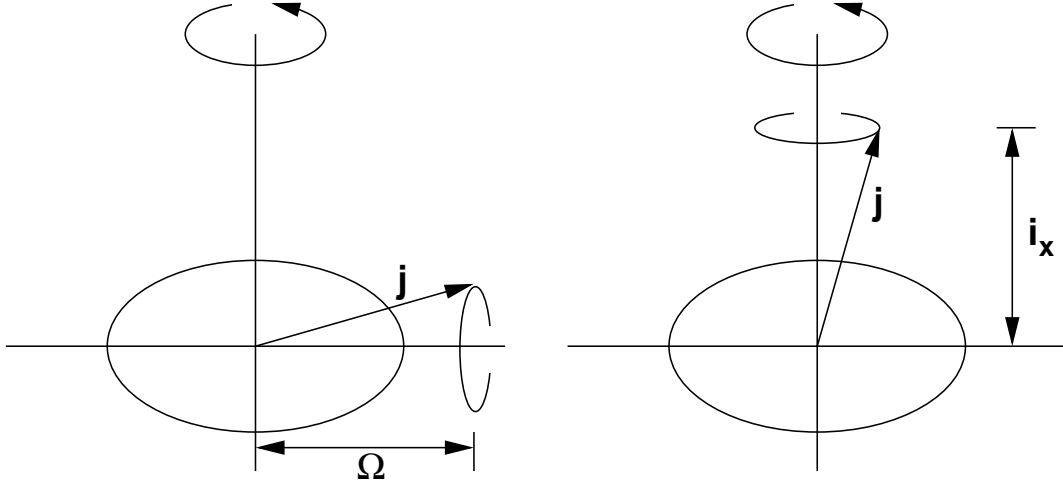


Figure 2.2: Coupling of the single-particle angular momentum for deformation alignment on the left and rotation alignment on the right.

where the decoupling parameter,  $a$ , has been introduced. It is calculated from the Nilsson expansion in equation (2.17) and is given by

$$a = \sum_j (C_{jl}^{\Omega=\frac{1}{2}})^2 (-1)^{j-1/2} (j + 1/2) \quad (2.29)$$

Note that the decoupling parameter is just the diagonal matrix element of  $j_+$ .

For a  $K = \frac{1}{2}$  band, the decoupling parameter has the effect of lowering one signature in energy compared to the other. For a pure- $j$  orbital, examination of equations (2.28) and (2.29) reveals that the signature which contains the state with spin  $I = j$  will be favoured in energy.

If the particle-rotor Hamiltonian is diagonalised within a set of high- $j$  states, the effects of the diagonal contribution to the  $K = \frac{1}{2}$  band are strongly propagated through to the other rotational bands via the Coriolis term. In the limit of very large Coriolis forces when the Fermi level is close to the  $\Omega = \frac{1}{2}$  orbitals, the particle angular momentum decouples from the deformation axis and couples instead to the rotation axis as shown in Figure 2.2. For complete decoupling,  $i_x \approx j$ , and the unfavoured signature is pushed high in energy, so typically only the favoured signature is observed. The separation of the energy levels is comparable to that expected in the even-even core nucleus, the rotational energies being given approximately by

$$E_I \approx E_K + \frac{\hbar^2}{2\mathfrak{I}} (I - j)(I - j + 1) \quad (2.30)$$

The two limiting cases are known as deformation alignment and rotation align-

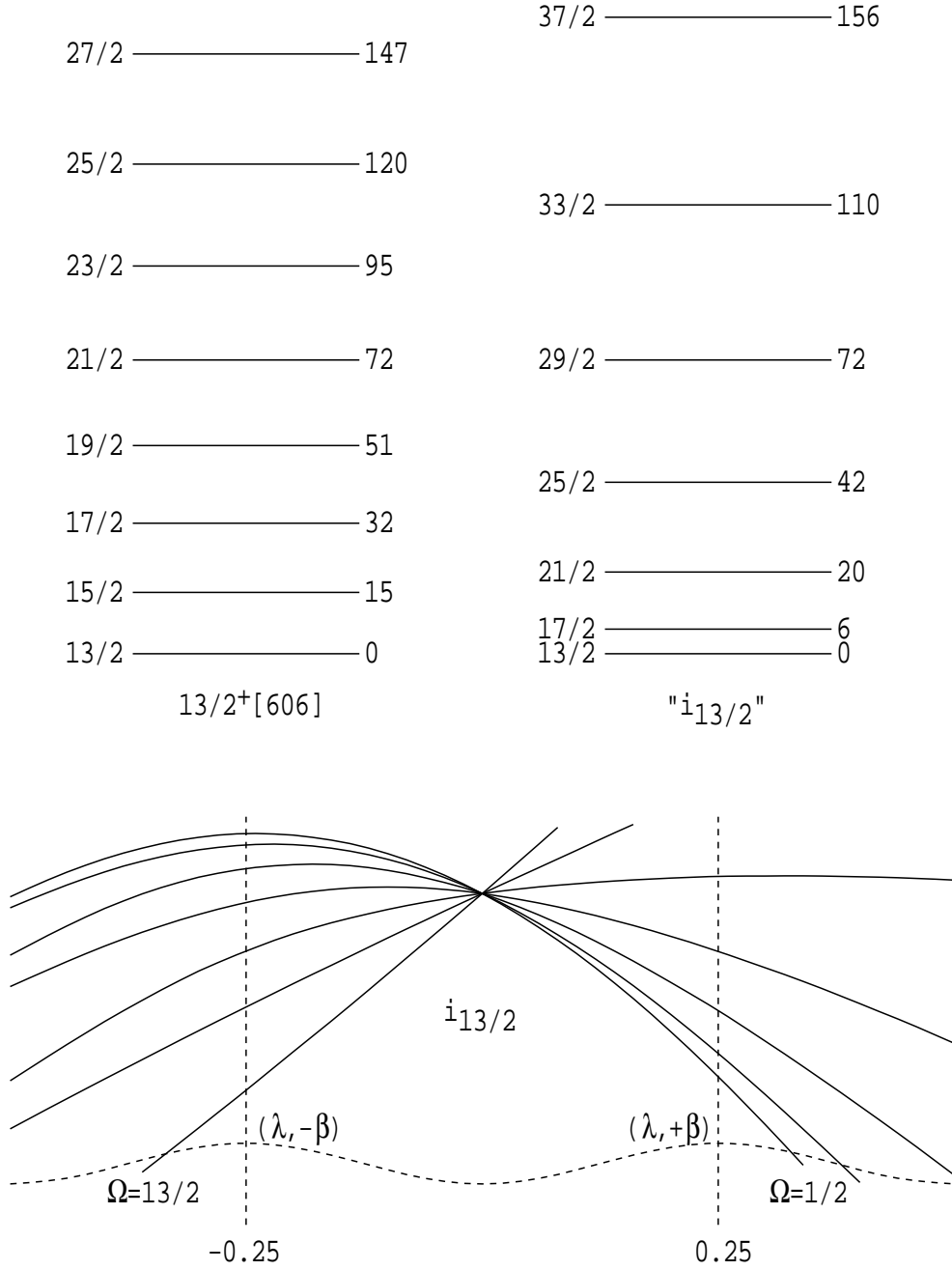


Figure 2.3: Idealised rotational bands for the two situations of deformation alignment (on the left) and rotation alignment (on the right). These would be the lowest energy levels obtained by diagonalising the particle-rotor Hamiltonian in the space of  $i_{13/2}$  orbitals with the Fermi level near the high- $\Omega$  and low- $\Omega$  orbitals at oblate and prolate deformation respectively. The labelled energies are in units of  $\frac{\hbar^2}{2\mathcal{I}}$  and are obtained from equations (2.27) and (2.30).

ment and the associated band structures are often referred to as strongly-coupled and decoupled respectively. This describes the fact that  $j$  is either coupled or decoupled from the deformation axis, as shown in Figure 2.2. The rotational band energies for the two limiting cases, as given by equations (2.27) and (2.30),

are compared in Figure 2.3 for a  $\frac{13}{2}^+[606]$  deformation aligned band and an  $i_{13/2}$  rotation aligned band. Further information on the particle-rotor model may be found in the review article by Stephens [Ste75].

## 2.6 Cranked Shell Model

It is often useful to transform the experimentally observed quantities such as the excitation energy and spin, into the rotating frame of the nucleus. This makes it possible to separate the collective and quasiparticle properties of the nucleus, at the expense however, of having to deal with quantities in terms of the rotational frequency,  $\omega$ , rather than the experimentally observed quantity,  $I$ . The excitation energy in the rotating system is known as the Routhian and is given by [Ben79]

$$E^\omega = E - \hbar\omega I_x \quad (2.31)$$

(Note that  $I_x$  denotes the projection of the total angular momentum on the rotational axis. Previously in Figure 2.1 this was called the  $x'$ -axis.) In terms of experimental quantities the Routhian is defined by

$$E^\omega(I) = \frac{E(I+1) + E(I-1)}{2} - \hbar\omega(I)I_x(I) \quad (2.32)$$

where  $I_x$  can be seen from Figure 2.1 to be

$$I_x(I) = \sqrt{I(I+1) - K^2} \approx \sqrt{(I + \frac{1}{2})^2 - K^2} \quad (2.33)$$

The rotational frequency,  $\omega$ , can be estimated from the classical expression,  $\omega = \frac{dE}{dI_x}$ , to be

$$\hbar\omega(I) = \frac{E(I+1) - E(I-1)}{I_x(I+1) - I_x(I-1)} \quad (2.34)$$

From these equations applied at each spin value a locus of points can be obtained which defines the experimental Routhian, however, this still includes a component due to the collective rotation. This collective component can be characterised by a frequency dependent moment-of-inertia,  $\mathfrak{I}(\omega)$ , which can be parameterised using the Harris expansion [Har65]

$$\mathfrak{I}(\omega) = \mathfrak{I}_0 + \mathfrak{I}_1\omega^2 \quad (2.35)$$

The collective rotational energy,  $E_g(\omega)$ , and collective angular momentum,  $I_{xg}(\omega)$ , are then given by

$$E_g(\omega) = -\frac{\omega^2}{2}\mathfrak{S}_0 - \frac{\omega^4}{4}\mathfrak{S}_1 + \frac{1}{8\mathfrak{S}_0} \quad (2.36)$$

$$I_{xg}(\omega) = \mathfrak{S}\omega = \mathfrak{S}_0\omega + \mathfrak{S}_1\omega^3 \quad (2.37)$$

The subscript  $g$  is used because this reference configuration is often obtained from fitting the low frequency region of the ground state band of a nearby even-even nucleus where there are no quasiparticle excitations.

It is now possible to define the quasiparticle Routhian,  $e'(\omega)$ , and aligned angular momenta,  $i_x(\omega)$ , by subtraction of the collective components,

$$e'(\omega) = E^\omega(\omega) - E_g(\omega) \quad (2.38)$$

$$i_x(\omega) = I_x(\omega) - I_{xg}(\omega) \quad (2.39)$$

These quasiparticle properties,  $e'$  and  $i_x$ , are additive quantities, so that the alignments and Routhians for multi-quasiparticle states can be constructed from those measured for the single-quasiparticle states. One must remember however, that the additivity rests upon the assumption of identical reference configurations described by equation (2.35) for all of the single-quasiparticle states.

Theoretical Routhians are obtained by “cranking” the single particle Hamiltonian. This is done by including a term  $-\hbar\omega I_x$  in the Hamiltonian, equivalent to rotating the nucleus around the  $x$ -axis. The cumulative effect on the single particle levels after adding various terms to the Hamiltonian is shown in Figure 2.4.

The cranking term incorporates the Coriolis and centrifugal forces and mixes the orbitals of different  $\Omega$  so that  $j_z$  is no longer conserved, and only the signature,  $\alpha$ , and the parity,  $\pi$ , remain good quantum numbers. The right-hand part of Figure 2.4 gives examples of theoretical Routhians. Such plots can be used to deduce the aligned angular momentum,  $i_x$ , using the relation

$$i_x = -\frac{\partial e'}{\partial \omega} \quad (2.40)$$

The theoretical Routhians and alignments are usually compared with experiment, however, because detailed comparisons were not performed for the nuclei investigated in this thesis, full details of the Cranked Shell Model are not presented here. (See Ref. [Ben79] for more information on the CSM.) Since a brief comparison of alignment frequencies in the mercury isotopes is presented in Chapter 6, the phenomenon of particle alignment is briefly discussed.

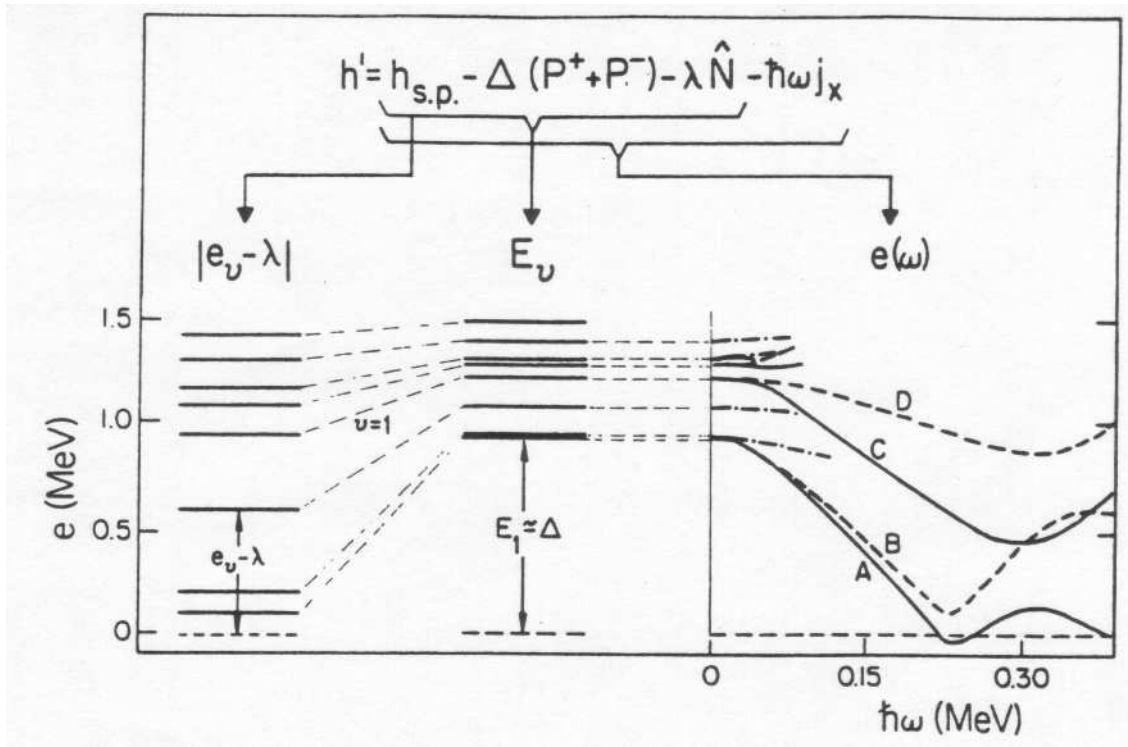


Figure 2.4: The figure is taken from Ref. [Eji89] and shows the cumulative effects of adding terms to the single particle Hamiltonian.

In an even-even nucleus the ground state band has signature and parity  $(0,+)$ , and, at low frequency, is formed by filling all the negative energy levels up to the Fermi level. At  $\hbar\omega \approx 0.25$  MeV in Figure 2.4, the two lowest positive energy levels interact with the two highest negative energy levels. This corresponds to the ground state band changing configuration to the S-band, with the levels labelled A and B now occupied and the two associated quasiparticles aligning their angular momenta with the rotation axis. The change in slope of the Routhians implies an increase in aligned angular momentum (see equation (2.40)), known as an upbend or backbend. In an odd-mass nucleus, a quasi-particle will occupy one of the positive energy levels and certain band-crossings can be blocked, resulting in the observation of different alignment frequencies.

## 2.7 “Signatures” of Shape Coexistence

The Nilsson diagram for protons (p 87) shows that the Fermi level for the thallium nuclei at prolate deformation lies amongst the low- $\Omega$  orbitals of the  $i_{13/2}$ ,  $h_{9/2}$  and  $f_{7/2}$  shells. These high- $j$  orbitals experience large Coriolis forces so that the prolate deformed odd-mass thallium isotopes are expected to exhibit rotation-

aligned bands due to the  $i_{13/2}$ ,  $h_{9/2}$  and  $f_{7/2}$  protons. Indeed in  $^{189}\text{Tl}$ , Porquet *et al.* [Por91] observed a rotation-aligned band with signature and parity  $(\frac{1}{2}, +)$  that they assigned as an  $i_{13/2}$  rotational band corresponding to prolate deformation.

At oblate deformation, the proton Fermi level for the thallium isotopes lies amongst the high- $\Omega$  orbitals of the same shells. These orbitals have  $\Omega = j$  so that strongly coupled band structures are expected. Such bands are seen experimentally, built upon the  $\frac{9}{2}^- [505]$  and  $\frac{13}{2}^+ [606]$  intrinsic states in  $^{189}\text{Tl}$  and the heavier isotopes (see §1.3.2 and Refs. [Hey83, Rev95, Por91, Rev92, New74]).

Such a coexistence between deformation and rotation-aligned bands due to the same high- $j$  protons is characteristic of shape coexistence in odd-proton nuclei near closed proton shells. Another good example is provided by the iodine nuclei with  $Z = 53$  (just above the  $Z = 50$  closed shell), which exhibit rather complete decoupled and strongly coupled band structures built upon low- $\Omega$  and high- $\Omega$  orbitals from the  $h_{11/2}$  proton [Lia90, Lia92].

The signatures for shape coexistence in the odd-neutron nuclei near the  $Z = 82$  closed proton shell are not as clear cut. Nevertheless, the deformation can often be deduced from the observed level structures after consideration of the available neutron orbitals at the different deformations. The situation is simplified for the positive parity states in the neutron-deficient mercury nuclei because the only positive parity orbitals available are those from the  $i_{13/2}$  shell. (See the Nilsson diagram on page 97.) For  $N \approx 104$ , the neutron Fermi level is near the middle of the  $i_{13/2}$  shell and the high- $j$  nature of the orbitals implies that signature splitting is expected at both prolate and oblate deformation. However, at weak oblate deformation the orbitals are more compressed in energy than at the larger prolate deformation, resulting in greater Coriolis mixing and the formation of a rotation aligned band. Such bands are observed in all the odd-mass mercury nuclei with  $A \geq 185$ , built upon a  $\frac{13}{2}^+$  isomer [Han88a, Han88, Beu74, Pro74a]. In contrast, the prolate  $i_{13/2}$  band will exhibit a smaller signature splitting, resulting in a level structure somewhere in between the idealised rotation and deformation aligned limits discussed in §2.5. Such bands are observed in  $^{185}\text{Hg}$  [Han88a] and  $^{187}\text{Hg}$  [Han88], coexisting with the oblate, decoupled bands built upon the  $\frac{13}{2}^+$  isomers.



# Chapter 3

## Methods of $\gamma$ -ray Spectroscopy

This chapter describes some of the apparatus and techniques used to perform  $\gamma$ -ray spectroscopy, beginning with the use of heavy ion fusion reactions to produce nuclei at high spin. Gamma-ray detection and the characteristics of the CAESAR Compton-suppressed detector array are also discussed. Finally, the sorting of the data, the measurement of nuclear lifetimes and the assignment of transition multipolarities are described. Details particular to the experiments performed for this thesis are presented where appropriate.

### 3.1 Heavy Ion Fusion Reactions

Some of the methods used to produce an excited nucleus include Coulomb excitation and transfer and neutron capture reactions, however, the most widely used method is the heavy ion fusion reaction. (For reviews see Refs. [New74a, Pel82].) When an incident ion has enough energy to overcome the Coulomb barrier between it and a target nucleus, there is a probability that the two nuclei will fuse together and create a hot, spinning compound system, as shown in Figure 3.1. The compound nuclei are formed with their spins aligned in a plane perpendicular to the beam direction, thus allowing the possibility of measuring angular distributions of the emitted particles or  $\gamma$ -rays with respect to the beam axis. Conservation of linear momentum implies that the nuclei all recoil with a well-defined speed which is typically 1–5% of the speed of light. The Doppler shifts of the emitted  $\gamma$ -rays can be used to both distinguish between different reaction mechanisms and also enable the measurement of level lifetimes [Pel82].

Initially, the cooling of the compound nucleus occurs by the evaporation of light particles. The ratio of the decay widths for neutron and proton emission is

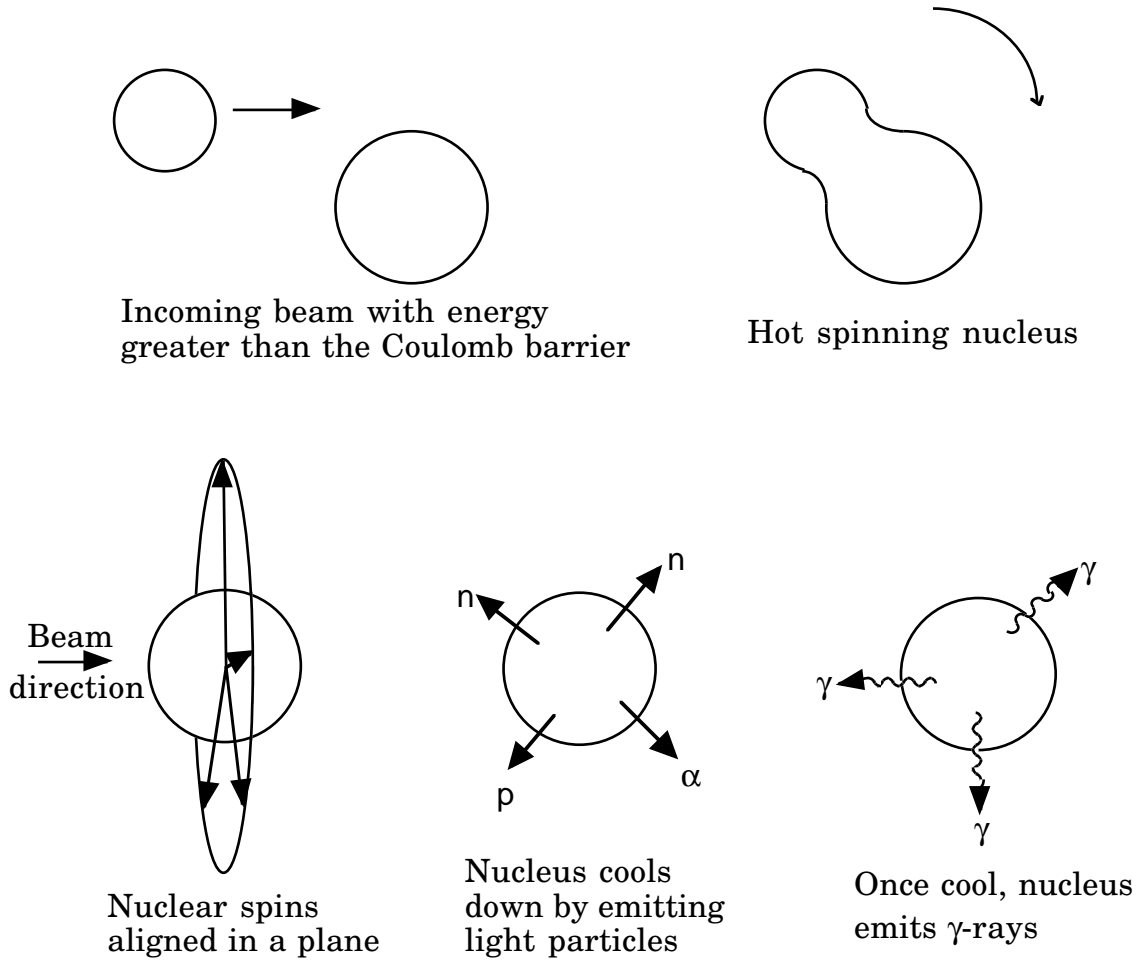


Figure 3.1: Schematic picture of a heavy-ion fusion reaction.

given approximately by [Bas80]

$$\frac{\Gamma_\nu}{\Gamma_p} \sim \exp\left(\frac{V_{C_p} + B_p - B_\nu}{T}\right) \quad (3.1)$$

where  $T$  is the nuclear temperature,  $V_{C_p}$  is the Coulomb barrier for the proton and  $B_p$  and  $B_\nu$  are the proton and neutron binding energies. (The analogous expression for alpha-particle versus neutron emission is easily obtained.) For nuclei near stability neutron emission is favoured, however, when  $B_p$  decreases, the probability of proton emission increases. As the proton drip line is approached,  $B_p \rightarrow 0$ , and the exponential in equation (3.1) means that the emission of protons becomes highly probable over a change of just a couple of mass units.

It is also possible for the compound nucleus to fission, with this probability increasing quickly with the angular momentum of the compound nucleus. Hence the fission cross-section rapidly rises with increasing beam energy [Bas80].

Once a number of particles have been evaporated and the nucleus is bound

to particle emission, cooling occurs by  $\gamma$ -ray emission. At this point the nuclear level density is high and at first a series of statistical E1 transitions are emitted. Eventually regions of low state density are reached, until finally the nucleus is constrained to decay along the yrast line<sup>1</sup>. These yrast states are the most strongly populated, resulting in a discrete  $\gamma$ -ray spectrum overlaying an unresolved, statistical continuum.

### 3.1.1 Statistical model calculations

The nuclei under investigation in this thesis are very neutron-deficient. As an illustration, the mass tables of Audi and Wapstra [Aud93] predict that the proton drip line for thallium and mercury isotopes lies near  $^{183}\text{Tl}$  and  $^{174}\text{Hg}$ . This means that for the compound nuclei formed in the current series of experiments, the probability for charged particle emission is large, and, because both charged particle and neutron evaporation are possible, there is a fragmentation of the residue cross-section amongst the various (HI, $xpynz\alpha$ ) channels. Also, the compound nuclei have a high probability for fission, lowering the absolute production cross-section for the evaporation residues.

The statistical model code PACE2 [Gav80] has been used to calculate the cross-section for formation of different evaporation residues after compound nucleus decay. Sample calculations for the reactions used in this work to make  $^{187}\text{Tl}$  and  $^{183}\text{Hg}$  appear in Figure 3.2, indicating also the range of energies sampled in the thick target experiments as the beams slow down in the target (see Table 4.1).

The top panels show the results of calculations using liquid drop fission barriers, while the lower panels show the effect of lowering the fission barriers by 20%. Addressing firstly the calculations with unadjusted barriers, the reaction chosen to make  $^{187}\text{Tl}$  is predicted to be selective, with little proton emission and a small fission cross-section for energies close to the barrier. This contrasts with that for  $^{183}\text{Hg}$ , where proton and alpha-particle emission is becoming increasingly important and there is more fragmentation of the fusion cross-section amongst various evaporation residues. Note that in both cases the fission cross-section increases rapidly, so that a balance must be struck between keeping the beam energy low to avoid fission, while also bringing in enough angular momentum to populate high spin states. The calculations for the bombardment of  $^{35}\text{Cl}$  on  $^{154}\text{Gd}$ , which

---

<sup>1</sup>The yrast states are the set of states with lowest energy at each spin. The second lowest states are called the yrare states, although this term has come to collectively mean the lowest few states in energy rather than just the second lowest.

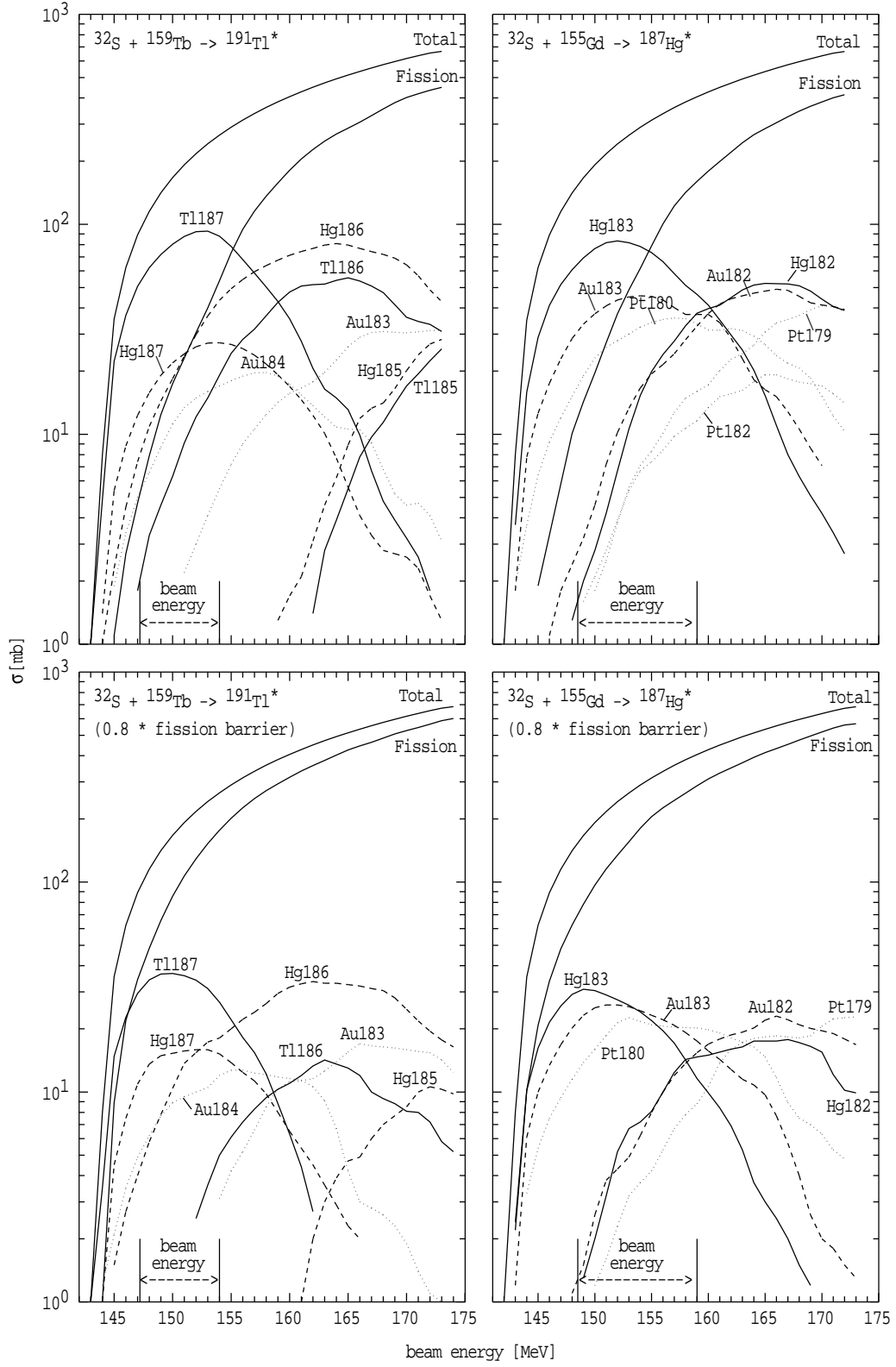


Figure 3.2: Statistical model calculations for the reactions used to make  $^{187}\text{Tl}$  and  $^{183}\text{Hg}$ . The residue cross-sections are labelled as follows: solid lines indicate  $(\text{Hi},\text{xn})$  reactions, dashed lines indicate one proton is emitted and dotted lines indicate two protons or an  $\alpha$ -particle are emitted. The top two panels are calculations with liquid drop fission barriers, while the lower panels show the effect of lowering these barriers by 20%.

are not presented here, indicate that  $^{185}\text{Tl}$  will be the dominant reaction product at a beam energy of 166 MeV, with however, significant cross-sections for the formation of  $^{185}\text{Hg}$  and  $^{182}\text{Au}$ .

The comparison with the calculations in the lower panels, which use adjusted fission barriers, indicates the sensitivity of the calculated cross-sections to the size of the barrier. With the lower barriers, not only is there a drastic decrease in the absolute cross-section for residue formation, but there is also a shift towards higher relative cross-sections for production of lower- $Z$  nuclei. This is because the lower- $Z$  nuclei are more stable against fission and have a greater chance of survival. Prior experience in studying nuclei in this mass region has shown that reduced values for the fission barrier are often appropriate [Dra93]. In these cases the sensitivity to the size of the fission barrier is such that it was difficult to make firm predictions of the absolute cross-sections prior to experiment. Nevertheless, for both values of the fission barriers,  $^{183}\text{Hg}$  and  $^{187}\text{Tl}$  are predicted to be the most strongly populated residues and the calculations in Figure 3.2 were used to select the appropriate beam energies at which to collect data.

### 3.1.2 Nucleus identification

When a range of final nuclei are populated in a heavy-ion fusion reaction, it can be difficult to identify the origin of an emitted  $\gamma$ -ray. A large fission cross-section also creates problems by giving rise to a background of  $\gamma$ -rays from fission products which can make identification of weak  $\gamma$ -rays from the evaporation residues impossible. A similar problem occurs when using a heavy beam on a target of deformed rare-earth nuclei, as a large flux of  $\gamma$ -rays from Coulomb excitation of the target is produced. Various methods can be used to either discriminate against unwanted background  $\gamma$ -rays and/or identify the evaporation residues. Examples include:

1. Using the Doppler shifts of the  $\gamma$ -ray energies to measure the recoil speed of the nucleus.
2. Measuring coincidences between  $\gamma$ -rays and characteristic atomic X-rays to identify the proton number of the nucleus.
3. Measuring the production cross-section as a function of beam energy (an excitation function). Near the Coulomb barrier the peak cross-sections for formation of nuclei after emission of  $n$  or  $n + 1$  or  $n + 2, \dots$  particles,

occur approximately 12-15 MeV apart in beam energy. If  $\gamma$ -rays from the neighbouring mass nuclei are known, it is often simple to assign  $\gamma$ -rays to the intervening mass nucleus.

4. Measuring the fold and sum energy of the  $\gamma$ -ray cascade to estimate the initial nuclear excitation energy and discriminate between different reaction channels [Eji89].
5. Using a recoil mass spectrometer [Jam88, Dav89, Dav92] to identify the mass (and in some cases also the atomic number) of the recoiling residues.
6. Using other simpler particle detectors to measure residue- $\gamma$ -ray coincidences and discriminate against  $\gamma$ -rays from Coulomb excitation and fission. An example is the Recoil Filter Detector developed by the Berlin and Krakow groups [Spo94].
7. Direct measurement and identification of the charged particles and/or neutrons emitted during compound nucleus decay so as to preferentially enhance and identify different reaction channels. An example of a charged particle detector is the ANU Particle Detector Ball [Lan91, Reg95].

In practice a combination of methods is usually used. For example,  $\gamma$ -X-ray coincidences, prior knowledge of the  $\gamma$ -rays from neighbouring isotopes and checks that the Doppler shifts of  $\gamma$ -rays were appropriate for evaporation residues, were all used to assign  $\gamma$ -rays to specific isotopes in the spectroscopic measurements at the ANU. Also, for  $^{185}\text{Tl}$  and  $^{187}\text{Tl}$ , the Fragment Mass Analyzer at Argonne National Laboratory was used to obtain mass-gated  $\gamma$ -ray spectra.

## 3.2 Gamma-Ray Detectors

Gamma-ray detectors are usually either scintillators or semiconductors. Both work by detecting the energetic electrons and positrons produced when  $\gamma$ -rays interact in the detector. Examples of scintillation detectors include crystals of sodium iodide, barium fluoride and bismuth germanate, with the energy resolution obtainable with such crystals varying between  $\sim 8 - 30\%$  of the  $\gamma$ -ray energy. Much better resolution is obtained with germanium semiconductor detectors such as the Ortec Gamma-X HPGe detectors which were used in the current work. They have typical resolutions of 2.5 keV for the 1408 keV  $^{152}\text{Eu}$  decay line ( $\sim 0.2\%$ ).

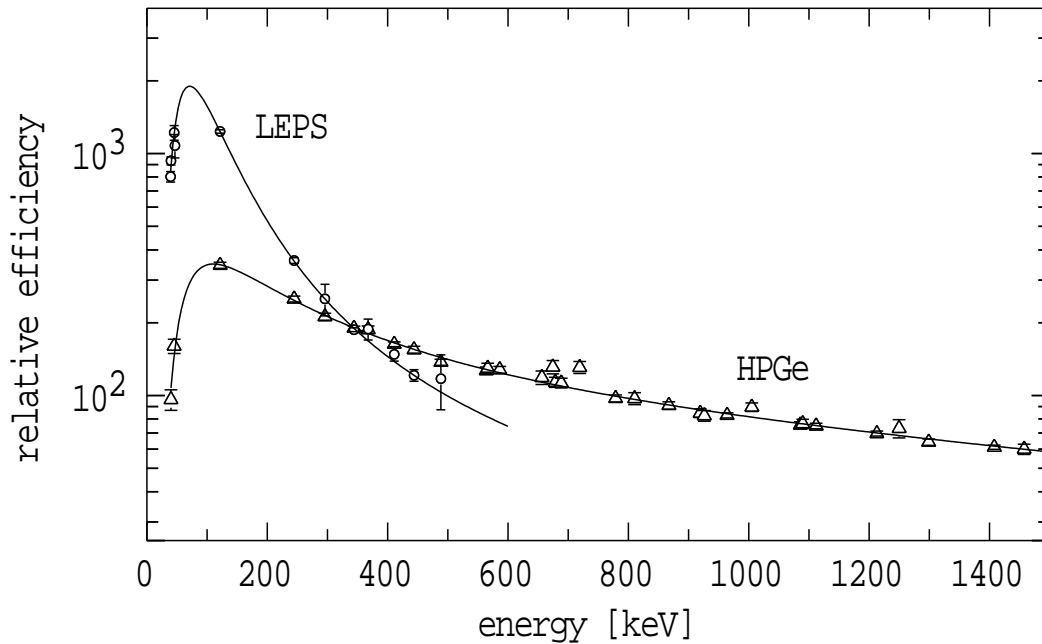


Figure 3.3: Efficiency curves measured with a  $^{152}\text{Eu}$  source for both a Compton suppressed Gamma-X detector and an unsuppressed LEPS detector from the CAESAR array. The curves are normalised to the same efficiency for the 344 keV  $\gamma$ -ray.

For the thallium experiments at the ANU an Ortec Low Energy Photon Spectrometer, or LEPS detector, was also used. This detector has a planar geometry and a small volume of germanium only 10 mm thick. The regular electric field and small size makes for a uniform and fast collection of the deposited charge, giving the LEPS detector excellent timing and energy resolution. This comes however, at the expense of  $\gamma$ -ray efficiency at high energy, as illustrated by the relative efficiency curves in Figure 3.3.

In the current set of experiments with the CAESAR array, the HPGe detectors were shielded by 0.25 mm thick iron absorbers while the LEPS detector was bare. With this arrangement and the glass target chamber, all the detectors in the CAESAR array are capable of detecting  $\gamma$ -rays with good efficiency to below the thallium/mercury X-ray region.

### 3.2.1 Compton suppression

The Compton scattered events in the  $\gamma$ -ray spectrum give rise to a large background which can obscure weak  $\gamma$ -rays. These can be suppressed by surrounding the primary detector crystal with another detector which is shielded from the direct flux of  $\gamma$ -rays and is used to detect  $\gamma$ -rays Compton-scattered from the primary detector. Events in which coincident  $\gamma$ -rays are detected in both the

primary detector and the suppression shield are ignored. The suppression shields in the CAESAR array are made of bismuth germanate and are an asymmetric design where the HPGe detector enters from the side [Byr85]. The suppression increases the peak to total ratio for the 662 keV  $\gamma$ -ray from a  $^{137}\text{Cs}$  source from  $\sim 30\%$  to  $\sim 70\%$  [Byr85, Dav90]. This is especially significant when  $\gamma - \gamma$  coincidences are being measured, as the proportion of useful peak-peak coincidence events increases from  $(30\%)^2$  to  $(70\%)^2$ , a greater than fivefold increase.

### 3.3 The CAESAR Detector Array

The spectroscopic measurements reported in this thesis were performed at the ANU using the detector array, CAESAR, consisting in these experiments of six Compton-suppressed HPGe detectors in a vertical plane, as shown in Figure 3.4. An unsuppressed LEPS detector was also included for the thallium experiments. It was placed at  $45^\circ$  to the beam axis, as described in the figure caption.

The electronics for the CAESAR array are shown in Figure 3.5 and are based around standard NIM modules with some CAMAC components. Note that this is not a complete picture (for example, the  $\gamma$ -beam TAC is not shown) but it does show the important components for the current work. Although interwoven,

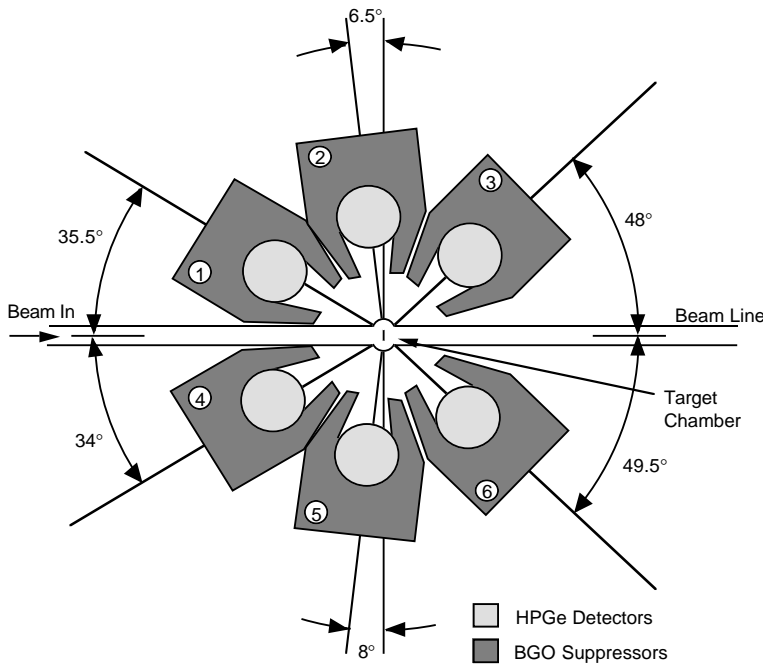


Figure 3.4: Schematic of the CAESAR array with six suppressed detectors. A seventh can be included at  $0^\circ$  directly behind the target chamber. Unsuppressed LEPS detectors can be included at  $45^\circ$  and  $135^\circ$  to the beam axis,  $90^\circ$  out of the plane of the page.



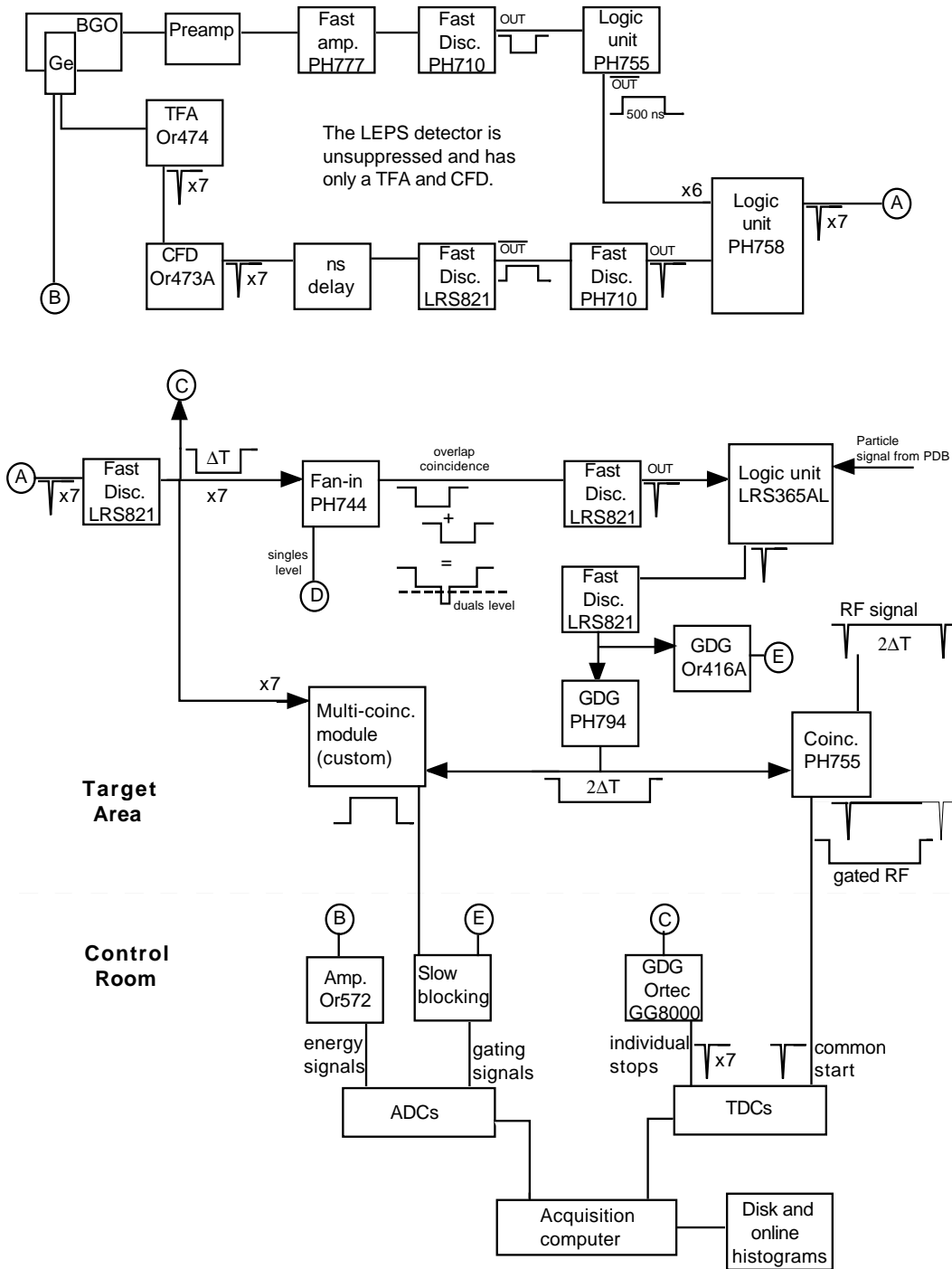


Figure 3.5: CAESAR electronics.

the electronics can be broadly split into four parts. These are the Compton suppression, the  $\gamma$ -ray coincidence logic, the measurement of the absolute times of detection for the  $\gamma$ -rays and the acquisition system.

### 3.3.1 Compton suppression

The top part of Figure 3.5 shows the Compton suppression where the PH758 logic unit ensures that an output signal is only produced when the germanium detector signal is not in coincidence with a signal from its suppression shield. (Note that the LEPS detector is unsuppressed.) The suppression coincidence overlap is  $\pm 250$  ns and the signals are matched in time using the adjustable widths in the discriminator units and the ns delay boxes.

### 3.3.2 Coincidence logic

The signals from point A are stretched into pulses  $\Delta T$  wide (432 ns in the current work), and are fanned out to three other parts of the system where they are used to register the detection of  $\gamma$ -rays in specific detectors.

One set of the  $\Delta T$  signals are fanned-in by the PH744 module and the summed signal is fed into a fast discriminator. The level on the discriminator is set as shown in the figure to trigger whenever two or more signals are coincident in time to within  $\pm \Delta T$ . The output logic signal is input to the LRS365AL Logic unit (used to check for particle coincidences whenever the ANU Particle Detector Ball is in use). The output signal from this box drives another fast discriminator, whose output is input into two gate and delay generators. The signals from these gate and delay generators are used in the rest of the system to indicate that a valid coincidence event has occurred between two detectors. For example, the positive logic signal from the Or416A unit is patched through to the Control room at point E where it is used to produce the master gate signal (see §3.3.4). The second gate and delay generator produces a negative voltage signal with a width  $2\Delta T$  which is used for two purposes; (i) to strobe the multi-coincidence module which produces positive logic signals for prompt gating of the ADCs (see §3.3.4), and (ii) to produce the “gated RF” signal (see §3.3.3).

To collect singles rather than coincidence data is a simple matter of providing an additional voltage level at the fan-in (point D), so that the “coincidence” condition is satisfied even if only one  $\gamma$ -ray has been detected.

### 3.3.3 Gamma-ray detection times

The times of detection of each  $\gamma$ -ray are measured relative to an RF pulse train in which the pulses are separated by  $2\Delta T$ . This separation is required to allow for delayed coincidences where two  $\gamma$ -rays are emitted  $\Delta T$  and  $2\Delta T$  after the

formation of the nucleus. The RF signal is derived from the oscillator which sets the frequencies for the pulsing system so that when a pulsed beam is in use the RF signals are in a fixed phase relationship with the beam bursts. Note however, that the RF pulse train must be present irrespective of whether or not the beam is pulsed, as it provides the reference against which the absolute times are measured.

A particular pulse from the RF train is selected by the PH755 coincidence module using the  $2\Delta T$  wide signal from the PH794 gate and delay generator. This is called the “gated RF” and is used to start the TDCs. The coincidence requirement at the PH755 module ensures that the TDCs are only started when a valid coincidence event has occurred. The TDC stop signals, which originate at point C, must be delayed so that they arrive after the start signal. The delays of  $\sim 1.2 \mu\text{s}$  are provided by the GG8000 gate and delay generator.

### 3.3.4 Data acquisition

The third set of  $\Delta T$  signals (see §3.3.2) are input into the custom built multi-coincidence module. This box contains latches that are set whenever a particular detector has fired. These latches are automatically cleared after a set time interval, unless a valid coincidence signal arrives from the PH794 gate and delay generator. In this case the multi-coincidence module outputs individual positive logic signals for every germanium detector that has fired. These logic signals are suitable for prompt coincidence gating of the linear energy signals at the ADCs.

The TDCs are read whenever the ADCs register events, however, they have a much longer conversion time than the ADCs. If new  $\gamma$ -ray signals fire the ADCs too soon after the arrival of the previous signals, then the TDCs will still be busy and the  $\gamma$ -ray energy signals will have no corresponding time signals. To prevent this, the Slow Blocking unit inhibits the passage of any new ADC gating signals for  $180 \mu\text{s}$  after the arrival of a master gate signal (point E).

The final step in the data acquisition involves the digital data being processed by the acquisition computer. On-line sorting and histogramming of all or a fraction of the data can be performed, while the energies and times of detection of the  $\gamma$ -rays are recorded on magnetic disk in event by event mode. The event lists are later backed up to DAT tapes for subsequent off-line analysis.

### 3.3.5 Off-line analysis

The construction of nuclear decay schemes most often utilises coincidence matrices which allow the deduction of the time relationship between  $\gamma$ -rays. For each coincidence event the time difference between the detection of the  $\gamma$ -rays can be determined from the absolute times of detection. Figure 3.6 shows a typical time difference spectrum, peaked at zero due to transitions in prompt coincidence and with side lobes out to  $\sim \pm 170$  ns due to the low-energy  $\gamma$ -rays and X-rays which experience time walk in the detectors. (The time walk is due to a combination of factors such as non-uniform electric fields and different  $\gamma$ -ray interaction positions in the detector crystal.) The time regions far from zero correspond to both correlated  $\gamma$ -rays which are truly emitted either delayed or early with respect to other  $\gamma$ -rays, as well as random coincidences.

In the current work, the different data sets were typically sorted into prompt coincidence matrices with coincidence overlaps of  $\pm 20$  and  $\pm 170$  ns, as well as matrices with 20 – 170 and 170 – 430 ns time differences between detection of the  $\gamma$ -rays. The latter matrices are used to look for  $\gamma$ -rays which are in “early”

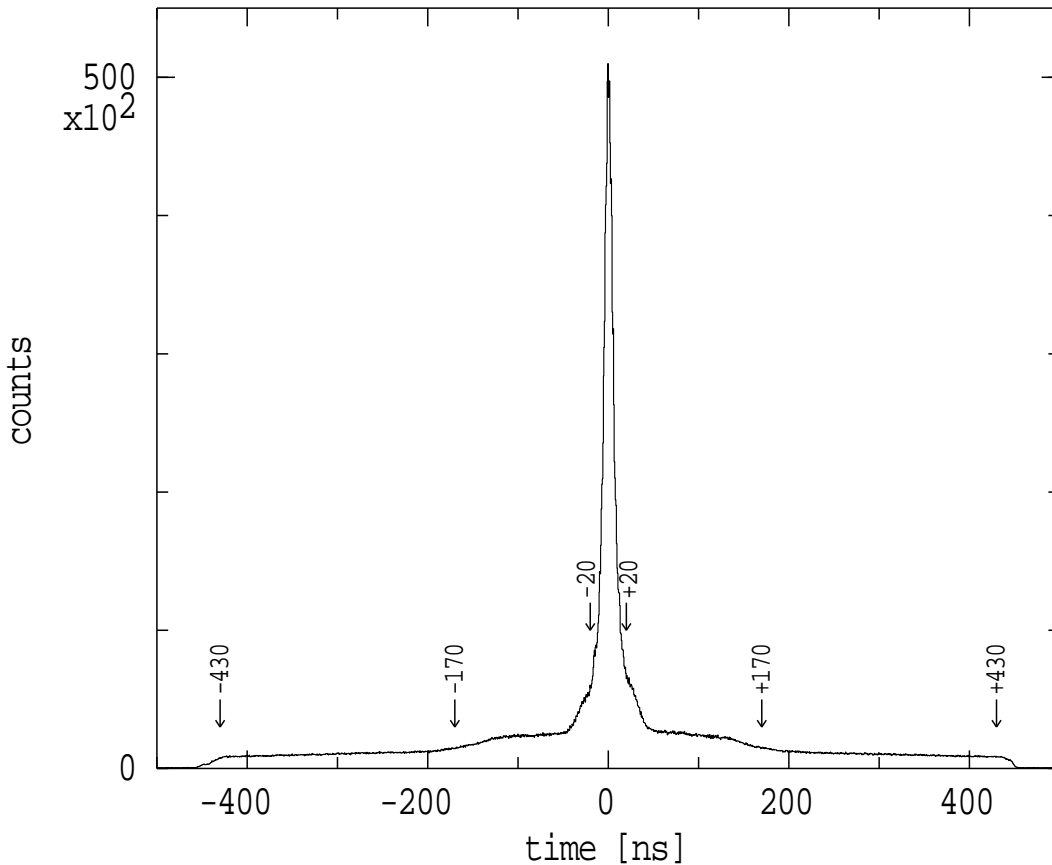


Figure 3.6: Typical time difference spectrum.

or “delayed” coincidence with other  $\gamma$ -rays and thus identify isomeric states. The prompt coincidence matrices are used to identify which  $\gamma$ -rays are or are not in mutual coincidence. A spectrum of  $\gamma$ -rays in prompt, early or delayed coincidence with a particular energy  $\gamma$ -ray is obtained from the appropriate matrix by gating on the  $\gamma$ -ray peak on one axis and projecting the spectrum of coincident  $\gamma$ -rays onto the other axis. Because a peak lies upon a background due to a combination of Compton scattered  $\gamma$ -rays of higher energy, statistical continuum  $\gamma$ -rays and unresolved  $\gamma$ -rays from fission products, a simple projection for a peak shows not only the coincidences due to the peak, but also real coincidences due to the background. Representative coincidence spectra for the background are constructed by gating on featureless regions of the total projection which are at the level of the background. Background-subtracted spectra for the peaks are obtained by subtracting, after suitable normalisation, the coincidence spectrum for the background from the raw projection for the peak.

### 3.3.6 Lifetime analysis

It is also possible to sort the data into matrices which have the absolute times of detection or the time difference data on one axis. These matrices can be used to obtain time spectra showing the time of detection of a  $\gamma$ -ray with respect to a pulsed beam or the time relationship between pairs of  $\gamma$ -rays. For the  $^{185}\text{Tl}$  thick target experiment, a matrix with the energy of a  $\gamma$ -ray on one axis and its time of detection on the other, was used to produce spectra showing the times of detection of  $\gamma$ -rays with respect to the pulsed beam.

The intermediate times between detection of  $\gamma$ -rays may be obtained by sorting the coincidence data into a three-dimensional  $\gamma - \gamma - \text{time}$  matrix, with the two  $\gamma$ -ray energies on the  $y$  and  $z$  axes and the time difference between them on the  $x$ -axis. A time spectrum obtained by projecting onto the  $x$ -axis with gates on  $\gamma_1$  on the  $y$ -axis and  $\gamma_2$  on the  $z$ -axis is referred to as a  $(\gamma_1, \gamma_2)$  slice. If  $\gamma_1$  is above an isomer and  $\gamma_2$  is below it, then this time spectrum will show a positive time difference. The opposite slice,  $(\gamma_2, \gamma_1)$ , would show a negative time difference.

Because both the time resolution and the time walk vary with each  $\gamma$ -ray energy, the prompt response function for a  $\gamma - \gamma - \text{time}$  measurement is a function of both energies. This function has been comprehensively investigated for the CAESAR array during a number of different experiments performed under a wide variety of conditions. A summary can be found in the recent work of Byrne *et al.* [Byr93], which used a series of known states in  $^{218}\text{Ra}$  with lifetimes

less than 50ps to characterise the prompt response function in terms of the  $\gamma$ -ray energies. Strongly populated isomers with meanlives of several nanoseconds are immediately apparent and the lifetimes can be measured directly by fitting the  $\gamma - \gamma - time$  slices with the prompt response function convoluted with an exponential decay curve. With favourable intensities it is possible to measure lifetimes down to about 0.5ns.

Such a  $\gamma - \gamma - time$  matrix was constructed for the  $^{187}\text{Tl}$  thick target experiment. Time spectra showing small intermediate times less than 2ns were fitted with a Gaussian prompt response function for which the time zero was allowed to vary, while the widths were fixed according to the parameterisation of Byrne *et al.* [Byr93]. The centroid shifts for slices  $(E_1, E_2)$  and  $(E_2, E_1)$  had a consistent magnitude but the opposite sign and thus could be combined appropriately.

### 3.4 Angular Distributions

The normalised intensity distribution as a function of angle, for the  $\gamma$ -radiation from a  $J_i \rightarrow J_f$  transition in an aligned ensemble of nuclei, can be expressed in the form,

$$W(\theta) = 1 + A_2 P_2(\cos \theta) + A_4 P_4(\cos \theta) \quad (3.2)$$

The  $P_k$  are the Legendre polynomials and the coefficients  $A_k$  are defined by [Mat74, Yam67]

$$A_k = \alpha_k(J_i) \frac{1}{1 + \delta^2} [B_k(J_i) F_k(J_f L_1 L_1 J_i) + 2\delta B_k(J_i) F_k(J_f L_1 L_2 J_i) + \delta^2 B_k(J_i) F_k(J_f L_2 L_2 J_i)] \quad (3.3)$$

The attenuation coefficient,  $\alpha_k$ , depends upon the degree of alignment, while  $\delta$  is a mixing ratio giving the relative transition amplitudes of the  $L_1$  and  $L_2$  multipoles. It is defined by

$$\delta^2 = \frac{T(L_2)}{T(L_1)} \quad (3.4)$$

where  $T(L_i)$  denotes the intensity of the  $L_i$  multipole component of the radiation. The sign of  $\delta$  is determined by the wavefunctions of the initial and final states and is related to the relative phase of the two multipole components. The coefficients,  $\alpha_k$ ,  $F_k$  and  $B_k$ , are defined in Refs. [Mat74, Yam67], where they are also tabulated

as a function of the spins  $J_i$ ,  $J_f$ , and an alignment parameter,  $\sigma/J$ . The parameter  $\sigma$  describes the half-width of the  $m$ -substate distribution, which is assumed to be Gaussian and centred on  $m = 0$ . For an assumed value of  $\sigma/J$ , the theoretical  $A_k$  coefficients can be determined for a particular multipolarity transition between states with given initial and final spins. These theoretical values can then be compared with the experimental values determined by measuring the intensity of  $\gamma$ -radiation as a function of angle and fitting the data to equation (3.2). The CAESAR array as used in these experiments has detectors at three angles, so it was only meaningful to fit the intensity and the  $A_2$  coefficient of the angular distributions, with the  $A_4$  coefficient fixed at zero. Where possible, the fitted  $A_2$  coefficients were used to deduce the transition multipolarities.

The initial alignment of the nuclear spins which is produced in a heavy ion fusion reaction (see §3.1), is eventually lost due to hyperfine interactions [Gol82, Spr83]. The angular distributions in the current work were obtained from the thick target data (avoiding problems due to vacuum deorientation), and the longest lived isomeric state identified was a 12 ns isomer in  $^{185}\text{Tl}$ . Thus the angular distributions showed no attenuation due to loss of alignment.

### 3.5 Angular Correlations and DCO ratios

Having observed a  $\gamma$ -ray at a particular angle, the angular distribution of the coincident radiation contains information on the multipolarity of the radiation, and, since the coincidence spectra are cleaner and less complex than the singles spectra, it is often possible to use this angular correlation information to infer the multipolarities for transitions that are obscured in the singles spectra.

For a cascade of two transitions,  $\gamma_2$  followed by  $\gamma_1$ , the intensity of the transition  $\gamma_2$  measured at an angle  $\theta_2$ , gated on the transition  $\gamma_1$  observed at angle  $\theta_1$ , is denoted by  $W(\theta_1, \theta_2, \phi)$  [Kra73]. (The angle  $\phi$  is the angular separation of the detectors measured around the beam axis. A diagram of this geometry can be found in Ref. [Kra73].) When the observation angles are reversed, the intensity is denoted by  $W(\theta_2, \theta_1, \phi)$ . The ratio of these two measurements is called a DCO ratio and can be used to infer the transition multipolarities [Krä89]. (Note that DCO stands for Directional Correlation from Oriented states and the methodology described below assumes the nuclear spins are aligned with a Gaussian  $m$ -substate distribution centred around  $m = 0$ .)

For the CAESAR array, the detectors at  $\pm 147^\circ$  and  $\pm 48^\circ$  are labelled as group

A and the two at  $\pm 97^\circ$  are labelled as group B. The coincidence data were sorted into two matrices, one with group A on one axis and group B on the other, the second with group A on one axis and group A on the other. The experimentally measured DCO ratio was

$$R_{DCO} = \frac{I[\gamma_1 \text{ in A gated by } \gamma_2 \text{ in A}] + I[\gamma_1 \text{ in A gated by } \gamma_2 \text{ in B}]}{I[\gamma_1 \text{ in B gated by } \gamma_2 \text{ in A}]} \quad (3.5)$$

The theoretical DCO ratio can be estimated by the ratio of two sums of  $W(\theta_2, \theta_1, \phi)$  terms, with angles from groups A and B and with  $\phi$  either  $0^\circ$  or  $180^\circ$ .

From the measured angular distributions of stretched E2 transitions in  $^{187}\text{Tl}$  and  $^{183}\text{Hg}$  (see Tables 4.2 and 4.5), an estimate for the spin alignment,  $\sigma/J \approx 0.3$ , can be obtained using the methods of the previous section. A computer program based upon the formalism of Ref. [Kra73] was then used to calculate  $W(\theta_2, \theta_1, \phi)$  for the different possible sets of detector angles. The resultant theoretical DCO ratios for different combinations of gating and observed transitions are summarised in Table 3.1. The calculations have been made for a cascade of two transitions with a spin alignment of  $\sigma/J = 0.3$  and the middle level having  $I = 8$ . Although the calculated DCO ratios change significantly at low spins, the values in the table are a good guide to what might be expected experimentally for  $I \geq 4$ .

Note that the gating transition can be either above or below the transition whose DCO ratio is being measured. Also, results are only given in the table for when the gating transition is a pure stretched quadrupole or dipole and the observed transition is a pure quadrupole or dipole with  $\Delta I$  as shown. The results

Table 3.1: Theoretical DCO ratios for the CAESAR array

Measured transition	Gating Transition			
	Above <sup>a)</sup>		Below <sup>a)</sup>	
	quad.	dipole	quad.	dipole
quad., $\Delta I = 2$	1.46	1.58	1.46	1.87
quad., $\Delta I = 1$	1.01	1.21	1.12	1.19
quad., $\Delta I = 0$	1.00	1.21	1.01	1.31
dipole, $\Delta I = 1$	0.95	1.17	1.06	1.17
dipole, $\Delta I = 0$	1.48	1.60	1.50	1.92

<sup>a)</sup> See the text for full details of the gating procedure.



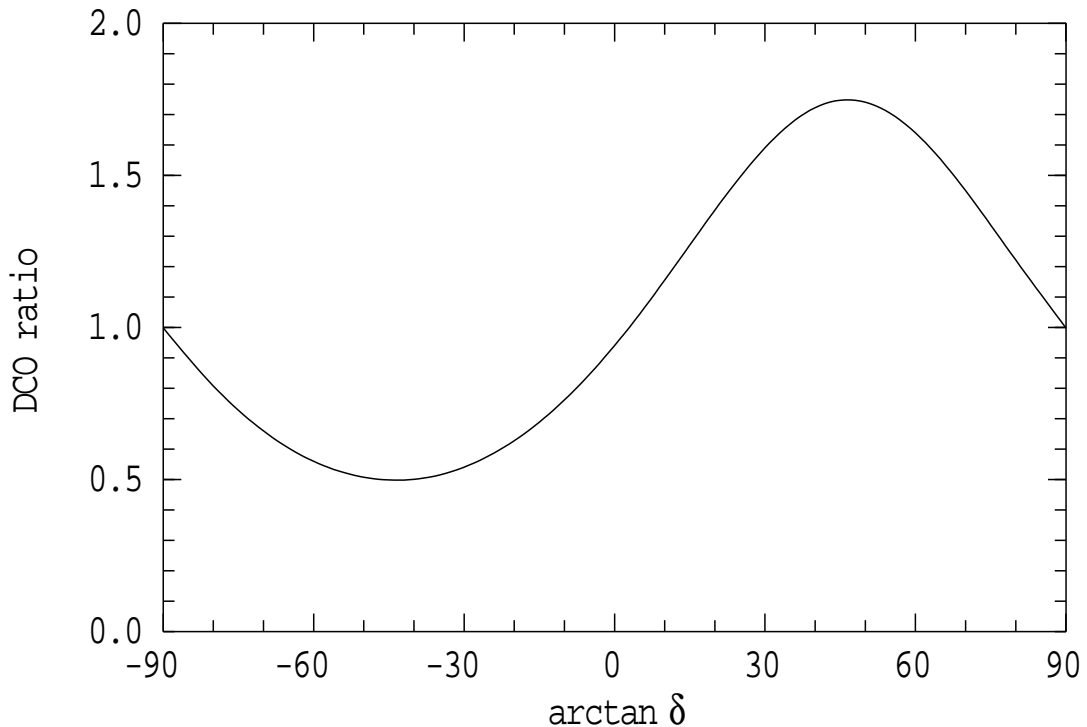


Figure 3.7: Theoretical DCO ratio for a  $\Delta I = 1$ , mixed dipole/quadrupole transition, gated above by a stretched E2 transition, as a function of the mixing ratio.

show a distinctive pattern when the gating and observed transitions are both stretched (first and fourth rows). No matter whether the gating transition is a quadrupole or dipole above or below the observed transition, the DCO ratio for a stretched quadrupole transition ( $\sim 1.5 \rightarrow \sim 1.9$ ) is always greater than that for a stretched dipole transition ( $\sim 1.0 \rightarrow 1.2$ ).

Table 3.1 only contains the DCO ratios expected for pure dipole and quadrupole transitions. Figure 3.7 shows the theoretical DCO ratio expected for a  $\Delta I = 1$ , mixed dipole/quadrupole transition, gated above by a stretched E2 transition, as a function of the mixing ratio. (The curve for when the gating transition is below the observed transition has the same phase but a smaller modulation.) Regardless of whether the E2 gating transition is above or below, DCO ratios less than one correspond to negative mixing ratios.

A brief statement should be made regarding the possible loss of spin alignment for nuclei recoiling in vacuum in the thin target experiments (vacuum deorientation). Nordhagen *et al.* [Nor70] suggest that the loss of alignment depends on the ratio of  $I/J$ , where  $I$  and  $J$  are the nuclear and electronic spins, and showed that the lower the nuclear spin, the more of the alignment is lost. In the thallium experiments, only states above the  $\frac{9}{2}^-$  isomers are seen and there is

no experimental evidence for an attenuation of the alignment in the thin target data. In fact, the DCO ratios for the thin and thick target experiments were in satisfactory agreement down to the lowest spins observed, so that it was possible to use the results from the thin target experiments almost exclusively and thus benefit from the increased statistics. (See Table 4.1 for the details of the number of coincidence events collected for each experiment.)

In the case of  $^{183}\text{Hg}$ , the lowest spin transitions for which DCO ratios were determined were the  $\frac{9}{2}^- \rightarrow \frac{7}{2}^-$  dipole and  $\frac{9}{2}^- \rightarrow \frac{5}{2}^-$  quadrupole transitions from the  $\frac{7}{2}^-$ [514] and  $\frac{1}{2}^-$ [521] bands (see Figure 4.16 and Table 4.5). Again the thin target data was used to determine the DCO ratios because of the greater statistics. The  $\frac{9}{2}^- \rightarrow \frac{7}{2}^-$  transition did show a larger DCO ratio than the other dipole transitions in the  $\frac{7}{2}^-$ [514] band, consistent with a possible loss of alignment, however, the  $\frac{9}{2}^- \rightarrow \frac{5}{2}^-$  transition showed a DCO ratio consistent with that expected for a stretched E2 transition. The results for the DCO ratios in Figure 4.16 show a clear separation between quadrupole and dipole transitions and suggest that there was reasonable alignment down to low spins for the thin target data.

### 3.6 Internal Conversion

Another transition process which can occur is internal conversion, where the transition energy is transferred to a bound atomic electron, which is then ejected from the atom with an energy equal to the transition energy minus its initial binding energy. The relative probability of the two processes is described by the conversion coefficient,  $\alpha_T$ , given by

$$\alpha_T = \frac{I_e}{I_\gamma} \quad (3.6)$$

where  $I_e$  and  $I_\gamma$  are the intensities of the electron and  $\gamma$ -ray transitions respectively. The conversion coefficient can be calculated from the electronic wavefunctions and is tabulated in Ref. [Rös78], from which all theoretical conversion coefficients quoted in this thesis are obtained by interpolation. The conversion coefficient is a strong function of both the transition energy and multipolarity, and can often be used to provide an unambiguous determination of the transition multipolarity.

Conversion coefficients were not measured directly in the current work, but were inferred from intensity balances for a number of transitions.

# Chapter 4

## Analysis and Results

This chapter provides details of the results and analysis of the experiments performed for this work. The bulk of the studies were performed at the Australian National University using the 14UD tandem accelerator in conjunction with the CAESAR detector array. Results were also obtained from experiments at Argonne National Laboratory using the ATLAS facility in conjunction with the Fragment Mass Analyzer and detectors from the Argonne-Notre Dame array. A brief summary of the experiments performed appears in Table 4.1.

Details of the construction of the level schemes for  $^{187}\text{Tl}$ ,  $^{185}\text{Tl}$  and  $^{183}\text{Hg}$  are presented. The most comprehensive account is given for  $^{187}\text{Tl}$ , as it provides a good example of the methods of data analysis, while only the particularly important facets of the analysis are presented for  $^{185}\text{Tl}$  and  $^{183}\text{Hg}$ .

### 4.1 Analysis and Results for $^{187}\text{Tl}$

High spin states in  $^{187}\text{Tl}$  were populated by bombarding metallic terbium targets with beams of 154 MeV  $^{32}\text{S}$  ions from the ANU 14UD tandem accelerator. The first measurement used a 1.1 mg/cm<sup>2</sup>  $^{159}\text{Tb}$  target with a 3.9 mg/cm<sup>2</sup> natural lead backing, thick enough to stop the recoiling nuclei. The second measurement, with a 0.55 mg/cm<sup>2</sup>  $^{159}\text{Tb}$  target, allowed the nuclei to recoil into the vacuum and decay in flight, enhancing the observation of high spin states. The  $\gamma$ -ray energies for the thin target measurement were Doppler corrected off-line according to the expected recoil velocity of  $\frac{v}{c} = 1.58\%$ .

The total projection of the prompt coincidence matrix obtained for the  $^{32}\text{S} + ^{159}\text{Tb}$  bombardment with a thin target appears in the top panel of Figure 4.1, with the strongest peaks assigned to  $^{187}\text{Tl}$  and  $^{187}\text{Hg}$  [Han88] labelled. The  $\gamma$ -

Table 4.1: Summary of experiments performed for this thesis

Nucleus	Location	Reaction	Target thickness [mg/cm <sup>2</sup> ]	Isotopic enrich- ment	Backing <sup>a)</sup> (nat. lead) [mg/cm <sup>2</sup> ]	Beam energy [MeV]	Measured	Detectors	Total number of coincidences [ $\times 10^6$ ]
<sup>187</sup> Tl	ANU	<sup>159</sup> Tb( <sup>32</sup> S,4n)	1.1	100%	3.9	154	$\gamma\gamma(t), \gamma\gamma(\theta)$	6 HPGe + 1 LEPS	13.9 $\gamma\gamma$ , 2.7 $\gamma$ -LEPS
	ANU	<sup>159</sup> Tb( <sup>32</sup> S,4n)	0.55	100%	—	154	$\gamma\gamma(t), \gamma\gamma(\theta)$	6 HPGe + 1 LEPS	67.4 $\gamma\gamma$ , 12.9 $\gamma$ -LEPS
	Argonne <sup>b)</sup>	<sup>155</sup> Gd( <sup>36</sup> Ar,p3n)	0.37	95%	—	174	FMA- $\gamma$	10 HPGe + FMA	0.30 $\gamma$ -residue
<sup>185</sup> Tl	ANU	<sup>154</sup> Gd( <sup>35</sup> Cl,4n)	$2 \times 0.4^c)$	67%	4.0	166 <sup>d)</sup>	$\gamma\gamma(t), \gamma\gamma(\theta)$	6 HPGe + 1 LEPS	58.2 $\gamma\gamma$ , 10.5 $\gamma$ -LEPS
	ANU	<sup>154</sup> Gd( <sup>35</sup> Cl,4n)	$2 \times 0.4^e)$	67%	—	166	$\gamma\gamma(t), \gamma\gamma(\theta)$	6 HPGe + 1 LEPS	105 $\gamma\gamma$ , 18.3 $\gamma$ -LEPS
	Argonne <sup>b)</sup>	<sup>154</sup> Gd( <sup>36</sup> Ar,p4n)	0.38	67%	—	184	FMA- $\gamma$	10 HPGe + FMA	0.030 $\gamma$ -residue
<sup>183</sup> Hg	ANU	<sup>155</sup> Gd( <sup>32</sup> S,4n)	1.7	91%	5.0	159	$\gamma\gamma(t), \gamma\gamma(\theta)$	6 HPGe	13.4 $\gamma\gamma$
	ANU	<sup>155</sup> Gd( <sup>32</sup> S,4n)	0.8	91%	—	159	$\gamma\gamma(t), \gamma\gamma(\theta)$	6 HPGe	91.3 $\gamma\gamma$

<sup>a)</sup> For the <sup>187</sup>Tl and <sup>183</sup>Hg experiments the lead was evaporated onto the foil. The <sup>185</sup>Tl experiment used a lead foil  $\sim 0.3$  mm behind the stacked target.

<sup>b)</sup> Data collected by A.M. Baxter, G.D. Dracoulis, A.P. Byrne and their collaborators at Argonne [Bax93].

<sup>c)</sup> Foils sandwiched together.

<sup>d)</sup> Pulsed beam with 1 ns wide pulses, 864 ns apart.

<sup>e)</sup> Foils  $\sim 2.5$  mm apart.

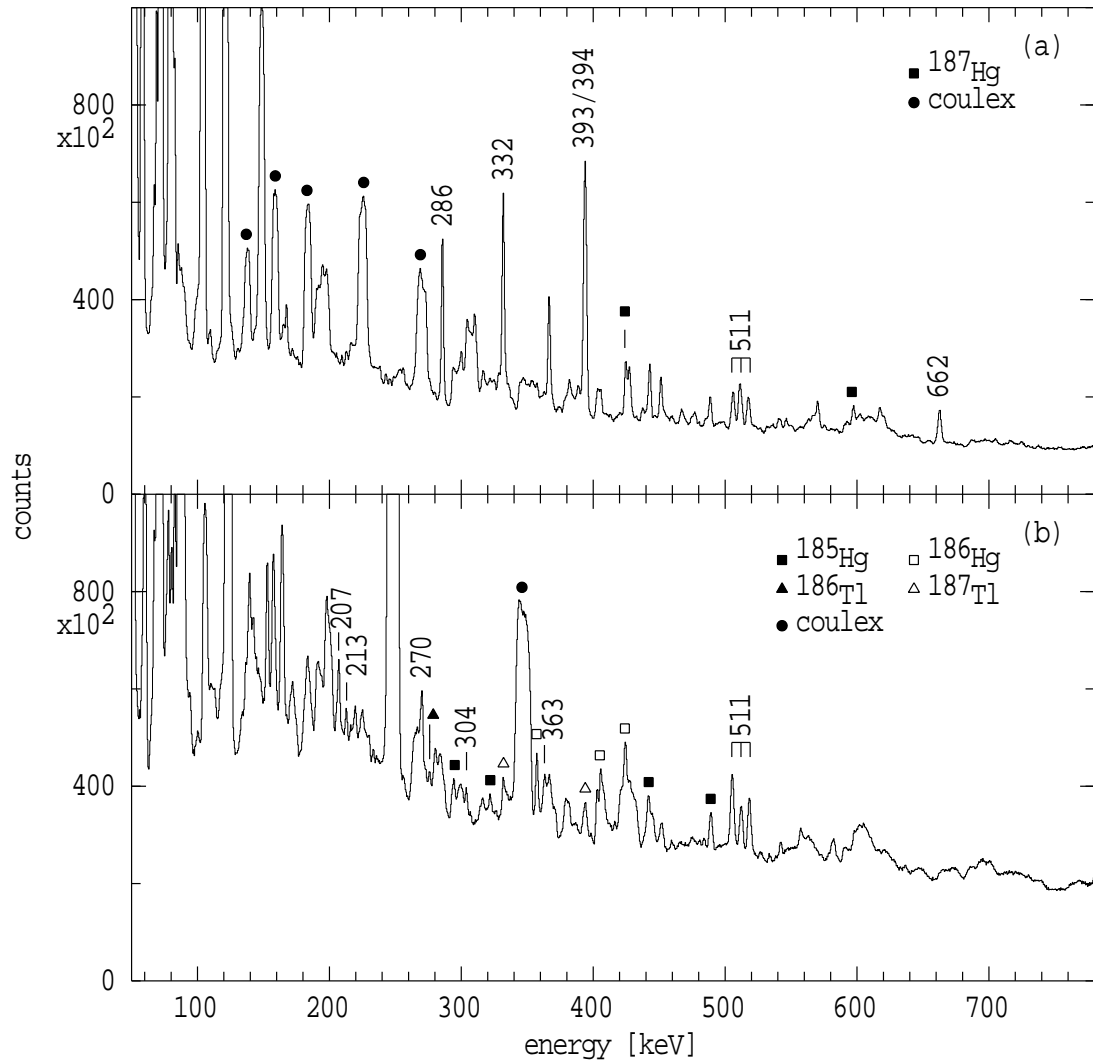


Figure 4.1: Comparison of the total projections of the  $\gamma - \gamma$  coincidence matrices for the bombardments used at the ANU to make, (a)  $^{187}\text{Tl}$  and (b)  $^{185}\text{Tl}$ , with thin targets. The strongest  $\gamma$ -rays from  $^{185}\text{Tl}$  and  $^{187}\text{Tl}$  are marked by their energies, with symbols labelling contaminating transitions. The 511 keV annihilation radiation is also labelled by its energy and is split into three peaks due to the Doppler corrections. Note also that some of the broad lines from Coulomb excitation of the rare-earth targets (which dominate the low energy regions) go off-scale. The difference in the peak to background levels for the two bombardments is due to the greater number of unresolved  $\gamma$ -rays from fission products for the reaction leading to the lighter compound nucleus.

ray intensities in this spectrum show that the production cross-sections for  $^{187}\text{Tl}$  and  $^{187}\text{Hg}$  were in the ratio of approximately 4:1. This is in good agreement with the predictions of the statistical model calculations with default liquid drop fission barriers presented in §3.1.1. The figure also shows an obvious distinction between the narrow peaks due to evaporation residues and the broad peaks which dominate the low energy region and are due to Coulomb excitation of the target.

The larger widths for the coulex lines are caused by the Doppler shift corrections being appropriate for the recoil velocity of the residues and not for the spread of different recoil velocities exhibited by the Coulomb excited target nuclei.

The ANU experiments provided the main spectroscopic measurements, while independent confirmation of the assignment of  $\gamma$ -rays to  $^{187}\text{Tl}$  was obtained using mass-selected  $\gamma$ -ray spectra measured at Argonne National Laboratory. The reaction used was  $^{155}\text{Gd}(^{36}\text{Ar}, p3n)^{187}\text{Tl}$  at 174 MeV, with a 95% enriched, self-supporting, metallic gadolinium foil of  $\sim 0.37 \text{ mg/cm}^2$  thickness. Details of the experimental arrangement may be found in both the preliminary published results of this work [Lan94] and the published results for the study of  $^{186}\text{Pb}$  [Bax93]. The compound nucleus formed at ANL,  $^{191}\text{Pb}$ , is more neutron deficient than the compound system formed in the ANU reaction. Consequently there was significant population of thallium nuclei via the proton emission channels.

The coincidence data from the ANU were sorted into matrices as outlined in §3.3.5. Background-subtracted spectra generated from these matrices were used to define the coincidence relationships and thus construct the level scheme. Details of the time relationships between  $\gamma$ -rays and the identification of an isomeric state in  $^{187}\text{Tl}$  are discussed below in §4.2.7.

The assignment of  $\gamma$ -rays to  $^{187}\text{Tl}$  was based on coincidences with characteristic thallium X-rays and comparison with the calculated yields from the statistical model calculations. Since the in-beam spectroscopy of  $^{186}\text{Tl}$  and  $^{188}\text{Tl}$  had previously been studied [Kre81], there was no ambiguity in assigning the strongest  $\gamma$ -rays in coincidence with thallium X-rays to  $^{187}\text{Tl}$ . Some  $\gamma$ -rays were also known previously in  $^{187}\text{Tl}$  from decay studies and preliminary in-beam experiments (see §4.2.1 below). Confirmation of the correct assignment to  $^{187}\text{Tl}$  was obtained from the mass-selected  $\gamma$ -ray spectra obtained in the Argonne experiments. A  $\gamma$ -ray spectrum measured in coincidence with mass-187 residues is shown in Figure 4.2, with the  $\gamma$ -rays due to  $^{187}\text{Tl}$  labelled by their energies. A small number of  $\gamma$ -rays from  $^{187}\text{Hg}$  [Han88] are also present in the spectrum.

Intensities for  $\gamma$ -rays in  $^{187}\text{Tl}$  were estimated from the projection of the  $\gamma - \gamma$  coincidence matrix for the thin target experiment, from the mass-187 gated  $\gamma$ -ray spectrum, and, for some of the weaker or contaminated lines, from the coincidence spectra for individual lines. It should be noted that in all the spectroscopic measurements performed at the ANU, the singles spectra were strongly contaminated by Coulomb excitation  $\gamma$ -rays from the deformed rare-earth targets, rendering singles intensity measurements very difficult. Instead, the projections of the  $\gamma - \gamma$

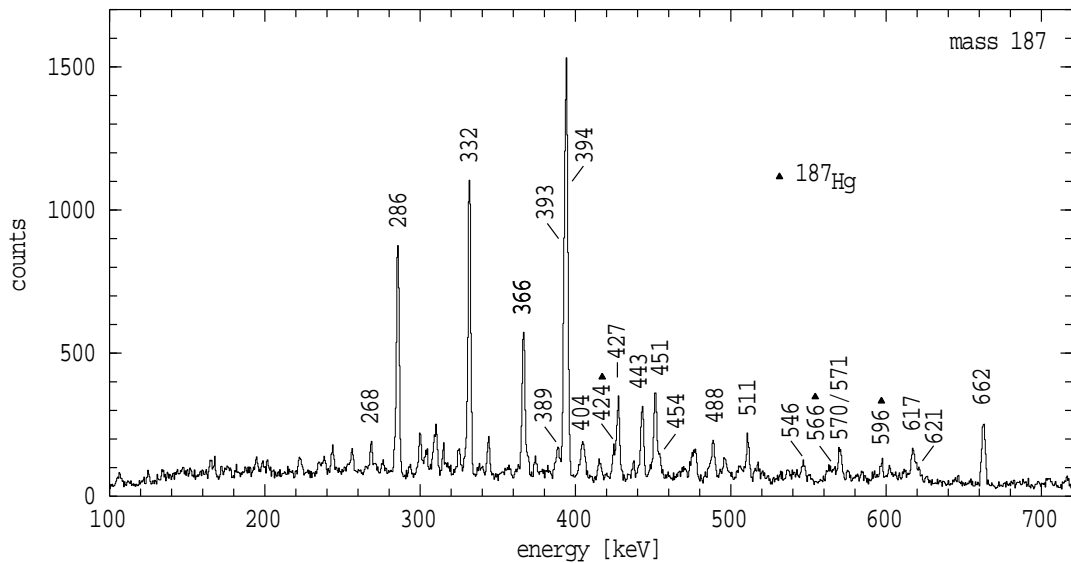


Figure 4.2: Spectrum of  $\gamma$ -rays in coincidence with mass-187 residues measured at Argonne. The majority of the cross-section for mass-187 residues leads to  $^{187}\text{Tl}$ , with  $\sim 10\%$   $^{187}\text{Hg}$ .

coincidence matrices were used, as the coincidence requirement reduced the interference from the low-multiplicity Coulomb excitation  $\gamma$ -rays. (Note that this has the effect of biasing the intensities towards higher values for the high spin transitions due to their being associated with a higher average  $\gamma$ -ray multiplicity.)

Angular distributions were obtained by projecting, from the  $\gamma-\gamma$  coincidence data for the backed target experiments, spectra corresponding to  $\gamma$ -rays observed at the three angles of detection in the CAESAR array. The coincidence requirement reduced the interference from Coulomb excitation and allowed an estimate of the intensities at the three detector angles, so that  $A_2$  coefficients for five of the intense  $\gamma$ -rays in  $^{187}\text{Tl}$  could be determined. Some of these angular distributions are shown in Figure 4.3. Strictly speaking, these are not true angular distributions because the intensities are taken from the coincidence data, not the singles data. However, if the intensity of a  $\gamma$ -ray is measured at a particular angle, the  $\gamma$ -rays in coincidence with it have a range of multipolarities and can be detected at any of the three angles of observation. Hence any correlation effects tend to cancel out, at least within the precision with which the  $A_2$  coefficients are measured.

The limited angular distribution information was extended by extracting DCO ratios using the method described in §3.5. As discussed there, the effects of vacuum deorientation on the DCO ratios appear to be negligible and results from the thin target experiment were used because of their greater statistics. Selected DCO ratios obtained from gating on both stretched quadrupole and dipole tran-

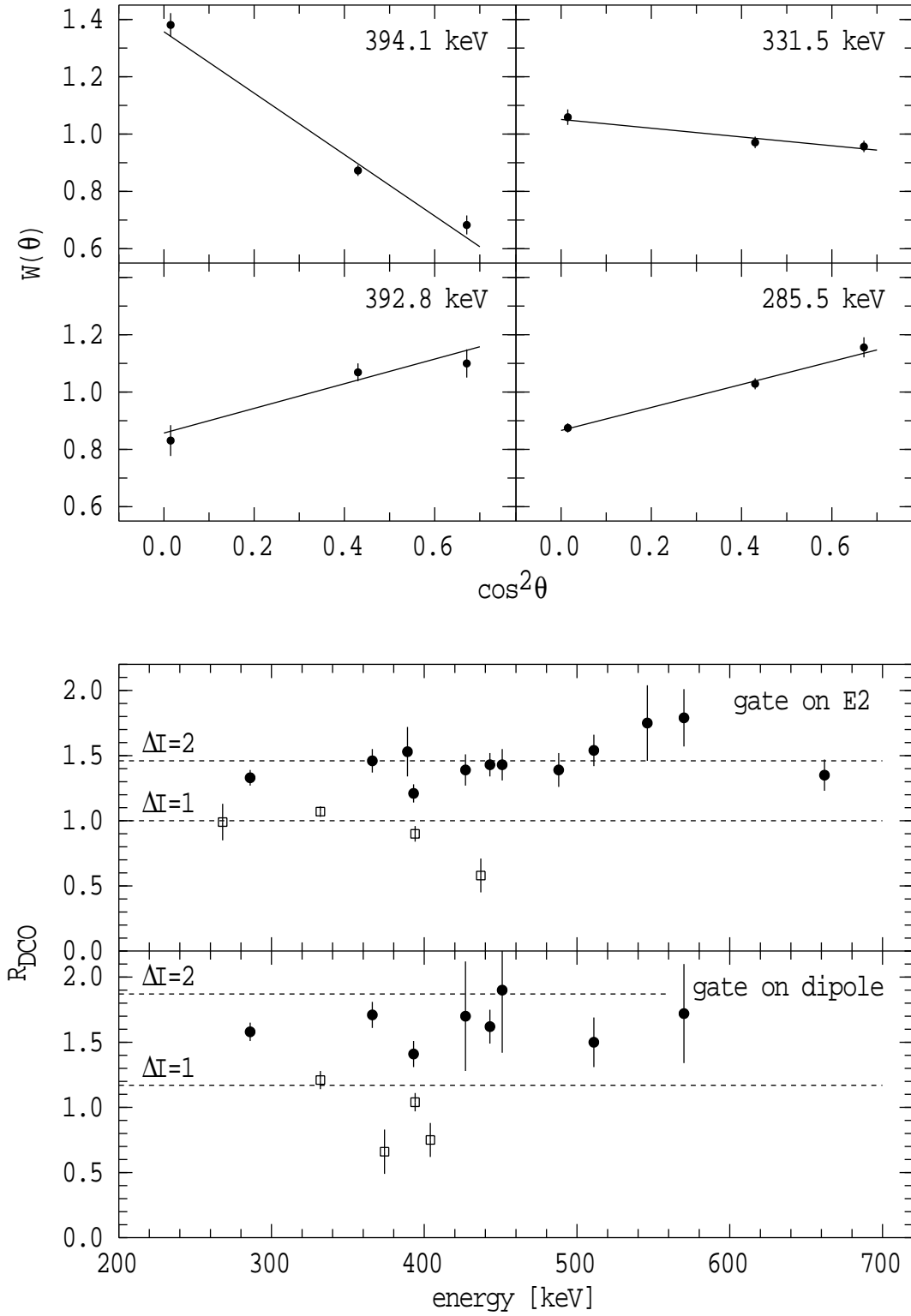


Figure 4.3: The top four panels show the measured angular distributions for the bottom four transitions in the yrast cascade of  $^{187}\text{Tl}$  together with fitted angular distributions of the form  $W(\theta) = 1 + A_2 P_2(\cos\theta)$ . The bottom panels show DCO ratios for selected quadrupole (circles) and dipole (squares) transitions in  $^{187}\text{Tl}$ . The dashed lines indicate theoretically expected values for pure dipole and quadrupole transitions (see §3.5). (Note that the theoretical predictions in the lowest panel assume the gating transition is a pure dipole, whereas the 394.1 keV gating transition is in fact M1/E2.)



sitions in  $^{187}\text{Tl}$  are plotted in Figure 4.3, together with theoretically calculated values for stretched dipole and quadrupole transitions. The experimental results show a reasonably clear distinction between the two types of transitions.

The  $\gamma$ -rays assigned to  $^{187}\text{Tl}$  are collected in Table 4.2, together with their intensities, angular distribution coefficients, DCO ratios and placements. Some weak  $\gamma$ -rays shown in the table have been definitively assigned to  $^{187}\text{Tl}$  but could not be placed in the level scheme.

Table 4.2: Transitions assigned to  $^{187}\text{Tl}$ 

$E_\gamma$ [keV]	$I_\gamma^{rel}$	$E_i \rightarrow E_f$ [keV]	$J_i^\pi \rightarrow J_f^\pi$	$A_2^{a)}$	$R_{\text{DCO}}$ (dip. gate) <sup>b)</sup>	$R_{\text{DCO}}$ (E2 gate)	Multi- polarity
164.8(2)	1.4(4)	1427 $\rightarrow$ 1262	$\left(\frac{15}{2}^-\right) \rightarrow \left(\frac{13}{2}^-\right)$				(M1)
201.8(4) <sup>c)</sup>	1.2(3)						
221.5(5) <sup>c)</sup>	2.1(4)						
237.9(3) <sup>d)</sup>	1.9(4)						
242.6(2)	3.7(9)	1448 $\rightarrow$ 1205	$\frac{17}{2}^- \rightarrow ( )$			1.36(51)	
253.7(3) <sup>e)</sup>	1.0(3)						
255.4(3) <sup>e)</sup>	2.9(5)						
256.4(2)	1.5(5)						
268.3(1)	4.2(6)	997 $\rightarrow$ 729	$\frac{13}{2}^- \rightarrow \frac{11}{2}^-$			0.99(14)	M1/E2
275.6(3) <sup>d)</sup>	1.7(3)						
285.5(1)	37(4)	1739 $\rightarrow$ 1453	$\frac{21}{2}^+ \rightarrow \frac{17}{2}^+$	+0.27(3)	1.58(7)	1.33(6)	E2
293.0(2) <sup>d)</sup>	1.4(3)						
299.0(2) <sup>d)</sup>	1.4(3)						
299.8(2)	1.4(5)						
304.2(2)	3.5(6)	1731 $\rightarrow$ 1427	$\left(\frac{17}{2}^-\right) \rightarrow \left(\frac{15}{2}^-\right)$				(M1)
309.8(2)	6.6(10)	1262 $\rightarrow$ 952	$\left(\frac{13}{2}^-\right) \rightarrow \left(\frac{11}{2}^-\right)$				(M1)
310.3(2) <sup>e)</sup>	weak						
324.0(2)	1.2(4)						
325.1(2)	3.4(8)	1587 $\rightarrow$ 1262	$\left(\frac{15}{2}^-\right) \rightarrow \left(\frac{13}{2}^-\right)$				(M1)
331.5(1)	55(4)	1061 $\rightarrow$ 729	$\frac{13}{2}^+ \rightarrow \frac{11}{2}^-$	-0.10(3)	1.21(7)	1.07(4)	E1/M2
343.8(2)	7.1(7)	679 $\rightarrow$ 335	$( ) \rightarrow \frac{9}{2}^-$				
362.7(2)	1.6(4)	1950 $\rightarrow$ 1587	$\left(\frac{17}{2}^-\right) \rightarrow \left(\frac{15}{2}^-\right)$				(M1)
366.3(1)	31(2)	2105 $\rightarrow$ 1739	$\frac{25}{2}^+ \rightarrow \frac{21}{2}^+$		1.71(10)	1.46(9)	E2
374.1(2)	2.7(5)	1839 $\rightarrow$ 1465	$\frac{17}{2}^+ \rightarrow \frac{15}{2}^+$		0.66(17)		M1
388.8(1)	5(1)	1823 $\rightarrow$ 1434	$\frac{19}{2}^- \rightarrow \frac{15}{2}^-$		1.33(23)	1.53(19)	E2
392.8(1)	41(4)	1453 $\rightarrow$ 1061	$\frac{17}{2}^+ \rightarrow \frac{13}{2}^+$	+0.29(8)	1.41(10)	1.21(7)	E2
393.2(3) <sup>d)</sup>	weak						
394.1(1)	77(5)	729 $\rightarrow$ 335	$\frac{11}{2}^- \rightarrow \frac{9}{2}^-$	-0.71(5)	1.04(7)	0.90(6)	M1/E2
404.2(2)	4.0(4)	1465 $\rightarrow$ 1061	$\frac{15}{2}^+ \rightarrow \frac{13}{2}^+$		0.75(13)		M1/E2
427.3(1)	19(1)	1876 $\rightarrow$ 1448	$\frac{21}{2}^- \rightarrow \frac{17}{2}^-$		1.70(42)	1.39(12)	E2
436.9(2)	3.2(5)	1434 $\rightarrow$ 997	$\frac{15}{2}^- \rightarrow \frac{13}{2}^-$			0.58(13)	M1/E2
442.6(1)	18(1)	2548 $\rightarrow$ 2105	$\frac{29}{2}^+ \rightarrow \frac{25}{2}^+$		1.62(13)	1.43(9)	E2
448.4(3)	2.7(5)	1446 $\rightarrow$ 997	$\left(\frac{15}{2}^-\right) \rightarrow \frac{13}{2}^-$			0.93(67)	(M1/E2)
451.1(1)	23(1)	1448 $\rightarrow$ 997	$\frac{17}{2}^- \rightarrow \frac{13}{2}^-$	+0.34(7)	1.90(48)	1.43(12)	E2
453.8(2)	5.7(6)	2277 $\rightarrow$ 1823	$\frac{23}{2}^- \rightarrow \frac{19}{2}^-$		1.60(65)	1.66(44)	E2
468.8(2)	2.9(5)	1731 $\rightarrow$ 1262	$\left(\frac{17}{2}^-\right) \rightarrow \left(\frac{13}{2}^-\right)$				(E2)

Table 4.2: continued

$E_\gamma$ [keV]	$I_\gamma^{rel}$	$E_i \rightarrow E_f$ [keV]	$J_i^\pi \rightarrow J_f^\pi$	$A_2^{a)}$	$R_{DCO}$ (dip. gate) <sup>b)</sup>	$R_{DCO}$ (E2 gate)	Multi- polarity
474.9(2)	5.4(7)	1427→952	$(\frac{15}{2}^-) \rightarrow (\frac{11}{2}^-)$				(E2)
476.9(3)	7.8(8)	1205→729	$( ) \rightarrow \frac{11}{2}^-$		1.21(41)	1.47(93)	
477.3(2)	1.1(2)	2583→2105	$( ) \rightarrow \frac{25}{2}^+$				
488.4(1)	10.7(8)	2364→1876	$\frac{25}{2}^- \rightarrow \frac{21}{2}^-$			1.39(13)	E2
510.6(1)	11.8(8)	3058→2548	$\frac{33}{2}^+ \rightarrow \frac{29}{2}^+$		1.50(19)	1.54(12)	E2
517.1(2)	4.3(9)	2794→2277	$(\frac{27}{2}^-) \rightarrow \frac{23}{2}^-$		3.1(1.5)	1.35(35)	(E2)
535.6(2)	1.9(4)	2641→2105	$( ) \rightarrow \frac{25}{2}^+$				
546.3(1)	6.4(6)	2910→2364	$\frac{29}{2}^- \rightarrow \frac{25}{2}^-$			1.75(29)	E2
562.7(2)	2.2(5)	2302→1739	$( ) \rightarrow \frac{21}{2}^+$				
564.4(2)	1.6(4)	2440→1876	$( ) \rightarrow \frac{21}{2}^-$			0.72(53)	
569.9(1)	7.0(9)	3628→3058	$\frac{37}{2}^+ \rightarrow \frac{33}{2}^+$		1.72(38)	1.79(22)	E2
570.7(2)	2.4(6)	3365→2794	$(\frac{31}{2}^-) \rightarrow (\frac{27}{2}^-)$				(E2)
575.8(3)	1.4(4)	3486→2910	$( ) \rightarrow \frac{29}{2}^-$				
584.6(2)	3.2(5)	2949→2364	$( ) \rightarrow \frac{25}{2}^-$				
601.4(2)	2.9(4)	3512→2910	$(\frac{33}{2}^-) \rightarrow \frac{29}{2}^-$			1.25(31)	(E2)
611.9(4)	1.3(5)	3977→3365	$(\frac{35}{2}^-) \rightarrow (\frac{31}{2}^-)$				(E2)
616.9(2)	12.7(9)	952→335	$(\frac{11}{2}^-) \rightarrow \frac{9}{2}^-$				(M1)
620.6(1)	4.8(4)	4249→3628	$(\frac{41}{2}^+) \rightarrow \frac{37}{2}^+$				(E2)
627.6(3)	1.2(3)	4139→3512	$(\frac{37}{2}^-) \rightarrow (\frac{33}{2}^-)$				(E2)
646.4(2)	2.1(6)	1376→729	$( ) \rightarrow (\frac{11}{2}^-)$				
662.3(1)	23(1)	997→335	$\frac{13}{2}^- \rightarrow \frac{9}{2}^-$			1.35(12)	E2
662.4(1)	3.3(6)	4911→4249	$(\frac{45}{2}^+) \rightarrow (\frac{41}{2}^+)$				(E2)
687.2(2)	1.0(2)	3746→3058					
697.6(3)	0.7(2)	5609→4911	$(\frac{49}{2}^+) \rightarrow (\frac{45}{2}^+)$				(E2)
705.1(3)	3.8(6)	1434→729	$\frac{15}{2}^- \rightarrow \frac{11}{2}^-$				E2
716.2(3)	3.8(7)	1446→729	$(\frac{15}{2}^-) \rightarrow \frac{11}{2}^-$				(E2)
726.4(4)	1.8(4)	1061→335	$\frac{13}{2}^+ \rightarrow \frac{9}{2}^-$				M2
778.6(5) <sup>f)</sup>	≤1.1	1839→1061	$\frac{17}{2}^+ \rightarrow \frac{13}{2}^+$				E2
798.8(2)	2.2(5)	2675→1876	$( ) \rightarrow \frac{21}{2}^-$				

<sup>a)</sup> From the backed target experiment.

<sup>b)</sup> Only the 394.1 and 331.5 keV transitions were used as gates.

<sup>c)</sup> Present in the mass-187 spectrum and in coincidence with thallium X-rays, but unplaced.

<sup>d)</sup> Associated with band 4, but unplaced.

<sup>e)</sup> Associated with band 2, but unplaced.

<sup>f)</sup> Tentatively assigned.

## 4.2 Level Scheme for $^{187}\text{Tl}$

The level scheme for  $^{187}\text{Tl}$  obtained in the current work is shown in Figure 4.4, with the different rotational structures numbered for easy description. Before describing the details of its construction, the results of other spectroscopic studies are briefly presented.

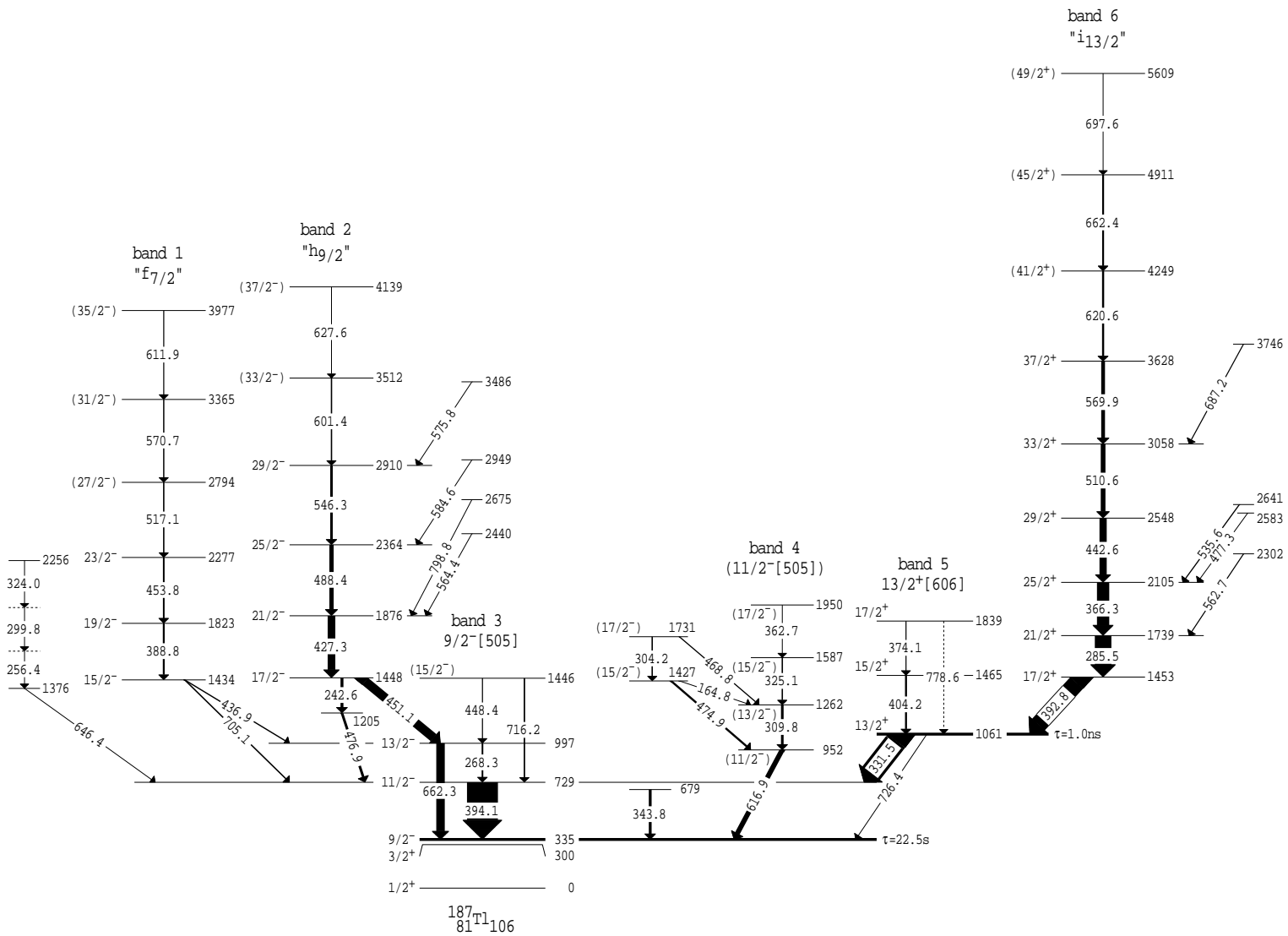


Figure 4.4: Level scheme for  $^{187}\text{Tl}$  obtained in the current work. The widths of the transitions are proportional to the  $\gamma$ -ray intensities. Spin and parity assignments are based upon the transition multipolarities, assuming the 22.5 s isomer has spin and parity  $9^-$ .

### 4.2.1 Other spectroscopic studies

Before this work only a few levels were known in  $^{187}\text{Tl}$ . The  $\beta$ -decay study of Misaelides *et al.* [Mis81] had identified the beginnings of a band built on the  $\frac{1}{2}^+$  ground state, as well as 394 and 331 keV  $\gamma$ -rays in cascade, feeding a  $\frac{9}{2}^-$  isomer with a meanlife of 22.5 s. They assigned the 394 keV  $\gamma$ -ray as the first transition in the band built on the  $\frac{9}{2}^-$  state and the 331 keV  $\gamma$ -ray as a transition from a  $\frac{13}{2}^+$  state. They also observed a 300 keV  $\gamma$ -ray which followed the decay of the  $\frac{9}{2}^-$  isomer, but could not measure the excitation energy of the isomer due to an intervening low-energy transition which was unobserved. The alpha decay work of Coenen *et al.* [Coe85] later placed the isomer at an excitation energy of  $335 \pm 7$  keV.

The only in-beam experiment reported prior to the start of this work was a preliminary heavy-ion study using the reaction  $^{159}\text{Tb}(^{32}\text{S},4\text{n})$  by Goettig *et al.* [Goe88]. They provided independent confirmation of the previously known  $\gamma$ -rays above the  $\frac{9}{2}^-$  isomer as well as evidence for 286 and 366 keV  $\gamma$ -rays feeding above the 331 keV transition. Part of their experiment also involved an attempted recoil distance measurement of the lifetimes of the states in the rotational bands built upon the  $\frac{9}{2}^-$  isomers in  $^{187}\text{Tl}$ ,  $^{189}\text{Tl}$  and  $^{191}\text{Tl}$ . The attempt failed because the short lifetimes in the rotational band were rendered unmeasurable because of an unidentified feeding state with a longer lifetime of approximately 300 ps. In the case of  $^{187}\text{Tl}$  this may be related to the isomeric  $\frac{13}{2}^+$  state which has been identified in the current work. (See §4.2.7 below.)

The  $^{32}\text{S}$  induced reaction used in the current work preferentially populates high-spin states and no  $\gamma$ -rays were observed that could be assigned as feeding directly into the  $\frac{1}{2}^+$  ground state. However, the previously known level scheme above the  $\frac{9}{2}^-$  isomer has been extended up to a tentative spin of  $\frac{49}{2}\hbar$ . High-spin spectroscopy of  $^{187}\text{Tl}$  by Reviol *et al.* [Rev94] using the  $^{156}\text{Gd}(^{35}\text{Cl},4\text{n})$  reaction has proceeded in parallel to, and independently of, this work. They also identified new states above the  $\frac{9}{2}^-$  isomer, but with significant differences to the present decay scheme, as discussed below.

### 4.2.2 Band 6.

Most of the population of  $^{187}\text{Tl}$  comes through band 6, then feeds through the base of bands 5 and 3. The negative  $A_2$  values for both the 394.1 keV transition in band 3 and the 331.5 keV interband transition, indicates that they both have

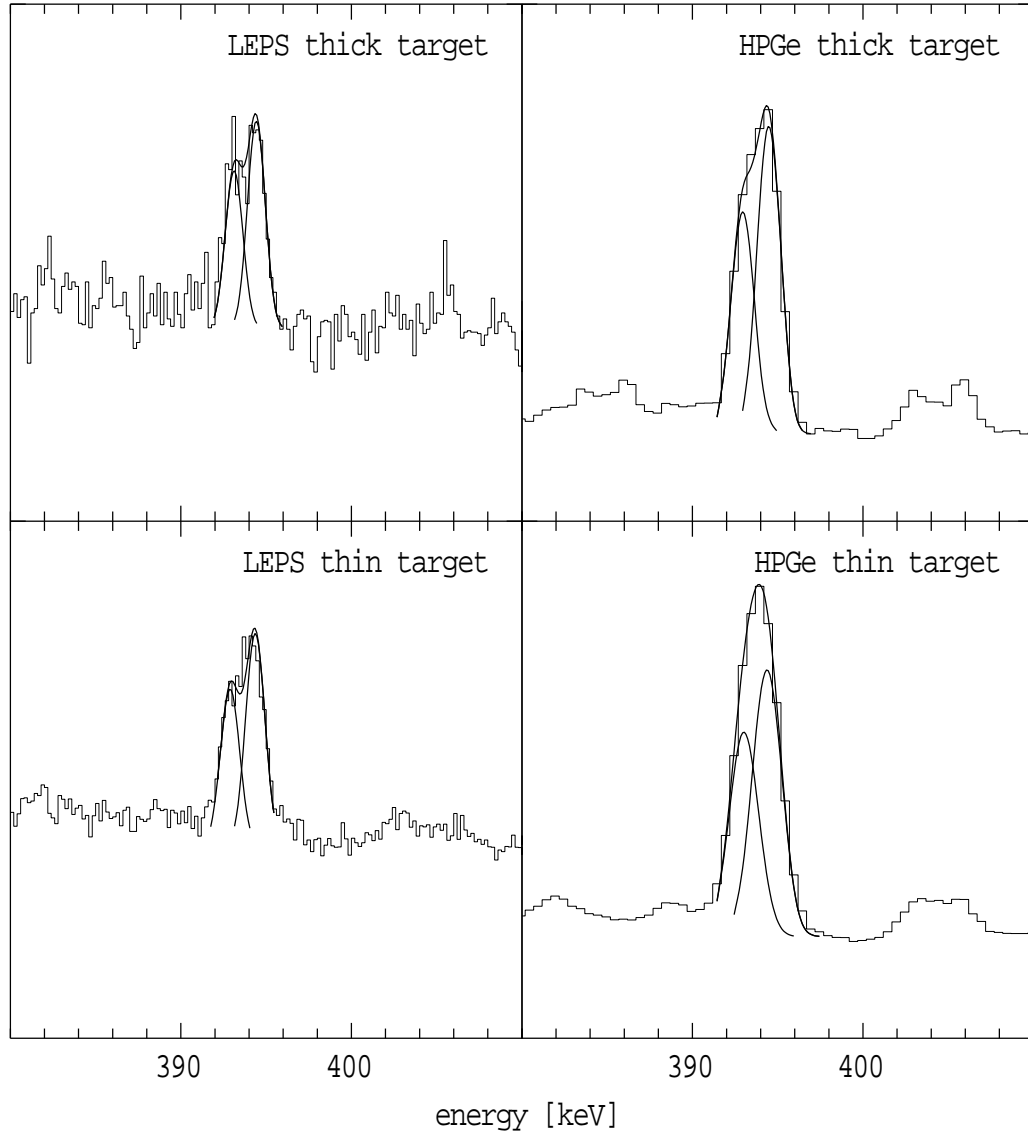


Figure 4.5: Projections of the  $\gamma-\gamma$  and  $\gamma$ -LEPS coincidence matrices from both the thin and thick target experiments showing the 392.8/394.1 keV doublet.

dipole character, while the 392.8 and 285.5 keV transitions at the base of band 6 have  $A_2 \approx 0.3$ , indicating quadrupole character. The DCO ratios for the higher transitions in band 6 are also consistent with quadrupole character. The current work differs from that of Reviol *et al.* [Rev94] in two crucial aspects. Reviol *et al.* assign the 331.5 keV  $\gamma$ -ray to be an M1 transition, in contrast to our E1 assignment, and they also reverse the ordering of the 285.5 and 392.8 keV transitions on the basis of a 617 keV transition crossing the 285.5 and 331.5 keV transitions.

Addressing firstly the ordering; unfolding of the 392.8/394.1 doublet, which is partially resolved in the present work (see Figure 4.5), results in the two coinci-

Table 4.3: Intensities of transitions in the unfolded coincidence spectra for the 392.8/394.1 keV doublet

Transition [keV]	Multipolarity	$1+\alpha_T$	Relative intensities <sup>a)</sup>	
			394.1 keV gate	392.8 keV gate
394.1	M1/E2	1.179 <sup>b)</sup>	—	14.4(4)
331.5	E1	1.023	14.5(4)	15.6(3)
392.8	E2	1.052	12.1(5)	—
285.5	E2	1.131	10.2(2)	14.9(4)
366.3	E2	1.064	7.8(4)	10.5(3)

<sup>a)</sup> Corrected for efficiency and internal conversion.

<sup>b)</sup> Calculated assuming a mixing ratio of  $\delta = -0.4$  (see §5.2.1),  $\alpha_T(\text{M1}) = 0.199$  and  $\alpha_T(\text{E2}) = 0.052$ .

dence spectra shown in Figure 4.6<sup>1</sup>. (The presence of the 268.3 keV  $\gamma$ -ray in only the 394.1 keV coincidence spectrum and not the 392.8 keV spectrum indicates the quality of the unfolding.) The efficiency and conversion corrected relative intensities for the  $\gamma$ -rays in both coincidence spectra appear in Table 4.3. In this region of spin and excitation energy, there is only a marginal difference in intensities due to the lack of side-feeding, but the results in Table 4.3 clearly show that in the 394.1 keV unfolded coincidence spectrum, the 285.5 keV transition is less intense than the 392.8 keV transition. This is in agreement with the relative intensities found from the projections of both the  $\gamma - \gamma$  and  $\gamma$ -LEPS coincidence matrices for the backed and unbacked experiments and also from the mass-187 gated  $\gamma$ -ray spectrum, supporting the ordering given in Figure 4.4.

With respect to the purported 617 keV cross-over transition, note that the ordering in Figure 4.4 does not allow for such a transition. Irrespective of this, Figure 4.6 shows the 366 keV coincidence spectrum with an expanded view of the 600 keV region in the inset. Superimposed is a *simulated* spectrum with a 617 keV transition of the intensity expected from the branching ratio of  $L_\gamma(617)/L_\gamma(286)=6.0/90.6$  obtained by Reviol *et al.* There is no evidence in the observed spectrum for such a transition. It should be noted that a 616.9 keV transition has been placed in band 4 and it shows coincidences with an unplaced

<sup>1</sup>Note that these spectra are from the thin target experiment. Unless otherwise noted, all coincidence spectra presented in this thesis will be from the thin target data sets and will be shown at a dispersion of 0.5 keV per channel.

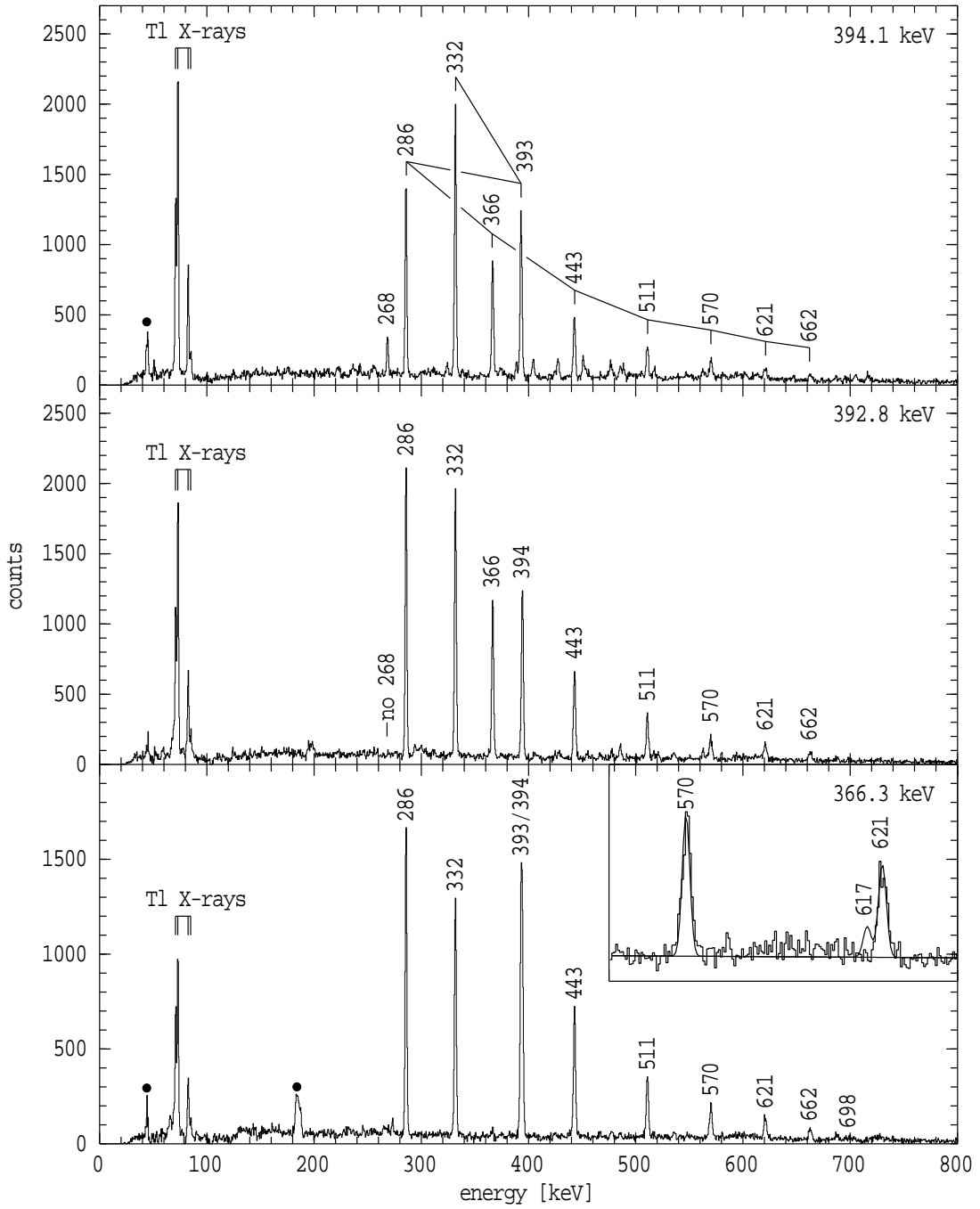


Figure 4.6: The upper panels show the unfolded coincidence spectra for the 392.8/394.1 keV  $\gamma$ -ray doublet. The ordering of transitions is indicated by the connecting lines in the 394.1 keV coincidence spectrum. The bottom panel contains the coincidence spectrum for the 366.3 keV transition. The expanded region around 600 keV has a solid line overlaying the data showing the spectrum that would have been expected if the results of Reviol *et al.* [Rev94] were correct. Solid circles indicate known contaminants.

393.2 keV  $\gamma$ -ray (see below in §4.2.5). This lies between the energies of the 392.8/394.1 doublet, so that gates on these transitions show weak, but misleading, 617 keV coincidences.

The multipolarity of the 331.5 keV transition can be obtained from the intensity balance on the 394.1 and 331.5 keV transitions in the 392.8 keV coincidence spectrum. Both this work and that of Reviol *et al.* agree that the 394.1 keV transition has M1/E2 multipolarity. Using the mixing ratio of  $\delta = -0.4$  obtained in §5.2.1, the expected total conversion coefficient for this transition is  $\alpha_T = 0.179$ . The intensities in Table 4.3 use this value for the 394.1 keV transition and  $\alpha_T = 0.023$  for the 331.5 keV transition, corresponding to a pure E1 assignment. These assignments approximately balance the intensities of the 394.1 and 331.5 keV transitions. M1 character for the 331.5 keV transition would require  $\alpha_T(331.5) = 0.32$ , giving a total transition intensity of 20.2(4) and a severe intensity imbalance.

The E1 assignment for the 331.5 keV transition together with the stretched dipole character deduced from its angular distribution and DCO ratios, establishes a  $\frac{13}{2}^+$  level at 1061 keV, while the E2 character of the transitions above defines a sequence of levels up to a tentative spin of  $\frac{49}{2}\hbar$  and an excitation energy of 5.6 MeV. The higher levels are grouped into a decoupled band beginning at spin  $\frac{17}{2}^+$ , with the 392.8 keV  $\gamma$ -ray as a transition connecting the decoupled band to the  $\frac{13}{2}^+$  state.

### 4.2.3 Bands 3 and 5.

The 394.1 keV M1 transition at the base of band 3, shows coincidences with a 268.3 keV dipole  $\gamma$ -ray and both 448.4 and 716.2 keV  $\gamma$ -rays. The coincidence spectra for the 268.3 keV and 716.2 keV transitions in Figure 4.7 show clearly that the 662.3 keV transition is parallel to the 268.3 and 394.1 keV transitions. Furthermore, the 716.2 keV transition crosses over the 268.3 and 448.4 keV transitions. These coincidence relationships establish a band built upon the  $\frac{9}{2}^-$  isomer.

Band 5 consists of 404.2 and 374.1 keV transitions feeding the  $\frac{13}{2}^+$  state with DCO ratios indicating dipole character and the ordering based upon the observed intensities (see the coincidence spectra for the 394.1 keV transition in Figure 4.6). A 778.6 keV crossover transition is also assigned tentatively.



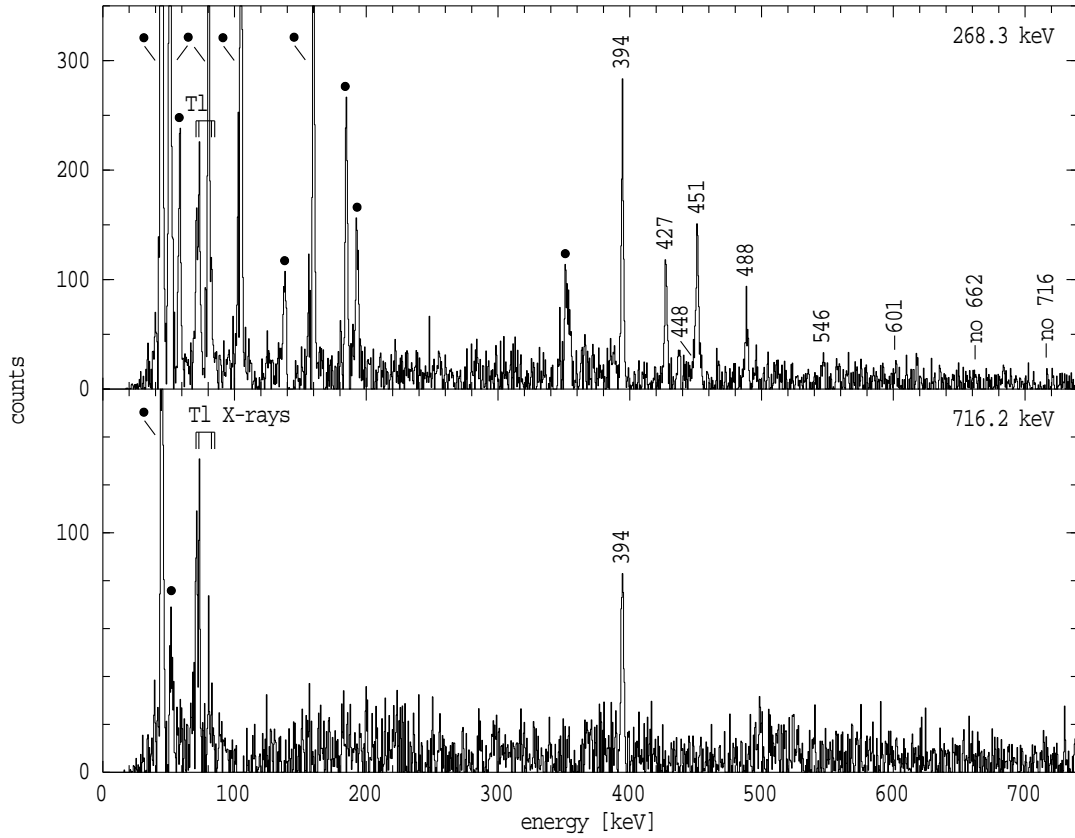


Figure 4.7: Coincidence spectra for the 268.3 and 716.2 keV transitions associated with band 3 in  $^{187}\text{Tl}$ , with known contaminants indicated by filled circles. The large number of low energy contaminating transitions in the 268.3 keV coincidence spectrum arise from the 269 keV,  $\frac{13}{2}^+ \rightarrow \frac{9}{2}^+$  transition in  $^{159}\text{Tb}$ . These lines are broad in the original spectrum and have been partially removed by subtraction of a neighbouring gate, however, because the coincidence peaks shift in energy from gate to gate due to Doppler effects, the “edges” of the lines remain after the subtraction.

#### 4.2.4 Bands 1 and 2.

A coincidence spectrum for the 451.1 keV transition appears in Figure 4.8 and shows the sequence assigned as band 2. The coincidence information for the side-feeding transitions at 564.4, 575.8, 584.6 and 798.8 keV, together with the intensity information, gives the ordering of the cascade. The position at which band 2 feeds band 3 is apparent from the coincidence relationships with the 268.3 and 662.3 keV transitions. The quadrupole character of the 451.1 keV transition and the alternative decay path established by the 242.6 and 476.9 keV transitions, indicate a  $\frac{17}{2}^-$  assignment for the 1448 keV state, while the DCO ratios support stretched E2 assignments for the transitions above this state. There are other transitions also associated with this band which could not be placed unambiguously, namely the 253.7 and 255.4 keV transitions which appear to feed near the  $\frac{21}{2}^-$  level and a 310.3 keV transition.

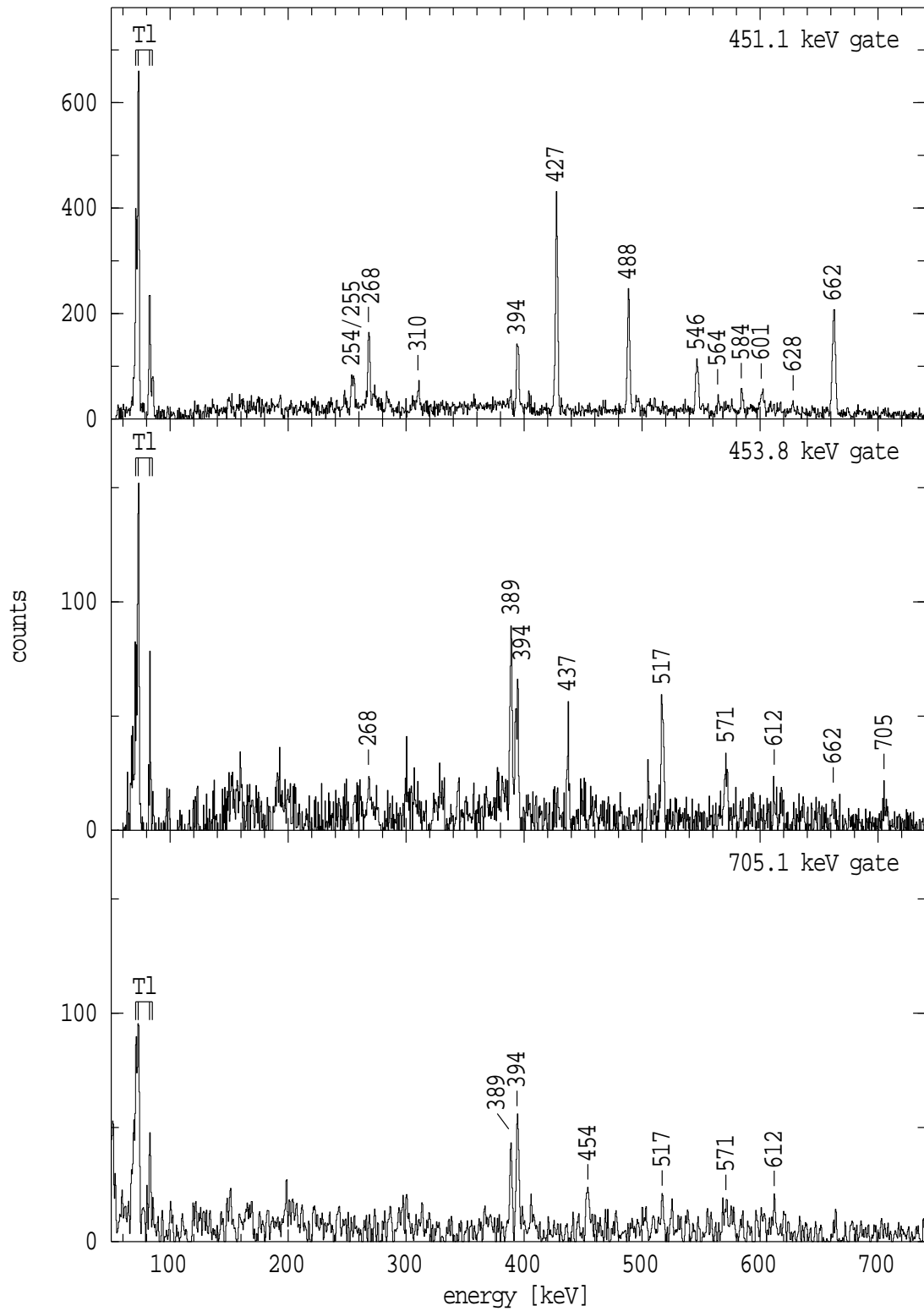


Figure 4.8: Coincidence spectra for transitions associated with the decoupled bands 1 and 2.

Band 1 can be seen in the coincidence spectra for the 705.1 and 453.8 keV transitions in Figure 4.8. The 705.1 keV  $\gamma$ -ray shows no coincidences with the 268.3 or 662.3 keV transitions, and, since the 394.1 keV  $\gamma$ -ray is the most intense in its coincidence spectrum, must feed into the 729 keV level. The ordering of the rotational sequence is established from the intensities of the higher transitions with the DCO ratios, although not definitive, suggesting E2 character. (Note that a 705 keV transition feeding the 729 keV level was also placed by Reviol *et al.* [Rev94], but as an E2 crossover in the band built upon the  $\frac{9}{2}^-$  isomer.) The presence of the 436.9 keV transition, with a DCO ratio suggesting a  $\Delta I=1$ , mixed dipole/quadrupole assignment, leads to a  $\frac{15}{2}^-$  assignment for the 1434 keV level, as does the lesser feeding this band receives relative to band 2.

It is perhaps possible that the 436.9 keV transition is E1 and the 705.1 keV transition is M2. Assuming this is true and that these transitions have the same decay strengths as the 331.5 keV E1 and 726.4 keV M2 transitions, the  $\frac{I_{\gamma}(331.5)}{I_{\gamma}(726.4)}$  branching ratio out of the  $\frac{13}{2}^+$  state at 1061 keV can be used to predict that the 436.9 keV transition should be  $\sim 80$  times more intense than the 705.1 keV transition, in conflict with the measured intensity ratio of  $\sim 1$ . Later analysis in §5.3.2 will show that the B(M2) and B(E1) values for the 726.4 and 331.5 keV transitions are 0.21(6) W.U. and  $7.7(16) \times 10^{-6}$  W.U. respectively <sup>2</sup>, in agreement with expectations based upon the intrinsic structures. E1 and M2 assignments for the 436.9 and 705.1 keV transitions would result in their decay strengths being somewhat unusual, so that M1 and E2 assignments are instead favoured.

### 4.2.5 Band 4

Most of the  $\gamma$ -rays in the coincidence spectrum for the 616.9 keV transition shown in Figure 4.9 have been assigned to  $^{187}\text{Tl}$ , with others arising from contaminating lines in  $^{187}\text{Hg}$  [Han88] and  $^{159}\text{Tb}$  [Lee88]. Although the 237.9, 275.6, 293.0, 299.0 and 393.2 keV  $\gamma$ -rays in the 616.9 keV coincidence spectrum have been assigned to  $^{187}\text{Tl}$ , there was insufficient information to place them in the level scheme. A piece of the evidence for the tentative level structure associated with the other

---

<sup>2</sup>A Weisskopf Unit (W.U.) is a simple estimate of the single particle decay strength for each multipolarity. Decay strengths are often expressed in Weisskopf Units as this allows a semi-quantitative comparison between different multipolarity transitions. Furthermore, the collectivity of a transition can be directly expressed because one Weisskopf Unit corresponds to one “single particle unit.” A convenient table for the evaluation of Weisskopf estimates for decay strengths can be found on page 149 of Ref. [Löb75].

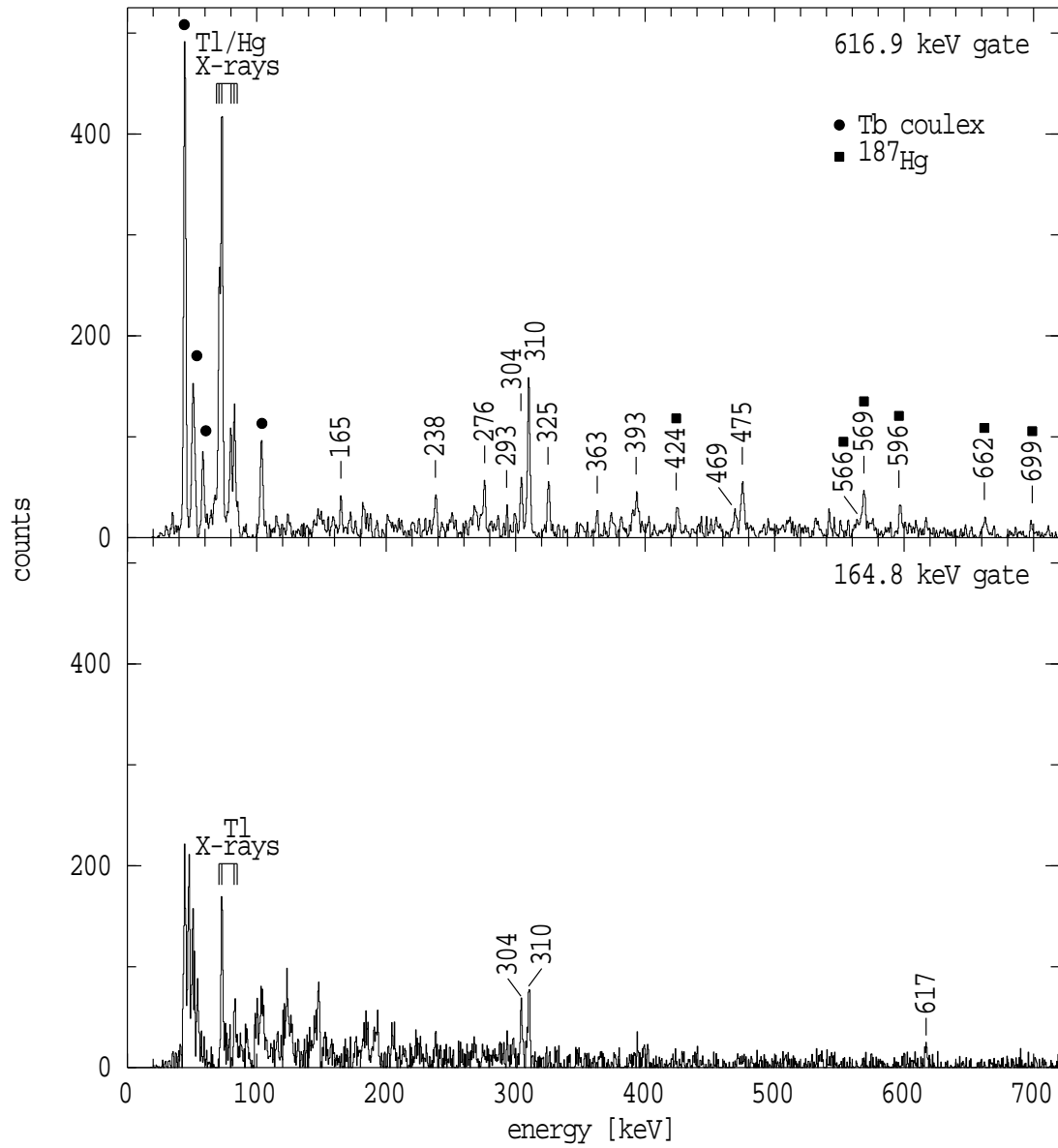


Figure 4.9: Coincidence spectra for transitions associated with band 4. The broad lines between 100 and 200 keV and the group of lines with energy less than 60 keV which are present in the 164.8 keV coincidence spectrum, are also present in neighbouring gates and are obviously not due to evaporation residues. Subtraction of a neighbouring gate has been performed in an attempt to clean up the spectrum, however, their removal is not complete.

$\gamma$ -rays in the 616.9 keV coincidence spectrum can be seen in the coincidence spectrum for the 164.8 keV transition in Figure 4.9. It shows that the 164.8 keV transition sees the 309.8 keV transition but not the 325.1 and 362.7 keV transitions. Coincidence relationships from other coincidence spectra also agree with the proposed structure. The placement of the band is based on the fact that there are no clear coincidences with any of the strong transitions already assigned to  $^{187}\text{Tl}$ . It presumably therefore feeds either the  $\frac{9}{2}^-$  isomer or the ground state,

however, its population is such that the latter is unlikely. The tentatively assigned spins are based upon feeding arguments and the presence of the 474.9 keV crossover transition. M1 character has been assumed for most of the transitions for theoretical reasons associated with the assumed configuration (see §5.3.5).

#### 4.2.6 Other transitions.

The cascade of 646.4, 256.4, 299.8 and 324.0 keV  $\gamma$ -rays is only in coincidence with the 394.1 keV transition, indicating that it feeds into the 729 keV state. The ordering of the three lower energy transitions is uncertain due to their similar intensities and no information on the spins and parities could be obtained. However, dipole transitions are probable otherwise the levels would be yrast and more intense feeding would be expected.

The 343.8 keV transition has strong coincidences with thallium X-rays and shows no other coincidences with  $\gamma$ -rays assigned to  $^{187}\text{Tl}$ . It has been placed as feeding the  $\frac{9}{2}^-$  isomer, in accordance with the previous  $\beta$ -decay work of Misaelides *et al.* [Mis81].

A number of transitions appear to feed directly into bands 2 and 6 as shown in the level scheme.

#### 4.2.7 Isomeric states.

Initial investigations for  $^{187}\text{Tl}$  indicated no  $\gamma$ -rays with delayed intensity components. However, the study of  $^{185}\text{Tl}$  found that the  $\frac{13}{2}^+$  state was isomeric, and, based upon the observed transition strengths, the  $\frac{13}{2}^+$  state in  $^{187}\text{Tl}$  would be expected to be a nanosecond isomer. The presence of a short-lived isomer in  $^{187}\text{Tl}$  was subsequently deduced from analysis of the  $\gamma - \gamma - \text{time}$  matrix for the backed target experiment. Details of the  $\gamma - \gamma - \text{time}$  technique for measuring lifetimes were presented in §3.3.6.

Due to time walk in the detectors, the centroids of the time difference spectra for transitions in prompt coincidence are functions of both  $\gamma$ -ray energies. Although the time responses for the CAESAR array are well understood (see §3.3.6), the close proximity in energy for the 392.8 and 394.1 keV transitions in  $^{187}\text{Tl}$  meant that the time walk associated with these  $\gamma$ -rays cancelled each other, so that no corrections needed to be made for the time walk when comparing centroid positions for time spectra associated with these transitions. (It is also important that the two lines are partially resolved, as was seen in Figure 4.5, and

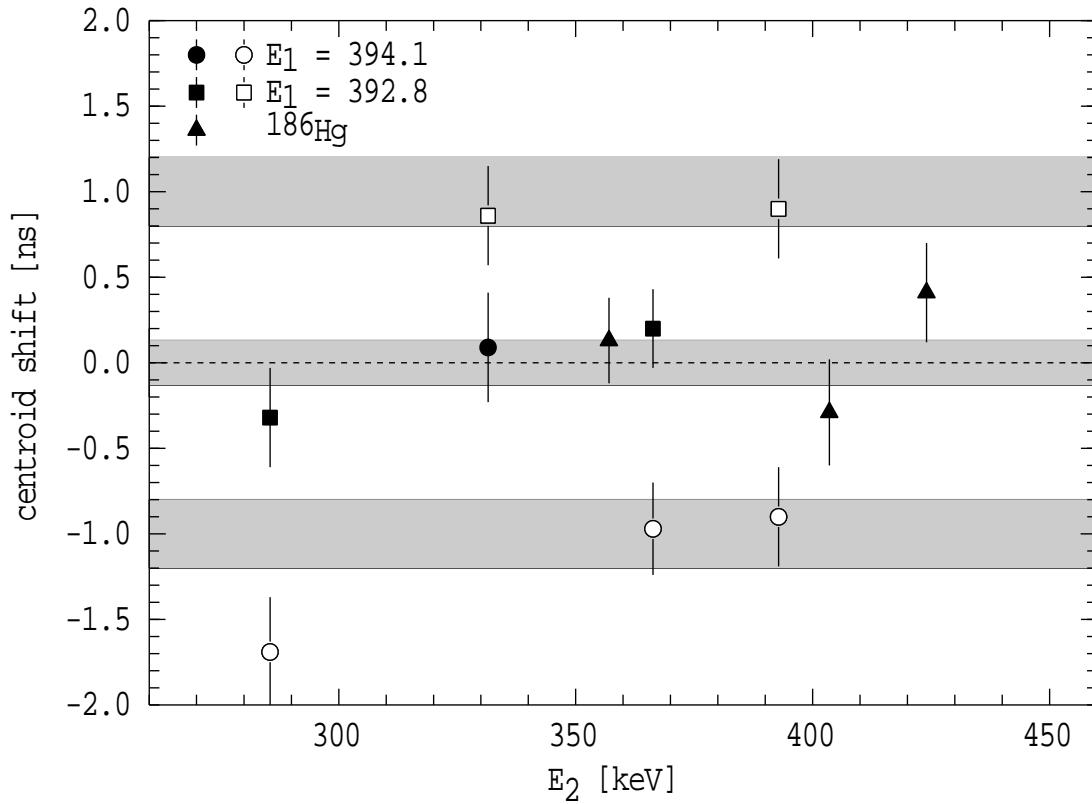


Figure 4.10: Centroid shifts for double-gated time difference spectra from the  $^{187}\text{Tl}$  backed target experiment where the first gate is on either the 392.8 or 394.1 keV transitions. Centroid shifts are also shown for transition pairs in  $^{186}\text{Hg}$  where one gate is on either the 403 or 405 keV transitions. (See the text for further details.)

their relative components can be unfolded.)

The ordering of the transitions in the yrast cascade is based upon the intensities, and, if there were no lifetimes present, the time spectra for the (392.8,331.5) and (394.1,331.5) slices would have the same centroid position. Instead, the (392.8,331.5) spectrum is shifted to a positive time difference with respect to the (394.1,331.5) slice, indicating the presence of an isomer at either or both of the  $\frac{11}{2}^-$  or  $\frac{13}{2}^+$  levels at 729 and 1061 keV respectively. Figure 4.10 plots, for a number of  $\gamma - \gamma - \text{time}$  slices, the difference between the observed centroid positions and the expected value for transitions in prompt coincidence, obtained from the parameterisation of Byrne *et al.* [Byr93]. The shaded region around zero is an estimate of the error associated with taking this difference and shows the region expected for a prompt coincidence. The energy of the second gating transition,  $E_2$ , is plotted on the x-axis, while circles indicate the results obtained when the first gate,  $E_1$ , is set on the 394.1 keV  $\gamma$ -ray, and squares indicate when it is on the 392.8 keV  $\gamma$ -ray. The triangles are results for  $\gamma$ -rays from  $^{186}\text{Hg}$  in which the

states are all known to have very short lifetimes [Pro74]. For the  $^{186}\text{Hg}$  slices, the first gate is either the 403 or 405 keV  $\gamma$ -ray, and the results are corrected for the energy dependence of the centroid position [Byr93]. This permits a direct comparison between the mercury and thallium results, despite the difference in energy of the first gating transitions. A negative centroid shift indicates that  $E_2$  is *earlier* than  $E_1$ , while a positive shift indicates that  $E_2$  is *later*. It can be seen that the filled symbols are consistent with prompt coincidences. For example, the 392.8 keV transition is observed to be in prompt coincidence with both the 285.5 and 366.3 keV transitions, while the 394.1 keV transition is in prompt coincidence with the 331.5 keV transition. The open symbols involve measurement across the  $\frac{13}{2}^+$  state and are shifted in directions consistent with the ordering in the level scheme, while the shaded regions centred on  $\pm 1.0$  ns indicate the fitted value for the meanlife of the  $\frac{13}{2}^+$  state,  $\tau_m = 1.0 \pm 0.2$  ns.

As previously mentioned in §4.2.1, Goettig *et al.* [Goe88] report in a conference proceeding that they observed a long feeding lifetime in their attempted recoil distance measurement of lifetimes for the states in the  $\frac{9}{2}^-$  [505] bands of  $^{187}\text{Tl}$ ,  $^{189}\text{Tl}$  and  $^{191}\text{Tl}$ .

One may speculate that this is in fact due to a  $\frac{13}{2}^+$  isomeric state in each nucleus. Using the measured E1 transition energies in  $^{189}\text{Tl}$  and  $^{191}\text{Tl}$  [Por91, New74, Rev95] and assuming the same  $B(E1)$  strength as in  $^{187}\text{Tl}$ , the “isomers” are predicted to have meanlives of  $\sim 330$  and  $\sim 160$  ps respectively. Further lifetime measurements for these isotopes would be of interest.

### 4.3 Analysis and Results for $^{185}\text{Tl}$

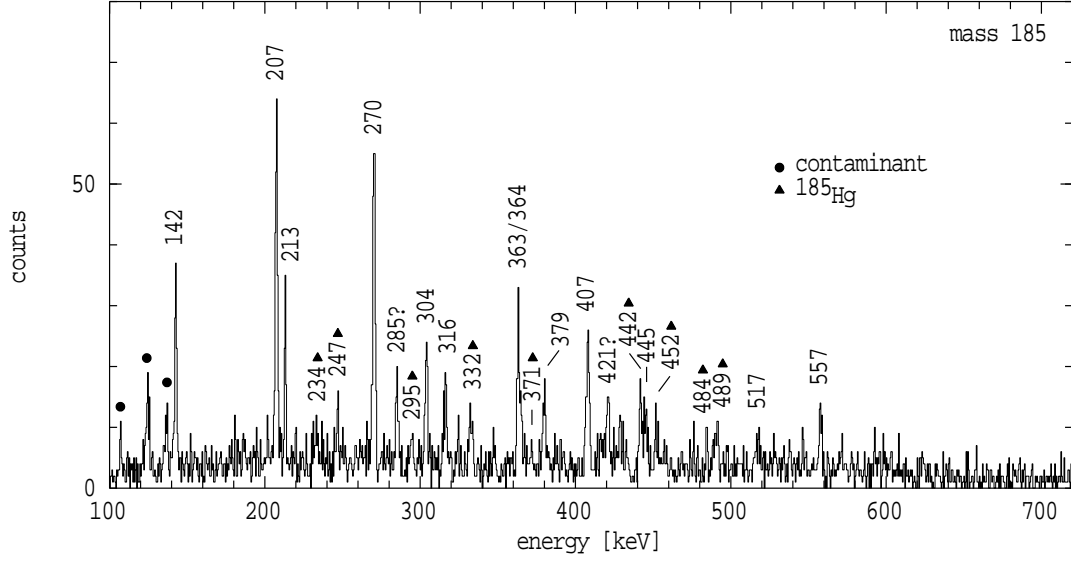
High-spin states in  $^{185}\text{Tl}$  were populated in three separate experiments as described in Table 4.1.  $^{185}\text{Tl}$  is more neutron-deficient than  $^{187}\text{Tl}$  and statistical model calculations for the  $^{35}\text{Cl} + ^{154}\text{Gd}$  bombardment predicted that the production cross-section for  $^{185}\text{Tl}$  would suffer from competition with both channels involving emission of charged particles and also fission. Nevertheless, the  $4n$  channel was predicted to be the dominant evaporation channel, at least for an isotopically pure target. However, the isotopic enrichment of the target was only 67%  $^{154}\text{Gd}$ , with sizeable percentages of  $^{155}\text{Gd}$  and  $^{156}\text{Gd}$ . The compound systems formed from bombardment of the heavier impurities are more neutron rich and less prone to fission, resulting in higher cross-sections for the production of evaporation residues. This means that the production of heavier isotopes due to these impurities is larger than would be expected from the relative isotopic enrichments. Experimentally, transitions in  $^{185}\text{Tl}$  were found to be the most intense, however,  $\gamma$ -rays from  $^{183}\text{Au}$  [Zho88],  $^{185}\text{Hg}$  [Han88a],  $^{186}\text{Hg}$  [Por92, Ma93],  $^{186}\text{Tl}$  [Kre81] and  $^{187}\text{Tl}$  were also identified. The intensity level of the contaminating transitions can be seen in the total projection of the  $\gamma - \gamma$  coincidence matrix from the thin target experiment shown in Figure 4.1. The figure also shows that the peak to background level is considerably worse than in the reaction used to make  $^{187}\text{Tl}$ . This is probably due to an increase in the fission cross-section due to the more neutron-deficient compound nucleus and a consequent increase in the number of unresolved  $\gamma$ -rays from fission products.

The  $\gamma$ -rays which showed coincidences with characteristic thallium X-rays were possibly due to  $^{185}\text{Tl}$ , and, since no (HI,xn) or (HI,pxn) channels were observed to lead to mass-184 nuclei,  $\gamma$ -rays not known to be from  $^{186}\text{Tl}$  or  $^{187}\text{Tl}$  were assigned to  $^{185}\text{Tl}$ . The correct assignment of transitions to  $^{185}\text{Tl}$  was confirmed by the mass-selected  $\gamma$ -ray spectra obtained in the Argonne experiments and shown in Figure 4.11.

An isomer in  $^{185}\text{Tl}$  causes considerable distortion of the intensities at low spin, so that the intensities of  $\gamma$ -rays in  $^{185}\text{Tl}$  were estimated from the projection of the  $\gamma - \gamma$  coincidence matrix from the backed target experiment, supplemented by coincidence information from the thin target experiment and intensities from the mass-185 gated  $\gamma$ -ray spectrum.

Angular distributions and DCO ratios for transitions in  $^{185}\text{Tl}$  were obtained in a similar manner to  $^{187}\text{Tl}$ . The  $\gamma$ -rays assigned to  $^{185}\text{Tl}$  are shown in Table 4.4, together with their intensities, angular distributions, DCO ratios and placements.



Figure 4.11: Spectrum of  $\gamma$ -rays in coincidence with mass-185 residues measured at Argonne.Table 4.4: Transitions assigned to  $^{185}\text{Tl}$ 

$E_\gamma$ [keV]	$I_\gamma^{rel}$	$E_i \rightarrow E_f$ [keV]	$J_i^\pi \rightarrow J_f^\pi$	$A_2^{a)}$	$R_{DCO}^{b)}$	Multipolarity
142.3(1)	92(5)	1003 $\rightarrow$ 860	$\frac{13}{2}^+ \rightarrow \frac{11}{2}^-$	0.19(5)	1.06(13)	E1
207.1(1)	77(7)	1210 $\rightarrow$ 1003	$\frac{17}{2}^+ \rightarrow \frac{13}{2}^+$		1.28(9)	E2
212.7(1)	23(8)	982 $\rightarrow$ 769	$\left(\frac{13}{2}^-\right) \rightarrow \left(\frac{9}{2}^-\right)$		1.23(22)	(E2)
270.2(2)	62(8)	1480 $\rightarrow$ 1210	$\frac{21}{2}^+ \rightarrow \frac{17}{2}^+$		1.34(11)	E2
303.5(2)	20(8)	1285 $\rightarrow$ 982	$\left(\frac{17}{2}^-\right) \rightarrow \left(\frac{13}{2}^-\right)$		1.26(21)	(E2)
315.8(2)	29(8)	769 $\rightarrow$ 453	$\left(\frac{9}{2}^-\right) \rightarrow \frac{9}{2}^-$		1.39(20)	(M1/E2)
362.9(2)	50(6)	1843 $\rightarrow$ 1480	$\frac{25}{2}^+ \rightarrow \frac{21}{2}^+$		1.25(13)	E2
364.5(2)	20(9)	1375 $\rightarrow$ 1010				
379.0(2)	17(8)	1664 $\rightarrow$ 1285	$\left(\frac{21}{2}^-\right) \rightarrow \left(\frac{17}{2}^-\right)$		1.69(33)	E2
407.4(2)	100(6)	860 $\rightarrow$ 453	$\frac{11}{2}^- \rightarrow \frac{9}{2}^-$		1.07(22)	M1
416.3(2)	15(8)	1791 $\rightarrow$ 1375				
444.9(2)	29(8)	2288 $\rightarrow$ 1843	$\frac{29}{2}^+ \rightarrow \frac{25}{2}^+$		1.56(16)	E2
453.2(2)	6(3)	2117 $\rightarrow$ 1664	$\left(\frac{25}{2}^-\right) \rightarrow \left(\frac{21}{2}^-\right)$		1.71(51)	E2
484.2(3)	12(6)	2275 $\rightarrow$ 1791				
517.3(2)	21(3)	2805 $\rightarrow$ 2288	$\frac{33}{2}^+ \rightarrow \frac{29}{2}^+$		1.57(37)	E2
525	weak	$\rightarrow$ (2117)				
550.3(4)	$\sim 9^c$	(1003) $\rightarrow$ (453)	$\frac{13}{2}^+ \rightarrow \frac{9}{2}^-$			M2
557.0(2)	26(8)	1010 $\rightarrow$ 453				
581.2(3)	8(2)	3386 $\rightarrow$ 2805	$\left(\frac{37}{2}^+\right) \rightarrow \frac{33}{2}^+$			(E2)
622.0(3)	6(3)	4008 $\rightarrow$ 3386	$\left(\frac{41}{2}^+\right) \rightarrow \left(\frac{37}{2}^+\right)$			(E2)
662.3(4)	3(2)	4671 $\rightarrow$ 4008	$\left(\frac{45}{2}^+\right) \rightarrow \left(\frac{41}{2}^+\right)$			(E2)

<sup>a)</sup> From the backed target experiment.<sup>b)</sup> For transitions in band 4 the 207.1, 270.2 and 362.9 keV transitions were used as gates.

For transitions in band 1 the 212.7 and 303.5 keV transitions were used.

<sup>c)</sup>  $\frac{I_\gamma(550.3)}{I_\gamma(142.3)}$  estimated to be 0.10. The 550.3 keV transition is placed tentatively.

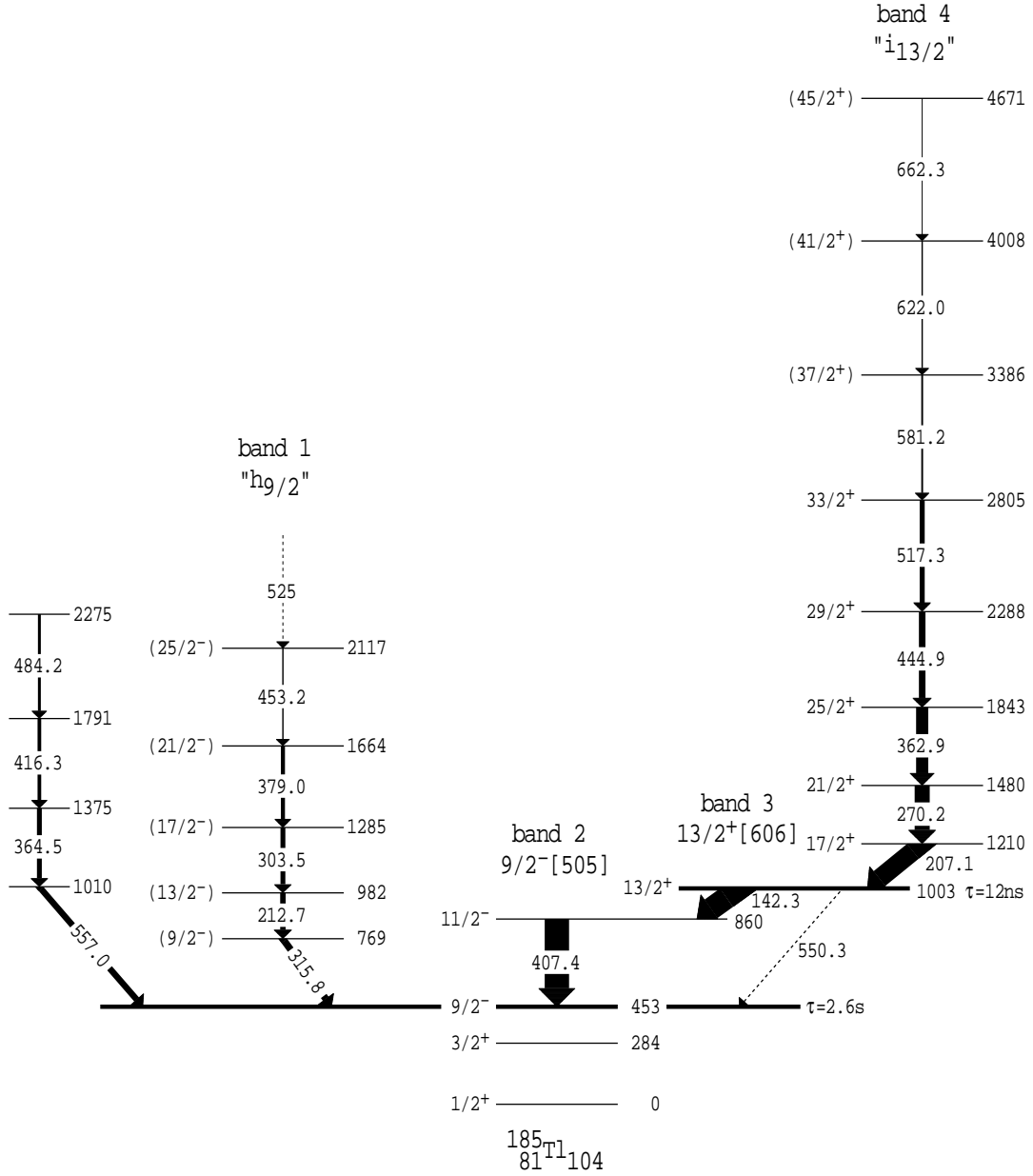
## 4.4 Level Scheme for $^{185}\text{Tl}$

Prior to these experiments only two excited states were known in  $^{185}\text{Tl}$ . The  $\gamma$ -decay work of Schmidt *et al.* [Sch77] established an isomeric state at 453 keV with a meanlife of 2.6 s and probable spin and parity  $\frac{9}{2}^-$ , as well as a  $\frac{3}{2}^+$  state at 284 keV. The ground state was assumed to have spin and parity  $\frac{1}{2}^+$ , in line with the expected  $s_{1/2}$  proton hole. These assignments were supported by Coenen *et al.* [Coe85], who observed enhanced  $\alpha$ -decay from suspected  $\frac{1}{2}^+$  and  $\frac{9}{2}^-$  states in  $^{189}\text{Bi}$  to the equivalent states in  $^{185}\text{Tl}$ . The present work has identified levels above the  $\frac{9}{2}^-$  isomer up to a tentative spin of  $\frac{45}{2}\hbar$  and an excitation energy of 4.7 MeV. The levels can be grouped into structures due to four different intrinsic states, labelled 1 to 4 in Figure 4.12.

### 4.4.1 Bands 2, 3 and 4.

The presence of another isomer besides the  $\frac{9}{2}^-$  level in  $^{185}\text{Tl}$  is apparent from a comparison of the two coincidence spectra for the 207.1 keV transition shown in Figure 4.13. The spectrum from the backed target experiment, in which the nuclei are stopped, shows an increased intensity for the 142.3 and 407.4 keV transitions compared to the thin target experiment, in which the recoiling nuclei decay out of the view of the  $\gamma$ -ray detectors. Furthermore, the higher energy transitions in the backed target experiment are split into three components. These correspond to the nuclei decaying while in flight between the target and the lead stopper foil and emitting  $\gamma$ -rays with Doppler shifted energies. The 142.3 and 407.4 keV  $\gamma$ -rays show only an unshifted component, indicating these transitions occur once the nuclei are at rest in the stopper foil. This implies the 142.3 and 407.4 keV transitions are beneath an isomer much longer than the flight-time of  $\sim 60$  ps between the target and the stopper foil. The coincidence spectrum for the 142.3 keV transition in Figure 4.13 shows that the 207.1 keV  $\gamma$ -ray has a mostly stopped component, with smaller Doppler shifted components, implying that it decays from a level with a lifetime of the same order as the  $\sim 60$  ps flight-time. The two lifetimes, the absolute intensities and the intensities in the coincidence gates, together establish the transition ordering shown in Figure 4.12.

The DCO ratios are consistent with dipole assignments for the 142.3 and 407.4 keV transitions and quadrupole assignments for the higher ones. The positive  $A_2$  coefficient obtained for the 207.1 keV  $\gamma$ -ray also agrees with a quadrupole assignment. The ratio of the intensities of the dipole transitions measured in

Figure 4.12: Level scheme for  $^{185}\text{Tl}$  obtained in the current work.

spectra gated by higher transitions is  $I_\gamma(407)/I_\gamma(142) = 0.89(8)$ , which should equal the ratio  $[1 + \alpha_T(142)]/[1 + \alpha_T(407)]$ , where  $\alpha_T(E_\gamma)$  indicates a total conversion coefficient. The intensities only balance if the 142.3 keV transition has E1 character ( $\alpha_T = 0.179$  for E1,  $\alpha_T \geq 1.44$  for other multiplicities) as values of  $\alpha_T$  for a 407 keV dipole transition are small ( $\alpha_T \leq 0.181$ ). The 407.4 keV,  $\Delta I=1$  transition is assumed to have M1 character from a comparison with the level structure of  $^{187}\text{Tl}$  and the heavier thallium isotopes [Por91, New74, Rev92].

The similarities with  $^{187}\text{Tl}$  lead to the level structure for  $^{185}\text{Tl}$  shown in Figure 4.12. The 407.4 keV transition is placed as the only observed transition in

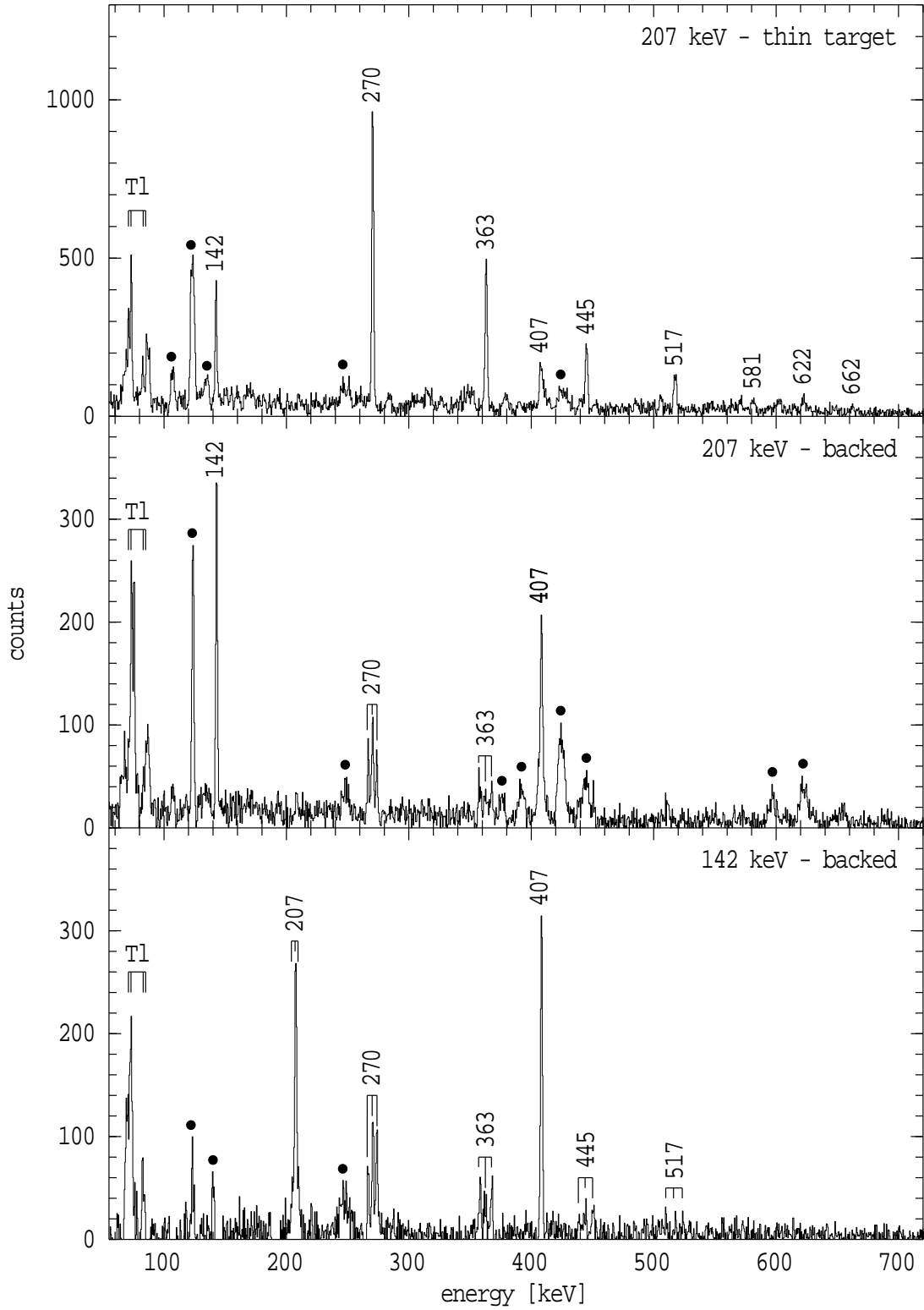


Figure 4.13: Coincidence spectra for transitions in the yrast cascade in  $^{185}\text{Tl}$ . Filled circles mark contaminating transitions. A broad contaminating line lies under the 407 keV  $\gamma$ -ray in the top two spectra.

band 2, while the 142.3 keV E1 transition decays from the only observed state in band 3. Band 4 is a positive parity rotational sequence with signature  $\alpha=+\frac{1}{2}$  and similar transition energies to the yrast sequence observed in  $^{187}\text{Tl}$ .

A 550.3 keV  $\frac{13}{2}^+ \rightarrow \frac{9}{2}^-$  crossover transition has been placed tentatively in  $^{185}\text{Tl}$ , analogous to the 726.4 keV M2 transition in  $^{187}\text{Tl}$ . The coincidence spectra for the 270.2, 362.9 and 444.9 keV transitions in the backed experiment do show coincidences with a  $\gamma$ -ray of energy 550.3 keV, however, its intensity relative to the 142.3 keV transition varies, possibly due to unidentified contamination. A branching ratio of  $I_\gamma(550)/I_\gamma(142) \sim 0.10$  has been estimated.

#### 4.4.2 Band 1

The coincidence spectrum in Figure 4.14 for the 212.7 keV transition shows the cascade labelled band 1 in Figure 4.12. The transitions are present in the mass-185 gated  $\gamma$ -ray spectrum in Figure 4.11 and all show coincidences with characteristic thallium X-rays. As there are no coincidences with  $\gamma$ -rays already assigned to  $^{185}\text{Tl}$ , band 1 has been placed as feeding directly into the  $\frac{9}{2}^-$  state. The DCO ratios, although ambiguous, are consistent with the 315.8 keV transition being an M1/E2,  $J \rightarrow J$  transition (see §3.5) and with E2 assignments for the higher transitions. The  $J \rightarrow J$  assignment is preferred over an E2,  $J \rightarrow J-2$  assignment because the latter possibility would mean that band 1 was yrast and a higher feeding would be expected.

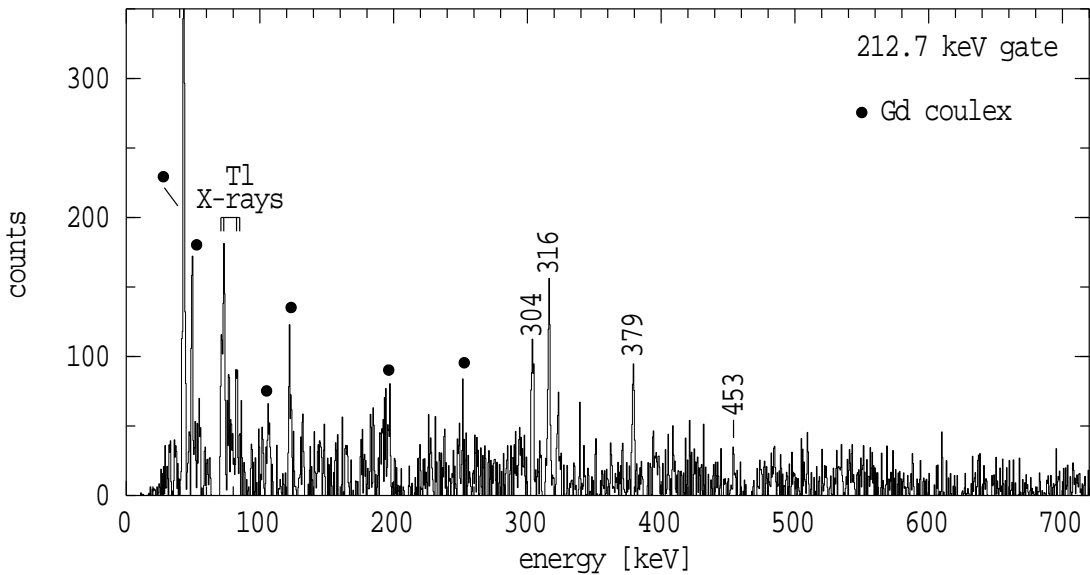


Figure 4.14: Coincidence spectrum for the 212.7 keV transition from band 1 in  $^{185}\text{Tl}$ . Filled circles indicate known contaminants.

### 4.4.3 Other transitions

The 484.2, 416.3, 364.5 and 557.0 keV  $\gamma$ -ray cascade in  $^{185}\text{Tl}$  is also placed as directly feeding the  $\frac{9}{2}^-$  isomer, although no spins or parities could be determined. Note that there are also  $\gamma$ -rays with energies of 285, 421 and 428 keV still unassigned in the mass-185 gated  $\gamma$ -ray spectrum shown in Figure 4.11.

### 4.4.4 Isomeric states

Figure 4.15 compares the time spectra with respect to the pulsed beam (obtained with the HPGe detectors) for both the 407 keV transition in  $^{185}\text{Tl}$  and the 405 keV,  $2^+$  to  $0^+$  transition in  $^{186}\text{Hg}$ . Both spectra are gated by known feeding transitions, ensuring no contamination<sup>3</sup>. The gating transitions for the 405 keV transition in  $^{186}\text{Hg}$  were the 403, 357, 424 and 589 keV transitions, while the 142.3, 207.1, 270.2 and 362.9 keV transitions were used to gate the 407 keV transition in  $^{187}\text{Tl}$ . The states in  $^{186}\text{Hg}$  are all known to have very short mean-lives [Pro74], so that the spectrum for the 405 keV  $\gamma$ -ray shows the time walk and resolution for  $\gamma$ -ray energies near 400 keV. Convoluting a 12 ns exponential decay with this prompt response function gives the fit shown for the 407 keV  $\gamma$ -ray in  $^{185}\text{Tl}$ .

Figure 4.15 also compares the time spectra obtained with the LEPS detector for the 142 keV transition in  $^{185}\text{Tl}$  and the 141 keV,  $\frac{11}{2}^- \rightarrow \frac{9}{2}^-$  transition in  $^{155}\text{Gd}$  [Lee87]. The LEPS detector is used despite the limited statistics because it provides superior energy and time resolution at these low energies. States in  $^{155}\text{Gd}$  are populated via Coulomb excitation of the target and the time spectrum for the 141 keV transition is clearly prompt with respect to the beam pulse. The 142 keV time spectrum shows the presence of the 12 ns lifetime, with the combination of the fits for the 142 and 407 keV transitions yielding a meanlife of  $\tau_m = 12 \pm 2$  ns for the  $\frac{13}{2}^+$  state.

---

<sup>3</sup>This gating procedure only produces valid time spectra because the higher spin states are known to have short ( $< 0.5$  ns) lifetimes (see Ref. [Pro74] and Figure 4.13), so that the transitions used for the gates all decay promptly after the beam pulse.

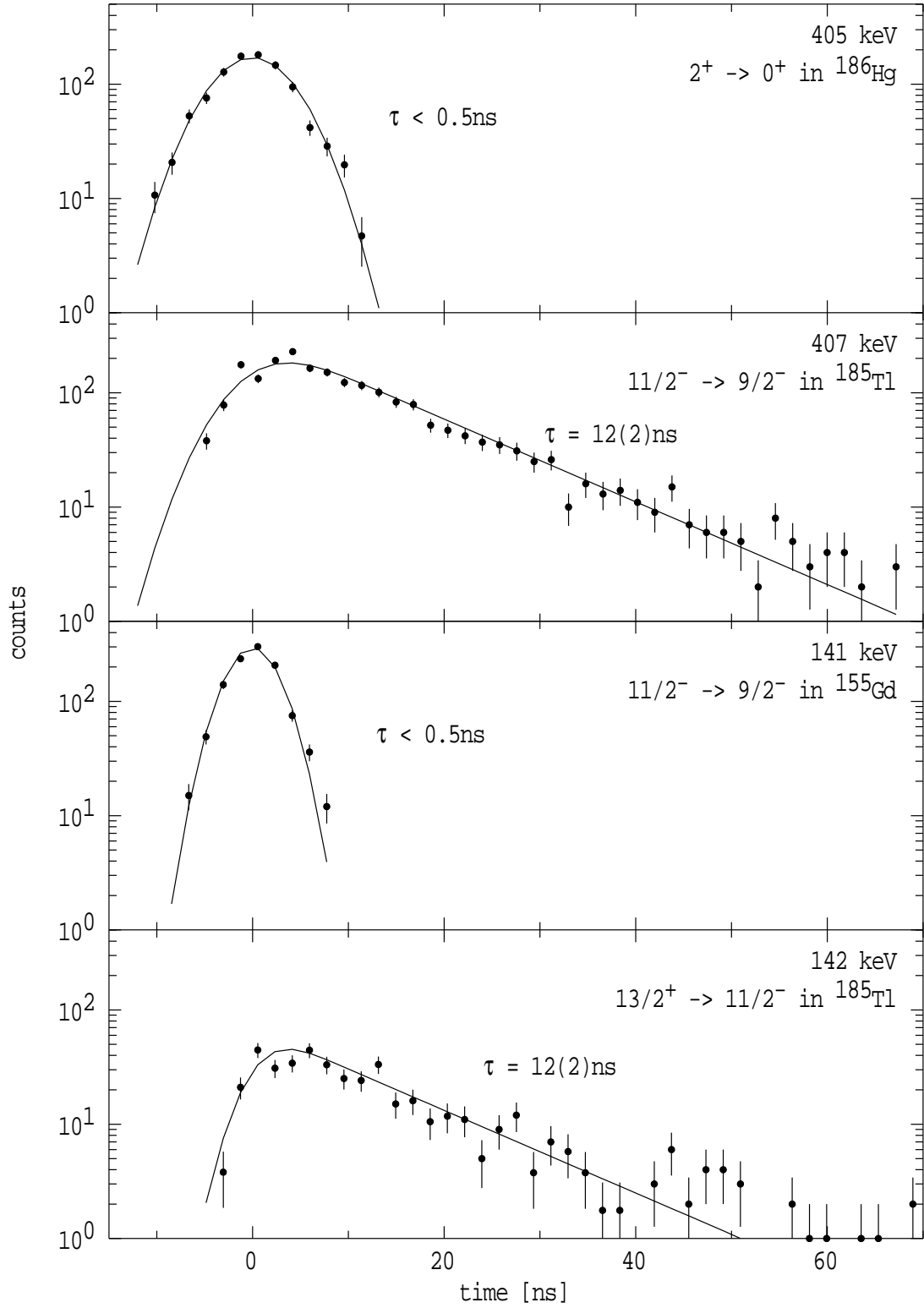


Figure 4.15: Time spectra with respect to the beam pulse for prompt transitions in  $^{186}\text{Hg}$  and  $^{155}\text{Gd}$  and delayed transitions in  $^{185}\text{Tl}$ . The top two panels are the summed time spectra for the six suppressed detectors, the bottom two panels are time spectra obtained with the LEPS detector. In both cases the gating transitions were observed in the suppressed detectors.

## 4.5 Analysis and results for $^{183}\text{Hg}$

High spin states in  $^{183}\text{Hg}$  were populated in thin and thick target experiments as described in Table 4.1. Statistical model calculations with unadjusted fission barriers indicated that the  $^{32}\text{S} + ^{155}\text{Gd}$  bombardment would be reasonably selective, predicting the cross-section for the production of  $^{183}\text{Hg}$  via the 4n evaporation channel to be approximately double those for making  $^{183}\text{Au}$  via the p3n channel and  $^{180}\text{Pt}$  via the  $\alpha$ 3n channel (see §3.1.1). Experimentally it was found that approximately equal amounts of  $^{183}\text{Hg}$ ,  $^{183}\text{Au}$  [Zho88] and  $^{180}\text{Pt}$  [Voi90] were formed, in better agreement with the statistical model calculations for which the liquid drop fission barriers were lowered by 20%.

Gamma-rays showing coincidences with characteristic mercury X-rays could be assigned to the mercury isotopes, and, since level schemes for the neighbouring mercury isotopes  $^{182}\text{Hg}$  [Ma84, Bin94] and  $^{184}\text{Hg}$  [Ma86] are known, there was no ambiguity in assignment of  $\gamma$ -rays to  $^{183}\text{Hg}$ .

The  $^{183}\text{Au}$  contaminant caused some difficulties because of the large number of nearly identical  $\gamma$ -ray energies between  $^{183}\text{Hg}$  and  $^{183}\text{Au}$ , complicating the coincidence gates and making intensities difficult to measure. Hence the intensity information was distilled from a combination of singles measurements, projections of the  $\gamma$ - $\gamma$  coincidence matrices, and from the individual coincidence gates. DCO ratios and angular distributions were obtained as described for  $^{187}\text{Tl}$ . Results for transitions assigned to  $^{183}\text{Hg}$  are shown in Table 4.5 together with their

Table 4.5: Transitions assigned to  $^{183}\text{Hg}$

$E_\gamma$ [keV]	$I_\gamma^{rel}$	$E_i \rightarrow E_f$ [keV]	$I_i^\pi \rightarrow I_f^\pi$	$A_2^{(a)}$	$R_{DCO}$	Multipolarity
66.8(3)	7(3)	$67 \rightarrow 0$	$\left(\frac{3}{2}^-\right) \rightarrow \frac{1}{2}^-$			(M1/E2)
75	weak <sup>b)</sup>	$429 + X' \rightarrow 354 + X'$	$\frac{17}{2}^+ \rightarrow \frac{15}{2}^+$			(M1/E2)
87	c)	$87 \rightarrow 0$	$\frac{5}{2}^- \rightarrow \frac{1}{2}^-$			(E2)
104.9(2)	6(2)	$105 + X \rightarrow 0 + X$	$\frac{9}{2}^- \rightarrow \frac{7}{2}^-$		1.15(27)	(M1/E2)
131.9(3)	3(1)	$833 + X' \rightarrow 701 + X'$	$\frac{21}{2}^+ \rightarrow \frac{19}{2}^+$			(M1/E2)
146.6(2)	29(6)	$252 + X \rightarrow 105 + X$	$\frac{11}{2}^- \rightarrow \frac{9}{2}^-$		0.79(24)	M1/E2
150.7(4)	2(1)	$1287 + X' \rightarrow 1136 + X'$	$\frac{25}{2}^+ \rightarrow \frac{23}{2}^+$		0.67(25)	M1/E2
155.2(3)	7(3)	$407 + X \rightarrow 252 + X$	$\frac{13}{2}^- \rightarrow \frac{11}{2}^-$		0.67(26)	M1/E2
174.7(3)	4(2)	$261 \rightarrow 87$	$\left(\frac{7}{2}^-\right) \rightarrow \frac{5}{2}^-$			(M1/E2)
178.8(3)	5(2)	$586 + X \rightarrow 407 + X$	$\frac{15}{2}^- \rightarrow \frac{13}{2}^-$		0.58(23)	M1/E2
193.7(3)	4(2)	$779 + X \rightarrow 586 + X$	$\frac{17}{2}^- \rightarrow \frac{15}{2}^-$			(M1/E2)
194.5(2)	15(3)	$261 \rightarrow 67$	$\left(\frac{7}{2}^-\right) \rightarrow \left(\frac{3}{2}^-\right)$			(E2)
199.1(2)	55(5)	$286 \rightarrow 87$	$\frac{9}{2}^- \rightarrow \frac{5}{2}^-$		1.51(13)	E2
213.2(4)	2(1)	$993 + X \rightarrow 779 + X$	$\frac{19}{2}^- \rightarrow \frac{17}{2}^-$			(M1/E2)



Table 4.5: continued

$E_\gamma$ [keV]	$I_\gamma^{rel}$	$E_i \rightarrow E_f$ [keV]	$I_i^\pi \rightarrow I_f^\pi$	$A_2^a)$	$R_{DCO}$	Multipolarity
226.4(4)	1(1)	1219 + $X \rightarrow 993 + X$	$\frac{21}{2}^- \rightarrow \frac{19}{2}^-$			(M1/E2)
251.6(2)	74(8)	252 + $X \rightarrow 0 + X$	$\frac{11}{2}^- \rightarrow \frac{7}{2}^-$	0.20(22)	1.21(25)	E2
252.7(3)	16(4)	354 + $X' \rightarrow 102 + X'$	$\frac{15}{2}^+ \rightarrow (\frac{11}{2}^+)$	0.31(35)	1.38(48)	(E2)
257	< 1	542 $\rightarrow$ 286	$(\frac{11}{2}^-) \rightarrow \frac{9}{2}^-$			(M1/E2)
271.5(2)	16(3)	701 + $X' \rightarrow 429 + X'$	$\frac{19}{2}^+ \rightarrow \frac{17}{2}^+$	-0.39(19)	0.60(9)	M1/E2
280.9(2)	13(3)	542 $\rightarrow$ 261	$(\frac{11}{2}^-) \rightarrow (\frac{7}{2}^-)$			(E2)
291.4(2)	38(4)	577 $\rightarrow$ 286	$\frac{13}{2}^- \rightarrow \frac{9}{2}^-$	0.27(18)	1.34(17)	E2
302.0(2)	58(5)	407 + $X \rightarrow 105 + X$	$\frac{13}{2}^- \rightarrow \frac{9}{2}^-$	0.33(24)	1.25(20)	E2
303.4(2)	5(2)	1136 + $X' \rightarrow 833 + X'$	$\frac{23}{2}^+ \rightarrow \frac{21}{2}^+$		0.66(16)	M1/E2
329	< 1	906 $\rightarrow$ 577	$(\frac{15}{2}^-) \rightarrow \frac{13}{2}^-$			(M1/E2)
334.3(2)	55(7)	586 + $X \rightarrow 252 + X$	$\frac{15}{2}^- \rightarrow \frac{11}{2}^-$	0.30(9)	1.34(23)	E2
346.8(2)	36(9)	701 + $X' \rightarrow 354 + X'$	$\frac{19}{2}^+ \rightarrow \frac{15}{2}^+$		1.46(23)	E2
354.4(2)	20(6)	354 + $X' \rightarrow 0 + X'$	$\frac{15}{2}^+ \rightarrow \frac{13}{2}^+$	-0.65(49)	0.20(11)	M1/E2
364.0(2)	12(3)	906 $\rightarrow$ 542	$(\frac{15}{2}^-) \rightarrow (\frac{11}{2}^-)$			(E2)
372.5(2)	44(4)	779 + $X \rightarrow 407 + X$	$\frac{17}{2}^- \rightarrow \frac{13}{2}^-$	0.33(25)	1.29(20)	E2
376.0(2)	38(4)	953 $\rightarrow$ 577	$\frac{17}{2}^- \rightarrow \frac{13}{2}^-$	0.30(21)	1.34(17)	E2
403.7(2)	80(7)	833 + $X' \rightarrow 429 + X'$	$\frac{21}{2}^+ \rightarrow \frac{17}{2}^+$	0.11(14)	1.26(13)	E2
407.2(2)	32(6)	993 + $X \rightarrow 586 + X$	$\frac{19}{2}^- \rightarrow \frac{15}{2}^-$	0.50(26)	1.15(16)	E2
429.2(2)	100(8)	429 + $X' \rightarrow 0 + X'$	$\frac{17}{2}^+ \rightarrow \frac{13}{2}^+$	0.27(9)	1.43(14)	E2
435.7(2)	15(2)	1136 + $X' \rightarrow 701 + X'$	$\frac{23}{2}^+ \rightarrow \frac{19}{2}^+$	0.23(12)		E2
438.8(3)	11(3)	1345 $\rightarrow$ 906	$(\frac{19}{2}^-) \rightarrow (\frac{15}{2}^-)$			(E2)
440.0(2)	33(4)	1219 + $X \rightarrow 779 + X$	$\frac{21}{2}^- \rightarrow \frac{17}{2}^-$	0.37(14)	1.53(27)	E2
451.4(2)	26(4)	1405 $\rightarrow$ 953	$\frac{21}{2}^- \rightarrow \frac{17}{2}^-$	0.40(18)	1.85(27)	E2
454.3(2)	65(5)	1287 + $X' \rightarrow 833 + X'$	$\frac{25}{2}^+ \rightarrow \frac{21}{2}^+$	0.27(17)	1.58(18)	E2
472.8(2)	24(4)	1466 + $X \rightarrow 993 + X$	$\frac{23}{2}^- \rightarrow \frac{19}{2}^-$	0.25(19)	1.45(25)	E2
501.4(2)	24(3)	1721 + $X \rightarrow 1219 + X$	$\frac{25}{2}^- \rightarrow \frac{21}{2}^-$		1.63(29)	E2
503.9(3)	6(1)	1849 $\rightarrow$ 1345	$(\frac{23}{2}^-) \rightarrow (\frac{19}{2}^-)$			(E2)
513.2(2)	8(3)	1650 + $X' \rightarrow 1136 + X'$	$\frac{27}{2}^+ \rightarrow \frac{23}{2}^+$		1.28(22)	E2
516.8(2)	18(3)	1921 $\rightarrow$ 1405	$\frac{25}{2}^- \rightarrow \frac{21}{2}^-$	0.03(29)	1.29(19)	E2
521.3(2)	38(4)	1809 + $X' \rightarrow 1287 + X'$	$\frac{29}{2}^+ \rightarrow \frac{25}{2}^+$	0.20(24)	1.49(18)	E2
531.9(2)	16(3)	1998 + $X \rightarrow 1466 + X$	$\frac{27}{2}^- \rightarrow \frac{23}{2}^-$	0.27(26)	1.23(30)	E2
555.8(2)	23(3)	2277 + $X \rightarrow 1721 + X$	$\frac{29}{2}^- \rightarrow \frac{25}{2}^-$		1.42(25)	E2
559.7(3)	8(2)	2409 $\rightarrow$ 1849	$(\frac{27}{2}^-) \rightarrow (\frac{23}{2}^-)$			(E2)
570.5(3)	11(2)	2492 $\rightarrow$ 1921	$\frac{29}{2}^- \rightarrow \frac{25}{2}^-$		1.30(27)	E2
581.9(3)	5(2)	2232 + $X' \rightarrow 1650 + X'$	$\frac{31}{2}^+ \rightarrow \frac{27}{2}^+$	0.46(46)	1.27(36)	E2
583.0(2)	33(3)	2392 + $X' \rightarrow 1809 + X'$	$\frac{33}{2}^+ \rightarrow \frac{29}{2}^+$		1.27(21)	E2
585.1(2)	13(3)	2583 + $X \rightarrow 1998 + X$	$\frac{31}{2}^- \rightarrow \frac{27}{2}^-$		1.41(32)	E2
602.8(3)	15(3)	2879 + $X \rightarrow 2277 + X$	$\frac{33}{2}^- \rightarrow \frac{29}{2}^-$		1.47(31)	E2
610.1(3)	10(2)	3102 $\rightarrow$ 2492	$\frac{33}{2}^- \rightarrow \frac{29}{2}^-$		2.0(8)	E2
613.6(4)	3(1)	3022 $\rightarrow$ 2409	$(\frac{31}{2}^-) \rightarrow (\frac{27}{2}^-)$			(E2)
623.8(6)	5(2)	3726 $\rightarrow$ 3102	$(\frac{37}{2}^-) \rightarrow \frac{33}{2}^-$			(E2)
631.2(3)	8(3)	3214 + $X \rightarrow 2583 + X$	$(\frac{35}{2}^-) \rightarrow \frac{31}{2}^-$			(E2)
637.6(3)	12(2)	3029 + $X' \rightarrow 2392 + X'$	$(\frac{37}{2}^+) \rightarrow \frac{33}{2}^+$		1.25(28)	(E2)
640.5(4)	8(2)	3520 + $X \rightarrow 2879 + X$	$(\frac{37}{2}^-) \rightarrow \frac{33}{2}^-$		1.18(42)	(E2)
641.3(4)	3(1)	2873 + $X' \rightarrow 2232 + X'$	$(\frac{35}{2}^+) \rightarrow \frac{31}{2}^+$			(E2)
668.4(4)	4(2)	3883 + $X \rightarrow 3214 + X$	$(\frac{39}{2}^-) \rightarrow (\frac{35}{2}^-)$			(E2)
683.5(4)	4(2)	3713 + $X' \rightarrow 3029 + X'$	$(\frac{41}{2}^+) \rightarrow (\frac{37}{2}^+)$			(E2)
692.2(6)	1(1)	3565 + $X' \rightarrow 2873 + X'$	$(\frac{39}{2}^+) \rightarrow (\frac{35}{2}^+)$			(E2)
723.1(6)	2(1)	4436 + $X' \rightarrow 3713 + X'$	$(\frac{45}{2}^+) \rightarrow (\frac{41}{2}^+)$			(E2)

<sup>a)</sup> From the backed target experiment.<sup>b)</sup> Placed on the basis of coincidence data.<sup>c)</sup> See sect. 4.6.2.

placements. Sample DCO ratios and angular distributions are also presented in Figure 4.16. Although some of the DCO ratios for the E2 transitions agree with both theoretical values, there is still a clear grouping and distinction between the E2 and M1/E2 transitions.

## 4.6 Level scheme for $^{183}\text{Hg}$

The level scheme for  $^{183}\text{Hg}$  obtained in the current work appears in Figure 4.17 and consists of three separate sets of transitions in mutual coincidence, with no transitions observed to connect the three sets. This is possibly due to a combination of either the rotational bandheads being isomeric with a lifetime much longer than the  $\pm 432$  ns coincidence overlap, or the connecting transitions being too low in energy to be observed. Each set of transitions can be placed into a strongly coupled band with two  $\Delta I = 2$  sequences and weak M1/E2 connecting transitions. The spin and parity assignments for the bandheads are based upon the following arguments.

The spin and magnetic moment of the ground state of  $^{183}\text{Hg}$  have been measured by laser spectroscopy and are consistent with a  $\frac{1}{2}^-$  [521] assignment [Bon76]. Limited information was also available from previous decay studies [Mis81, Mac84]. The rotational bands in  $^{183}\text{Hg}$  were associated with particular quasi-neutron structures by comparison with both the N=103 isotones [Voi90a, Dra83, Bal93] and with  $^{185}\text{Hg}$  [Han88]. Since only the ground state spin and parity is unambiguously defined, the level scheme in Figure 4.17 has the spins labelled according to the assumption that the levels at 87,  $0+X$  and  $0+X'$  keV have spins and parities  $\frac{5}{2}^-$ ,  $\frac{7}{2}^-$  and  $\frac{13}{2}^+$  respectively. Furthermore, the transitions at the base of the  $\frac{1}{2}^-$  [521] band are only assigned tentatively and the relative excitation energies of the other bands are unknown. Thus the absolute excitation energies of all the excited states are unknown.

### 4.6.1 Other spectroscopic studies

The spectroscopy of  $^{183}\text{Hg}$  has been investigated previously via both  $\alpha$ -decay from  $^{187}\text{Pb}$  [Mis81] and  $\beta$ -decay from  $^{183}\text{Hg}$  [Mac84], but no studies of  $\beta$ -decay into  $^{183}\text{Hg}$  have been reported.

The  $\alpha$ -decay study by Misaelides *et al.* [Mis81] identified three  $\alpha$ -branches from  $^{187}\text{Pb}$ , depopulating two states in  $^{187}\text{Pb}$  as shown in Figure 4.18. One of the  $\alpha$ -decaying states was assigned as feeding low spin states in  $^{183}\text{Hg}$  with tentative

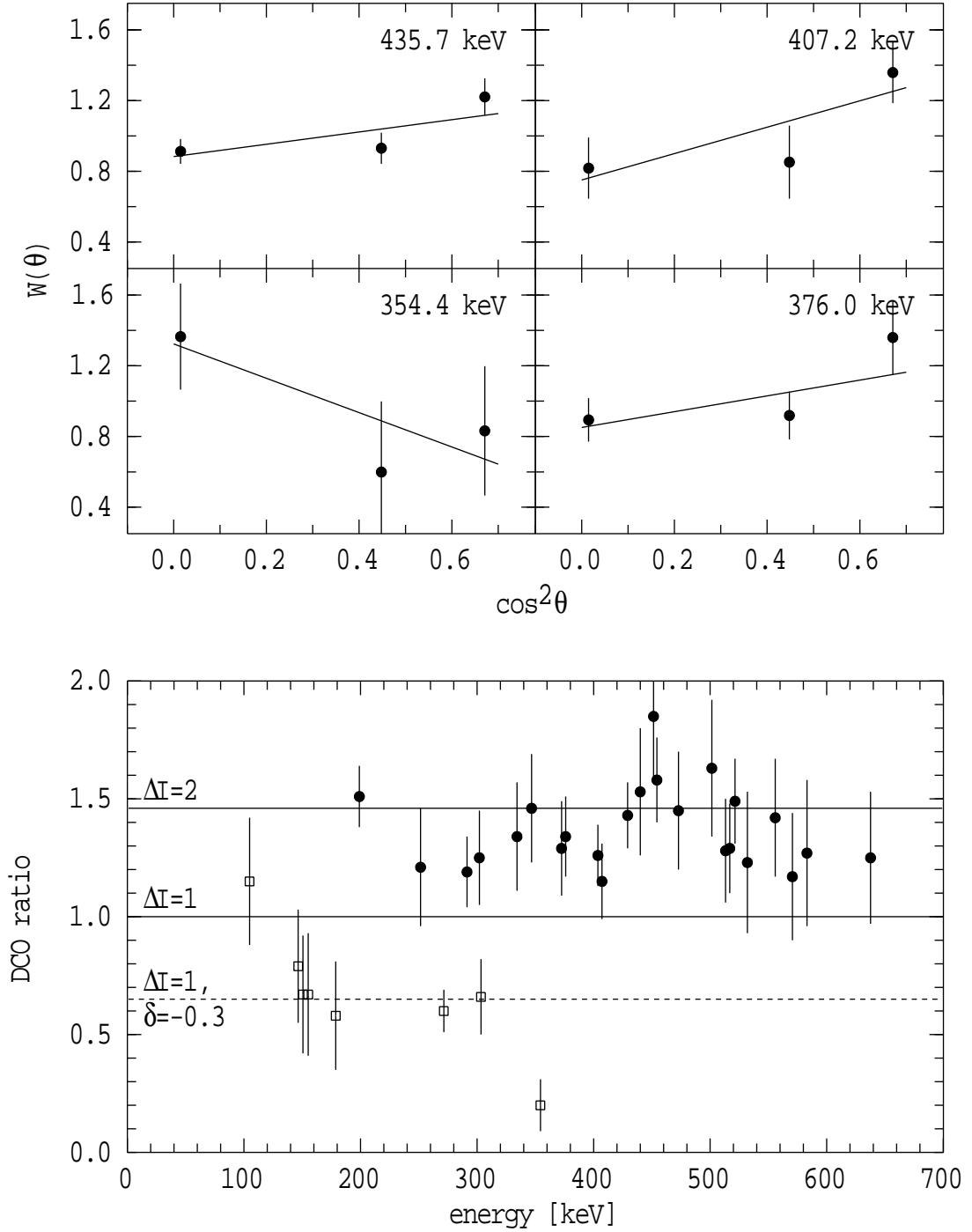


Figure 4.16: The upper four panels show selected angular distributions for transitions assigned to  $^{183}\text{Hg}$  with the fitted lines corresponding to the  $A_2$  values given in Table 4.5. Selected DCO ratios are shown in the lower panel for quadrupole (circles) and dipole (squares) transitions in  $^{183}\text{Hg}$  gated by stretched E2 transitions. The solid lines indicate the values expected for pure stretched quadrupole and dipole transitions. The dashed line at 0.65 indicates the value expected for a dipole/quadrupole transition with a mixing ratio of  $\delta = -0.3$ . (The theoretical calculations are described in §3.5.)

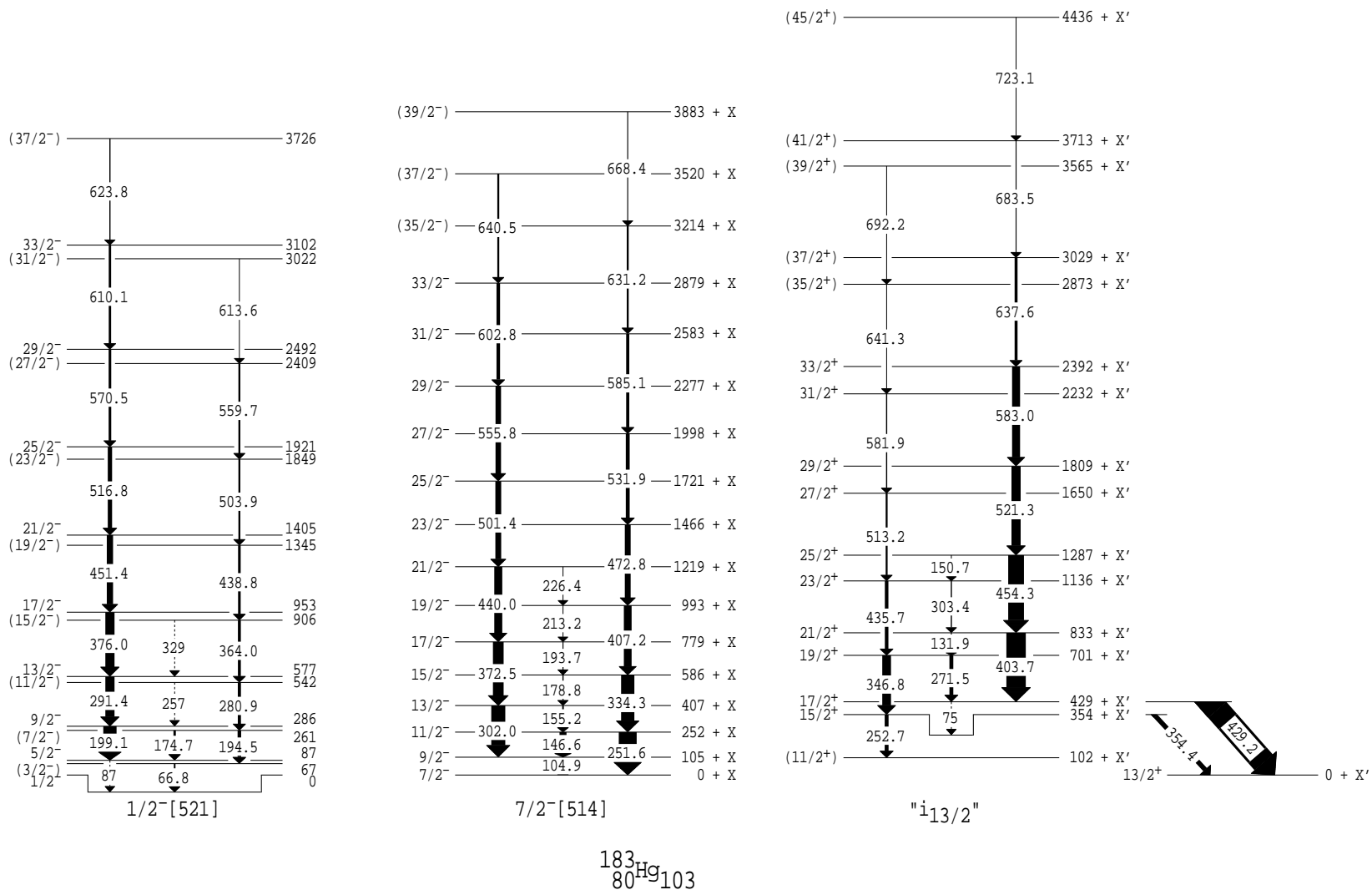


Figure 4.17: Level scheme deduced for  $^{183}\text{Hg}$  with the widths of the transitions proportional to the  $\gamma$ -ray intensities. (See the text for further details on the spin, parity and  $E_x$  assignments.)

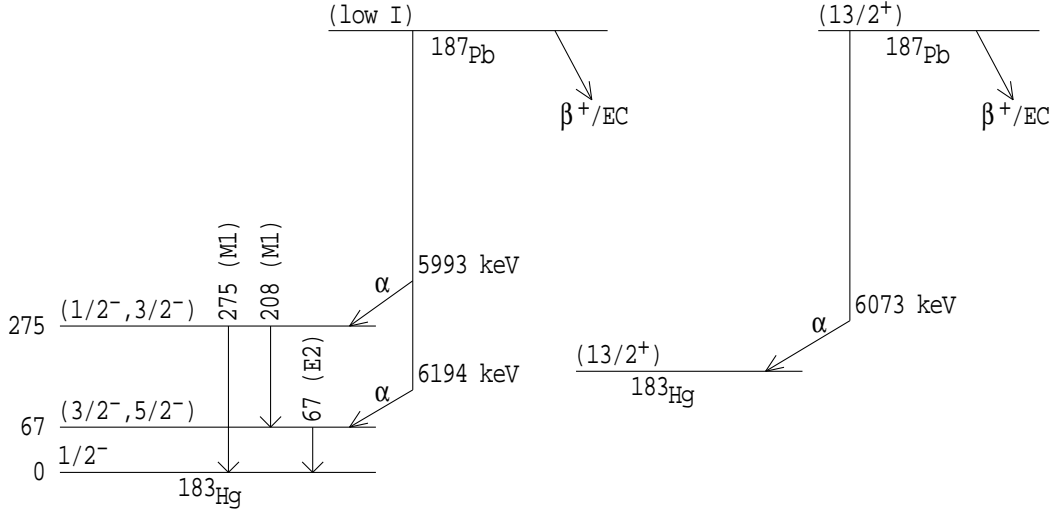


Figure 4.18: Level scheme deduced for  $^{183}\text{Hg}$  from the  $\alpha$ -decay work of Misaelides *et al.* [Mis81].

spins and parities as shown, while  $\alpha$ -decay from the second state showed no  $\gamma$ -ray coincidences and was tentatively placed as a decay from a  $\frac{13}{2}^+$  state in  $^{187}\text{Pb}$  to a  $\frac{13}{2}^+$  isomer in  $^{183}\text{Hg}$ . The  $\frac{13}{2}^+$  isomers in the heavier odd-mass mercury isotopes have been identified via laser and  $\gamma$ -spectroscopy (see Ref. [Ulm86] and references therein).

In contrast, the  $\beta$ -decay work of Macias-Marques *et al.* [Mac84] populated no states with spin  $I > \frac{11}{2}$  in  $^{183}\text{Au}$  and from this it was deduced that the parent nucleus,  $^{183}\text{Hg}$ , either has no  $\frac{13}{2}^+$  isomer, or that such a state occurs at a high enough energy that it can  $\gamma$ -decay in preference to  $\beta$ -decay.

Two other high spin spectroscopic studies of  $^{183}\text{Hg}$  have proceeded in parallel to, and independently of, this work [Bin93, Shi95]. The differences between the three level schemes are discussed in §4.6.5.

#### 4.6.2 $\frac{1}{2}^- [521]$ band

Figure 4.19a shows the  $\gamma$ -ray cascade in coincidence with the 376.0 keV  $\gamma$ -ray. The angular distributions and DCO ratios indicate stretched quadrupole assignments for the strong transitions. The weak 194.5 keV  $\gamma$ -ray in Figure 4.19a is part of another cascade, as evidenced by the coincidence spectrum for the 559.7 keV transition presented in Figure 4.19b. Figures 4.19a and b illustrate that the two sequences are in mutual coincidence, while Figure 4.19c presents evidence for the placement of the 174.7 keV transition. The two cascades are interpreted as transitions belonging to the two signatures of the  $\frac{1}{2}^- [521]$  band, which is expected

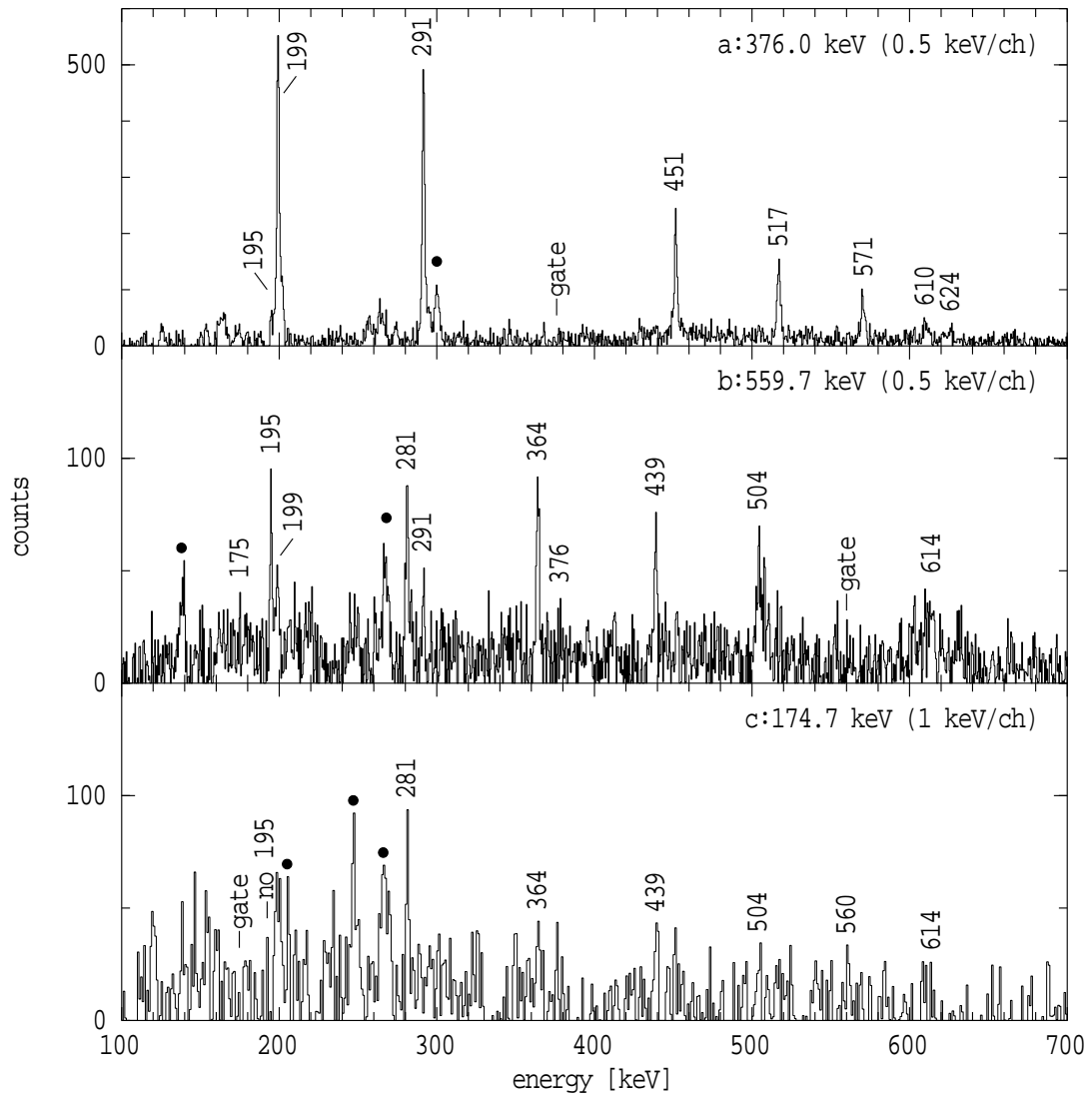


Figure 4.19: Coincidence spectra for transitions assigned to the  $\frac{1}{2}^- [521]$  band in  $^{183}\text{Hg}$ . Filled circles indicate known contaminant lines.

to show a pronounced signature splitting (see §2.5) and is seen in the isotones,  $^{181}\text{Pt}$  [Voi90a] and  $^{179}\text{Os}$  [Dra83, Bal93].

The evidence for the existence of the 66.8 keV transition at the base of the  $\frac{1}{2}^- [521]$  band is summarised in Figure 4.20, which shows the low-energy region of the coincidence spectrum for the 376.0 keV transition. The intensities of the mercury X-rays at 68.9, 70.8, 80.2 and 82.5 keV should be in the intensity ratio 59:100:35:10 [Led78], in reasonable agreement with the measured ratio of 72(15):100(13):31(8):6(3). In these units, the 66.8 keV  $\gamma$ -ray has an intensity of 31(9). If the 66.8 keV and 70.8 keV  $\gamma$ -rays were due solely to the gold  $K_{\alpha_2}$  and mercury  $K_{\alpha_1}$  X-rays respectively, then the 68.9 keV  $\gamma$ -ray should have an intensity of 112(17), larger than the measured value of 72(15). There should also be

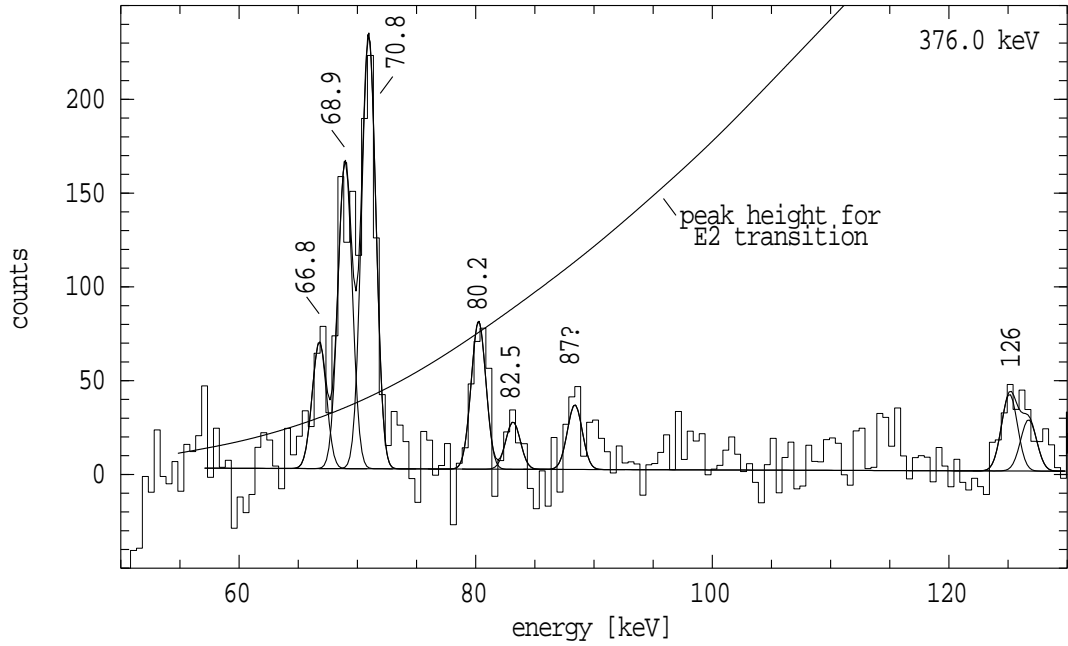


Figure 4.20: Low-energy region of the coincidence spectrum for the 376.0 keV transition in the  $\frac{1}{2}^-$  [521] band in  $^{183}\text{Hg}$ . Further details are in §4.6.2.

a gold  $K_{\beta_1}$  X-ray at 77.9 keV with an intensity of 5(3). There is no evidence for such a peak, which should be roughly the same size as the mercury  $K_{\beta_2}$  X-ray at 82.5 keV, in the spectrum. It appears therefore, that the peak at 66.8 keV can not be due to a gold X-ray and is possibly a  $\gamma$ -ray transition.

The solid curve in Figure 4.20 shows the expected peakheight (corrected for efficiency, internal conversion and peak shape) for a pure E2 transition which would balance the intensity of the 199 and 291 keV transitions (see Figure 4.19a). Apparently, the 66.8 keV transition is too intense to be an E2 transition fed by the 199 keV transition. Note that the level scheme of Misaelides *et al.* [Mis81], reproduced in Figure 4.18, places a 67 keV transition feeding the ground state. They do not observe an  $\alpha$ -decay directly to the ground state, which would perhaps be expected if the 67 keV level were a member of the ground state band. Nevertheless, since the M1 conversion coefficient for a 66.8 keV transition ( $\alpha_T \sim 5$ ) is much less than the E2 value ( $\alpha_T \sim 34$ ), it is possible for the 66.8 keV  $\gamma$ -ray in Figure 4.20 to be a mixed M1/E2 transition and it is placed tentatively as the  $\left(\frac{3}{2}^-\right) \rightarrow \frac{1}{2}^-$  transition. Taken together with the 174.7 keV,  $\left(\frac{7}{2}^-\right) \rightarrow \frac{5}{2}^-$  transition, this leads to an energy of 87 keV for the  $\frac{5}{2}^- \rightarrow \frac{1}{2}^-$ , E2 transition. Although there is a  $\gamma$ -ray near 87 keV in the spectrum in Figure 4.20, it is only assigned tentatively due to the strong  $\gamma$ -rays which occur at 86 keV ( $^{155}\text{Gd}$  [Led78]) and 89 keV ( $^{156}\text{Gd}$  [Led78]) from Coulomb excitation of the target and the associated

difficulty of background subtraction in this region. This contradicts the work of Shi *et al.* [Shi95], who have assigned 86.5 and 88.9 keV transitions at the base of the  $\frac{1}{2}^-$ [521] band in  $^{183}\text{Hg}$ . A more detailed comparison between the two level schemes is presented in §4.6.5.

### 4.6.3 $\frac{7}{2}^-$ [514] band

Examples of coincidence gates for the two signatures of the  $\frac{7}{2}^-$ [514] band are shown in Figure 4.21. The measured intensities and coincidence relationships establish the ordering, while the DCO ratios and angular distributions are in agreement with the assigned multipolarities and spins. A similar rotational band is seen in the N=103 isotones [Voi90a, Dra83, Bal93].

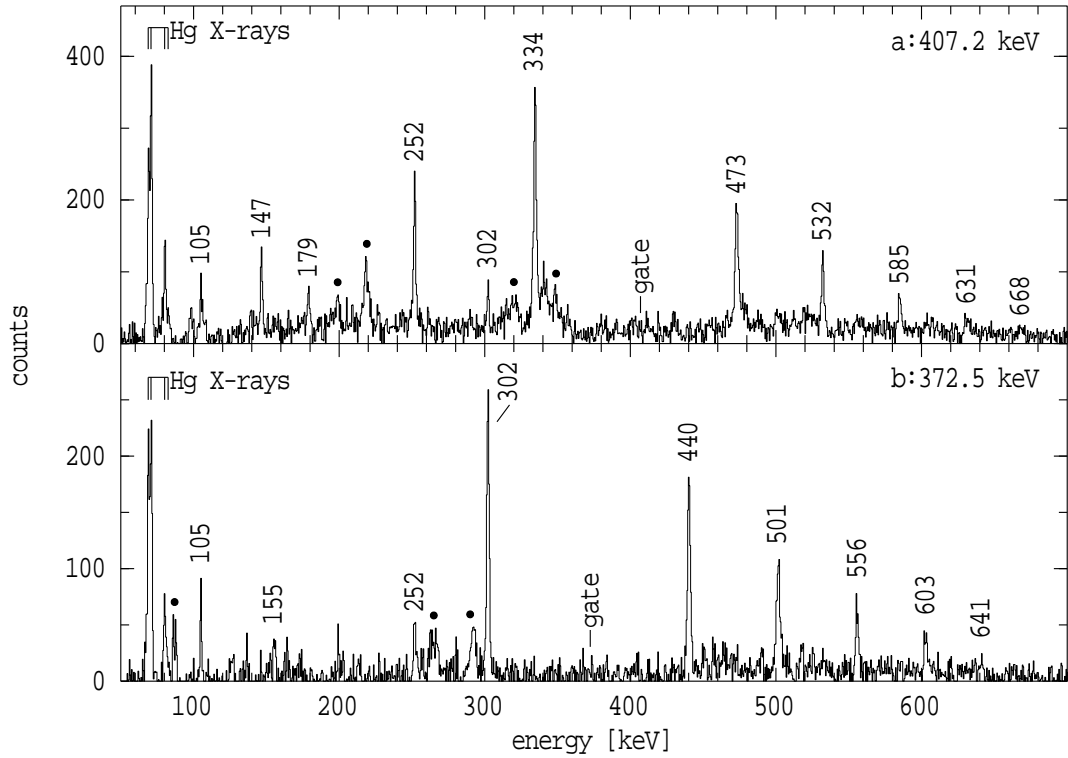


Figure 4.21: Coincidence spectra for transitions assigned to the  $\frac{7}{2}^-$ [514] band in  $^{183}\text{Hg}$ . Filled circles indicate known contaminant lines.

### 4.6.4 Positive parity states

A mixed  $i_{13/2}$  neutron band similar to that seen in  $^{185}\text{Hg}$  [Han88a] is assigned to  $^{183}\text{Hg}$  in the current work. Figures 4.22a and b show coincidence spectra for the 454.3 keV transition from the favoured signature and the 435.7 keV transition from the unfavoured signature. The coincidence spectrum in Figure 4.22c for the



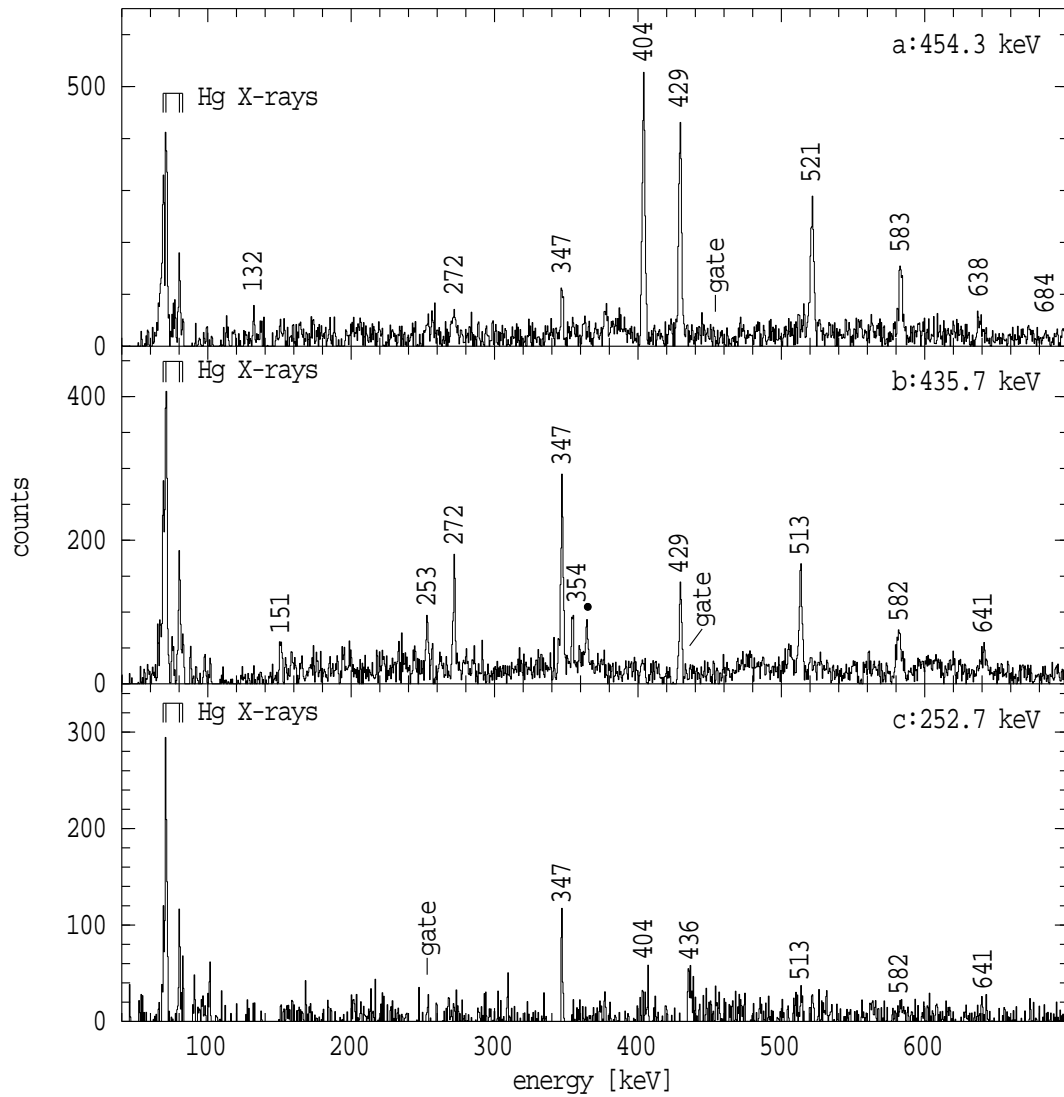


Figure 4.22: Coincidence spectra for transitions assigned to the mixed  $i_{13/2}$  neutron band in  $^{183}\text{Hg}$ . Filled circles indicate known contaminant lines.

252.7 keV  $\gamma$ -ray is of poorer quality due to the deconvolution required to separate it from the 251.6 keV  $\gamma$ -ray, however, it serves to demonstrate that the 252.7 keV transition is fed by the 346.8 keV transition. Hence the 346.8 and 252.7 keV  $\gamma$ -rays are placed as E2 transitions in the unfavoured signature, in agreement with the measured DCO ratios and angular distributions.

The energy summations, coincidence relationships and intensity information unambiguously give the ordering of the transitions and clearly establish the levels from which the 354.4 and 429.2 keV transitions decay. However, these transition energies are too large to fit smoothly into the rotational band, so they have been assigned as transitions across to an oblate  $\frac{13}{2}^+$  isomer, similar to the situation in  $^{185}\text{Hg}$  [Han88a]. There is no sign in the current data set of a rotation-aligned

band built upon the  $\frac{13}{2}^+$  isomer like those that are observed in  $^{187}\text{Hg}$  [Han88] and  $^{185}\text{Hg}$  [Han88a].

#### 4.6.5 Comparison with other work

The high spin study of  $^{183}\text{Hg}$  by Bindra *et al.* [Bin93] did not observe the  $\frac{1}{2}^-$ [521] band seen in the current work. This is possibly because of intensity distortions due to the sensitivity of the Argonne Fragment Mass Analyzer to the atomic charge state and therefore to internal conversion processes which can shift the charge state. The high rate of internal conversion for the low energy transitions in the  $\frac{1}{2}^-$ [521] band could shift the charge states of the recoiling  $^{183}\text{Hg}$  nuclei and artificially attenuate the yield. Indeed, the intensities of the contaminant  $\gamma$ -rays from  $^{183}\text{Au}$  are reduced in the measurement of Bindra *et al.* because of the low energy transitions in its level scheme [Bin93].

The rest of the current level scheme is in substantial agreement with that of Bindra *et al.* There are some extra transitions assigned in the current work, the most important being the 252.7 keV transition which has been assigned as the  $\frac{15}{2}^+ \rightarrow \left(\frac{11}{2}^+\right)$  transition in the unfavoured signature of the mixed  $i_{13/2}$  neutron band. Its presence suggests that the 346.8 keV transition is a  $\frac{19}{2}^+ \rightarrow \frac{15}{2}^+$  in-band transition, contrary to the  $\frac{19}{2}^+ \rightarrow \frac{17}{2}^+$  interband decay proposed by Bindra *et al.* This is supported by the DCO ratio for the 346.8 keV transition which suggests a quadrupole assignment. This implies the 354.4 keV transition must be a dipole, in agreement with its measured angular distribution and DCO ratio, whereas Bindra *et al.* assign it as a quadrupole transition.

After the results from the current work were accepted for publication [Lan95], another paper investigating high-spin states in  $^{183}\text{Hg}$  was published by Shi *et al.* [Shi95], with the main authors also in common to the previous work by Bindra *et al.* In this publication they change their assignment of the 354.4 keV transition to now be a dipole transition from the mixed  $i_{13/2}$  neutron band across to a  $\frac{13}{2}^+$  state, in agreement with the results presented in Ref. [Lan95] and this thesis.

They also report the observation of both signatures of the  $\frac{1}{2}^-$ [521] band. The main transitions are in agreement with the current work, however, there are disagreements for the low-energy transitions at the base of the band and for the E2 transitions at the top of the unfavoured signature. Looking firstly at the top of the unfavoured signature, Shi *et al.* assign 601.8, 621.9 and tentatively 637 keV transitions feeding the  $\frac{27}{2}^-$  level. The evidence they present consists of a summed coincidence spectrum with gates on the 194, 280, 364, 439, 559 and

602 keV transitions<sup>4</sup>. Note that a 602 keV transition is already assigned to the  $\frac{7}{2}^-$  [514] band and this transition is in true coincidence with a  $\gamma$ -ray at 440 keV, very close in energy to the 439 keV transition included in the sum of gates.

In contrast, the current work suggests that there is a 614 keV transition feeding the  $\frac{27}{2}^-$  level and makes no conclusions about higher transitions. The summed spectra which appear in Figures 4.23a and b show clear peaks at both 603 and 614 keV. The two spectra differ only by the inclusion of the coincidence spectrum for the 439 keV transition in panel (b). The inclusion of this spectrum changes the relative intensities of the 603 and 614 keV transitions due to contamination from the  $\frac{7}{2}^-$  [514] band, so that it is obviously more sensible to examine the individual coincidence spectra for each transition. In the current work, only the peak at 614 keV is clearly present in every spectrum. Furthermore, it is always in approximately the same intensity ratio with the 560 keV transition. Although there is some evidence in the individual coincidence spectra for a 603 keV transition associated with the band, it could not be assigned to  $^{183}\text{Hg}$  with any confidence due to the contamination from the  $\frac{7}{2}^-$  [514] band. In any case, the spectrum in Figure 4.23a shows that the peak at 614 keV is more intense than the peak at 603 keV, so that even if there was a 603 keV transition, it would have to be placed above the 614 keV transition. Concerning the 621 and 640 keV transitions suggested by Shi *et al.*, Figure 4.23 shows only weak evidence for peaks at those energies. Finally, it is worth noting that in the summed spectrum shown in Figure 2 of Ref. [Shi95], there is an unmarked peak at  $\sim 614$  keV which is more intense than either of the 621 and 640 keV transitions which Shi *et al.* have placed in their level scheme.

The current work also makes different assignments to Shi *et al.* for the transitions at the base of the  $\frac{1}{2}^-$  [521] band. The only evidence Shi *et al.* present for their placement of the 86.5 and 191.4 keV transitions connecting the two signatures is the summed spectrum for the unfavoured signature in their Figure 2. The 191.4 keV transition would correspond to the 174.7 keV transition assigned in the current work. This transition is clearly seen in the current work (see Figure 4.23) and its coincidence spectrum (see Figure 4.19) shows it to be in coincidence with transitions from the unfavoured signature. Also, there appears to be an unlabelled  $\gamma$ -ray near 175 keV in Figure 2 of Ref. [Shi95].

The origin of the 86.5 and 191.4 keV transitions in Figure 2 of Ref. [Shi95] is

---

<sup>4</sup>Transition energies from Ref. [Shi95]. Although transition energies from both works are used in this section, the differences are small and there should be no confusion.

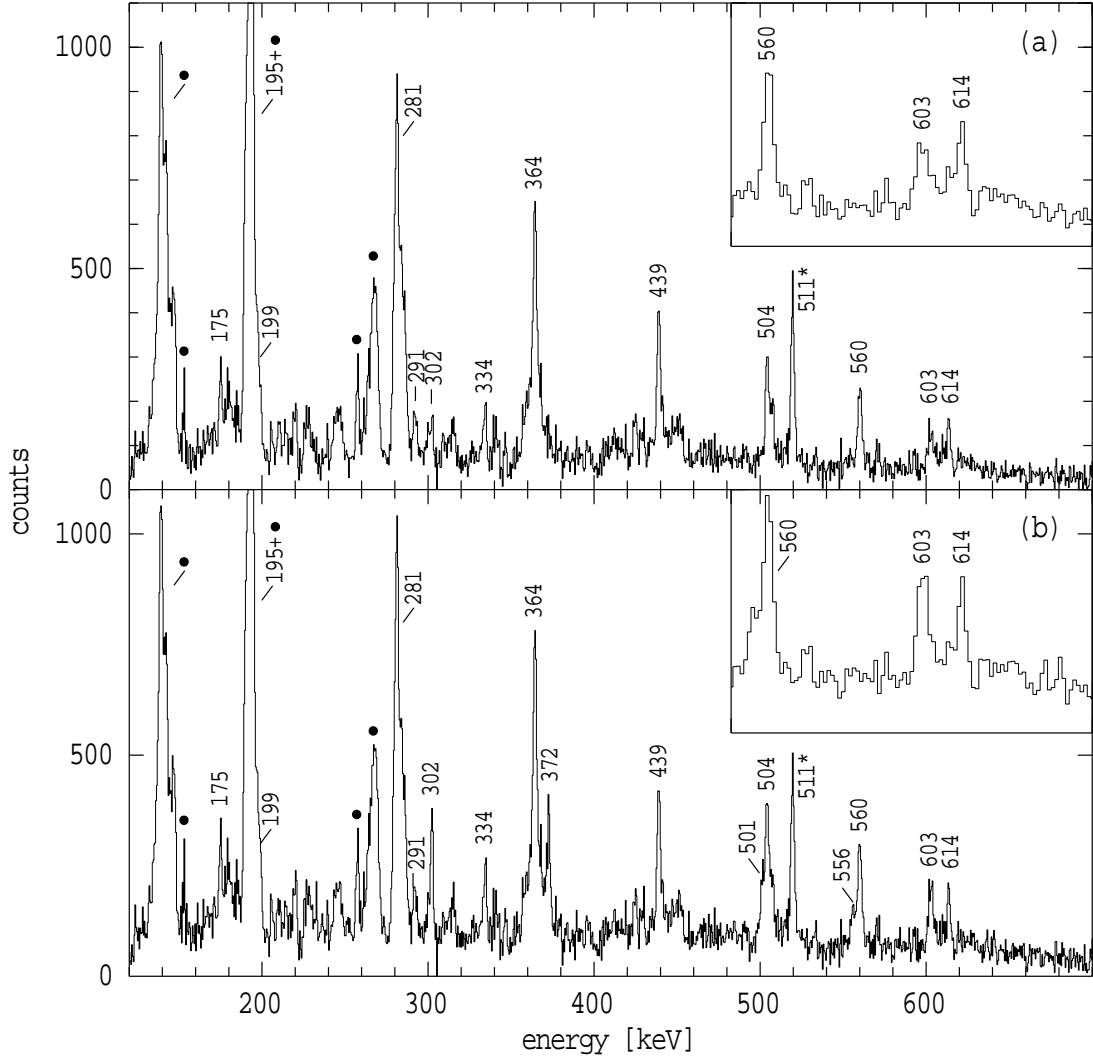


Figure 4.23: Panel (a) shows the summed coincidence spectra for the 194.5, 280.9, 364.0, 503.9 and 559.7 keV transitions from the unfavoured signature of the  $\frac{1}{2}^-$  [521] band in  $^{183}\text{Hg}$ . The  $\gamma$ -rays assigned to  $^{183}\text{Hg}$  are labelled by their energies. Panel (b) includes the coincidence spectrum for the 438.8 keV transition in the sum. Note how this changes the relative intensities of the 603 and 614 keV transitions (shown in the inset spectra compressed to 1 keV/chan), and results in a large amount of contamination by transitions from the  $\frac{7}{2}^-$  [514] band. (Note that the peak labelled 511\* is a Doppler shifted 511 keV  $\gamma$ -ray arising from the 503.9 keV coincidence spectrum. Filled circles indicate other known contaminants.)

possibly related to their inclusion of a gate on the 280.4 keV transition in their summed spectrum. This transition lies close in energy to the 282 keV,  $\frac{13}{2}^- \rightarrow \frac{9}{2}^-$  transition in  $^{155}\text{Gd}$ , which would be in true coincidence with  $\gamma$ -rays at 60, 86, 105, 146 and 191 keV [Led78]. (Excited states in  $^{155}\text{Gd}$  would be populated due to Coulomb excitation of their enriched  $^{155}\text{Gd}$  target.) In their Figure 2, a labelled  $\gamma$ -ray is seen at 86.5 keV, while unlabelled  $\gamma$ -rays appear to be present near 105, 146 and 191 keV. Thus the strongest M1/E2 transitions they assign to  $^{183}\text{Hg}$  at 86 and 191 keV are possibly due to Coulomb excitation of the target.

Finally, the summed coincidence spectrum which Shi *et al.* show for the favoured signature of the  $\frac{1}{2}^-$ [521] band includes a gate on the 198.9 keV transition. This can be expected to show  $\gamma$ -rays at 89 and 296 keV because of true coincidences between these  $\gamma$ -rays and the 199 keV,  $4^+ \rightarrow 2^+$  transition in  $^{156}\text{Gd}$  [Led78]. ( $^{156}\text{Gd}$  will be present in their target as an isotopic contaminant and will be strongly Coulomb excited.) There is evidence for the 296 keV transition in their Figure 2, suggesting that the 88.9 keV transition which Shi *et al.* assign as the  $\frac{5}{2}^- \rightarrow \frac{1}{2}^-$  transition in  $^{183}\text{Hg}$  is again due to Coulomb excitation of the target. (The current work tentatively assigns an 87 keV energy for this transition.)

# Chapter 5

## $^{185}\text{Tl}$ and $^{187}\text{Tl}$ : Configuration Assignments

The next two chapters discuss the states expected to occur in the odd-mass thallium and mercury nuclei, while also presenting justification for the assigned configurations in terms of particular nuclear properties such as isomeric decay strengths, alignments and in-band branching ratios. The implications for the microscopic structure of the deformed cores are left for later discussion in Chapters 7 and 8.

### 5.1 Expected Structures

The states predicted to occur in the light thallium isotopes reflect the fact that the proton Fermi level for large prolate deformation is near the low- $\Omega$  orbitals from the  $h_{9/2}$ ,  $i_{13/2}$  and  $f_{7/2}$  shells intruding from above the  $Z=82$  shell gap, while for a moderate oblate deformation, it is near their high- $\Omega$  orbitals (see Figure 5.1). The  $\frac{9}{2}^-$  isomer known in all of the neutron-deficient odd-mass thallium isotopes (see §1.3.2), has been shown to arise from the oblate minimum [Bou85], and, where seen, the rotational bands built on the isomer have properties consistent with the deformation-aligned coupling scheme discussed in §2.5, appropriate for the  $\frac{9}{2}^- [505]$  orbital at oblate deformation. Similar bands associated with the oblate  $\frac{13}{2}^+ [606]$  orbital have also been seen in  $^{189}\text{Tl}$  [Por91],  $^{191}\text{Tl}$  [Rev95] and  $^{193}\text{Tl}$  [Rev92], although these bands appear to lose their regular rotational character at spins as low as  $I = \frac{17}{2}$  [Rev92].

It is known from the mercury isotopes that the excitation energy of the prolate minimum in the even-even nuclei drops as the neutron number decreases (see

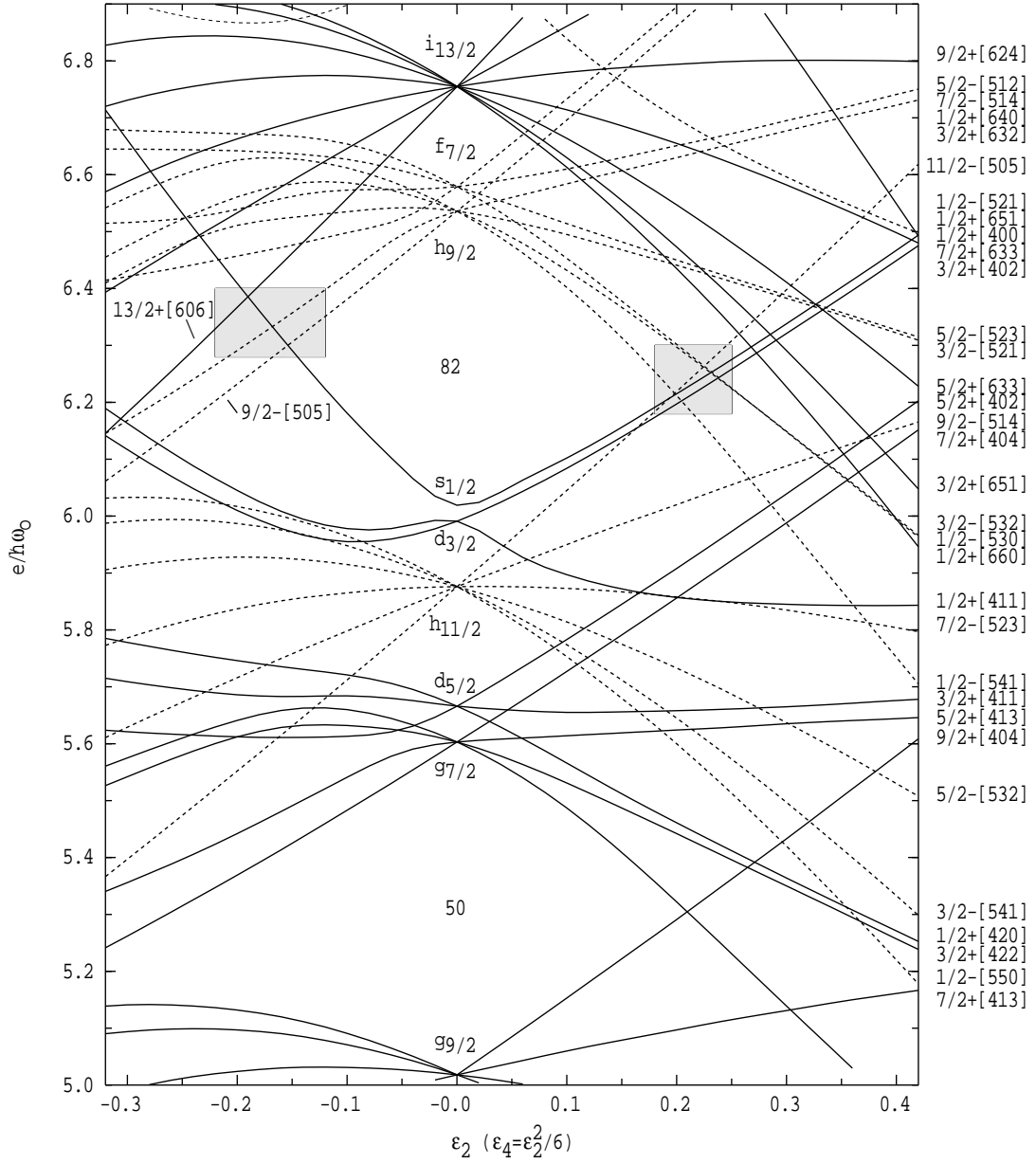


Figure 5.1: Nilsson scheme for protons using the modified  $(\kappa, \mu)$  parameters of Ref. [Zha87] and taking the hexadecapole deformation to lie along an approximate liquid-drop valley. Solid and dashed lines indicate positive and negative parity orbitals respectively.

§1.2). In  $^{189}\text{Tl}$ , a band corresponding to the  $i_{13/2}, \frac{1}{2}^+[660]$  orbital coupled to a prolate core was observed to compete with the oblate states at high spin [Por91]. The low- $\Omega$  and high- $j$  of this orbital lead to large Coriolis mixing so that the observed band has a large alignment and strong signature splitting, only the favoured signature being observed. This corresponds to the rotation-aligned coupling scheme discussed in §2.5. If the odd-proton nucleus follows the even-even core, this band should drop in excitation energy as the neutron number decreases and one might also expect to see similar bands based on the  $\frac{1}{2}^- [541]$  and  $\frac{1}{2}^- [530]$  orbitals from the  $h_{9/2}$  and  $f_{7/2}$  shells. In the simplest situation, the  $h_{9/2}$  and  $f_{7/2}$  proton orbitals at prolate deformation would produce two sets of signature-split sequences with the same spins and parities, with the  $\alpha = +\frac{1}{2}$  signature favoured for the  $h_{9/2}$  proton, and the opposite for the  $f_{7/2}$  proton. Ideally, the favoured signature of the  $h_{9/2}$  proton band would have an alignment of  $4.5\hbar$ , the unfavoured signature,  $3.5\hbar$ , while for the  $f_{7/2}$  proton the alignments would be  $3.5\hbar$  and  $2.5\hbar$  respectively. As will be shown below, the true situation is likely to be more complicated because of (i) mixing between the  $h_{9/2}$  and  $f_{7/2}$  orbitals due to both the deformed potential and the Coriolis force, and (ii) the presence of pairing giving rise to intruder-pair excitations and blocking. While the observation of decoupled negative parity bands with alignments around  $4\hbar$  could be taken to indicate the presence of either  $h_{9/2}$  or  $f_{7/2}$  protons coupled to a prolate core, the precise nature of the bands may be less obvious.

## 5.2 Band Properties

### 5.2.1 In-band decay properties

The configuration of a strongly coupled band is reflected in its in-band decay properties. This is discussed in Appendix A, where it is shown how the measured values of the crossover/cascade branching ratios,  $\lambda = \frac{I_\gamma(\Delta I=2)}{I_\gamma(\Delta I=1)}$ , can be used to determine the magnetic moments and cascade mixing ratios.

Reviol *et al.* have previously assumed a rotational g-factor of  $g_R = 0.3$  for the odd-mass thallium isotopes [Rev92, Rev95]. Using this value, the values of  $g_K$  deduced for the three strongly-coupled bands in  $^{187}\text{Tl}$  appear in Table 5.1. The quadrupole moments,  $Q_0$ , are calculated from the theoretical deformations (see §7.1), using the expression in Ref. [Naz94]. For a  $K \neq \frac{1}{2}$  band, the sign of  $\delta$  obeys the relation  $\text{sgn}[\delta] = \text{sgn}[Q_0/(g_K - g_R)]$  (see equation (A.2) in Appendix A). Moreover, since all the intrinsic states which could give rise to strongly-coupled



Table 5.1: Magnetic moments determined from crossover/cascade branching ratios in  $^{187}\text{Tl}$ 

State	Level	$\lambda = \frac{I_\gamma(\Delta I=2)}{I_\gamma(\Delta I=1)}$	$Q_0$ [eb]	$g_K - g_R$	$g_K^{a)}$	Calc. $g_K^{b)}$
$9/2^- [505]$	$\frac{13}{2}^-$	2.1(7)	-4.3	0.40(8)	0.70(8)	0.76
	$\frac{15}{2}^-$	1.4(4)	-4.3	0.29(7)	0.59(7)	0.76
$13/2^+ [606]$	$\frac{17}{2}^+$	$\leq 0.41^c)$	-5.1	$\geq 0.61$	$\geq 0.91$	1.22
$11/2^- [505]$	$\frac{15}{2}^-$	$\leq 0.20^c)$	+3.4	$\geq 0.56$	$\geq 0.86$	1.26

<sup>a)</sup> Assumes  $g_R = 0.3$ .

<sup>b)</sup> The method of calculation is discussed in Appendix A.

<sup>c)</sup> Based on upper limit for E2 crossover intensity.

bands at low excitation energy in the odd-mass thallium isotopes are proton states with large positive g-factors and  $K \neq \frac{1}{2}$ , the sign of  $\delta$  gives directly the sign of the quadrupole moment.

The large negative  $A_2$  value for the 394.1 keV  $\gamma$ -ray,  $-0.71(5)$ , implies (see §3.4) a negative value for the mixing ratio,  $\delta \sim -0.4$ , and therefore an oblate deformation. The magnitude of  $\delta$  is in good agreement with that obtained from the cross-over/cascade intensity ratio for the  $\frac{13}{2}^-$  state,  $|\delta| = 0.42(8)$ . In the two other cases shown in Table 5.1, the sign of the quadrupole moment was assumed in accordance with the theoretical deformations (see Table 7.1 in §7.1).

### 5.2.2 Aligned angular momenta

Experimental alignments for the decoupled positive parity sequences in  $^{185}\text{Tl}$  and  $^{187}\text{Tl}$  were obtained using the methods of §2.6 and are compared with the alignments for the yrast sequences of the even-mass mercury [Ma86, Por92, Ma93] and lead [Bax93, Hee93] core nuclei in Figure 5.2. The reference is the same for all nuclei and has been chosen to give a flat curve with zero alignment for the prolate deformed mercury and lead isotopes. The similarity of the odd-mass thallium isotopes with their even-even core nuclei has been remarked upon previously [Dra93, Lan94] and will be discussed in greater detail below. Figure 5.3 compares alignments in both the positive and negative parity decoupled bands in  $^{185}\text{Tl}$  and  $^{187}\text{Tl}$  with their gold isotones [Lar86, Zho88], using the same reference as that in Figure 5.2.

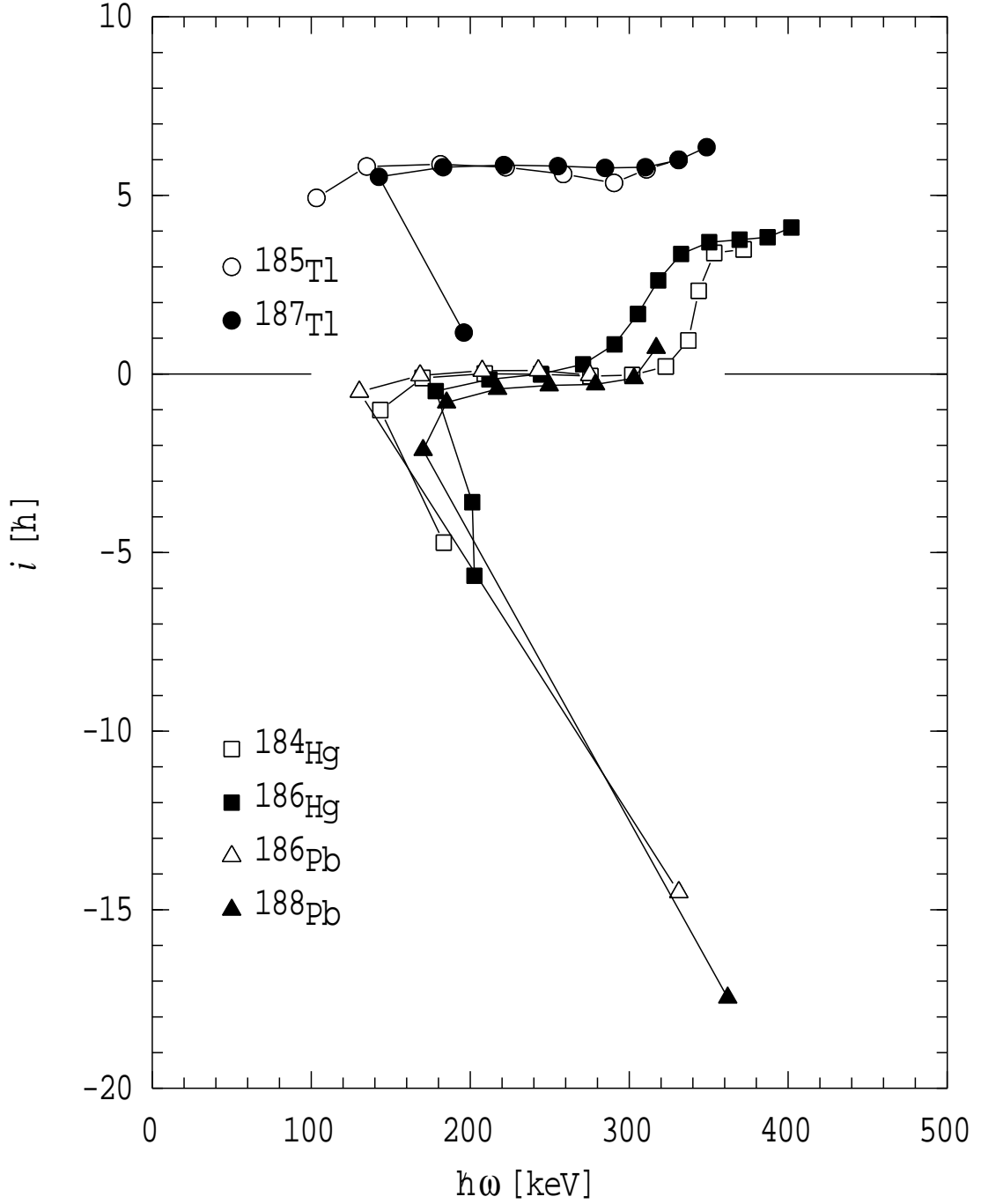


Figure 5.2: Alignments of the positive parity sequences in  $^{185}\text{Tl}$  and  $^{187}\text{Tl}$  compared to the alignments of the yrast cascades in the neighbouring mercury and lead nuclei. A common reference of  $\mathfrak{S}_0 = 27.5 \text{ MeV}^{-1}\hbar^2$  and  $\mathfrak{S}_1 = 190 \text{ MeV}^{-3}\hbar^4$  has been used for all nuclei.

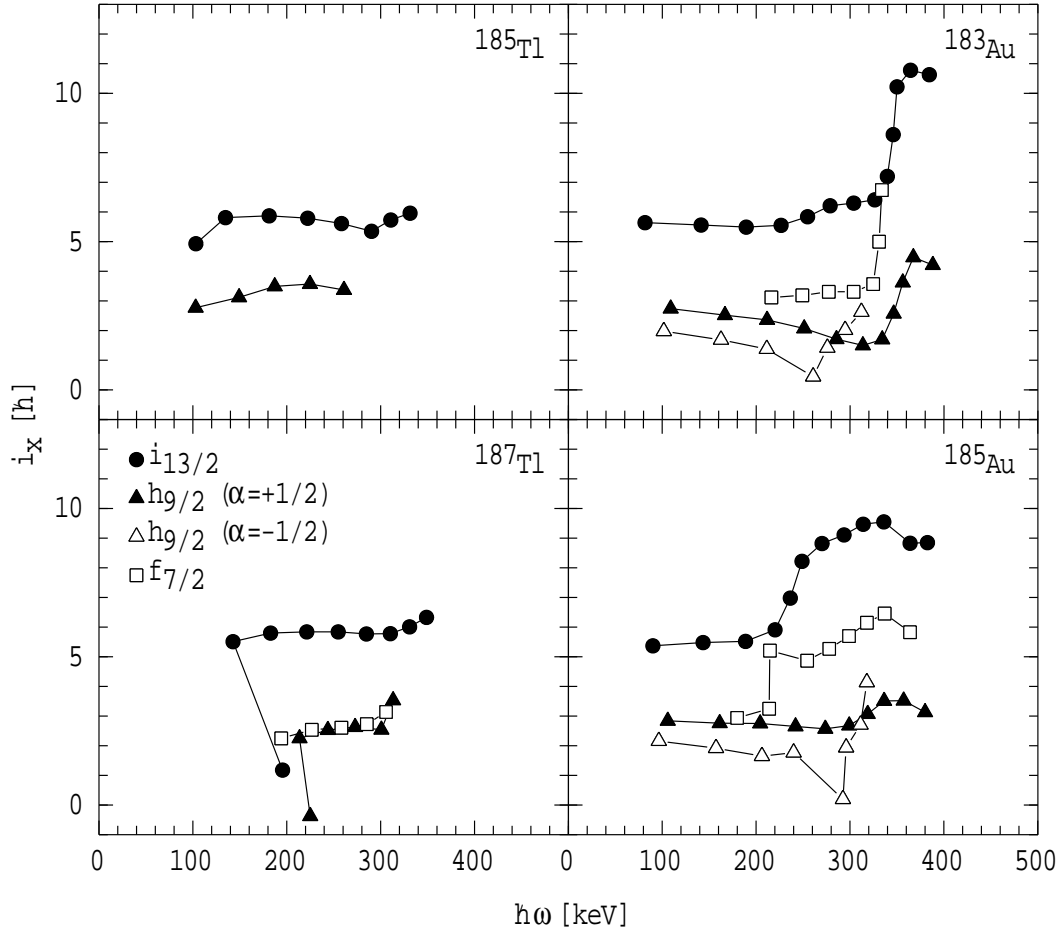


Figure 5.3: Alignments of the decoupled bands in  $^{185}\text{Tl}$  and  $^{187}\text{Tl}$  compared to the same bands in the gold isotones. A common reference of  $\mathfrak{S}_0 = 27.5 \text{ MeV}^{-1}\hbar^2$  and  $\mathfrak{S}_1 = 190 \text{ MeV}^{-3}\hbar^4$  has been used for all nuclei.

### 5.3 Band Assignments and Intrinsic States

In this section the rotational bands observed in  $^{185}\text{Tl}$  and  $^{187}\text{Tl}$  are interpreted in terms of specific configurations.

#### 5.3.1 $\frac{9}{2}^-$ [505] states, oblate deformation

Band 3 in  $^{187}\text{Tl}$ , built upon the  $\frac{9}{2}^-$  isomer, has a strongly coupled structure similar to that seen in the heavier odd-mass thallium isotopes [Hey83, Por91, New74, Rev92], suggesting a  $\frac{9}{2}^-$  [505] assignment. The assignment is supported by the measured  $g_K$  values for the  $\frac{13}{2}^-$  and  $\frac{15}{2}^-$  states, which are in good agreement with the calculated value for a  $\frac{9}{2}^-$  [505] state. The same assignment is made to band 2 in  $^{185}\text{Tl}$  on the basis of the similar M1 transition energy.

The signature splitting observed in the  $\frac{9}{2}^-$  [505] band in  $^{187}\text{Tl}$  is significantly larger than that observed in the heavier odd-mass isotopes. This may be an

indication of triaxiality, indeed in the heavier thallium isotopes the  $\frac{9}{2}^- [505]$  bands have previously been interpreted within the triaxial rotor plus particle model as  $h_{9/2}$  protons coupled to a near oblate, triaxial mercury core [Hey83].

### 5.3.2 $\frac{13}{2}^+ [606]$ states, oblate deformation

Band 5 in  $^{187}\text{Tl}$  has two dipole transitions with a tentatively assigned crossover. The limit on the intensity of the crossover gives a lower limit on the value of  $g_K$  in agreement with the value predicted for a  $\frac{13}{2}^+ [606]$  state. The lifetime of the  $\frac{13}{2}^+$  state at 1061 keV is evidence for its intrinsic nature, with the M2 decay strength of 0.21(6) W.U. for the 726.4 keV transition<sup>1</sup> comparing favourably with the value for the  $\pi i_{13/2}$  to  $\pi h_{9/2}$  decay in  $^{209}\text{Bi}$  of  $\sim 0.4$  W.U. [Mar91]. The  $\frac{13}{2}^+ [606]$  band is also signature split, although the degree of splitting is not as large as that seen in the  $\frac{9}{2}^- [505]$  band.

The  $\frac{13}{2}^+$  state at 1003 keV in  $^{185}\text{Tl}$  has been associated with a  $\frac{13}{2}^+ [606]$  intrinsic state and labelled as “band 3”, even though no rotational states are observed built upon it. This is supported by the E1 decay strength out of the  $\frac{13}{2}^+$  state,  $6.2(13) \times 10^{-6}$  W.U., which is in good agreement with the value of  $7.7(16) \times 10^{-6}$  W.U. found in  $^{187}\text{Tl}$ .

### 5.3.3 $\frac{1}{2}^+ [660]$ states, prolate deformation

Band 6 in  $^{187}\text{Tl}$  has a similar pattern of transition energies to band 4 in  $^{185}\text{Tl}$  and in neither case is the signature partner observed. The observed alignments of  $6\hbar$  agree with that expected for the rotation-aligned  $i_{13/2}$  proton and support the assigned  $\frac{1}{2}^+ [660]$  configuration. It is interesting to compare the alignments for the positive parity sequences with those of the even-even mercury and lead cores as shown in Figure 5.2. At low frequency, the lead/mercury isotopes show an initial negative slope with frequency and an increase in alignment, caused by the change from a spherical/oblate shape to the more deformed prolate shape at low spin [Dra93, Lan94]. The  $i_{13/2}$  bands in  $^{187}\text{Tl}$  and  $^{185}\text{Tl}$  show a related behaviour, with an increase in alignment at low frequency because of the change from the weakly oblate deformed  $\frac{13}{2}^+ [606]$  state to the more deformed prolate  $\frac{1}{2}^+ [660]$  state. The flatness of the alignment at higher frequency implies a deformation comparable to that of the prolate deformed bands in the mercury and lead cores, since the same reference has been used.

---

<sup>1</sup>See footnote on page 59.

### 5.3.4 $\frac{3}{2}^- [532]$ and $\frac{1}{2}^- [530]$ states, prolate deformation

Bands 1 and 2 in  $^{187}\text{Tl}$  are candidates for the two favoured signatures of the aligned  $h_{9/2}$  and  $f_{7/2}$  protons coupled to prolate mercury cores. Certainly, the absence of interconnecting transitions could imply separate intrinsic natures for the two bands. However, the alignments in Figure 5.3 do not differ by  $1\hbar$  as might be expected from the naive interpretation expressed in §5.1. Rather, they are identical, and have  $\sim 1\hbar$  less alignment than that expected for the  $h_{9/2}$  proton. Reviol *et al.* [Rev94] describe a lower alignment as possibly being due to the aligned band forming from the  $\frac{3}{2}^- [532]$  orbital rather than the  $\frac{1}{2}^- [541]$  orbital<sup>2</sup>. This is because in their equilibrium deformation calculations, the  $\frac{3}{2}^- [532]$  orbital reaches a deformation similar to that for the  $i_{13/2}$ ,  $\frac{1}{2}^+ [660]$  state, while the  $\frac{1}{2}^- [541]$  state has a considerably smaller deformation. (This agrees with the current calculations which are presented in §7.1 and shown graphically in Figure 7.2.) If this were the explanation, then the prolate deformed, aligned  $h_{9/2}$  proton bands in the gold isotones [Lar86, Zho88], for which potential energy surface calculations [Lar86] predict the same deformation for both the  $\frac{1}{2}^- [541]$  and  $\frac{3}{2}^- [532]$  states, might be expected to have a larger alignment for the  $h_{9/2}$  proton. However, Figure 5.3 reveals that the situation is nearly the same in all four nuclei, with the  $f_{7/2}$  band having an equal or greater alignment than the  $h_{9/2}$  band. This is probably related to the fact that the equilibrium deformation calculations presented in both Ref. [Rev94] and §7.1 do not include rotation. Once the nucleus is rotated the various orbitals mix and it is not correct to consider the  $\frac{1}{2}^- [541]$  and  $\frac{3}{2}^- [532]$  states to be distinct entities having the different equilibrium deformations predicted before rotation. More sophisticated calculations which include rotation are required to fully investigate this problem.

Although this means that the assignment of a specific configuration to the aligned bands is not strictly correct, for the purposes of comparison with theory the  $\frac{1}{2}^- [530]$  configuration is assigned to the “ $f_{7/2}$ ” band, while the  $\frac{3}{2}^- [532]$  configuration is assigned to the “ $h_{9/2}$ ” band rather than the  $\frac{1}{2}^- [541]$  configuration. This is done (despite the misgivings expressed in the preceding paragraph) on the basis of the similar moments-of-inertia observed for the  $f_{7/2}$ ,  $h_{9/2}$  and  $i_{13/2}$  bands, and the similar equilibrium deformations predicted for the  $\frac{1}{2}^- [530]$ ,  $\frac{3}{2}^- [532]$  and  $\frac{1}{2}^+ [660]$  states.

In summary, the simple expectations for two separate aligned  $h_{9/2}$  and  $f_{7/2}$

---

<sup>2</sup>Due to their different spin assignments, the alignments obtained by Reviol *et al.* [Rev94] for the  $i_{13/2}$  and  $h_{9/2}$  bands are  $2\hbar$  less than those in Figures 5.2 and 5.3.

protons are not fulfilled in the gold and thallium isotopes and the exact nature of the negative parity aligned bands appears to be incompletely understood. (Note that these are the orbitals which at low deformations exchange character and form a pseudo-spin doublet.)

### 5.3.5 $\frac{11}{2}^-$ [505] state, weak prolate deformation

Band 4 in  $^{187}\text{Tl}$  has been assigned tentatively as a strongly coupled band built upon the weakly prolate deformed  $\frac{11}{2}^-$  [505] state from the  $h_{11/2}$  proton orbital. This state is predicted to occur at low excitation energy in the equilibrium deformation calculations (see §7.1) and has already been observed in the isotone,  $^{185}\text{Au}$  [Lar86]. The 616.9 keV transition would correspond to an allowed M1,  $\pi h_{11/2}$  to  $\pi h_{9/2}$  transition, consistent with the absence of a measureable lifetime for the ( $\frac{11}{2}^-$ ) state at 952 keV. The non-observation of crossover transitions places a lower limit on the magnetic moment,  $g_K \geq 0.90$ , in agreement with the calculated value of  $g_K=1.22$ .

The structure feeding into the  $\frac{11}{2}^-$  [505] band is of unknown origin.

## 5.4 Nilsson Parameters

The observation of the  $f_{7/2}$  aligned band in the gold isotopes was one of the reasons for a suggested change to the Nilsson model parameters for the Au-Pt region [Lar86, Zha87] and its observation in the thallium isotopes allows further testing of this proposition. Table 5.2 compares the relative experimental excitation energies of the prolate  $h_{9/2}$ ,  $i_{13/2}$  and  $f_{7/2}$  aligned bands (see Table 7.2 and Table 7.2), with those obtained from the quasiparticle energies calculated with the Nilsson model using both the “Universal” parameters of Bengtsson and Ragnarsson [Ben85], and those modified by Zhang *et al.* [Zha87]. Energies taken from the present calculations using the Woods-Saxon potential are also included (see §7.1). The deformation parameters used in the Nilsson calculations were the average of those predicted by the present Woods-Saxon calculations for the three prolate states, but transformed into the  $(\epsilon_2, \epsilon_4)$  coordinates. The “Universal” parameters fail to reproduce the observed ordering of the states, unlike the modified parameters which do, and are also within  $\sim 150$  keV of the relative experimental energies. This is satisfactory agreement considering an average deformation was used, while calculations show that in fact each orbital drives the nucleus to a different shape. The present calculations with the Woods-Saxon potential repro-

Table 5.2: Energies of prolate intrinsic states in  $^{187}\text{Tl}$  relative to the prolate  $h_{9/2}$  state

Band	Experiment	Calculation		
		Nilsson <sup>a)</sup>		Woods-Saxon
		Universal <sup>b)</sup>	Modified <sup>c)</sup>	(This work)
$h_{9/2}$	0	0	0	0
$f_{7/2}$	161	326	12	82
$i_{13/2}$	493	228	609	776

<sup>a)</sup> Quasiparticle energies calculated using a pair gap of  $\Delta=963$  keV (estimated from the third order mass-differences).

<sup>b)</sup> Nilsson parameters from Ref. [Ben85].

<sup>c)</sup> Nilsson parameters from Ref. [Zha87].

duce the correct ordering, but overestimate the energy of the  $i_{13/2}$  state relative to the  $h_{9/2}$  state. Overall, it appears that the experimental situation for the prolate deformed low- $\Omega$  intruder states in the thallium isotopes is very similar to that in the gold isotones, and supports the modified Nilsson parameters of Ref. [Zha87].

# Chapter 6

## $^{183}\text{Hg}$ : Configuration

## Assignments

This chapter describes the rotational structures expected to occur in the odd-mass mercury nuclei and presents justification for the configuration assignments made in  $^{183}\text{Hg}$ . Also, the rotational band structures in  $^{183}\text{Hg}$  are compared with nearby odd-neutron nuclei, while the alignments are compared with other mercury nuclei and are used to show the presence of band-crossings. The nature of the  $s$ -band crossing is investigated within the Cranked Shell Model.

### 6.1 Expected Structures

There are significant differences in the nature of the orbitals at the proton and neutron Fermi surfaces for the mercury and thallium isotopes with  $N \approx 104$ . The proton Fermi surface at  $Z \approx 80$  is near the closed shell, so that at both prolate and oblate shape, the only available orbitals have either  $\Omega \approx j$  or  $\Omega \approx \frac{1}{2}$  (see Figure 5.1). These orbitals give rise to deformation-aligned and rotation-aligned bands in the odd-mass thallium isotopes. The Nilsson scheme for neutrons appears in Figure 6.1 and shows that at  $N \approx 104$  the available neutron orbitals have a range of  $\Omega$ . Thus the rotational bands in the odd-mass mercury isotopes can have structures which range between the simple deformation and rotation-aligned limits discussed in §2.5.

At  $N \approx 104$ , the Fermi surface is just below the middle of the  $i_{13/2}$  neutron shell. It was already shown in §2.7 that the  $i_{13/2}$  neutron in the odd-mass mercury isotopes gives rise to a decoupled band at weak oblate deformation and a strongly coupled band showing significant signature splitting at prolate deformation.



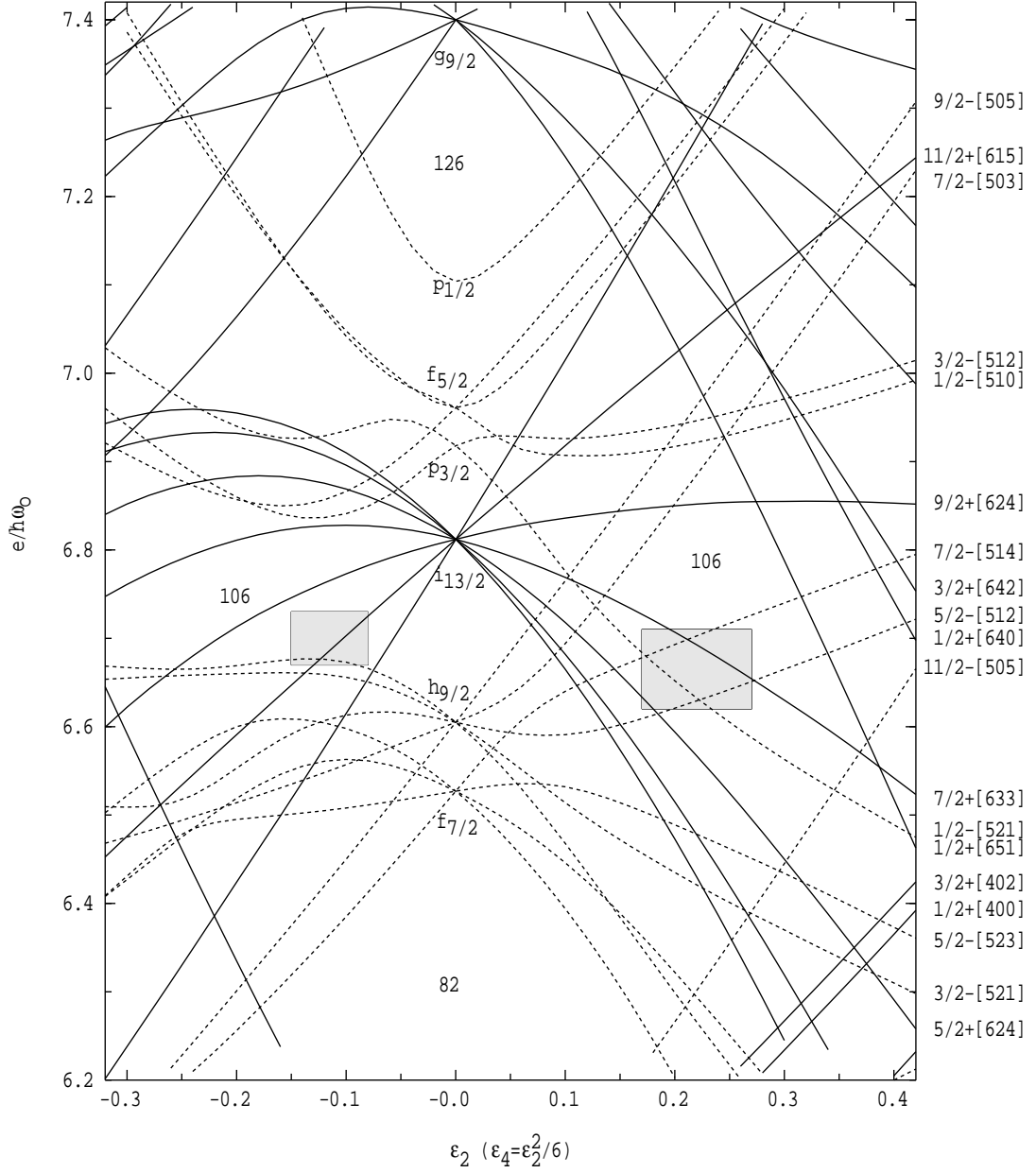


Figure 6.1: Nilsson scheme for neutrons using the  $(\kappa, \mu)$  parameters of Ref. [Ben85] and taking the hexadecapole deformation to lie along an approximate liquid-drop valley. Solid and dashed lines indicate positive and negative parity orbitals respectively.

Also at prolate deformation there are a range of orbitals other than those from the  $i_{13/2}$  shell. At  $\epsilon_2 \approx 0.2$  around  $N \approx 104$ , the  $\frac{1}{2}^- [521]$ ,  $\frac{5}{2}^- [512]$  and  $\frac{7}{2}^- [514]$  orbitals are near the Fermi surface. Out of these three orbitals the  $\frac{5}{2}^- [512]$  and  $\frac{7}{2}^- [514]$  states should both give rise to strongly-coupled bands, while the diagonal Coriolis matrix element for  $K = \frac{1}{2}$  states means that the  $\frac{1}{2}^- [521]$  band will be signature-split.

In  $^{185}\text{Hg}$ , bands built upon the  $\frac{1}{2}^- [521]$  and  $\frac{7}{2}^- [514]$  bands were observed corresponding to the prolate shape [Han88a]. That only one signature of the  $\frac{1}{2}^- [521]$  bands was observed is consistent with the expected signature splitting. Also, a positive parity, signature-split rotational band was observed to decay into the decoupled band built upon the  $\frac{13}{2}^+$  isomer. These two positive parity structures correspond to the couplings of the  $i_{13/2}$  neutron to prolate and oblate deformation. The current work makes similar assignments to the rotational structures observed in  $^{183}\text{Hg}$ , as discussed below.

## 6.2 Comparison with N=103 Isotones

Potential energy surface calculations for the neutron-deficient mercury, platinum and osmium isotopes all exhibit prolate minima at a deformation of  $\beta_2 \approx +0.24$  [Ben87, Naz90]. Due to the similar deformations one might expect to see prolate rotational bands with similar transition energies in the  $N = 103$  isotones  $^{183}\text{Hg}$ ,  $^{181}\text{Pt}$  and  $^{179}\text{Os}$ . Experimentally, these nuclei all exhibit rotational bands due to the  $\frac{1}{2}^- [521]$  and  $\frac{7}{2}^- [514]$  intrinsic states, together with a signature-split, mixed  $i_{13/2}$  neutron band. (A rotational band due to the  $\frac{5}{2}^- [512]$  state is also seen in  $^{181}\text{Pt}$  and  $^{179}\text{Os}$ .) The observed transition energies for the different bands in each nucleus are indeed similar, at least at low spins before the first alignment [Voi90a, Dra83, Bal93].

Looking now at the  $\frac{1}{2}^- [521]$  bands, based upon a comparison of the measured energies for the  $\frac{13}{2}^- \rightarrow \frac{9}{2}^-$ ,  $\frac{9}{2}^- \rightarrow \frac{5}{2}^-$  and  $\frac{5}{2}^- \rightarrow \frac{1}{2}^-$  transitions in each of the isotones, the  $\frac{5}{2}^- \rightarrow \frac{1}{2}^-$  transition in  $^{183}\text{Hg}$  is expected to have an energy of approximately 90 keV, in reasonable agreement with the tentatively assigned transition energy of 87 keV. Furthermore, a fit to the energies of the low spin levels in  $^{183}\text{Hg}$  yields a decoupling parameter of 0.82. This compares favourably with both the theoretical value of 0.88 calculated using equation (2.29) and with the measured values for  $^{181}\text{Pt}$  (0.79) and  $^{179}\text{Os}$  (0.81).

### 6.3 In-band Decay Properties

The crossover/cascade branching ratios,  $\lambda = \frac{I_\gamma(\Delta I=2)}{I_\gamma(\Delta I=1)}$ , contain information on the structure of the bands as discussed in Appendix A. This section uses the measured branching ratios to deduce the magnetic properties of intrinsic states in  $^{183}\text{Hg}$ , as summarised in Table 6.1.

Table 6.1: In-band decay properties for  $^{183}\text{Hg}$

Band	I	$E_\gamma$ ( $I \rightarrow I - 1$ ) [keV]	$E_\gamma$ ( $I \rightarrow I - 2$ ) [keV]	$\lambda = \frac{I_\gamma(\Delta I=2)}{I_\gamma(\Delta I=1)}$	$g_K - g_R$	$\text{sgn}[\delta]^a$
$\frac{7}{2}^- [514]$	$\frac{11}{2}$	146.6	251.6	$2.5 \pm 0.5$	$-0.10_{-3}^{+4}$	—
	$\frac{13}{2}$	155.2	302.0	$8.5 \pm 3.2$	$-0.12_{-4}^{+7}$	—
	$\frac{15}{2}$	178.8	334.3	$12 \pm 4$	$-0.11_{-4}^{+6}$	—
	$\frac{17}{2}$	193.7	372.5	$10 \pm 4$	$-0.22_{-4}^{+6}$	—
	$\frac{19}{2}$	213.2	407.2	$14 \pm 6$	$-0.20_{-5}^{+6}$	—
	$\frac{21}{2}$	226.4	440.0	$25 \pm 13$	$-0.15_{-5}^{+7}$	—
$\frac{9}{2}^+ [624]$	$\frac{19}{2}$	271.5	346.8	$2.2 \pm 0.4$	$-0.08_{-3}^{+6}$	—
	$\frac{21}{2}$	131.9	403.7	$22 \pm 5$	$-0.29_{-3}^{+3}$	—
	$\frac{23}{2}$	303.4	435.7	$3.0 \pm 1.0$	$-0.22_{-4}^{+4}$	—
	$\frac{25}{2}$	150.7	454.3	$30 \pm 12$	$-0.29_{-4}^{+5}$	—
$\frac{1}{2}^- [521]$	$\frac{7}{2}$	174.7	194.5	$3.9 \pm 1.4$	$0.16_{-10}^{+10}$	— <sup>b)</sup>
					$1.01_{-10}^{+10}$	+ <sup>b)</sup>

<sup>a)</sup> The assumption of the sign of  $\delta$  is described in the text.

<sup>b)</sup>  $g_K - g_R$  calculated for both signs of  $\delta$ .

#### 6.3.1 $\frac{7}{2}^- [514]$ and mixed $i_{13/2}$ neutron bands

The small DCO ratios for the 146.6, 155.2 and 178.8 keV transitions from the  $\frac{7}{2}^- [514]$  band imply negative mixing ratios (see Figure 4.16). Also, equation (A.2) in Appendix A implies that for  $K \neq \frac{1}{2}$ ,  $\text{sgn}[\delta] = \text{sgn}[\frac{g_K - g_R}{Q_0}]$ . Thus, assuming a prolate deformation ( $Q_0 > 0$ ), the sign of  $g_K - g_R$  for the  $\frac{7}{2}^- [514]$  band is determined to be negative. Similarly, the angular distributions and DCO ratios for the 150.7, 271.5 and 303.4 keV transitions imply negative mixing ratios, and, for a prolate deformation, negative values of  $g_K - g_R$  for the mixed  $i_{13/2}$  neutron

band. Assuming  $Q_0 = 7.5$  eb, values of  $g_K - g_R$  deduced from the branching ratios are shown in Table 6.1.

Theoretical values of  $g_K$  have been calculated according to the prescription in Appendix A, using the theoretical deformations from Ref. [Bin93]. The theoretical results are compared with experiment in Figure 6.2 using  $g_R = 0.35$ . Note that for the  $\frac{7}{2}^- [514]$  band the experimental values have been determined using two different values for both the bandhead spins,  $I_{bh}$ , and for the  $K$ -values. Figure 6.2b uses  $K = I_{bh} = \frac{7}{2}$ , while Figure 6.2c uses  $K = I_{bh} = \frac{5}{2}$ . The experimental results are only in agreement with the theoretical prediction for the  $\frac{7}{2}^- [514]$  orbital and do not agree with the predicted values for other Nilsson orbitals which are near the Fermi surface and could also result in rotational bands with a strongly-coupled structure.

In contrast, the results for the  $i_{13/2}$  neutron band are not in agreement with either of the simple Nilsson estimates. This is because the calculation assumes a pure configuration whereas the states in the observed band are mixed. Such disagreement is also seen in nearby nuclei. For example, the solid line in Figure 6.2 follows the trend of the experimental values of  $g_K - g_R$  measured for the  $i_{13/2}$  neutron band in  $^{179}\text{Os}$  [Dra83, Bal93] and displays a staggering pattern much like that in  $^{183}\text{Hg}$ . (These two nuclei have approximately the same value for  $g_R$  so that similar values of  $g_K - g_R$  imply similar values for  $g_K$ .)

### 6.3.2 $\frac{1}{2}^- [521]$ band

For the  $\frac{1}{2}^- [521]$  band only the branching ratio for the  $I = \frac{7}{2}$  state could be measured and the sign of the mixing ratio for the 174.7 keV transition is unknown. After solving equation (A.1) in Appendix A to get the magnitude of the mixing ratio, equations (A.2) and (A.3) can then be solved assuming the two possible signs of  $\delta$ , together with  $Q_0 = 7.5$  eb,  $g_R = 0.35$  and  $a = 0.82$ . This results in the two values of  $g_K - g_R$  shown in Table 6.1. These values can be compared with the results for  $\frac{1}{2}^- [521]$  bands in nearby odd-N nuclei which were compiled by Balabanski *et al.* [Bal93] and are reproduced in Table 6.2. (Note that some of the  $g_K$  values in the table for the choice  $\delta > 0$  are in addition to those shown in Ref. [Bal93] and have been calculated with the method described above except using the values of  $\lambda$ ,  $Q_0$  and  $g_R$  given in Ref. [Bal93].) Ignoring for the moment the result for the  $I = \frac{3}{2}$  state in  $^{179}\text{Os}$ , the different values of  $g_K$  in the table are all in good agreement with the other values with the same choice of  $\text{sgn}[\delta]$ . The  $g$ -factor for the  $I = \frac{3}{2}$  state in  $^{179}\text{Os}$  has been calculated by Balabanski

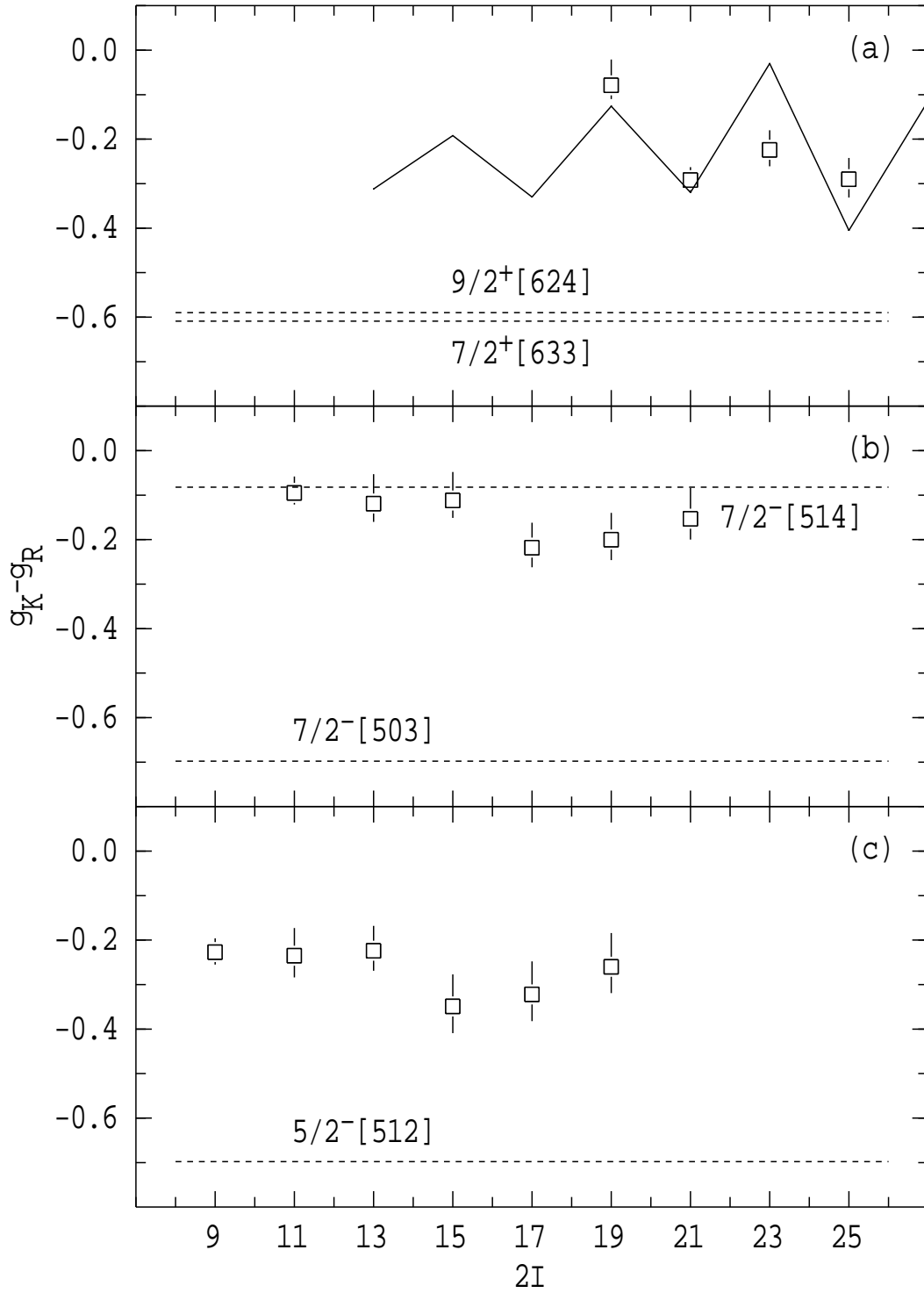


Figure 6.2: Comparison between measured  $g_K - g_R$  values and theoretical values from the Nilsson model. Panel (a) shows the experimental values obtained for the mixed  $i_{13/2}$  neutron band assuming  $K = \frac{9}{2}$ , while panels (b) and (c) show the values obtained from the branching ratios in the  $\frac{7}{2}^- [514]$  band assuming  $K$ -values and spins for the bandheads of  $K = I_{bh} = \frac{7}{2}$  and  $K = I_{bh} = \frac{5}{2}$  respectively. Details of the theoretically calculated values (dashed lines) are given in the text.

Table 6.2: Experimental  $g_K$  values deduced for  $\frac{1}{2}^- [521]$  bands in the  $A = 180$  region (adapted from Table 2 in Ref. [Bal93])

Nucleus	$I$	$a$	$\lambda$	$g_K$	
				$\delta < 0$	$\delta > 0$
$^{179}\text{Os}$	$\frac{3}{2}$	0.82	—	0.84(5)	1.96(16)
	$\frac{7}{2}$		$6.5 \pm 1.5$	0.71(14)	1.14(14)
	$\frac{11}{2}$		$8.0 \pm 2.0$	0.53(20)	1.32(20)
$^{175}\text{Os}$	$\frac{7}{2}$	0.73	$2.3 \pm 0.4$	0.51(20)	1.38(20)
	$\frac{11}{2}$		$2.8 \pm 0.6$	0.31(30)	1.57(30)
$^{181}\text{Os}$	$\frac{7}{2}$	0.90	$8.0 \pm 4.0$	0.76(30)	1.06(30)
$^{181}\text{Pt}$	$\frac{7}{2}$	0.80	$4.2 \pm 2.3$	0.63(30)	1.23(30)
$^{183}\text{Hg}$	$\frac{7}{2}$	0.82	$3.9 \pm 1.4$	0.51(10)	1.36(10)

*et al.* using the values of  $\delta$  obtained from an analysis of the known angular distribution [Dra83] for the 86.3 keV,  $\frac{3}{2}^- \rightarrow \frac{1}{2}^-$  transition. The result for  $\delta < 0$  is in the best agreement with the other determinations for  $^{179}\text{Os}$ , suggesting that the lower value of  $g_K = 0.51(10)$  is the correct result for  $^{183}\text{Hg}$ . This value agrees with the Nilsson model prediction of  $g_K = 0.64$ .

## 6.4 Band crossings and Aligned Angular Momenta

Figure 6.3 compares the aligned angular momenta of the three rotational bands observed in  $^{183}\text{Hg}$  with the analogous bands in the isotone,  $^{181}\text{Pt}$  [Voi90a], and also  $^{185}\text{Hg}$  [Han88a].

### 6.4.1 Shape changes in the $i_{13/2}$ bands

The apparent increase in alignment near  $\hbar\omega = 0.2$  MeV in the  $\alpha = +\frac{1}{2}$  signature of the  $i_{13/2}$  neutron bands in  $^{183}\text{Hg}$  and  $^{185}\text{Hg}$ , is attributed to the crossing of the weakly deformed oblate band with the more deformed prolate band. Similar distortions are seen at low frequency in the yrast bands of the even-mass mercury isotopes (see Figure 5.2), but not, for example, in the  $i_{13/2}$  neutron band in the isotone,  $^{181}\text{Pt}$ , where such a shape change is not expected.

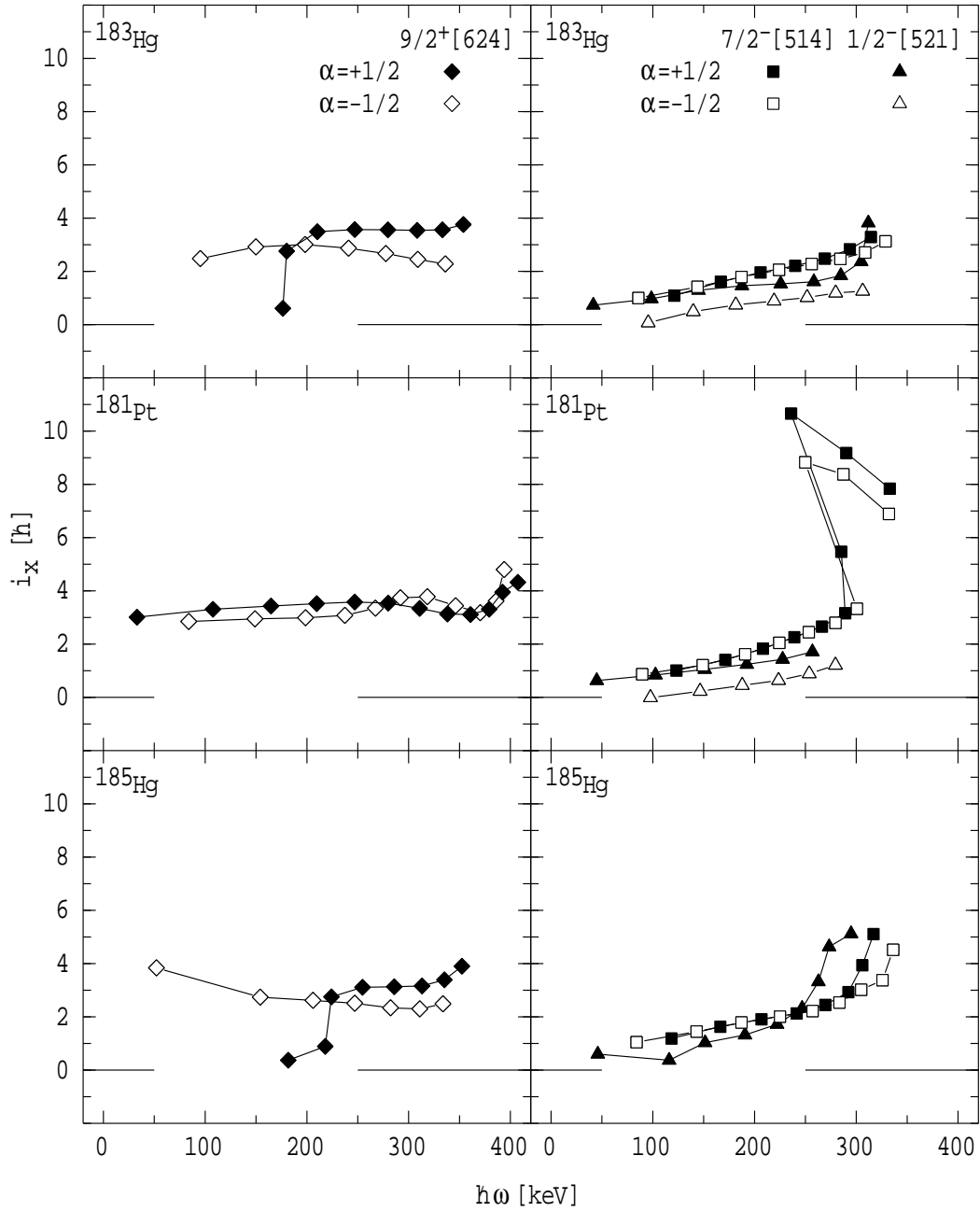


Figure 6.3: Aligned angular momenta for the rotational bands in  $^{183}\text{Hg}$ ,  $^{185}\text{Hg}$  and  $^{181}\text{Pt}$ . The reference parameters used for all three nuclei,  $\mathfrak{S}_0 = 28.7 \text{ MeV}^{-1} \hbar^{-2}$  and  $\mathfrak{S}_0 = 172 \text{ MeV}^{-3} \hbar^{-4}$ , are averages of those which give zero alignment for the prolate deformed bands in  $^{182}\text{Hg}$  and  $^{184}\text{Hg}$ .

At higher frequency however, the alignment curves for the two signatures in  $^{181}\text{Pt}$  cross and recross, an indication of oscillations in the sign of the signature splitting. The same behaviour is observed in  $^{177,179}\text{Os}$  [Dra83] and  $^{183}\text{Pt}$  [Nyb90]. Although not well understood, the oscillations have been interpreted as being due to variations in the shape of the nucleus for the two signatures as a function of rotational frequency [Voi90a, Nyb90]. In the same frequency region, the signature splitting for the  $i_{13/2}$  bands in  $^{183}\text{Hg}$  and  $^{185}\text{Hg}$  does not oscillate, and it would be interesting to see if theoretical calculations could reproduce the differences between isotopes.

#### 6.4.2 $\frac{1}{2}^- [521]$ and $\frac{7}{2}^- [514]$ bands

The  $\frac{1}{2}^- [521]$  and  $\frac{7}{2}^- [514]$  bands all show a smooth increase in alignment up to  $\hbar\omega \sim 0.25 - 0.30$  MeV. The orbitals forming these bands have  $\Omega \approx j$  and should have little or no alignment. The smooth increase at low frequency could be due to the choice of a reference which describes the prolate deformed even-even mercury isotopes, or possibly to real differences in deformation or pairing. Nevertheless, it is common to all cases.

#### 6.4.3 S-band crossing

At higher frequency in the  $\frac{7}{2}^- [514]$  band in  $^{181}\text{Pt}$ , the  $s$ -band crossing occurs due to the rotation alignment of a pair of high- $j$  particles, in this case  $i_{13/2}$  neutrons [Bal93]. Alignment gains are less well defined in  $^{183}\text{Hg}$  and  $^{185}\text{Hg}$ , only upbends being observed. The different  $s$ -band crossing frequencies for the rotational bands in the odd-mass mercury isotopes are compared with those for the prolate deformed bands in the even-mass mercury isotopes in Table 6.3.

To the extent that they can be defined, there is an experimental trend towards larger crossing frequency for the lighter isotopes. At first sight, the fact that no backbends are observed in the  $i_{13/2}$  neutron bands in the odd-mass isotopes could lead to the conclusion that the first alignment is due to the  $i_{13/2}$  neutrons. However, the first crossing in the  $\frac{7}{2}^- [514]$  band is delayed past that of the  $\frac{1}{2}^- [521]$  band, showing that the situation is more complicated. In fact, the  $s$ -band crossing in the mercury isotopes has previously been interpreted in terms of both  $h_{9/2}$  proton and  $i_{13/2}$  neutron alignments [Ma86, Han88a, Por92].

It is useful to first investigate the theoretical crossing frequency in the even-mass isotopes. Examination of the third order mass-differences for the range of



Table 6.3: S-band crossing frequencies in the mercury isotopes

Band (Expt.)	Observed $\hbar\omega_c^{a)}$ [MeV]								
	$^{180}\text{Hg}$	$^{181}\text{Hg}$	$^{182}\text{Hg}$	$^{183}\text{Hg}$	$^{184}\text{Hg}$	$^{185}\text{Hg}$	$^{186}\text{Hg}$	$^{187}\text{Hg}$	$^{188}\text{Hg}$
prolate	> 0.33		> 0.36		0.34		0.31		0.32
$\frac{1}{2}^-$ [521]				0.31		0.26			
$\frac{7}{2}^-$ [514]				> 0.32		0.31			
$\frac{9}{2}^+$ [624]				> 0.36		> 0.35		> 0.36	

Aligning particles	Theoretical $\hbar\omega_c^{b)}$ [MeV]								
	$^{180}\text{Hg}$	$^{181}\text{Hg}$	$^{182}\text{Hg}$	$^{183}\text{Hg}$	$^{184}\text{Hg}$	$^{185}\text{Hg}$	$^{186}\text{Hg}$	$^{187}\text{Hg}$	$^{188}\text{Hg}$
$(\nu i_{13/2})^2$	0.24		0.25		0.26		0.26		0.27
$(\pi h_{9/2})^2$	0.35		0.37		0.36		0.37		0.39

<sup>a)</sup> Data:  $^{180}\text{Hg}$  [Dra88],  $^{182}\text{Hg}$  [Ma84, Bin94],  $^{184}\text{Hg}$  [Ma86],  $^{185}\text{Hg}$  [Han88a],  $^{186}\text{Hg}$  [Por92, Ma93],  $^{187}\text{Hg}$  [Han88],  $^{188}\text{Hg}$  [Han88].

<sup>b)</sup> Frequency for the first proton/neutron alignment from the CSM (see text for further details).

mercury isotopes from  $A=180$  to  $A=188$  leads to estimates for the pair gaps of  $\Delta_n = 0.9$  MeV and  $\Delta_p = 1.0$  MeV. The only parameters expected to change between even-mass isotopes are the nuclear deformation and the Fermi level. Using the theoretical deformations from Ref. [Ben87], the calculated frequencies for the first  $i_{13/2}$  neutron and  $h_{9/2}$  proton alignments for each even-mass isotope are shown in Table 6.3. The calculations predict that the  $i_{13/2}$  neutron alignment should be favoured over the  $h_{9/2}$  proton alignment, however, in neither case is the magnitude of the crossing frequency well-predicted. (It should be noted that some experimental data for nuclei in this transitional region has been interpreted in terms of the  $h_{9/2}$  proton alignment occurring at low frequency [Car90].) Perhaps more importantly, the theoretical trend is in both cases towards an increase with mass number, in direct contrast to experiment.

The changes in the frequency of the  $s$ -band crossing for the different quasineutron bands in the odd-mass isotopes can perhaps shed light upon the nature of the particles responsible for the first alignment. However, the failure in the even-mass isotopes to even predict the trend with mass does not bode well for a quantitative description of the various crossing frequencies. Triaxiality, blocking of the pairing field and deformation effects all need to be considered in determining the nature of the first alignment. The situation for  $^{185}\text{Hg}$  is very similar to that in  $^{183}\text{Hg}$ , and Hannachi *et al.* [Han88a] came to the conclusion that alternative explanations of

the different crossing frequencies in the odd-mass isotope were possible. Similar conclusions have been reached for other nuclei in this transitional region [Car90]. In summary, it is difficult to know whether it is the  $h_{9/2}$  protons or the  $i_{13/2}$  neutrons which are aligning, and the different crossing frequencies require further explanation.

# Chapter 7

## Proton Configurations of the Core Nuclei

This chapter investigates the proton structure of the even-mass mercury core nuclei by examination of the structure of the odd-mass thallium neighbours. Theoretical calculations of the proton quasiparticle structure in the thallium and mercury nuclei are presented and the relative importance of the different deformation driving orbitals is examined. The prolate-oblate energy differences for the mercury and thallium nuclei are compared with each other and also with theoretical predictions. Blocking arguments suggest that the  $h_{9/2}$  proton is more important than the  $i_{13/2}$  proton in stabilising the prolate deformation, in agreement with the occupation probability calculations.

### 7.1 Equilibrium Deformation Calculations

In Chapter 5 the rotational bands observed in  $^{185}\text{Tl}$  and  $^{187}\text{Tl}$  were associated with particular intrinsic configurations and nuclear shapes. In order to investigate the shape coexistence, theoretical deformations and excitation energies were calculated by Sheikh and Nazarewicz for the intrinsic states in a range of odd-mass thallium isotopes between  $A=181$  and  $A=199$ . The calculations are similar to those of Ref. [Naz90] using the Woods-Saxon potential, except that in this case a direct minimisation is performed (see Ref. [Naz93]). In order to keep track of individual Nilsson configurations, axial symmetry is assumed, although it will be shown later that the  $\gamma$ -degree of freedom is likely to be important. The pairing energy is computed using the Lipkin-Nogami approach [Lip60, Pra73] with the recent prescription of Möller and Nix [Möl92] for the pairing strength,

Table 7.1: Calculated deformations and excitation energies for some of the low-lying states in  $^{185}\text{Tl}$  and  $^{187}\text{Tl}$ 

Spherical parent	Orbital	$^{185}\text{Tl}$			$^{187}\text{Tl}$		
		Deformation		Energy <sup>a)</sup> (keV)	Deformation		Energy <sup>a)</sup> (keV)
		$\beta_2$	$\beta_4$		$\beta_2$	$\beta_4$	
$i_{13/2}$	$1/2^+[660]$	0.267	-0.003	1115	0.267	-0.017	1746
$i_{13/2}$	$3/2^+[651]$	0.281	-0.008	1390	0.271	-0.022	1996
$i_{13/2}$	$11/2^+[615]$	-0.165	-0.027	2886	-0.167	0.029	3488
$i_{13/2}$	$13/2^+[606]$	-0.190	0.005	1791	-0.189	0.002	1735
$h_{9/2}$	$1/2^-[541]$	0.170	-0.006	634	0.164	-0.015	897
$h_{9/2}$	$3/2^-[532]$	0.245	-0.013	569	0.234	-0.027	970
$h_{9/2}$	$7/2^-[514]$	0.006	0.019	1254	0.005	0.018	1301
$h_{9/2}$	$9/2^-[505]$	-0.162	-0.011	475	-0.162	-0.014	444
$f_{7/2}$	$1/2^-[530]$	0.258	-0.015	606	0.250	-0.030	1052
$h_{11/2}$	$1/2^-[550]$	-0.170	-0.019	1608	-0.172	-0.023	1631
$h_{11/2}$	$3/2^-[541]$	-0.161	-0.012	1845	-0.167	-0.016	1875
$h_{11/2}$	$9/2^-[514]$	0.266	-0.004	1135	0.255	-0.018	1789
$h_{11/2}$	$11/2^-[505]$	0.114	-0.013	354	0.116	-0.020	478
$g_{7/2}$	$7/2^+[404]$	0.329	-0.021	1503	0.285	-0.035	1799
$d_{5/2}$	$5/2^+[402]$	0.280	-0.019	917	0.272	-0.034	1421
$d_{3/2}$	$3/2^+[402]$	0.232	-0.011	589	0.216	-0.026	972
$d_{3/2}$	$1/2^+[411]$	-0.016	0.000	899	-0.019	0.000	890
$s_{1/2}$	$1/2^+[400]$	-0.085	-0.009	0	-0.084	-0.010	0

<sup>a)</sup> Relative to the  $s_{1/2}$  ground state.

while the macroscopic energy has been taken from the finite-range liquid-drop model [Möl88]. The deformations and energies of the states calculated to lie at low excitation energy in  $^{185}\text{Tl}$  and  $^{187}\text{Tl}$  are presented in Table 7.1, while the predicted excitation energies of selected intruder states in a range of thallium nuclei are shown in Figure 7.1. Other calculations which use the Nilsson potential have also been reported for the intruder states in the thallium isotopes [Rev94, Hey76]. The calculations of Ref. [Hey76] are also plotted in Figure 7.1 and show a similar behaviour with neutron number to the present calculations. There is however, a large difference between the two calculations for the energies of the  $i_{13/2}$  states

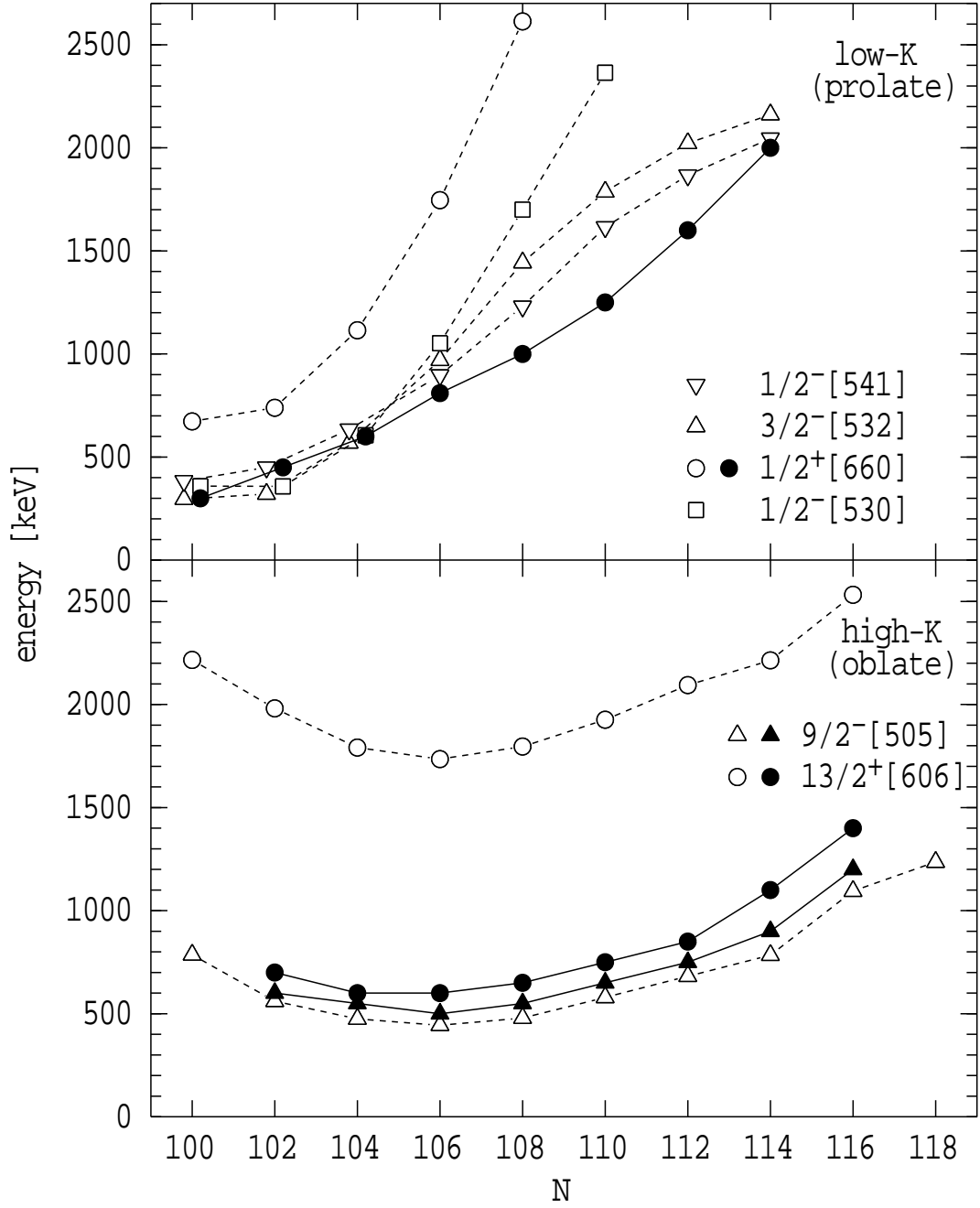


Figure 7.1: Comparison between this work using the Woods-Saxon potential (open symbols) and Ref. [Hey76] using the Nilsson potential (filled symbols) for theoretical excitation energies of selected intruder states in the odd-mass thallium nuclei.

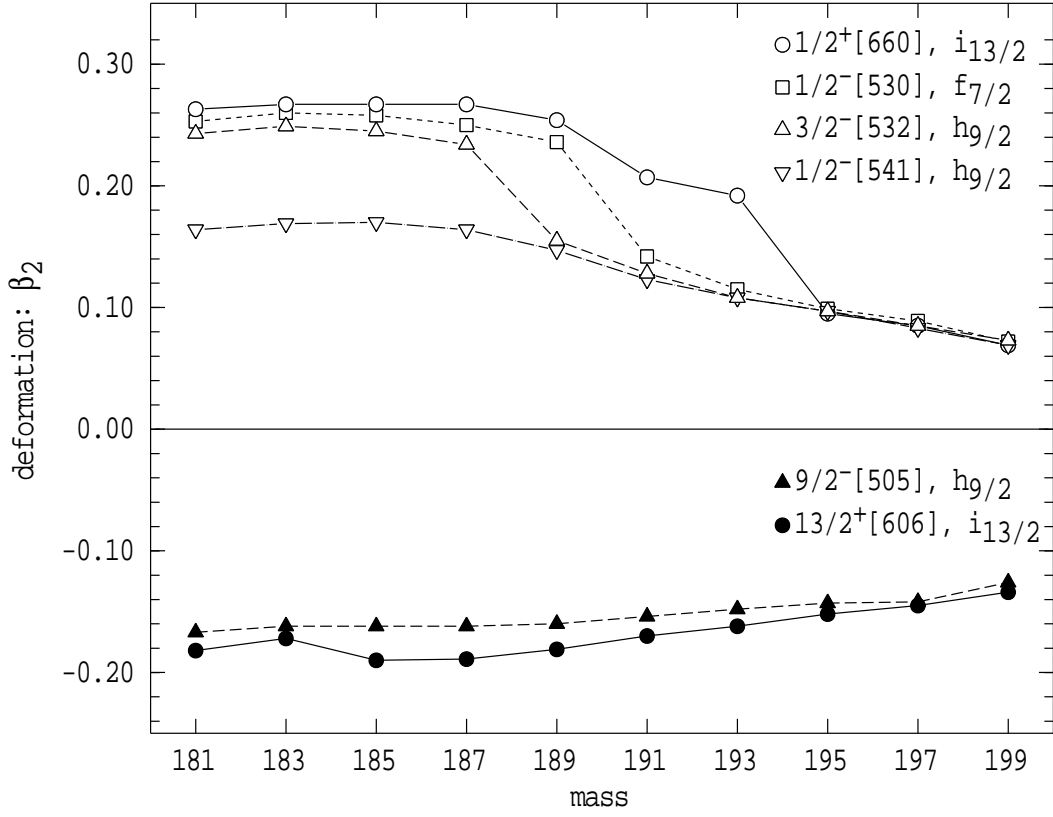


Figure 7.2: Predicted deformations from the present calculations for high- $j$  intruder states in the odd-mass thallium isotopes.

which is not understood in the present analysis.

Figure 7.2 plots the predicted deformations of states from the high- $j$  intruder orbitals, and shows that, as the distance from the  $N=126$  ( $^{207}\text{Tl}$ ) closed shell increases, the magnitudes of the calculated deformations for the states from the low- $\Omega$  (prolate) and high- $\Omega$  (oblate) deformation driving orbitals also increase. There are however, systematic differences in the way the deformation develops. For example, it is consistently larger for the  $i_{13/2}$  states, as expected, and the  $i_{13/2}$  prolate deformation develops more quickly with decreasing neutron number than the other prolate states. There are differences in detail between the (nominally)  $f_{7/2}$  and  $h_{9/2}$  cases and, for example, between the  $\Omega = \frac{3}{2}$  and  $\Omega = \frac{1}{2}$  states from the  $h_{9/2}$  configuration, the latter of which does not develop a large prolate deformation. Note also (see Figure 7.1), that the  $\Omega = \frac{3}{2}$  orbital from the  $h_{9/2}$  proton shell has a lower excitation energy than the  $\Omega = \frac{1}{2}$  orbital for  $A \leq 185$ , contrary to the other proton intruders for which the  $\Omega = \frac{1}{2}$  orbital is always calculated to be lowest. The causes of these differences can be traced back to the structural differences between corresponding quasi-particle vacua and will be discussed later in §7.3 in terms of occupation probabilities.

## 7.2 Intrinsic State Energies

An experimental determination of the excitation energies of the prolate intrinsic states which give rise to the aligned bands is complicated by the fact that the bands are not necessarily observed down to their bandheads. The excitation energies in  $^{185}\text{Tl}$ ,  $^{187}\text{Tl}$  and  $^{189}\text{Tl}$  [Por91] were therefore estimated by using a Variable Moment of Inertia (VMI) expression to fit the band level energies, as summarised in Table 7.2. (Details of the VMI parameterisation and the fitting process are given in §B.1 of Appendix B.) The aligned angular momentum was fixed for each band and reasonably consistent moment-of-inertia parameters were derived in the different fits. The excitation energies of the states giving rise to the oblate strongly coupled bands in the thallium isotopes from  $A=185$  to  $A=199$  [Hey83, New74, Rev92] were simply taken to be the observed energy of the bandhead.

The comparison of experimental and theoretical excitation energies in Figure 7.3 shows that general trends with mass number are reproduced, in particular the lowering of the prolate states and the presence of minima for the oblate states. However, precise agreement is not obtained either in absolute energy or with respect to the positions of the minima.

For example, the experimental position of the minimum varies for different intrinsic states. While the oblate  $\frac{9}{2}^- [505]$  state has its lowest energy near  $N \sim 108$ – $110$ , the oblate  $\frac{13}{2}^+ [606]$ , and prolate  $\frac{3}{2}^- [532]$  and  $\frac{1}{2}^+ [660]$  states, have not yet minimised at  $N=104$ . In contrast, both the current work and the calculations of

Table 7.2: VMI parameters used to fit the aligned bands in  $^{185}\text{Tl}$ ,  $^{187}\text{Tl}$  and  $^{189}\text{Tl}$

Nucleus	Band	VMI parameters			
		$\mathfrak{I}_0 \times 10^{-2}$	$C \times 10^6$	$i^a$	$E_0$
		[keV $^{-1}$ ]	[keV $^3$ ]	[ $\hbar$ ]	[keV]
$^{185}\text{Tl}$	$i_{13/2}$	2.70	2.88	6.0	1057
$^{185}\text{Tl}$	$(h_{9/2})$	2.04	1.38	3.5	726
$^{187}\text{Tl}$	$i_{13/2}$	2.45	2.22	6.0	1290
$^{187}\text{Tl}$	$h_{9/2}$	2.25	2.13	3.0	797
$^{187}\text{Tl}$	$f_{7/2}$	2.17	1.97	3.0	958
$^{189}\text{Tl}$	$i_{13/2}$	2.75	3.78	6.0	1851

<sup>a)</sup>  $i$  was fixed during fitting.

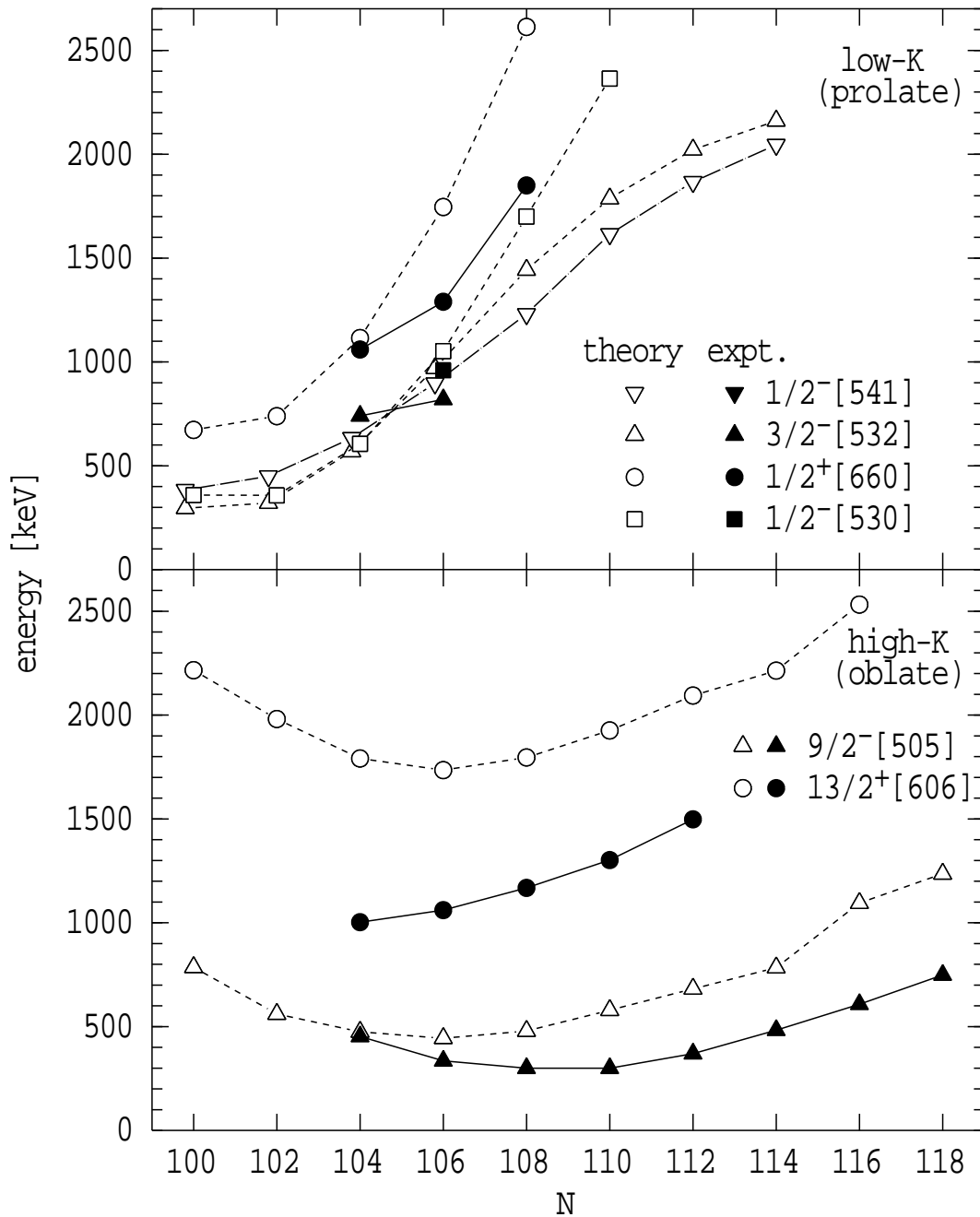


Figure 7.3: Experimental excitation energies for the intrinsic states in the odd-mass thallium isotopes are compared with the theoretical predictions of the current calculations.

Heyde *et al.* [Hey76] predict that the oblate  $\frac{9}{2}^- [505]$  and  $\frac{13}{2}^+ [606]$  states should have common minima at  $N=106$ . (See Figure 7.1; only the current calculations are plotted in Figure 7.3.) Neither calculation predicts a definite theoretical minimum for the prolate states, both showing similar curves down to an apparent minimum at  $N \approx 100$ . The reason why the theoretical calculations predict the oblate states to minimise near mid-shell, while the prolate states continue to drop in energy past mid-shell, is not understood in the present analysis. (These results



are in disagreement with the calculations of Reviol *et al.* [Rev94], which do show a rise at lower neutron numbers for the prolate states.) The failure to predict the configuration dependence of the position of the minimum requires investigation.

There could be several reasons for the disagreement between the calculated equilibrium energies and the experimental bandhead energies. The most important reason is probably the neglect of the rotational perturbations and triaxiality in the present calculations. (It should also be mentioned that the position of the minimum for the  $\frac{9}{2}^- [505]$  state is sensitive to details of the nuclear potential and different calculations have predicted different positions [Bou85, Naz90]. The current work and that of Refs. [Rev94, Hey76] are, however, the only calculations for the thallium isotopes where states other than the  $\frac{9}{2}^- [505]$  state have also been considered.)

### 7.3 Occupation Number Calculations

Given the general acceptance that the deformed structures in nuclei near closed shells are associated with particle-hole excitations into steeply sloping intruder orbitals (see §1.2), it is of some interest to examine the underlying occupation probabilities. These have been calculated by Nazarewicz and Sheikh using the Lipkin-Nogami method [Lip60, Pra73] for both the prolate deformed intrinsic states in the thallium isotopes and for the prolate minima in the even mercury cores<sup>1</sup>. The upper panel in Figure 7.4 shows the calculated deformations for the prolate states (reproducing part of Figure 7.2), while the lower panels show the occupation numbers for the intruder orbitals. (The results for the mercury isotopes are presented in detail in Table 7.3; for corresponding Nilsson model results see Ref. [Rev94].) It is important in the odd-mass thallium nuclei to note the distinction between the particular intrinsic state under discussion, labelled throughout with its Nilsson configuration, and the occupation numbers of the various intruder orbitals that are components of the wave function of that state. This is because the intruder orbitals near the Fermi surface for the odd-mass system can give rise to the intrinsic states. For example, the  $\frac{1}{2}^+ [660]$  *intrinsic state* is formed from the  $\frac{1}{2}^+ [660]$  *intruder orbital*, and thus has, by definition, an occupation number of unity for the  $\frac{1}{2}^+ [660]$  orbital<sup>2</sup>. Due to the pairing force, pairs of particles also occupy other proton orbitals, including the  $\frac{1}{2}^- [541]$ ,  $\frac{3}{2}^- [532]$

---

<sup>1</sup>The explicit expression for the occupation probability,  $v^2$ , is given in Ref. [Ben89b].

<sup>2</sup>The occupation probabilities used in the current work refer to *particles* as opposed to *pairs*. Thus the occupation probability for an orbital ranges between zero and two, and the term

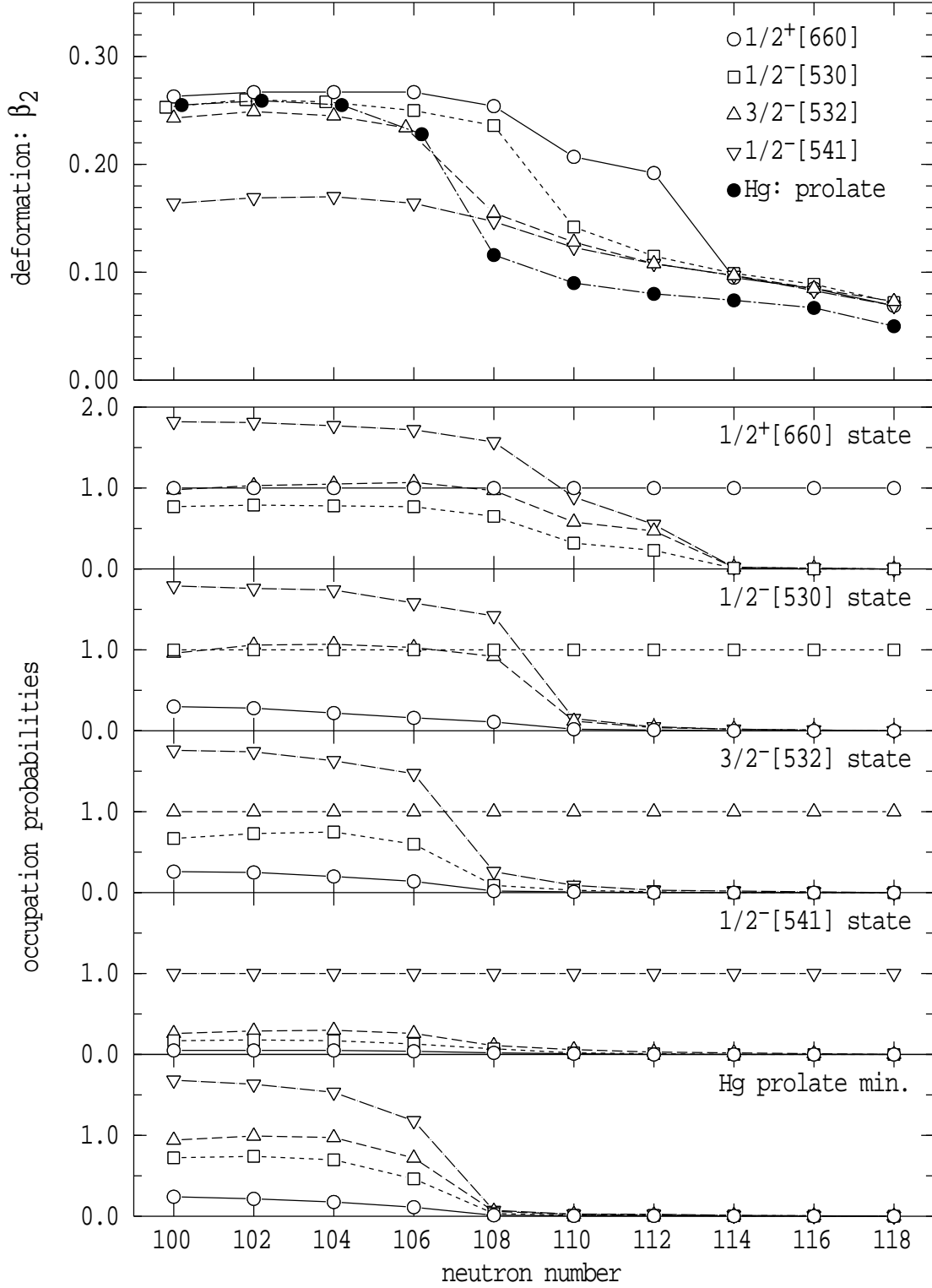


Figure 7.4: The upper panel shows the calculated deformations for both the prolate intruder states in the odd-mass thallium isotopes (reproducing part of Figure 7.2) and also for the prolate even-mass mercury cores. The lower panels gives the calculated occupation numbers of the high- $j$  orbitals for the various states shown in the upper panel.

Table 7.3: Calculated deformations of the prolate minima for the even-mass mercury isotopes and occupation probabilities for the intruder orbitals

N	Deformation			Occupation probabilities			
	$\beta_2$	$\beta_4$	$\beta_6$	$\frac{1}{2}^- [541]$	$\frac{3}{2}^- [532]$	$\frac{1}{2}^- [530]$	$\frac{1}{2}^+ [660]$
100	0.255	0.017	-0.015	1.683	0.943	0.724	0.242
102	0.259	-0.001	-0.014	1.633	0.993	0.741	0.216
104	0.255	-0.017	-0.011	1.533	0.974	0.699	0.177
106	0.228	-0.033	0.000	1.180	0.721	0.463	0.113
108	0.116	-0.025	0.001	0.073	0.062	0.034	0.013
110	0.090	-0.020	0.002	0.027	0.024	0.014	0.006
112	0.080	0.019	0.002	0.026	0.017	0.011	0.006
114	0.074	-0.022	0.004	0.012	0.011	0.006	0.003
116	0.067	-0.023	0.005	0.007	0.007	0.004	0.002
118	0.050	-0.022	0.006	0.003	0.003	0.002	0.001
120	0.009	-0.001	0.000	0.000	0.000	0.000	0.000

and  $\frac{1}{2}^- [530]$  intruder orbitals.

It is seen in Figure 7.4 that the deformation dependence of individual states is very closely linked to the behaviour of the occupation numbers. For instance, at  $A \geq 195$  ( $N = 114$ ), the  $\frac{1}{2}^+ [660]$  intrinsic state is weakly prolate deformed, and the only intruder orbital occupied is the  $\frac{1}{2}^+ [660]$ . For  $A = 191$  and 193 there is significant population of the  $h_{9/2}$  and  $f_{7/2}$  proton orbitals and an increase in deformation. There is a further rise in deformation for the  $\frac{1}{2}^+ [660]$  state at  $A = 189$  ( $N = 108$ ) when there is yet another increase in the  $h_{9/2}$  and  $f_{7/2}$  proton orbital occupation. In the mass region from  $A = 189$  down to  $A = 181$  the  $\frac{1}{2}^+ [660]$  state has an approximately constant deformation and the effective populations for the  $\frac{1}{2}^- [541]$ ,  $\frac{3}{2}^- [532]$  and  $\frac{1}{2}^- [530]$  orbitals are also constant.

The state which is predicted to have the next largest deformation in Figure 7.4 is the  $\frac{1}{2}^- [530]$  state from the  $f_{7/2}$  orbital. It experiences a large jump in deformation at  $A = 189$  when the  $h_{9/2}$  proton orbitals suddenly become occupied, the  $f_{7/2}$  orbital being blocked. In contrast, the deformation of the  $\frac{3}{2}^- [532]$  state from the  $h_{9/2}$  proton rises at a lower mass number,  $A = 187$ . Again there is an increase in  $f_{7/2}$  and  $h_{9/2}$  proton orbital occupation associated with the rise in deformation.

---

occupation *number* will generally be used (see also §2.4).

Note however, that for both of these intrinsic states the  $\frac{1}{2}^+[660]$  orbital does not have a large occupation.

The correlation between prolate deformation and occupation of the  $h_{9/2}$  and  $f_{7/2}$  proton orbitals, especially the  $\frac{1}{2}^- [541]$  orbital, is apparent. However, there is a question as to whether these calculations truly indicate that these particular orbitals are deformation driving. Since the Fermi level for a well-deformed, prolate thallium nucleus will be near the low- $\Omega$  intruder orbitals, it is not surprising that their occupation numbers are large. Nevertheless, the significance of the occupation numbers lies in the fact that they are calculated for a particular minimum in the potential energy surface, and, the presence of this minimum is at least partly caused by the deformation driving character of the intruder orbitals. That the population of the  $\frac{1}{2}^- [541]$  orbital is the dominant deformation driving force, can be seen in the results for the  $\frac{1}{2}^- [541]$  intrinsic state itself. In this case the  $\frac{1}{2}^- [541]$  orbital is blocked and the resulting deformation is less. The small occupation probabilities for the other intruder orbitals follow because at such a low deformation they are far above the Fermi surface. Another indication of the importance of the  $h_{9/2}$  protons in driving the deformation, is that both the  $i_{13/2}$  and  $f_{7/2}$  intrinsic states become well deformed at a higher mass number than the  $h_{9/2}$  intrinsic states.

## 7.4 Microscopic Structure of the Mercury Cores.

Recent calculations have suggested that the prolate and oblate states in the mercury and lead nuclei differ in complexity [Ben89, Naz93]. While the oblate states are predicted to be primarily due to the excitation of a pair of protons into the  $\frac{9}{2}^- [505]$  orbital, the prolate states are supposed to be due to more complicated 4p-4h configurations, with excitations into the low- $\Omega$  orbitals from the  $h_{9/2}$ ,  $f_{7/2}$  and  $i_{13/2}$  shells. Because the rotational bands observed in  $^{187}\text{Tl}$  and  $^{185}\text{Tl}$  are built on intrinsic states due to these orbitals, they contain information on both the character of the states and the involvement of specific orbitals in the structure of the prolate and oblate states in the neighbouring even-mass nuclei.

The theoretical occupation probabilities presented in Table 7.3 and Figure 7.4 show that the prolate mercury cores with  $A < 188$  have one  $f_{7/2}$  and three  $h_{9/2}$  proton orbitals occupied, consistent with the 4p-4h configurations suggested in Refs. [Ben89, Naz93]. The lesser role for the  $i_{13/2}$  proton in the prolate mercury

cores is consistent with the theoretical results obtained for the thallium isotopes and is due to its relatively high energy above the Fermi surface. The deformation driving tendency of the low- $\Omega$  orbitals is also apparent for  $A \geq 188$  where it can be seen that the odd-thallium isotopes with one deformation driving orbital occupied, have greater deformations than the even-even mercury isotopes where there are no low- $\Omega$  orbitals occupied.

The experimental observation of the prolate aligned bands due to the  $i_{13/2}$ ,  $h_{9/2}$  and  $f_{7/2}$  protons in  $^{187}\text{Tl}$ , and also the  $i_{13/2}$  and (tentatively)  $h_{9/2}$  protons in  $^{185}\text{Tl}$ , shows that population of different low- $\Omega$  proton orbitals does not preclude the development of a large prolate deformation. The absence of a shape blocking effect is experimental support for the concept of a more complicated proton configuration for the prolate deformed mercury cores. (Other evidence for a more complicated configuration is seen in the dependence of the unperturbed  $2^+ \rightarrow 0^+$  energies of the prolate intruder bands in the nearby even-even nuclei on the product of the valence proton and neutron numbers [Dra94].)

## 7.5 Absence of the $h_{9/2}$ Decoupled Band in $^{189}\text{Tl}$

Blocking arguments also have implications for the energies of the intrinsic states in the odd-mass thallium isotopes. For  $^{187}\text{Tl}$ , the present calculations predict that the  $\frac{3}{2}^- [532]$  and  $\frac{1}{2}^- [530]$  states from the  $h_{9/2}$  and  $f_{7/2}$  proton shells should have a prolate deformation comparable to that for the  $\frac{1}{2}^+ [660]$  state from the  $i_{13/2}$  proton shell. Experimentally, rotation-aligned bands associated with all three of these protons coupled to a prolate core have been observed in  $^{187}\text{Tl}$ . This contrasts with the situation in  $^{189}\text{Tl}$ , where the only prolate rotational band observed was that due to the  $i_{13/2}$  proton. Porquet *et al.* [Por91] argued that the non-observation of a prolate  $h_{9/2}$  band was due to blocking of a sizeable  $(\pi h_{9/2})^2$  component in the wavefunction of the  $^{188}\text{Hg}$  core. Since the situation in the lighter mercury isotopes need not be any different, the obvious question arises as to why such a prolate  $h_{9/2}$  band is not observed in  $^{189}\text{Tl}$ , yet is observed in the lighter thallium isotopes. The present explanation follows from the calculations in §7.1 and concurs with that of Reviol *et al.* [Rev94]. From Figures 7.2 and 7.4, neither the  $\Omega = \frac{1}{2}$  state nor the  $\Omega = \frac{3}{2}$  state from the  $h_{9/2}$  proton in  $^{189}\text{Tl}$  have a deformation larger than  $\beta_2 = 0.18$ , compared to  $\beta_2 \approx 0.26$  for the low- $\Omega$  orbitals from the  $i_{13/2}$  and  $f_{7/2}$  protons. The absence of a well-deformed minimum for the  $h_{9/2}$  proton states means that any  $h_{9/2}$  decoupled band would have a small moment of inertia and

be well above the yrast line, and consequently difficult to observe.

In contrast, the  $\Omega = \frac{3}{2}$  states from the  $h_{9/2}$  proton have a larger deformation with  $\beta_2 > 0.24$  in the thallium isotopes with  $A < 189$ . The presence of this more deformed minimum allows, with the inclusion of rotation, the development of a  $h_{9/2}$  decoupled band with a larger moment-of-inertia. It is this band which is strongly populated and observed. (It should be noted that Reviol *et al.* [Rev95] recently reported preliminary results from an experiment performed at GAMMASPHERE investigating high spin states in  $^{189}\text{Tl}$ . They report a candidate for a prolate,  $h_{9/2}$  aligned band with a moment-of-inertia less than the  $h_{9/2}$  aligned band observed in  $^{187}\text{Tl}$ , perhaps consistent with a smaller deformation.)

## 7.6 Prolate-Oblate Energy Differences

While the blocking of the odd-particle in the thallium nuclei does not appear to hinder the development of the prolate shape, the excitation energy of the prolate well may depend on which particle occupies the odd orbit. Figure 7.5 compares (for both the  $h_{9/2}$  and  $i_{13/2}$  cases) the difference between the experimental excitation energies of the low- $\Omega$ , prolate deformed band and the high- $\Omega$ , oblate deformed band, with the energy differences obtained from the current calculations. Figure 7.5 also shows the experimental prolate-oblate energy differences for the even mercury core isotopes [Dra94, Ham75, Col84], together with the theoretical predictions of Ref. [Ben87]. (Note that the experimental mercury results for  $A \leq 184$  are the unperturbed energy differences obtained from a two-band mixing analysis [Dra94], while the thallium results are the difference between the excitation energies deduced in §7.2, where mixing effects were ignored.) The theoretical prolate-oblate energy difference is overestimated for the even mercury isotopes and underestimated for the lighter odd-mass thallium isotopes. The theoretical calculations for the thallium isotopes consistently give a lower value for the  $i_{13/2}$  proton compared to the  $h_{9/2}$  proton, as observed in experiment, but fail to reproduce the general feature seen experimentally, that the odd- $A$  cases appear to follow the same trend as the even-even cores. It was previously shown in Figure 7.3 that the drop in absolute energy of the prolate states with neutron number is overestimated by the calculations and that the experimental prolate state energies appear to approach a minimum at  $N = 104$ , whereas the theoretical prediction is for a continued drop down to  $N \approx 100$ . The different trends between theory and experiment for the prolate-oblate energy differences in Figure 7.5 are

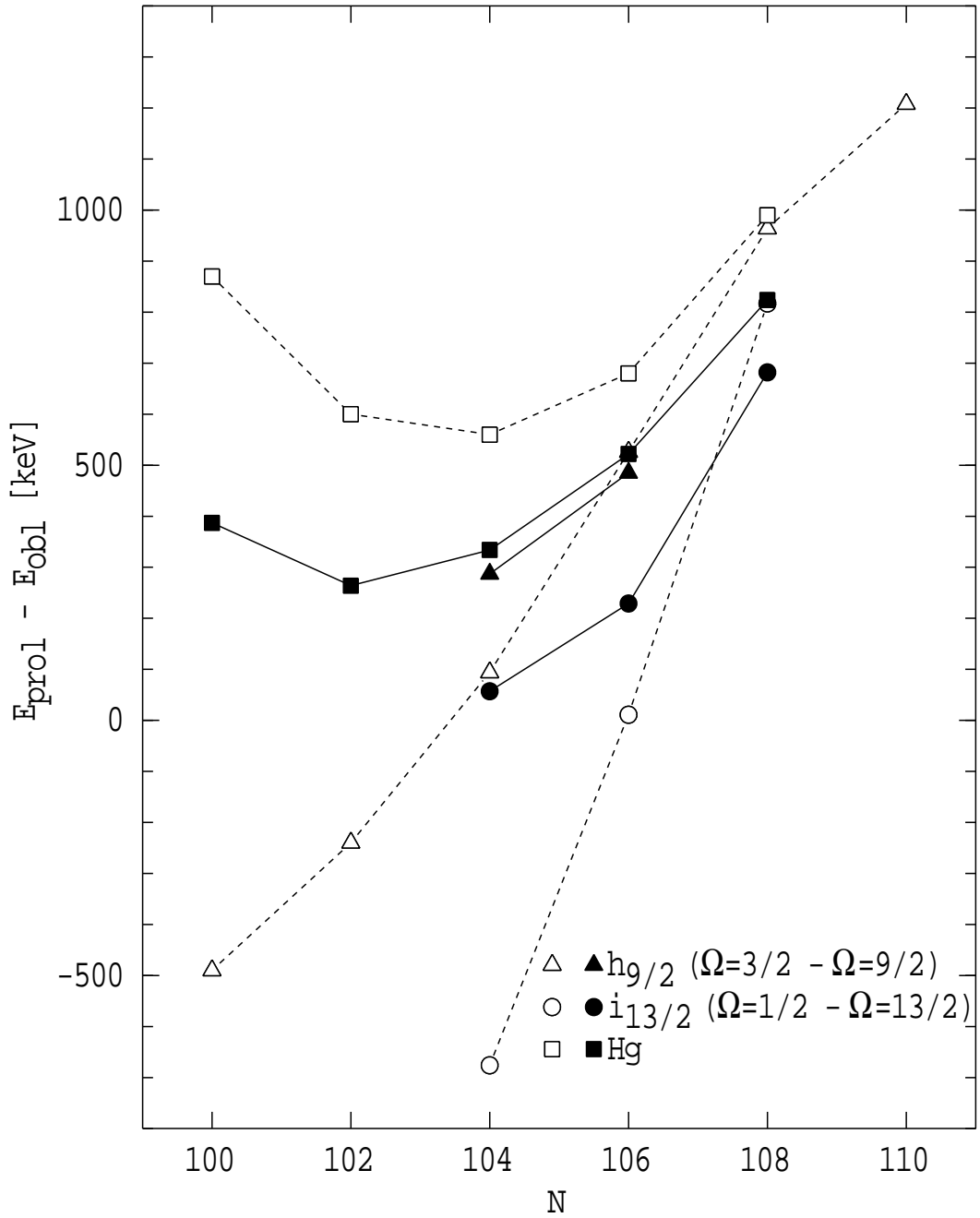


Figure 7.5: Experimental prolate-oblate energy differences for the even-mass mercury isotopes and their odd-mass thallium neighbours (filled symbols) are compared with theoretical predictions (open symbols). For the thallium isotopes, separate prolate-oblate energy differences are obtained for the  $i_{13/2}$  and  $h_{9/2}$  states using the experimental energy differences as well as the predicted energies from the current calculations. The experimental mercury results for  $A \leq 184$  are unperturbed energy differences from Ref. [Dra94], while  $0_2^+ - 0_1^+$  energy differences from Refs. [Ham75, Col84] are used for  $A \geq 186$ . The theoretical mercury results are taken from Ref. [Ben87].

related to this. Investigations of  $^{183}\text{Tl}$  could confirm whether or not the prolate states do actually minimise in energy near  $N = 104$ .

Examination of the occupation probabilities for the even-even cores can test whether the difference between the  $h_{9/2}$  and the  $i_{13/2}$  proton cases is due to blocking. As the  $h_{9/2}$  aligned band has been associated with the  $\frac{3}{2}^- [532]$  orbital, the relevant occupation probabilities in the mercury core nuclei are  $\sim 1$  for the  $h_{9/2}$  proton and  $\sim 0.2$  for the  $i_{13/2}$  proton (see Table 7.3). This means that any increase in the excitation energy of the prolate states in the thallium isotopes due to blocking of a particular orbital would be greater for the  $h_{9/2}$  prolate deformed band, consistent with the experimentally observed energy differences. The present excitation energy calculations include the effects of blocking, but do not consider triaxiality and shape mixing, both of which could also effect the energy difference between the low- $\Omega$  and high- $\Omega$  states. (Triaxiality was noted earlier as a possible cause of the signature splitting observed in the bands built upon the oblate  $\frac{9}{2}^- [505]$  and  $\frac{13}{2}^+ [606]$  states.)



# Chapter 8

## Odd-Mass Mercury Isotopes

This chapter examines aspects of the structure of the even-mass mercury cores as revealed by studies of the odd-mass mercury nuclei. Band mixing analyses of both the band excitation energies and also the E2 strengths for transitions within and between the rotational bands are presented. In both cases the results agree with a picture of coexistence between two bands based on different shapes, but with some inconsistencies in the required interactions. The analysis of the E2 transition strengths for  $^{187}\text{Hg}$  suggests that the coexisting bands have the same sign for their quadrupole moments, raising questions as to the nature of the coexisting shapes in the mercury isotopes. Finally, the prolate-oblate energy differences are extracted from the band-mixing analysis of the excitation energies. They show a pronounced odd-even staggering, most likely due to blocking by the odd neutron in the odd-mass isotopes.

### 8.1 Band-Mixing Analysis of the State Energies

The anomalous transition energy at the base of the  $i_{13/2}$  neutron band in  $^{183}\text{Hg}$  is taken as a sign of a transition across to an oblate, isomeric  $\frac{13}{2}^+$  state, similar to the situation in the heavier mercury isotopes,  $^{185}\text{Hg}$  [Han88a] and  $^{187}\text{Hg}$  [Han88]. In both these isotopes decoupled bands built upon the  $\frac{13}{2}^+$  isomers are observed. The non-observation of such a band in  $^{183}\text{Hg}$  might be because the prolate shape is especially favoured and the oblate band is only weakly populated. Indeed the prolate well in the even-even core nuclei minimises in energy at  $^{182}\text{Hg}$  [Dra88, Dra94]. It could also be because the mixing between the two rotational bands in  $^{183}\text{Hg}$  is such that the cross-over transitions analogous to those seen in  $^{185}\text{Hg}$  and  $^{187}\text{Hg}$  are suppressed. The analysis presented here uses a phenomenological band-mixing

model to evaluate the mixing between the prolate and oblate states. Such a model has previously been used to characterise shape coexistence in the even-mass mercury, platinum and osmium isotopes [Dra94] and also in the odd-mass rhenium and osmium isotopes [Dra88a, Bar91]. In the odd-mass mercury isotopes, both the prolate and oblate  $i_{13/2}$  neutron bands have significant signature splitting. To allow for this, Bark's extension [Bar94] to the band-mixing model of Refs. [Dra88a, Bar91, Dra94] is used, as described briefly below. (See Appendix B for full details including definitions for the parameters.)

The unperturbed bands may have different values of the parameters  $C$ ,  $\Im_0$ ,  $K$ ,  $i_x$ ,  $a_{sig}$  and  $E_0$ , allowing for the coexistence of bands based upon different deformations, or with different  $K$ -values, alignments or signature splitting. The perturbed energies are calculated assuming a spin-independent interaction,  $V$ , between states in the unperturbed bands with the same spin. The values of parameters are varied to obtain the best possible fit to the observed state energies.

This model is used in the current work to investigate the rotational bands due to the  $i_{13/2}$  neutron coupled to the prolate and oblate deformation in  $^{183}\text{Hg}$ ,  $^{185}\text{Hg}$  and  $^{187}\text{Hg}$ . Figure 8.1 gives level schemes for the positive parity states in these nuclei showing the bands of interest. It is necessary to estimate, and fix, the value of  $K$  for each band so that  $\sqrt{(I + \frac{1}{2})^2 - K^2}$  does not become imaginary during the fitting process (see eqn (B.3) in Appendix B). However, because the signature splitting in the  $i_{13/2}$  neutron bands arises from  $K$ -mixing,  $K$  is no longer a good quantum number. Thus it was necessary to estimate values of  $K = \frac{1}{2}$  for the oblate, decoupled bands and  $K = \frac{9}{2}$  for the prolate, mixed  $i_{13/2}$  neutron bands.

In fitting the band energies there is a strong correlation between the alignment,  $i_x$ , and the band-head energy,  $E_0$ . This is because for restricted regions of spin, an increase in alignment has much the same effect as an increase in the moment of inertia. Therefore, if only the high spin region is fitted, alternative combinations of values for  $\Im_0$ ,  $C$ ,  $i_x$  and  $E_0$  can all give a reasonable reproduction of the band energies. Since the important parameters in this study are the band-head energies and the moments-of-inertia, the procedure adopted was to fix the alignments from other information. For the mixed  $i_{13/2}$  neutron bands this was done by examining the aligned angular momenta for  $^{183}\text{Hg}$ ,  $^{185}\text{Hg}$  and  $^{187}\text{Hg}$  (see Figure 6.3). A common value of  $i_x = 2.6 \hbar$  was chosen to describe the prolate, mixed  $i_{13/2}$  neutron bands in each nucleus. The alignment for the oblate bands is discussed below.

Table 8.1 gives the results of the band-mixing calculations for the  $i_{13/2}$  bands

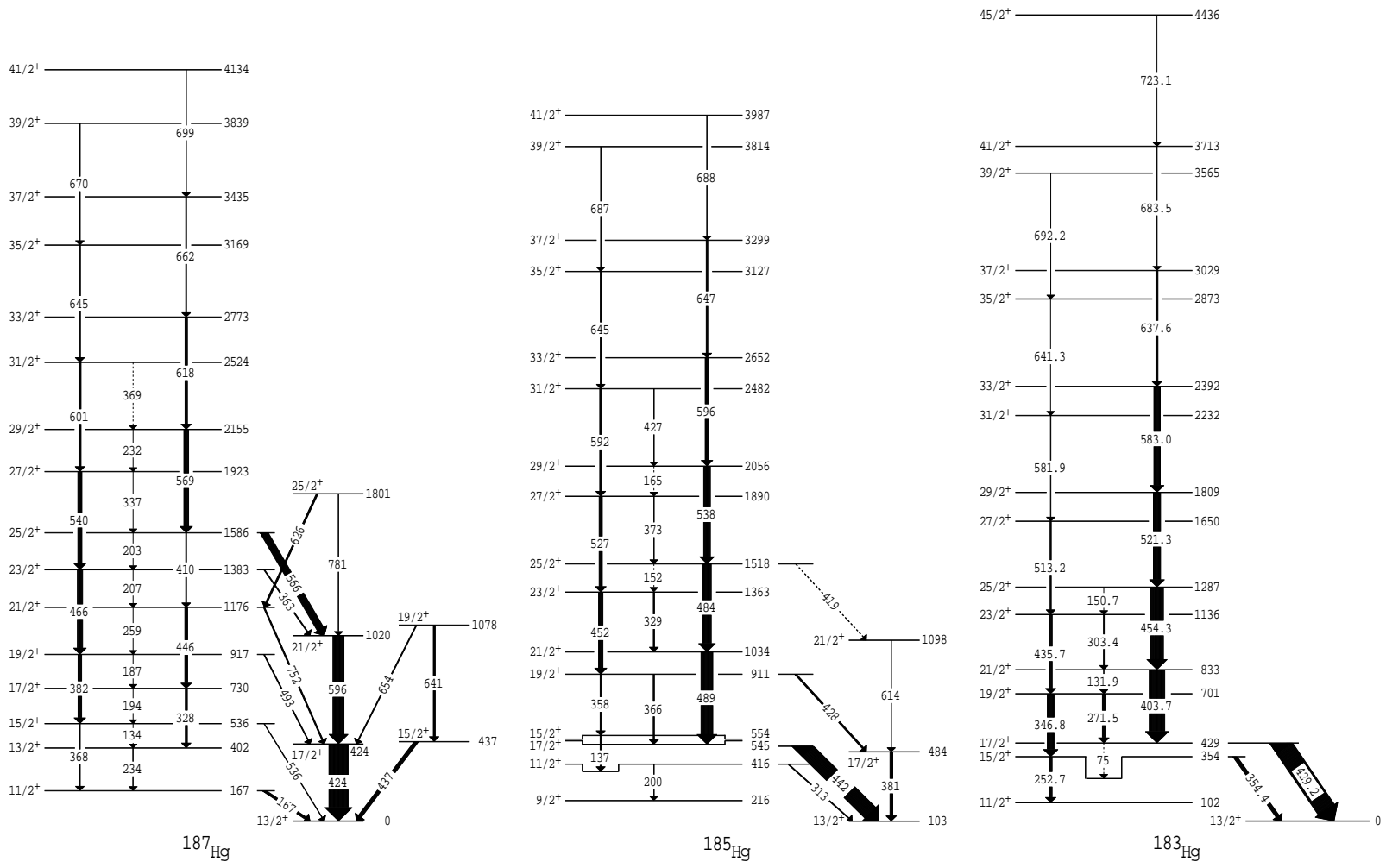


Figure 8.1: Partial level schemes showing the coexisting  $i_{13/2}$  neutron bands in  $^{183}\text{Hg}$ ,  $^{185}\text{Hg}$  [Han88a] and  $^{187}\text{Hg}$  [Han88]. Note that only the excitation energies in  $^{185}\text{Hg}$  are given relative to the ground state. The energies in the other two nuclei are given relative to the energy of the  $\frac{13}{2}^+$  isomer.

Table 8.1: VMI parameters used to fit the coexisting  $i_{13/2}$  neutron bands in  $^{183}\text{Hg}$ ,  $^{185}\text{Hg}$  and  $^{187}\text{Hg}$ 

Nucleus	Band <sup>b)</sup>	VMI parameters <sup>a)</sup>							
		$\Im_0 \times 10^{-2}$	$C \times 10^6$	$K$	$i$	$a_{sig}$	$V$	$E_0$	$E_{\beta>} - E_{\beta<}$
		[keV <sup>-1</sup> ]	[keV <sup>3</sup> ]	[ $\hbar$ ]	[ $\hbar$ ]		[keV]	[keV]	[keV]
$^{187}\text{Hg}$	$\beta>$	2.75	2.75	$\equiv \frac{9}{2}$	$\equiv 2.6$	0.032	70.5	282	230
	$\beta<$	0.92	7.13	$\equiv \frac{1}{2}$	5.3	0.045		52	
$^{185}\text{Hg}$	$\beta>$	2.57	2.30	$\equiv \frac{9}{2}$	$\equiv 2.6$	0.080	0.2	186	54
	$\beta<$	1.03	$\equiv 7.13$	$\equiv \frac{1}{2}$	$\equiv 5.3$	$\equiv 0.045$		132	
$^{183}\text{Hg}$	$\beta>$	3.02	2.80	$\equiv \frac{9}{2}$	$\equiv 2.6$	0.080	$\equiv 0$	57	16
	$\beta<$	<sup>c)</sup>	<sup>c)</sup>	<sup>c)</sup>	<sup>c)</sup>	<sup>c)</sup>		$\equiv 41^d)$	

<sup>a)</sup> Calculation of the band energies is described in Appendix B. Parameters preceded by “ $\equiv$ ” have been fixed during fitting.

<sup>b)</sup>  $\beta>$  refers to the signature-split mixed  $i_{13/2}$  neutron band.  $\beta<$  refers to the decoupled band built upon the  $\frac{13}{2}^+$  isomer.

<sup>c)</sup> Parameter not used in the fit.

<sup>d)</sup> Approximate energy found as described in §8.1.3.

in  $^{183}\text{Hg}$ ,  $^{185}\text{Hg}$  and  $^{187}\text{Hg}$ . It is important to remember that the fits for the odd-mass isotopes are not as accurate as those performed for the even-mass mercury isotopes in Ref. [Dra94]. This is because the even-mass isotopes have rotational bands with  $K = 0$ ,  $i_x = 0$  and  $a_{sig} = 0$ , so that there is less uncertainty in the fitting procedure, and, since the band-crossing occurs at higher energy in the even-even cases, the perturbations are more distinct. The result for the even-mass isotopes is that the band energies are reproduced to within one or two keV. In contrast, the parameters for the odd-mass isotopes presented in Table 8.1 result in fits with RMS deviations ranging between 6 keV for  $^{187}\text{Hg}$  and 20 keV for  $^{185}\text{Hg}$ .

### 8.1.1 $^{187}\text{Hg}$

The first attempt was to fit the energies of all states in both signatures of the two bands, fixing  $K$  for each band and  $i_x$  for the prolate band, and allowing all other parameters to vary. The fitted value for the interaction was  $V = 61$  keV. This is not consistent with the 99 keV separation of the unperturbed  $\frac{15}{2}^+$  states for which two-band mixing would imply  $V < 49.5$  keV. The parameter values given in Table 8.1 correspond to an improved fit ignoring the two  $\frac{15}{2}^+$  states where the fitted interaction increased to  $V = 70.5$  keV. Band-mixing calculations for the even-mass mercury nuclei give values for the mixing matrix element between 84

and 121 keV [Dra94], of similar magnitude to the result obtained here. However, it would appear from this analysis that the interaction between the bands is different for the two signatures in  $^{187}\text{Hg}$ . This is not unexpected as the mixing is far less clearcut in the odd-mass nuclei than in the even-mass nuclei. In the even nuclei, the prolate and oblate shapes give rise to only the  $K = 0$  bands, at least at low excitation energy<sup>1</sup>, so that they are the only two bands involved in the band-crossing region. However, in the odd-mass nuclei there are many other bands lying relatively close in energy so that two-state mixing is only an approximation. Therefore the similarity between  $^{187}\text{Hg}$  and the even isotopes for the deduced interaction strength may not be meaningful.

The magnitudes of the deformations can be deduced from the fitted moments-of-inertia using equations (B.4) and (B.5) from Appendix B, resulting in values of  $|\beta_2| \sim 0.26$  for the mixed  $i_{13/2}$  band and  $|\beta_2| \sim 0.15$  for the decoupled band. These deformations are consistent with those obtained from lifetime measurements for the even-even core nucleus,  $^{186}\text{Hg}$  [Pro74]. The fitted alignment of the oblate, decoupled band is  $5.3 \hbar$ , in reasonable agreement with the  $\sim 6 \hbar$  expected for a rotation-aligned  $i_{13/2}$  neutron.

The fit using the parameters in Table 8.1 reproduces the experimental energies with an RMS deviation of  $\sim 6$  keV. Examination of the  $\chi^2$ -surface as a function of the parameter values shows that the excitation energy of the prolate band is determined to within 10 or 15 keV. However, the excitation energy of the oblate band has a large associated error due to the smaller number of experimental states known. The shape of the  $\chi^2$ -surface was used to estimate a value of  $E_0(\beta^<) = 52^{+30}_{-120}$  for the oblate band-head energy. Because the lower values of  $E_0(\beta^<)$  correspond to small alignments, inconsistent with the rotation-aligned nature expected for the band,  $E_0(\beta^<) = 50 \pm 30$  keV was taken to be a better estimate.

### 8.1.2 $^{185}\text{Hg}$

There are only three experimental states known in the oblate, decoupled band in  $^{185}\text{Hg}$ . As there are potentially five free parameters for this band ( $K$  being fixed), it was necessary to also fix  $i_x$ ,  $a_{sig}$  and  $C$  to the values obtained for  $^{187}\text{Hg}$ . The fitted  $\mathfrak{S}_0$  value from Table 8.1 gives a deformation of  $|\beta_2| \sim 0.16$  for the oblate, decoupled band, consistent with the result obtained for  $^{187}\text{Hg}$ .

The fitted interaction,  $V = 0.2$  keV, is consistent with zero, and is in disagree-

---

<sup>1</sup>Vibrational  $\gamma$ - and  $\beta$ -bands as well as two-quasiparticle bands are expected for both shapes, although they are expected to occur at higher energy away from the band-crossing region.

ment with the larger values obtained for the even-mass mercury isotopes [Dra94] and for  $^{187}\text{Hg}$ . It is worth noting that within the two-band mixing model it is extremely difficult to reproduce the experimental state energies in the band-crossing region for  $^{185}\text{Hg}$ . The reason for this is apparent from a closer examination of the excitation energies of the  $\frac{17}{2}^+$  states. Figure 8.2 shows the experimental excitation energies of the  $i_{13/2}$  bands in  $^{183}\text{Hg}$ ,  $^{185}\text{Hg}$  and  $^{187}\text{Hg}$  plotted against  $I(I+1)$  with a nominal rotor energy subtracted. The solid lines are the calculated energies for the mixed  $i_{13/2}$  neutron bands using parameters from Table 8.1 but with  $V = 0$ , i.e. the unperturbed band energies. The energies of the high spin states are reproduced, with the extrapolation down to the band-crossing region showing discrepancies due to the effects of mixing. The dashed lines connect the experimentally observed energies of the states in the oblate bands. In both  $^{183}\text{Hg}$  and  $^{187}\text{Hg}$  the yrare  $\frac{17}{2}^+$  state lies above the extrapolation, presumably due to the interaction with the  $\frac{17}{2}^+$  state in the oblate well. However, for  $^{185}\text{Hg}$ , the yrare  $\frac{17}{2}^+$  state is  $\sim 80$  keV *below* the extrapolation. Removal of any interaction will lower the energy of this state and further increase the disagreement. The solution to this dilemma may lie in the presence of a third, unobserved  $\frac{17}{2}^+$  state, or there may be an unidentified problem with the  $^{185}\text{Hg}$  level scheme.

### 8.1.3 $^{183}\text{Hg}$

In  $^{183}\text{Hg}$  only the  $\frac{13}{2}^+$  state is known from the oblate well. Table 8.1 gives the result of the fit to the state energies of the mixed  $i_{13/2}$  neutron band, ignoring the effects of any oblate states. The parameter values obtained for this band are consistent with those for  $^{185}\text{Hg}$  and  $^{187}\text{Hg}$ . Note that the oblate bandhead energy,  $E_0(\beta^<)$ , has been estimated without fitting any state energies. This was done by calculating, in both  $^{187}\text{Hg}$  and  $^{185}\text{Hg}$ , the difference between the fitted oblate bandhead energies,  $E_0(\beta^<)$ , and the observed energies of the  $\frac{13}{2}^+$  isomers. The differences are 52 and 29 keV respectively, while the average of these two values is used to estimate the parameter  $E_0(\beta^<)$  for  $^{183}\text{Hg}$ .

### 8.1.4 Mixed wavefunctions

Diagonalisation of the energy matrix not only gives the state energies, but also the breakdown of the wavefunctions in terms of the unperturbed wavefunctions which would occur in the coexisting minima in the absence of any interaction between them. Denoting the amplitudes of the components due to the less and

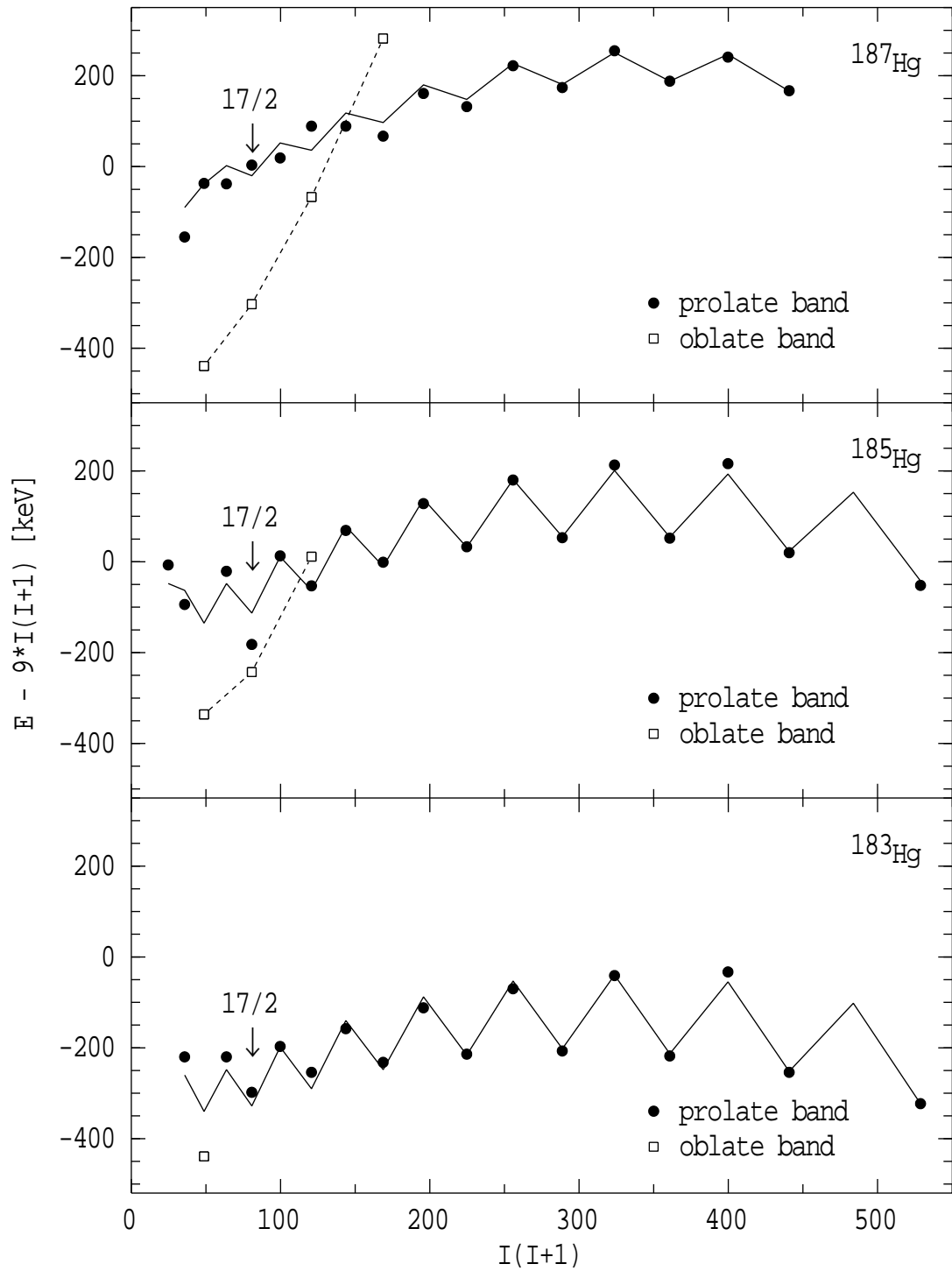


Figure 8.2: Excitation energies of the states in the prolate and oblate  $i_{13/2}$  bands in  $^{183}\text{Hg}$ ,  $^{185}\text{Hg}$  and  $^{187}\text{Hg}$  with a nominal rotor energy subtracted. The solid lines are fits to the prolate band energies using parameters from Table 8.1, but with  $V$  set to zero so as to indicate where the unperturbed band energies would lie. The dashed lines connect the experimental energies of the states in the favoured signature of the oblate band.

Table 8.2: Mixed wavefunctions for states in  $^{187}\text{Hg}$ 

State	Observed	Calculated	Wavefunction amplitudes	
	energy [keV]	energy [keV]	$a_{\beta<}$	$a_{\beta>}$
$\frac{13}{2}^{+}$	0	-2	-0.985	0.174
	402	409	0.174	0.985
$\frac{17}{2}^{+}$	424	433	-0.968	0.245
	730	725	0.245	0.968
$\frac{21}{2}^{+}$	1020	1010	-0.844	0.537
	1176	1166	0.537	0.844
$\frac{25}{2}^{+}$	1586	1587	-0.345	0.939
	1801	1805	0.939	0.345

more deformed minima by  $a_{\beta<}$  and  $a_{\beta>}$  respectively, the wavefunctions for some of the states in the favoured signatures of the  $i_{13/2}$  neutron bands in  $^{187}\text{Hg}$  are shown in Table 8.2. The yrast states start off at low spin with a large  $\beta^{<}$  component, while after the band crossing at higher spin they are mostly  $\beta^{>}$ . The yrare states show the opposite behaviour.

Using these mixed wavefunctions it is possible to calculate the expected transition strengths using the rotational model as outlined in Appendix B. Reversing the argument, it is also possible to use the measured absolute or relative transition strengths to deduce the mixed wavefunctions and the mixing matrix elements. The next section performs such an analysis.

## 8.2 Band-Mixing Analysis of the B(E2) Branching Ratios

The strengths of transitions within and between the coexisting rotational bands depend on the nature of the states and their admixtures. This section evaluates the mixing matrix elements between the prolate and oblate states by examining the B(E2) ratios for transitions within and between the coexisting bands. The



Table 8.3: Experimental B(E2) ratios for the odd-mass mercury isotopes<sup>a)</sup>

Nucleus	$I \rightarrow I - 2$	$E_1$ [keV]	$E_2$ [keV]	$E_3$ [keV]	$E_4$ [keV]	$\frac{B(E2,1 \rightarrow 3)}{B(E2,1 \rightarrow 4)}$	$\frac{B(E2,2 \rightarrow 4)}{B(E2,2 \rightarrow 3)}$
<sup>187</sup> Hg	$\frac{25}{2}^+ \rightarrow \frac{21}{2}^+$	1801	1586	1176	1020	6.1(27)	1.05(29)
	$\frac{21}{2}^+ \rightarrow \frac{17}{2}^+$	1176	1020	424	730	0.032(13)	< 3.74
<sup>185</sup> Hg	$\frac{21}{2}^+ \rightarrow \frac{17}{2}^+$	1098	1034	545	484	< 2.64	< 0.054

<sup>a)</sup> Gamma-ray branching ratios were deduced from the intensities in Refs. [Han88, Han88a].

Table 8.4: Predicted deformations and quadrupole moments for the coexisting  $i_{13/2}$  bands in <sup>183</sup>Hg, <sup>185</sup>Hg and <sup>187</sup>Hg

Nucleus	Band	$\beta_2^a)$	$\beta_4^a)$	$Q^b)$
<sup>183</sup> Hg	$\frac{9}{2}^+[624]$	0.266	-0.003	8.2
	oblate	-0.155	-0.017	-4.0
<sup>185</sup> Hg	$\frac{9}{2}^+[624]$	0.257	-0.015	7.9
	oblate	-0.155	-0.018	-4.1
<sup>187</sup> Hg	$\frac{9}{2}^+[624]$	0.248	-0.028	7.5
	oblate	-0.146	-0.019	-3.9

<sup>a)</sup> Values distilled from Refs. [Bin93, Ulm86, Ben87].

<sup>b)</sup> Calculated using the prescription given in Ref. [Naz94].

relevant theory is presented in Appendix B.

Using the experimental B(E2) ratios and excitation energies summarised in Table 8.3, the interaction strength between the states can be obtained from equations (B.18) through to (B.28) in Appendix B. Some assumptions must be made concerning the values of the quadrupole moment,  $Q$ , and also the values of  $K$ , to be used for the states formed from the  $i_{13/2}$  neutron coupled to the oblate and prolate shapes. As in §8.1 the approximations are made that  $K = \frac{1}{2}$  for the rotation-aligned  $i_{13/2}$  neutron bands built upon the  $\frac{13}{2}^+$  isomers and  $K = \frac{9}{2}$  for the mixed  $i_{13/2}$  neutron bands. The values assumed for the quadrupole moment appear in Table 8.4 and are calculated from deformation parameters for the rotational bands synthesised from a number of theoretical and experimental sources. The validity of the assumptions made for  $K$  and  $Q$  is discussed below for the case

of  $^{187}\text{Hg}$ .

### 8.2.1 $^{187}\text{Hg}$

The deduced interaction strengths are summarised in Table 8.5. Note however, that two different solutions are given corresponding to the two choices for the sign of  $R$ . The quantity  $R$  is defined by

$$R = \frac{\langle IK_\psi 20 | I - 2K_\psi \rangle Q_\psi}{\langle IK_\phi 20 | I - 2K_\phi \rangle Q_\phi} \quad (8.1)$$

and is the ratio of the Clebsch-Gordan coefficients which appear in the expressions for the B(E2) strengths, times the ratio of the quadrupole moments for the two bands. (See Appendix B for more detail.) It thus incorporates the parameters  $K$  and  $Q$  which describe the different intrinsic natures of the shape-coexisting states. Note that since the ratio of the Clebsch-Gordan coefficients is always positive, the sign of  $R$  is positive (negative) for coexisting bands with the same (opposite) signs of the quadrupole moment.

For the assumption  $R < 0$  the four experimental B(E2) ratios give inconsistent solutions for the mixing matrix element,  $V$ . However, if the quadrupole moments of the two bands are assumed to have the same sign ( $R > 0$ ), then consistent results are obtained, leading to an estimate for the mixing matrix element of

Table 8.5: Mixing matrix elements deduced from the B(E2) ratios in  $^{183}\text{Hg}$ ,  $^{185}\text{Hg}$  and  $^{187}\text{Hg}$

Nucleus	$(E_i)_I \rightarrow (E_f, E_{f'})_{I-2}^a)$	$V$ [keV]	
		$(R > 0)$	$(R < 0)$
$^{187}\text{Hg}$	$(E_1)_{\frac{25}{2}^+} \rightarrow (E_3, E_4)_{\frac{21}{2}^+}$	$73.0^{+2.5}_{-3.1}$	$b)$
	$(E_2)_{\frac{25}{2}^+} \rightarrow (E_3, E_4)_{\frac{21}{2}^+}$	$71.2^{+3.2}_{-3.9}$	$b)$
	$(E_1)_{\frac{21}{2}^+} \rightarrow (E_3, E_4)_{\frac{17}{2}^+}$	$73.5^{+2.4}_{-3.5}$	$23.6^{+4.5}_{-4.3}$
	$(E_2)_{\frac{21}{2}^+} \rightarrow (E_3, E_4)_{\frac{17}{2}^+}$	$> 74.0$	$63.9^{+8.0}_{-20.2}$
$^{185}\text{Hg}$	$(E_1)_{\frac{21}{2}^+} \rightarrow (E_3, E_4)_{\frac{17}{2}^+}$	$< 23.3$	$< 30.5$
	$(E_2)_{\frac{21}{2}^+} \rightarrow (E_3, E_4)_{\frac{17}{2}^+}$	$< 8.5$	$< 28.7$

$a)$  The B(E2) ratio for the decays  $(E_i)_I \rightarrow (E_f)_{I-2}$  and  $(E_i)_I \rightarrow (E_{f'})_{I-2}$  is considered.

$b)$  No solution for  $V$ .

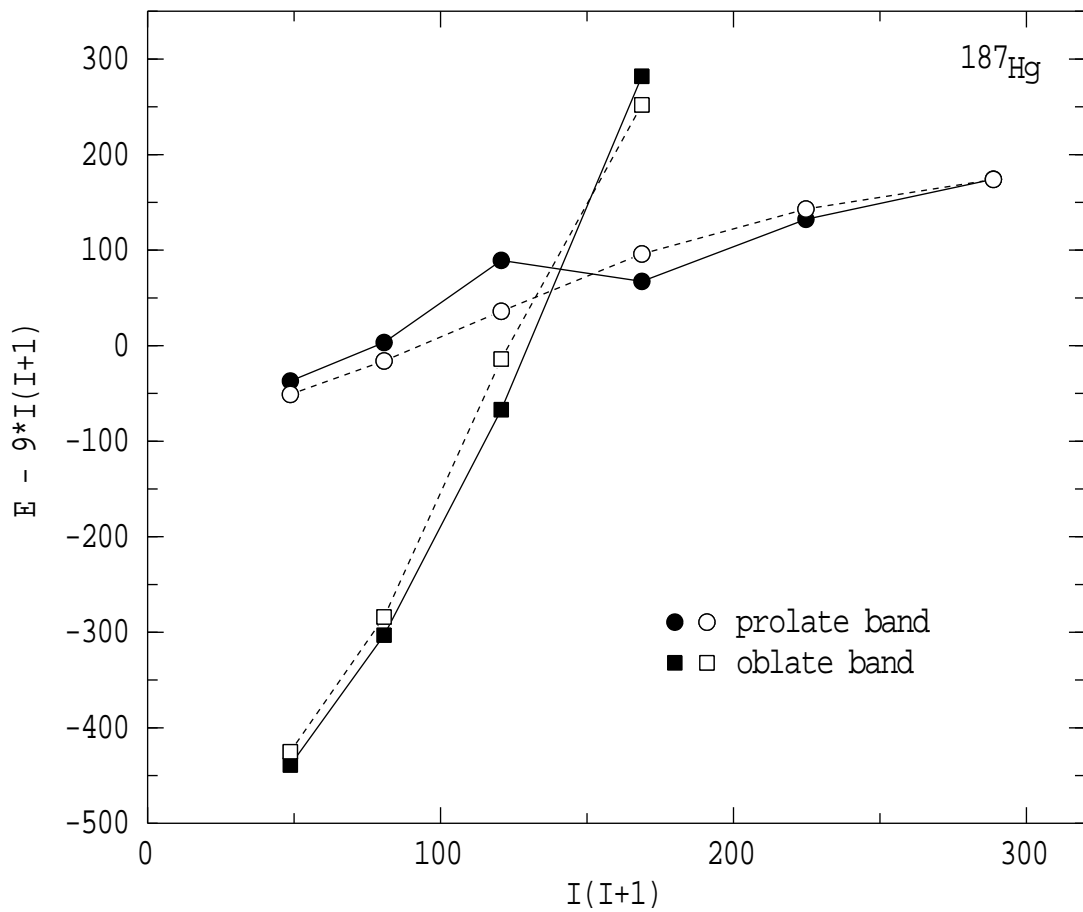


Figure 8.3: Excitation energies of the states in the favoured signatures of the prolate and oblate  $i_{13/2}$  bands in  $^{187}\text{Hg}$  with a nominal rotor energy subtracted. The solid points are the perturbed states while the open points are unperturbed energies where the effects of a spin-independent interaction of strength  $V = 73$  keV has been removed.

$V = 73$  keV. The effects of this matrix element can be seen in Figure 8.3, where the excitation energies of the two bands have been plotted against  $I(I+1)$  with a nominal rotor energy subtracted. The perturbed rotational bands are visibly smoothed when an interaction of strength  $V = 73$  keV is removed.

The interaction is not very sensitive to the  $K$ -value, for example assuming  $K = \frac{9}{2}$  for both bands changes  $V$  by only two or three keV. This is because the Clebsch-Gordan coefficients are slowly varying functions of  $K$  whenever  $I$  is reasonably large compared to  $K$ . The sensitivity to the quadrupole moment is far more pronounced. Assuming that both bands have  $Q = 7.5$  eb changes  $V$  by up to 40 keV and in the case of some branches no solution for  $V$  is possible. This is apparent in Figure 8.4 which shows the ranges of the interaction strengths obtained from the branching ratios out of the  $\frac{25}{2}^+$  states, as a function of the ratio  $Q(K = \frac{9}{2})/Q(K = \frac{1}{2})$ . Solutions for both branches are only obtained when

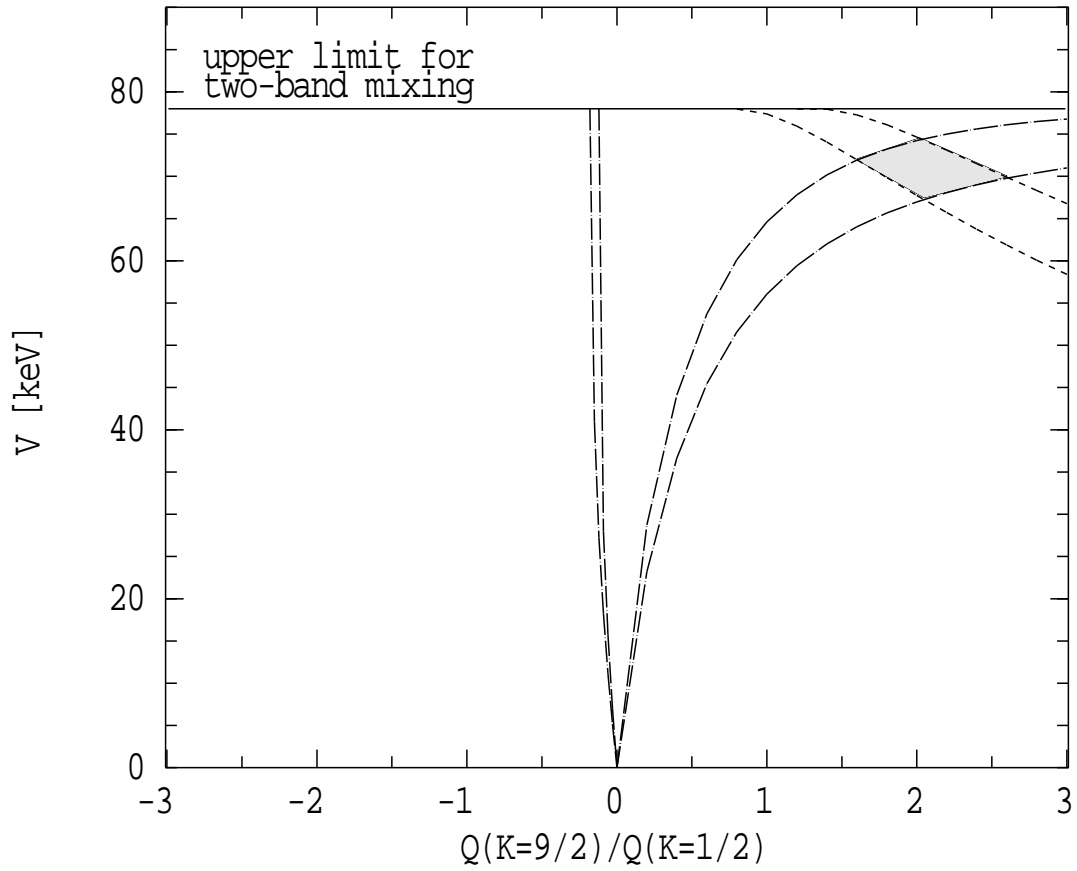


Figure 8.4: Deduced value of the interaction matrix elements from the branching ratios of the  $\frac{25}{2}^+ \rightarrow \frac{21}{2}^+$  transitions in  $^{187}\text{Hg}$  as a function of the ratio of the quadrupole moments of the coexisting bands. The solid line is the upper limit for two-band mixing, i.e. half the energy separation of the  $\frac{21}{2}^+$  states. The dashed lines are the upper and lower limits deduced from the branching ratio out of the yrare  $\frac{25}{2}^+$  state, while the dot-dashed lines are the limits using the branching out of the yrast  $\frac{25}{2}^+$  state. Over most of the region where the ratio of the quadrupole moments is negative there is no solution for the interaction matrix element for either branching, while results in mutual agreement for the two branches are only found in the shaded region near  $Q(K = \frac{9}{2})/Q(K = \frac{1}{2}) = 2$ .

the ratio of the quadrupole moments is positive and consistent results between the two branches are only obtained when the ratio of the quadrupole moments is  $Q(K = \frac{9}{2})/Q(K = \frac{1}{2}) \approx +2$ .

The mixing matrix element deduced here is in good agreement with the value of 70.5 keV found in §8.1.1 from the two band-mixing analysis of the level energies. In §8.1.1 it was also noted that the energy separation between the experimental  $\frac{15}{2}^+$  states shows that the unfavoured signatures of the prolate and oblate bands experience a smaller interaction than the favoured signatures. This is consistent with the absence of connecting transitions between the unfavoured signatures of

the prolate and oblate bands.

### 8.2.2 $^{185}\text{Hg}$

In  $^{185}\text{Hg}$ , the perturbed  $\frac{17}{2}^+$  states are only 61 keV apart, so for two-band mixing the matrix element is restricted to  $V < 30.5$  keV. Also, only one inter-band transition is observed and the  $\frac{13}{2}^+$  state in the prolate well is not known experimentally. The results of the analysis for the  $\frac{21}{2}^+ \rightarrow \frac{17}{2}^+$  transitions show that for  $R > 0$ ,  $V < 8.5$  keV and for  $R < 0$ ,  $V < 28.7$  keV. These can be compared to the value close to zero obtained from the fit to the state energies in §8.1.2.

Because the second  $\frac{13}{2}^+$  state was not observed, a proper analysis of the B(E2) ratios for transitions out of the  $\frac{17}{2}^+$  states could not be performed. This is unfortunate as it is at the  $\frac{17}{2}^+$  level where the intensity quickly decays out of the prolate band towards the oblate band. By assuming both the existence of a second  $\frac{13}{2}^+$  level at  $x$  keV and unobserved  $\gamma$ -rays with energies  $(545 - x)$  and  $(484 - x)$  keV, limits are obtained on the mixing matrix element for the various possible energies of the unobserved  $\frac{13}{2}^+$  level. It was found that the two values determined for the mixing matrix element were inconsistent with each other no matter what sign of  $R$  or value for  $x$  was chosen. This may be related to the anomalous energy of the  $\frac{17}{2}^+$  state discussed in §8.1.2.

### 8.2.3 $^{183}\text{Hg}$

There are too few experimental states known to facilitate an analysis of the type carried out for  $^{185}\text{Hg}$  and  $^{187}\text{Hg}$ . In view of the apparent differences observed between  $^{185}\text{Hg}$  and  $^{187}\text{Hg}$ , it would be of great interest to obtain further information on other excited states in both  $^{183}\text{Hg}$  and  $^{185}\text{Hg}$ .

## 8.3 Signs of the Deformations

In §8.2.1 the observed branching ratios in  $^{187}\text{Hg}$  could only be reproduced if the two rotational bands had the same sign of the quadrupole moment. The two-band mixing analysis by Guttormsen came to the same conclusion regarding analogous B(E2) ratios in the even-mass mercury isotopes [Gut81]. One assumption implicit in both calculations is that the two bands have *rotational* character, which leads to opposite sign for the phases of the E2 matrix elements for the intrinsic oblate and prolate shapes. A different approach was taken by Dickmann and Dietrich [Dic74]

Table 8.6: Comparison of experimental B(E2) branching ratios in  $^{188}\text{Hg}$  with theoretical predictions (adapted from Table II in Ref. [Col84])

Transitions	Two-band mixing <sup>a)</sup>			Bohr	Experimental results
	( $R > 0$ )	( $R < 0$ )	IBM <sup>b)</sup>	Hamiltonian <sup>c)</sup>	
$\frac{2_2^+ \rightarrow 2_1^+}{2_2^+ \rightarrow 0_1^+}$	43.0	10.1	87.2	54	$15 \pm 3$
$\frac{4_2^+ \rightarrow 2_2^+}{4_2^+ \rightarrow 2_1^+}$	77.6	6.5	15.2	16	$81 \pm 6$
$\frac{6_1^+ \rightarrow 4_2^+}{6_1^+ \rightarrow 4_1^+}$	2.5	28.3	0.8	0.6	$2.7 \pm 0.2$
$\frac{6_2^+ \rightarrow 4_2^+}{6_2^+ \rightarrow 4_1^+}$	0.88	0.0	1.8	2.9	$1.3 \pm 0.1$
$\frac{8_2^+ \rightarrow 6_2^+}{8_2^+ \rightarrow 6_1^+}$	69.6	5.0	34.0	85	$45 \pm 10$
$\sum \left( \frac{\text{expt} - \text{theory}}{\text{error}} \right)^2 / N$	22.4	3345.2	163.2	133.7	

<sup>a)</sup> Ref. [Gut81].

<sup>b)</sup> Ref. [Bar83].

<sup>c)</sup> Ref. [Lea78] quoted in Ref. [Col84].

who used the measured B(E2) for the  $2^+ \rightarrow 0^+$  transitions in  $^{184}\text{Hg}$  and  $^{186}\text{Hg}$  to estimate the E2 matrix elements for a ground state spherical vibrator. Assuming the same phase for the “spherical” vibrational band and the prolate rotational band, they could reproduce the measured B(E2) ratios in  $^{184}\text{Hg}$  and  $^{186}\text{Hg}$ . However, their assumption of a “spherical” vibrator for the ground state disagrees with potential energy surface and dynamical calculations [Dic73, Kol75] which predict the nuclear wavefunction to be well-localised in the prolate and oblate minima despite the low potential barrier between them.

Cole *et al.* [Col84] compare the experimental B(E2) ratios in  $^{188}\text{Hg}$  with various theoretical calculations, including an IBM2 calculation [Bar83] which considers two interacting bands with predominantly prolate deformations, one less deformed, and one more deformed. They also present the results of a calculation solving the Bohr Hamiltonian in a potential  $V(\beta, \gamma)$  which reproduces the observed state energies and has minima representing coexisting prolate and oblate shapes. In this case the bands representative of the two minima have opposite signs for the quadrupole moment. Examination of Table 8.6 (which is partly reproduced from Ref. [Col84]) reveals that while no theoretical calculation gives

complete agreement with the experimental  $B(E2)$  ratios in  $^{188}\text{Hg}$ , Guttormsen's mixing calculation with  $R > 0$  gives much better agreement with experiment than both the IBM2 and Bohr Hamiltonian results. Not only is the RMS deviation smaller than for any of the other calculations, it is also the only calculation which reproduces the current ranking in magnitude of the different  $B(E2)$  ratios.

The present analysis of the  $E2$  branching ratios in  $^{187}\text{Hg}$  reinforces the earlier suggestions by Guttormsen that there is an inconsistency in the assumption of well-defined prolate and oblate deformations in the mercury nuclei. For the even-mass isotopes, the Bohr Hamiltonian and the mixing calculations with  $R < 0$ , both of which assume what are expected to be the correct relative phases for the  $E2$  matrix elements, do not reproduce the experimental results as well as the mixing calculations which assume two rotational bands with the same sign of the quadrupole moment. In light of this, it may be appropriate to consider other possibilities, for example it is well known that these transitional nuclei have a tendency to be  $\gamma$ -soft. Indeed there are many potential energy surface calculations for nuclei in this region (see Refs. [Woo92, Hey83] and references therein), in which only a small triaxial barrier is present between the shape-coexisting minima. Recent calculations by Delaroche *et al.* have also emphasised the importance of the  $\gamma$ -degree of freedom in the mercury isotopes [Del94]. Furthermore, the collective structures associated with the “oblate” well are traditionally difficult to describe in transitional nuclei. Detailed experimental studies of the mercury isotopes in conjunction with theoretical work are needed to resolve this long-standing problem.

## 8.4 Prolate-Oblate Energy Differences

The previous section casts some doubt upon the by now traditional description of the coexisting shapes in the mercury nuclei as “prolate” and “oblate”. Nevertheless, the rest of this thesis will continue to call the states prolate and oblate for reasons of conciseness. This section will examine the prolate-oblate energy differences to see the effects of the odd-neutron.

Information on the prolate-oblate energy differences in the even-mass isotopes can be obtained in a number of ways. The simplest estimate is the energy difference between the two perturbed  $0^+$  states (if both are known), although a better estimate is given by the difference between the two *unperturbed* energies, as extracted from some form of band-mixing analysis [Dra94].

The unperturbed excitation energies of the prolate and oblate intrinsic states upon which the rotational bands in the odd-mass isotopes are based were fitted in §8.1. The paucity of known states in the oblate, decoupled band in  $^{185}\text{Hg}$  makes the deduced excitation energy for the oblate state less certain, however, the result for  $^{187}\text{Hg}$  is reliable. For  $^{183}\text{Hg}$  it was necessary to estimate the value of  $E_0(\beta^<)$  as described in §8.1.3. The  $E_0(\beta^>)$  parameter is well-determined in all three cases. The prolate-oblate energy differences deduced from the  $E_0$  parameters are compared with the even-mass results in Figure 8.5. (The even-mass results are unperturbed energy differences as obtained by Dracoulis [Dra94].) The approximate errors on the odd-mass results are derived from the estimates outlined in §8.1.1. Theoretical predictions of the prolate-oblate energy differences for the even-mass [Ben87] and odd-mass [Fra75] isotopes are also shown. The discrepancy with experiment is typically 200-400 keV.

The experimental even-mass results in Figure 8.5 lie close to a parabola, with the minimum occurring just above  $N=102$  as has been noted previously [Dra88, Dra94]. Varying only the constant in the parabolic fit gives the second curve for the odd-mass results, implying that the prolate well in the odd-mass isotopes is consistently lower than in the even-mass isotopes, at least for the  $i_{13/2}$  neutron states, by  $\sim 350$  keV.

Several explanations for this favouring of the prolate shape have been offered. For example, the  $\frac{1}{2}^- [521]$  orbital responsible for the ground state in  $^{183}\text{Hg}$  and  $^{185}\text{Hg}$  is steeply sloping with respect to the deformation, and can perhaps be expected to polarise the nucleus, favouring the prolate deformation [Kol75, Küh77]. However, in this mass region the Fermi level is near the middle of the  $i_{13/2}$  neutron shell where the  $i_{13/2}$  orbitals have small slopes with deformation. Despite this we still see a favouring of the prolate shape in the  $i_{13/2}$  neutron system. Also, the relative excitation energies of the quasineutron bands in  $^{185}\text{Hg}$  are known [Kil89], and are similar to those in the  $N=105$  isotones [Nes76, Nyb90], indicating that different orbitals are not particularly favoured in energy at the prolate shape. Clearly the odd neutron has a similar effect on the underlying potential energy surface independent of which orbital it occupies.

Dickmann and Dietrich investigate the coupling of the odd-neutron to the vibrations of the core, an effect which would lower the energy of the lowest states in both potential wells [Dic74]. While giving no numerical results, they do show that because the prolate minimum turns out to be shallow compared to the oblate minimum, the particle-vibration coupling can lower the prolate states more than



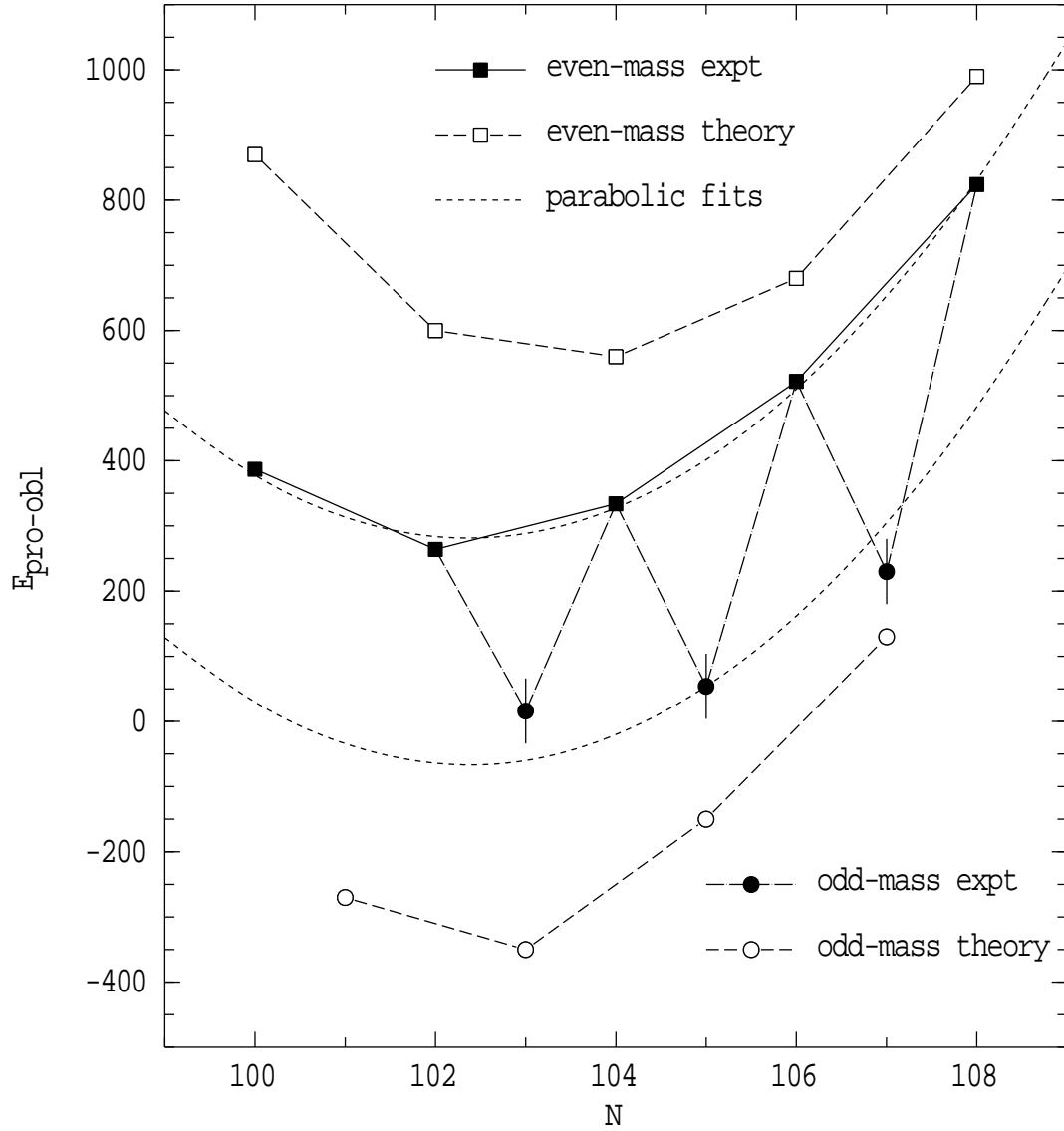


Figure 8.5: Prolate-oblate energy differences for the mercury isotopes with experimental results for the even and odd-mass isotopes taken from Ref. [Dra94] and the current work respectively. The theoretical values for even and odd-mass isotopes are taken from Refs. [Ben87] and [Fra75] respectively.

the oblate states, in qualitative agreement with experiment.

Yet another mechanism which could lower the prolate well in the odd-mass nuclei is blocking of the pairing correlations in the odd-neutron system [Dic74, Fra75, Wal89]. Around  $N=104$ , the level density of the neutron orbitals is larger for the weakly-deformed oblate shape than for the more-deformed prolate shape. Thus, there is a greater loss in pairing correlation energy due to blocking by the odd neutron at the oblate shape as compared to the prolate shape, and the energy of the prolate well is lowered relative to the oblate well in the odd-mass nucleus. Microscopically, this is really an “unfavouring” of the oblate shape rather than the experimental observation of a “favouring” of the prolate shape. Analogous staggering effects should perhaps be observed in other odd-mass nuclei where the even-even cores show a prolate-oblate shape coexistence. Obvious possibilities include extending the odd-mass mercury chain to  $^{181}\text{Hg}$ , as well as the light platinum and lead nuclei, with  $^{175}\text{Pt}$  and  $^{187}\text{Pb}$  being the best candidates. (Note that  $^{186}\text{Pb}$ , the core nucleus for  $^{187}\text{Pb}$ , is actually believed to exhibit a spherical-prolate shape coexistence [Bax93, Hee93].)

The mechanisms discussed here which could lower the energy of the prolate well are intimately related on a microscopic level, primarily through the pairing force. Detailed calculation of the pairing energy in the odd and even mass nuclei, including the effects of blocking, is likely to be instructive.

# Chapter 9

## Summary and Conclusions

This thesis has presented the results of spectroscopic studies of the neutron deficient odd-mass mercury and thallium nuclei,  $^{183}\text{Hg}$ ,  $^{185}\text{Tl}$  and  $^{187}\text{Tl}$ . The level schemes which were deduced for  $^{183}\text{Hg}$  and  $^{187}\text{Tl}$  are in partial agreement with parallel and independent studies reported during the course of this work [Rev94, Bin93, Shi95]. This chapter briefly summarises the experimental and theoretical results obtained, before commenting on the use of the odd nucleon as a structural probe, and finally presenting the conclusions.

### *Odd-Mass Thallium Isotopes:*

The three rotation-aligned bands observed in  $^{187}\text{Tl}$  have been assigned as  $i_{13/2}$ ,  $h_{9/2}$  and  $f_{7/2}$  protons coupled to prolate mercury cores. Similar bands due to  $i_{13/2}$ , and tentatively  $h_{9/2}$ , protons have been observed in  $^{185}\text{Tl}$ . Fragmentary rotational bands built upon the  $\frac{9}{2}^- [505]$  and  $\frac{13}{2}^+ [606]$  orbitals at oblate deformation have been observed in both nuclei. The configuration assignments are based upon expectations for the level structures and spins and parities, as well as measured properties such as the in-band branching ratios and aligned angular momenta. The  $\frac{13}{2}^+$  states due to the  $\frac{13}{2}^+ [606]$  intrinsic state were found to be isomeric, with measured meanlives of  $12 \pm 2$  and  $1.0 \pm 0.2$  ns in  $^{185}\text{Tl}$  and  $^{187}\text{Tl}$ . The M2 and E1 decay strengths for transitions decaying out of the isomeric states agree with expected values for the  $\pi i_{13/2} \rightarrow \pi h_{9/2}$  decay.

The excitation energies of the prolate deformed intrinsic states were estimated using a model to fit the decoupled band energies, while the excitation energies of the oblate deformed states, which give rise to deformation-aligned bands, were simply taken to be the energy of the bandhead. These experimental results were compared with the results of calculations of the intrinsic state energies and equilibrium deformations. Calculated microscopic proton configurations for the

different intrinsic states were also presented.

*Odd-Mass Mercury Isotopes:*

Two prolate-deformed bands due to the  $\frac{1}{2}^- [521]$  and  $\frac{7}{2}^- [514]$  orbitals have been observed in  $^{183}\text{Hg}$ . A signature split rotational band typical of a mixed  $i_{13/2}$  neutron band at prolate deformation was also observed, but with a pronounced perturbation at low spin interpreted as the decay into an oblate,  $\frac{13}{2}^+$  isomer. The configuration assignments are based upon similar arguments as those presented for the thallium isotopes above.

The shape coexistence seen in the  $i_{13/2}$  neutron systems for  $^{187}\text{Hg}$ ,  $^{185}\text{Hg}$  and  $^{183}\text{Hg}$  was investigated using a two-band mixing model to reproduce the state energies and E2 transition strengths. This allowed the deduction, albeit in a model-dependent fashion, of the inertial parameters and hence the magnitudes of the deformations, together with the mixing matrix elements between the prolate and oblate wells.

## 9.1 The Odd Nucleon as a Structural Probe

The deformed structures in the neutron-deficient mercury and thallium nuclei are believed to be formed from proton excitations across the shell gap into intruder orbitals which have strong slopes with deformation. The Fermi level for neutrons is near the middle of the shell, and intruder orbitals, in the sense of steeply sloping orbitals from a major shell once removed, are not expected to play a major role. Hence one might expect the addition of a neutron to the even-mass mercury nuclei to have less effect than the addition of a proton, the latter of which could conceivably block the orbitals which are responsible for driving the deformation.

In Chapter 8, it was shown that the only observable effect the odd neutron had on the core was to block the pairing correlations at prolate and oblate deformations by different amounts, and thus lower the excitation energy of the prolate states in the odd-mass isotopes.

The odd proton can have a more significant effect, as was proposed by Porquet *et al.* [Por91] in their study of  $^{189}\text{Tl}$ . They observed a rotational band due to the  $i_{13/2}$  proton at prolate deformation, but no analogous  $h_{9/2}$  proton band. This was interpreted to mean that the prolate mercury core nucleus had a large  $(\pi h_{9/2})^2$  component, and that Pauli blocking in  $^{189}\text{Tl}$  either forced the  $h_{9/2}$  band high in energy, or stopped the development of the prolate shape altogether. The current calculations predict a different scenario (in agreement with Ref. [Rev94]),

that there is a prolate  $h_{9/2}$  intrinsic state in  $^{189}\text{Tl}$ , but with a smaller deformation than the  $i_{13/2}$  intrinsic state. This would result in a band with a smaller moment-of-inertia whose states would be far from yrast and consequently difficult to observe. Also the calculations do predict well-deformed prolate intrinsic states due to the  $h_{9/2}$ ,  $i_{13/2}$  and  $f_{7/2}$  protons in the lighter thallium isotopes. Aligned rotational bands due to these states are seen in  $^{187}\text{Tl}$ , and also for the  $i_{13/2}$  (and tentatively  $h_{9/2}$ ) states in  $^{185}\text{Tl}$ . This shows that blocking of the different intruder orbitals in the lighter isotopes does not stop the formation of the well-deformed shape.

The effect of the blocking on the excitation energies can be determined by examination of the prolate-oblate energy differences, as deduced from the excitation energies of the prolate and oblate states. The energy difference determined from the  $i_{13/2}$  states is smaller than that obtained from the  $h_{9/2}$  states in both  $^{185}\text{Tl}$  and  $^{187}\text{Tl}$ . This agrees with the current theoretical predictions and perhaps indicates that, at the prolate shape, population of the  $h_{9/2}$  proton orbitals has a larger blocking effect than population of the  $i_{13/2}$  proton orbitals. This would imply the  $h_{9/2}$  proton is more important in stabilising the prolate shape, in agreement with the calculated occupation numbers for the different deformation driving orbitals.

The predictions of the calculations with regard to the occurrence of particular shapes in the odd-mass thallium nuclei appear to be correct, however, the details of the excitation energies are still imprecise, with the discrepancy between theory and experiment typically 500 keV. Also, it is found experimentally that the oblate,  $\frac{9}{2}^- [505]$  and  $\frac{13}{2}^+ [606]$  states minimise in excitation energy at different neutron numbers, contrary to the theoretical predictions of common minima at  $N = 106$ . The experimental information for the excitation energy of the prolate states is more limited, however, it does appear that the drop in energy with neutron number is overpredicted by the current calculations, with a possible theoretical minimum not appearing until  $N \approx 100$ , in contrast with the experimental trend which shows a possible minimum around  $N \approx 102 - 104$ . Further experimental information on  $^{183}\text{Tl}$  is needed before any firm conclusions can be drawn.

It is now appropriate to look at the usefulness of the odd proton as a probe of the nuclear structure. This is done by way of a couple of examples. It is arguable that the occurrence of prolate aligned bands due to the  $h_{9/2}$ ,  $f_{7/2}$  and  $i_{13/2}$  protons in  $^{187}\text{Tl}$  is an indication that blocking of single intruder orbitals does not inhibit the development of the prolate shape. Thus the core configuration must consist of excitations into a number of intruder orbitals. However, Porquet

*et al.* used the opposite argument to deduce a simpler  $(\pi h_{9/2})^2$  configuration for  $^{189}\text{Tl}$ . It is also possible that the smaller prolate-oblate energy difference for the  $i_{13/2}$  proton states compared to the  $h_{9/2}$  states in  $^{187}\text{Tl}$  and  $^{185}\text{Tl}$  is a blocking effect showing that the  $h_{9/2}$  proton makes up a larger component of the prolate core configuration than the  $i_{13/2}$  proton. However, the difference could also be due to the  $i_{13/2}$  and  $h_{9/2}$  protons driving the nucleus to different deformations and thus affecting the relative excitation energies of the prolate and oblate states.

What conclusion can be reached from this? The answer is that by themselves the effects of the odd proton can only give hints regarding the nature of the microscopic configuration of the core nuclei. It is in conjunction with theory that studies of the odd-mass nuclei gain their potency. The availability of various orbitals for the odd proton to occupy results in a broad range of possible intrinsic structures for the nucleus. This is in contrast to the even-mass nuclei where only the  $K = 0$  bands are observed at low excitation energy. The important point is that the odd-mass isotopes provide a stringent test of theory because the theory must reproduce the deformations and excitation energies of *a range of different states*. The predictions of a theory which is able to do this can be viewed with a fair degree of confidence.

## 9.2 Conclusions

The present work has shown that experimental studies of odd-mass nuclei are useful probes of the nuclear structure when undertaken in conjunction with theoretical calculations of the equilibrium deformations and excitation energies of the intrinsic states. In the odd-mass thallium isotopes,  $^{185}\text{Tl}$  and  $^{187}\text{Tl}$ , prolate and oblate rotational bands due to a range of different intruder orbitals have been identified. The behaviour of the deformations of the intrinsic states for the range of odd-mass thallium isotopes down to  $^{185}\text{Tl}$  are reproduced by theory, as is the general behaviour of the excitation energies of the intrinsic states with respect to the neutron number. In contrast, the fine details such as the excitation energies and the particular neutron number at which a state minimises in energy, tend to be less well reproduced. The overall agreement however, is enough to lend weight to the theoretical prediction that the prolate deformation in this region is caused predominantly by the excitation of four protons across the closed proton shell into strongly sloping intruder orbitals, especially the  $\frac{1}{2}^- [541]$  orbital from the  $h_{9/2}$  shell.

The present study of the odd-mass mercury nucleus,  $^{183}\text{Hg}$ , has observed rotational bands similar in character to the heavier isotope,  $^{185}\text{Hg}$ . Band-mixing fits to excitation energies of states in the coexisting  $i_{13/2}$  neutron bands in  $^{183}\text{Hg}$ ,  $^{185}\text{Hg}$  and  $^{187}\text{Hg}$ , yield results which are consistent with a coexistence between two bands of different deformation. The deduced value of the mixing matrix element is well determined in the case of  $^{187}\text{Hg}$ , and is in agreement with the values previously deduced for the even-mass isotopes. The results for  $^{185}\text{Hg}$  are more problematic as fewer states are known in the decoupled band built upon the  $\frac{13}{2}^+$  isomer, while only one state is known in that band for  $^{183}\text{Hg}$ .

The prolate-oblate energy differences deduced from the band-mixing fits show an odd-even staggering of  $\sim 350$  keV. This is probably due to the odd-neutron blocking the pairing correlations by different amounts at prolate and oblate deformation and highlights the need for a proper treatment of pairing if one is to obtain accurate calculations of potential energy surfaces.

The analysis of the B(E2) ratios for transitions within and between the coexisting  $i_{13/2}$  bands in  $^{187}\text{Hg}$  has shown that there is an inconsistency with the assumption of rotational bands built upon prolate and oblate shape. The results are in agreement with a previous analysis for the even-mass mercury isotopes which suggested that the coexisting bands have the same sign of the deformation [Gut81]. This seems to be at odds with the many potential energy surface calculations which almost universally predict a coexistence between prolate and oblate shapes. It is worthwhile noting that the “oblate” states are traditionally difficult to describe in transitional nuclei like the mercury isotopes. The shallow barrier between the coexisting minima and small oblate deformations may mean that triaxiality and shape fluctuations are required to explain the results. This point certainly merits continued experimental and theoretical study.

In summary, the present work has provided substantial insight into the nature of the microscopic configurations which govern the development and stability of the deformed shapes in these near closed shell nuclei. It has also reemphasised that there are aspects of the shape coexistence which are not understood, such as the behaviour of the B(E2) ratios in the mercury isotopes. Future experimental work which would be of benefit includes identification of the deformed rotational bands in  $^{183}\text{Tl}$  so as to provide further stringent tests of theory, and more detailed studies of both  $^{183}\text{Hg}$  and  $^{185}\text{Hg}$  so as to identify more states in the band-crossing region. This may help in resolving the problem with the B(E2) ratios and also determine the true nature of the “oblate” shape.

# Appendix A

## In-band Decay Properties

In a strongly coupled, or deformation-aligned, rotational band, the observed crossover/cascade branching ratios,  $\lambda = \frac{I_\gamma(\Delta I=2)}{I_\gamma(\Delta I=1)}$ , contain information about the intrinsic state upon which the band is built. In particular, the gyromagnetic and cascade mixing ratios can be obtained from the rotational formulae

$$\frac{1}{\delta^2} = \frac{1}{\lambda} \left[ \frac{E_\gamma(I \rightarrow I-2)}{E_\gamma(I \rightarrow I-1)} \right]^5 \frac{\langle IK20 | I-2K \rangle^2}{\langle IK20 | I-1K \rangle^2} - 1, \quad (\text{A.1})$$

$$\frac{g_K - g_R}{Q_0} \left[ 1 + \delta_{K, \frac{1}{2}} (-1)^{I+1/2} b_0 \right] = \frac{1}{\delta} \frac{0.933 E_\gamma(I \rightarrow I-1)}{\sqrt{I^2 - 1}} \quad (\text{A.2})$$

$$b_0 = \frac{1}{g_K - g_R} \left[ a(g_R - g_l) - \frac{1}{2} (-1)^l (g_s - 2g_l + g_K) \right] \quad (\text{A.3})$$

where  $E_\gamma$  is in units of MeV,  $Q_0$  is in units of eb,  $a$  is the decoupling parameter for  $K = \frac{1}{2}$  bands and  $g_s$  and  $g_l$  are the spin and orbital g-factors. Note that the sign of the mixing ratio for the M1/E2 cascade transitions can not be determined from equation (A.1) and must be either assumed or deduced from other means, usually angular distribution or correlation measurements. (Note also that the current work assumes the phase convention of Yamazaki for the mixing ratio [Yam67]. A minus sign must be included in equation (A.2) if the opposite phase convention is used.)

The theoretical  $g$ -factor for an intrinsic state is given by

$$g_K = g_l + \frac{g_s - g_l}{K} \langle s_3 \rangle \quad (\text{A.4})$$

where  $\langle s_3 \rangle$ , the projection of the particle spin on the symmetry axis, can be calculated using



$$\begin{aligned}
\langle s_3 \rangle = \sum_l \left( \frac{K}{2l+1} \left( (C_{j=l+\frac{1}{2}l}^K)^2 - (C_{j=l-\frac{1}{2}l}^K)^2 \right) \right. \\
\left. - C_{j=l+\frac{1}{2}l}^K C_{j=l-\frac{1}{2}l}^K \sqrt{1 - \left( \frac{2K}{2l+1} \right)^2} \right) \quad (\text{A.5})
\end{aligned}$$

The  $C_{jl}^K$  coefficients are those obtained from the Nilsson expansion given in equation (2.17).

The spin g-factors,  $g_s$ , are usually taken to be between 0.6 and 0.7 of the free space values. The values of  $g_s$  and  $g_l$  used in this thesis are

$$\begin{aligned}
\pi : \quad g_l = 1 \quad g_s = 0.7 \times 5.59 = 3.91 \\
\nu : \quad g_l = 0 \quad g_s = 0.7 \times -3.83 = -2.68
\end{aligned}$$

# Appendix B

## Band-mixing

This appendix provides details of a simple two-band mixing model [Dra88a, Bar91, Dra94] used to describe the state energies and E2 transition strengths for rotational bands. The first section outlines the modified Variable-Moment-of-Inertia (VMI) model used to describe the unperturbed rotational band energies in the current work. The second section looks at two-state mixing, and the final section shows how the B(E2) strengths for inter- and intra-band transitions are calculated using the mixed wavefunctions and the rotational model.

### B.1 VMI Model for the State Energies

Within the VMI model [Mar69], the state energies in a rotational band,  $E_I$ , are described by two parameters,  $\mathfrak{I}_0$  and  $C$ , with

$$E_I = E_0 + \frac{1}{2}C(\mathfrak{I}_I - \mathfrak{I}_0)^2 + \frac{I(I+1)}{2\mathfrak{I}_I} \quad (\text{B.1})$$

The moment-of-inertia at spin  $I$ , denoted  $\mathfrak{I}_I$ , is defined by the equilibrium condition  $\frac{\partial E_I}{\partial \mathfrak{I}_I} = 0$ .

To allow for the possibilities of non-zero  $K$  and alignment,  $i_x$ , the VMI model may be extended by replacing  $I(I+1)$  with the core angular momentum  $R(R+1)$ , with  $R$  defined by,

$$R \approx \sqrt{(I + \frac{1}{2})^2 - K^2 - i_x} - \frac{1}{2} \quad (\text{B.2})$$

Signature splitting is introduced phenomenologically by defining the parameter,  $a_{sig}$ , with

$$\begin{aligned}
R(R+1) = & \left(I + \frac{1}{2}\right)^2 - K^2 + i_x^2 - \frac{1}{4} \\
& - 2i_x \sqrt{\left(I + \frac{1}{2}\right)^2 - K^2} \left(1 - (-1)^{I+\frac{1}{2}} a_{sig}\right)
\end{aligned} \tag{B.3}$$

Different bands may have various values for  $C, \mathfrak{S}_0, K, i_x, a_{sig}$  and  $E_0$ , allowing for the modelling of coexistence between bands based upon different deformations, or with different alignments,  $K$ -values or signature splitting. Taking two rotational bands with unperturbed energies given by VMI expressions with different values for  $C, \mathfrak{S}_0, K, i_x, a_{sig}$  and  $E_0$ , the perturbed (observed) energies are calculated assuming a spin-independent interaction,  $V$ , between states in the unperturbed bands with the same spin<sup>1</sup>. The values of those parameters for each band which are not constrained by theory or experiment, are varied to obtain the best possible fit to the observed state energies. An empirical estimate of the quadrupole moments of the unperturbed bands can be found using [Mar69],

$$Q_0 \approx k\sqrt{\mathfrak{S}_0} \tag{B.4}$$

with the constant  $k = 45$  [eb][keV<sup>1/2</sup>] chosen to reproduce quadrupole moments in the A=170 mass region [Dra88a]. (Equation (B.4) is another way of writing the empirical rule, due to Grodzins [Gro62], expressing the proportionality between  $B(E2, 2^+ \rightarrow 0^+)$  and  $E(2^+)$  in even-even nuclei.) With this estimate of the quadrupole moment the approximate deformation can then be deduced using [Löb70]

$$\beta_2 \approx 91.7 Q_0 / (ZA^{2/3}) \tag{B.5}$$

Note that this only allows an estimate of the magnitude of the deformation.

## B.2 Two-State Mixing

Consider the levels shown in Figure B.1 where the unperturbed states with wavefunctions  $\phi$  and  $\psi$ , and energies  $e_1$  and  $e_2$ , correspond to eigenfunctions of the Hamiltonian  $H_0$ . The perturbed states have wavefunctions,  $\chi_i$ , and energies,  $E_i$ ,

---

<sup>1</sup>The details of the two-state mixing are presented in the next section. Mixing between three or more bands involves using a larger dimensional energy matrix and different mixing matrix elements,  $V_{if}$ , for each combination of unperturbed bands  $i$  and  $f$ .

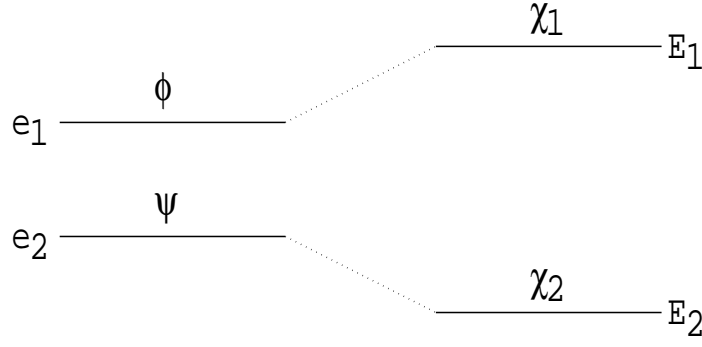


Figure B.1: Simple situation where two unperturbed levels (on the left) mix via an interaction giving rise to the perturbed levels (on the right).

and correspond to eigenfunctions of the Hamiltonian  $H_0 + H_{int}$ , where  $H_{int}$  is an interaction term defined by the mixing matrix elements

$$\langle \phi | H_{int} | \psi \rangle = \langle \psi | H_{int} | \phi \rangle = V \quad (\text{B.6})$$

The mixed wavefunctions  $\chi_i$  are linear expansions of the unperturbed basis functions,

$$\chi_i = a_i \phi + b_i \psi \quad (\text{B.7})$$

The Hamiltonian energy equation is

$$(H_0 + H_{int}) |\chi_i\rangle = E_i |\chi_i\rangle \quad (\text{B.8})$$

which, upon substituting for  $\chi_i$ , reduces to the matrix equation

$$\begin{pmatrix} e_1 - E_i & V \\ V & e_2 - E_i \end{pmatrix} \begin{pmatrix} a_i \\ b_i \end{pmatrix} = \mathbf{0} \quad (\text{B.9})$$

A solution can only be obtained if the determinant of the  $2 \times 2$  matrix vanishes, and hence the energies of the perturbed states are

$$\begin{aligned} E_1(+) &= \frac{e_1 + e_2}{2} \pm \frac{\sqrt{(e_1 - e_2)^2 + 4V^2}}{2} \\ E_2(-) & \end{aligned} \quad (\text{B.10})$$

From equation (B.9) the ratio of the coefficients  $a_i/b_i$  is given by

$$\frac{a_i}{b_i} = \frac{V}{E_i - e_1} \quad (\text{B.11})$$

A concise representation of the wave-functions is obtained by defining a parameter  $\beta$  by [Dav76]

$$\tan 2\beta = \frac{2V}{e_1 - e_2} \quad (\text{B.12})$$

Generality in the two state case is maintained with the choice  $e_1 > e_2$  and  $V > 0$ , so that  $2\beta \in [0, \frac{\pi}{2}]$  and simple trigonometry may be used to obtain expressions for  $\sin 2\beta$  and  $\cos 2\beta$ . Substitution of (B.10) into (B.11), together with use of the identities,

$$\cot \beta = \frac{\sin 2\beta}{1 - \cos 2\beta} \quad \tan \beta = \frac{\sin 2\beta}{1 + \cos 2\beta} \quad (\text{B.13})$$

gives the result

$$\frac{a_1}{b_1} = \cot \beta = \frac{\cos \beta}{\sin \beta} \quad \frac{a_2}{b_2} = -\tan \beta = \frac{-\sin \beta}{\cos \beta} \quad (\text{B.14})$$

From equations (B.7) and (B.14) the wavefunctions for the perturbed states are

$$\chi_1 = (\cos \beta) \phi + (\sin \beta) \psi \quad (\text{B.15})$$

$$\chi_2 = (-\sin \beta) \phi + (\cos \beta) \psi \quad (\text{B.16})$$

Note that the wavefunction for the higher energy state has both components in phase, while the lower energy state has the two components with opposite phase. This follows unambiguously from equation (B.11) if  $e_1 > e_2$  and  $V > 0$ .

The parameter  $\beta \rightarrow 0$  as either  $V \rightarrow 0$  or when  $e_1 \gg e_2$  and then the perturbed wavefunctions reduce to their unperturbed values. Fully mixed wavefunctions with  $\beta = \frac{\pi}{4}$  occur when either  $e_1 = e_2$  or  $V \gg e_1 - e_2$ . Note that the perturbed levels may never be closer than  $2V$  (see equation (B.10)), so that an upper limit for the interaction strength can be obtained directly from the observed level energies, although this is only true in the case of two-state mixing.

If the perturbed energies and the interaction matrix element are known, it is simple to determine the energies of the unperturbed states by rearranging equation (B.10). For reference purposes, the result is

$$\begin{matrix} e_1(+) \\ e_2(-) \end{matrix} = \frac{E_1 + E_2}{2} \pm \frac{\sqrt{(E_1 - E_2)^2 - 4V^2}}{2} \quad (\text{B.17})$$

Methods of determining the interaction matrix element experimentally include performing a band-mixing fit to the level energies, as described in the previous section, or through an analysis of the measured transition strengths for intra- and inter-band transitions, as described in the next section.

### B.3 Calculating B(E2) Strengths

Consider unperturbed rotational bands as shown in Figure B.2a, where states with the same spins and parities mix via a spin-independent interaction,  $V$ . The perturbed states have energies  $E_1, E_2, E_3$  and  $E_4$ , and (mixed) wave functions as

$$\begin{array}{c}
 \text{(a)} \\
 \begin{array}{c}
 \text{E}_1 \quad \frac{(\cos x) \phi_I + (\sin x) \psi_I}{\phantom{E_1}} \\
 \text{E}_2 \quad \frac{(-\sin x) \phi_I + (\cos x) \psi_I}{\phantom{E_2}} \\
 \begin{array}{c}
 \psi_I \quad \frac{\phi_I}{\phantom{\psi_I}} \\
 \hline
 \psi_{I-2} \quad \frac{\phi_{I-2}}{\phantom{\psi_{I-2}}}
 \end{array} \\
 \text{E}_3 \quad \frac{(\sin y) \phi_{I-2} + (\cos y) \psi_{I-2}}{\phantom{E_3}} \\
 \text{E}_4 \quad \frac{(\cos y) \phi_{I-2} + (-\sin y) \psi_{I-2}}{\phantom{E_4}}
 \end{array}
 \end{array}$$

$$\begin{array}{c}
 \text{(b)} \\
 \begin{array}{c}
 \text{E}_1 \quad \frac{(\cos x) \phi_I + (\sin x) \psi_I}{\phantom{E_1}} \\
 \text{E}_2 \quad \frac{(-\sin x) \phi_I + (\cos x) \psi_I}{\phantom{E_2}} \\
 \begin{array}{c}
 \psi_I \quad \frac{\phi_I}{\phantom{\psi_I}} \\
 \hline
 \psi_{I-2} \quad \frac{\phi_{I-2}}{\phantom{\psi_{I-2}}}
 \end{array} \\
 \text{E}_3 \quad \frac{(-\sin y) \phi_{I-2} + (\cos y) \psi_{I-2}}{\phantom{E_3}} \\
 \text{E}_4 \quad \frac{(\cos y) \phi_{I-2} + (\sin y) \psi_{I-2}}{\phantom{E_4}}
 \end{array}
 \end{array}$$

Figure B.2: Schematic picture of the mixing of two rotational bands showing the unperturbed states and wavefunctions in the middle and the perturbed states and wavefunctions on the outside. Two different arrangements of the unperturbed states are possible, labelled (a) and (b). (Note that the unperturbed states are drawn to a smaller scale than the perturbed states.)

shown, with  $x$  and  $y$  defined by,

$$\tan 2x = \frac{2V}{\sqrt{(E_1 - E_2)^2 - (2V)^2}} \quad (\text{B.18})$$

$$\tan 2y = \frac{2V}{\sqrt{(E_3 - E_4)^2 - (2V)^2}} \quad (\text{B.19})$$

Equations (B.18) and (B.19) are obtained by substitution of equation (B.17) into (B.12), together with an appropriate change of symbols for the energies and mixing parameters. The present analysis is similar to that of Ref. [Bec87], however, there are differences in both the choice of wavefunctions and the expressions for  $x$  and  $y$ . The present work also allows for the possibility of different intrinsic structures for the two bands. Such an extension is well known, for example see Ref. [Jen91] which uses a different formalism<sup>2</sup>. Assuming that the cross-term  $\langle \phi | \mathcal{M}(E2) | \psi \rangle = 0$ , and using the well known expressions [Boh75]

$$B(E2; \phi_I \rightarrow \phi_{I-2}) = \frac{1}{2I+1} |\langle K_\phi I - 2 | \mathcal{M}(E2) | K_\phi I \rangle|^2 \quad (\text{B.20})$$

and

$$\langle K_\phi I - 2 | \mathcal{M}(E2) | K_\phi I \rangle = \sqrt{2I+1} \langle IK_\phi 20 | I - 2K_\phi \rangle \sqrt{\frac{5}{16\pi}} eQ_\phi \quad (\text{B.21})$$

it is simple to evaluate the  $B(E2)$  for transitions between the mixed states. For transitions from  $E_1$  to  $E_3$  and from  $E_1$  to  $E_4$  the results are

$$\begin{aligned} B(E2; 1 \rightarrow 3) &= \frac{5}{16\pi} e^2 [\cos x \sin y \langle IK_\phi 20 | I - 2K_\phi \rangle Q_\phi \\ &\quad + \sin x \cos y \langle IK_\psi 20 | I - 2K_\psi \rangle Q_\psi]^2 \end{aligned} \quad (\text{B.22})$$

$$\begin{aligned} B(E2; 1 \rightarrow 4) &= \frac{5}{16\pi} e^2 [\cos x \cos y \langle IK_\phi 20 | I - 2K_\phi \rangle Q_\phi \\ &\quad - \sin x \sin y \langle IK_\psi 20 | I - 2K_\psi \rangle Q_\psi]^2 \end{aligned} \quad (\text{B.23})$$

After defining the quantity  $R$  by

---

<sup>2</sup>Note that Jensen *et al.* [Jen91] take the upper energy state at each spin to have the wavefunction components out of phase. The previous section showed that in the current work the lower energy state has the two components out of phase. Since Jensen *et al.* make the same assumption for all sets of mixed levels, the phases cancel and their expressions for the  $B(E2)$  ratios are identical to the current work after a suitable substitution of parameters.

$$R = \frac{\langle IK_\psi 20 | I - 2K_\psi \rangle Q_\psi}{\langle IK_\phi 20 | I - 2K_\phi \rangle Q_\phi} \quad (\text{B.24})$$

the ratio of the B(E2) values for the decay out of the state with energy  $E_1$  is

$$\frac{B(E2; 1 \rightarrow 3)}{B(E2; 1 \rightarrow 4)} = \left( \frac{\cos x \sin y + R \sin x \cos y}{\cos x \cos y - R \sin x \sin y} \right)^2 \quad (\text{B.25})$$

Similarly, for the decays out of the state with energy  $E_2$  the result is

$$\frac{B(E2; 2 \rightarrow 4)}{B(E2; 2 \rightarrow 3)} = \left( \frac{\cos x \sin y + \frac{1}{R} \sin x \cos y}{\cos x \cos y - \frac{1}{R} \sin x \sin y} \right)^2 \quad (\text{B.26})$$

It is also possible that the unperturbed states are in the alternative arrangement shown in Figure B.2b. For this second interleaved arrangement the B(E2) ratios are

$$\frac{B(E2; 1 \rightarrow 3)}{B(E2; 1 \rightarrow 4)} = \left( \frac{\cos x \sin y - R \sin x \cos y}{\cos x \cos y + R \sin x \sin y} \right)^2 \quad (\text{B.27})$$

$$\frac{B(E2; 2 \rightarrow 4)}{B(E2; 2 \rightarrow 3)} = \left( \frac{\cos x \sin y - \frac{1}{R} \sin x \cos y}{\cos x \cos y + \frac{1}{R} \sin x \sin y} \right)^2 \quad (\text{B.28})$$

Inspection reveals that, except for the signs, these equations are identical to the equations (B.25) and (B.26) which were obtained for the first arrangement of states shown in Figure B.2a.

The arrangement of the unperturbed states is not generally discernible just from observation of the perturbed levels. However, equations (B.25) to (B.28) show that the two arrangements do give different results for the B(E2) ratios. The problem is that in constructing a level scheme the decision as to which state lies in which band is often purely subjective, and is usually based upon the fact that there are strong transitions connecting levels. Because the strengths of the transitions are affected by the mixing this can create a confusing circular argument. In the shape coexistence situation of the mercury isotopes however, the unperturbed bands have quite different moments-of-inertia and the band-crossing region is localised in spin. Hence it is possible to extrapolate to where the unperturbed states would be using the states far from the crossing region which are not mixed. Knowing the arrangement of states, and the experimental B(E2) ratios and excitation energies, it is possible to solve for the interaction strength between the states.



# Bibliography

- [Åbe90] S. Åberg, H. Flocard and W. Nazarewicz, *Ann. Rev. Nucl. Part. Sci.* **40** (1990) 439.
- [Aud93] G. Audi and A.H. Wapstra, *Nucl. Phys.* **A565** (1993) 1.
- [Bal93] D.L. Balabanski, R.M. Lieder, T. Kutsarova, W. Gast, G. Hebbinghaus, A. Krämer-Flecken, T. Rzaca-Urban, H. Schnare, W. Urban, G. Sletten, K.H. Maier and K.O. Zell, *Nucl. Phys.* **A563** (1993) 129.
- [Bar83] A.F. Barfield, B.R. Barrett, K.A. Sage and P.D. Duval, *Z. Phys.* **A311** (1983) 205.
- [Bar91] R.A. Bark, *J. Phys.* **G17** (1991) 1209.
- [Bar94] R.A. Bark, computer code BANDMIX, unpublished.
- [Bas80] R. Bass, *Nuclear reactions with heavy ions*, (Springer-Verlag, Berlin, 1980) p365.
- [Bax93] A.M. Baxter, A.P. Byrne, G.D. Dracoulis, R.V.F. Janssens, I.G. Bearden, R.G. Henry, D. Nisius, C.N. Davids, T.L. Khoo, T. Lauritsen, H. Penttillä, D.J. Henderson and M.P. Carpenter, *Phys. Rev.* **C48** (1993) R2140.
- [Bea94] I.G. Bearden, R.V.F. Janssens, M.P. Carpenter, E.F. Moore, I. Ahmad, P.J. Daly, R. Mayer, M.W. Drigert, P.B. Fernandez, B. Fornal, U. Garg, Z.W. Grabowski, T.L. Khoo, T. Lauritsen, W. Reviol and D. Ye, *Nucl. Phys.* **A576** (1994) 441.
- [Bec87] E.M. Beck, J.C. Bacelar, M.A. Delaplanque, R.M. Diamond, F.S. Stephens, J.E. Draper, B. Herskind, A. Holm, P.O. Tjom, *Nucl. Phys.* **A464** (1987) 472.

- [Ben79] R. Bengtsson and S. Frauendorf, Nucl. Phys. **A314** (1979) 27; R. Bengtsson and S. Frauendorf, Nucl. Phys. **A327** (1979) 139.
- [Ben85] T. Bengtsson and I. Ragnarsson, Nuc. Phys. **A436** (1985) 14.
- [Ben87] R. Bengtsson, T. Bengtsson, J. Dudek, G. Leander, W. Nazarewicz and J.-Y. Zhang, Phys. Lett. **B183** (1987) 1.
- [Ben89] R. Bengtsson and W. Nazarewicz, Z. Phys. **A334** (1989) 269.
- [Ben89a] R. Bengtsson, J. Dudek, W. Nazarewicz and P. Olanders, Phys. Scr. **39** (1989) 196.
- [Ben89b] L. Bennour, P-H. Heenen, P. Bonche, J. Dobaczewski and H. Flocard, Phys. Rev. **C40** (1989) 2834.
- [Beu74] H. Beuscher, W.F. Davidson, R.M. Lieder, A. Neskakis and C. Mayer-Böricke, Phys. Rev. Lett. **32** (1974) 843.
- [Bin93] K.S. Bindra, A.V. Ramaya, W.C. Ma, B.R.S. Babu, J.H. Hamilton, L. Chaturvedi, J. Kormicki, R.V.F. Janssens, C.N. Davids, I. Ahmad, I.G. Bearden, M.P. Carpenter, W. Chung, D. Henderson, R.G. Henry, T.L. Khoo, T. Lauritsen, Y. Liang, H. Penttilä, F. Soramel, C. Baktash, W. Nazarewicz and J.A. Sheikh, Phys. Lett. **B318** (1993) 41.
- [Bin94] K.S. Bindra, P.F. Hua, B.R.S. Babu, C. Baktash, J. Barreto, D.M. Cullen, C.N. Davids, J.K. Deng, J.D. Garrett, M.L. Halbert, J.H. Hamilton, N.R. Johnson, A. Kirov, J. Kormicki, I.Y. Lee, W.C. Ma, F.K. McGowan, A.V. Ramaya, D.G. Sarantites, F. Soramel and D. Winchell, Phys. Rev. **C51** (1995) 401.
- [Boh75] A. Bohr and B.R. Mottelson, *Nuclear Structure*, Vol. II, (W.A. Benjamin, 1975)
- [Bon72] J. Bonn, G. Huber, H.-J. Kluge, L. Kugler and E.W. Otten, Phys. Lett. **B38** (1972) 308.
- [Bon76] J. Bonn, G. Huber, H.-J. Kluge and E.W. Otten, Z. Phys. **A276** (1976) 203.
- [Bou85] J.A. Bounds, C.R. Bingham, P. Juncar, H.K. Carter, G.A. Leander, R.L. Mlekodaj, E.H. Spejewski and W.M. Fairbank, Phys. Rev. Lett. **55** (1985) 2269; and Phys. Rev. **C36** (1987) 2560.

- [Bra72] M. Brack, J. Damgaard, A.S. Jensen, H.C. Pauli, V.M. Strutinsky and C.Y. Wong, *Rev. Mod. Phys.* **44** (1972) 320.
- [Byr85] A.P. Byrne and G.D. Dracoulis, *Nucl. Instr. and Meth. in Phys. Res.* **A234** (1985) 281.
- [Byr93] A.P. Byrne, H.M. Stodart, G.D. Dracoulis, G.J. Lane, T. Kibédi and A.E. Stuchbery, ANU annual report (1993), ANU-P/1145, to be published.
- [Car90] M.P. Carpenter, C.R. Bingham, L.H. Courtney, V.P. Janzen, A.J. Larabee, Z.-M. Liu, L.L. Riedinger, W. Schmitz, R. Bengtsson, T. Bengtsson, W. Nazarewicz, J.-Y. Zhang, J.K. Johansson, D.G. Popescu, J.C. Waddington, C. Baktash, M.L. Halbert, N.R. Johnson, I.Y. Lee, Y.S. Schutz, J. Nyberg, A. Johnson, R. Wyss, J. Dubuc, G. Kajrys, S. Monaro, S. Pilotte, K. Honkanen, D.G. Sarantites and D.R. Haenni, *Nucl. Phys.* **A513** (1990) 125.
- [Chi66] B.E. Chi, *Nucl. Phys.* **83** (1966) 97.
- [Coe85] E. Coenen, K. Deneffe, M. Huyse, P. van Duppen and J.L. Wood, *Phys. Rev. Lett.* **54** (1985) 1783.
- [Col76] J.D. Cole, J.H. Hamilton, A.V. Ramayya, W.G. Nettles, H. Kawakami, E.H. Spejewski, M.A. Ijaz, K.S. Toth, E.L. Robinson, K.S.R. Sastry, J. Lin, F.T. Avignone, W.H. Brantley and P.V.G. Rao, *Phys. Rev. Lett.* **37** (1976) 1185.
- [Col84] J.D. Cole, J.H. Hamilton, A.V. Ramayya, W. Lourens, B. van Nooijen, H. Kawakami, L.A. Mink, E.H. Spejewski, H.K. Carter, R.L. Mleko-daj, G.A. Leander, L.L. Riedinger, C.R. Bingham, E.F. Zganjar, J.L. Wood, R.W. Fink, K.S. Toth, B.D. Kern and S.R. Sastry, *Phys. Rev.* **C30** (1984) 1267.
- [Dab79] P. Dabkiewicz, F. Buchinger, H. Fischer, H.-J. Kluge, H. Kremmling, T. Kuhl, A.C. Muller and H.A. Schuessler, *Phys. Lett.* **B82** (1979) 199.
- [Dav89] C.N. Davids and J.D. Larson, *Nucl. Instr. and Meth. in Phys. Res.* **B40/41** (1989) 1224.

- [Dav90] P.M. Davidson, MSc thesis, Auckland University, (unpublished, 1990)
- [Dav92] C.N. Davids, B.B. Back, K. Bindra, D.J. Henderson, W. Kutschera, T. Lauritsen, Y. Nagame, P. Sugathan, A.V. Ramayya and W.B. Walters, Nucl. Instr. and Meth. in Phys. Res. **B70** (1992) 358.
- [Dav76] A.S. Davydov, *Quantum Mechanics*, (Pergamon, Oxford, 1976) 191.
- [Dic73] F. Dickmann and K. Dietrich Z. Phys. **263** (1973) 211.
- [Dic74] F. Dickmann and K. Dietrich Z. Phys. **271** (1974) 417.
- [Del94] J.P. Delaroche, M. Girod, G. Bastin, I. Deloncle, F. Hannachi, J. Libert, M.G. Porquet, C. Bourgeois, D. Hojman, P. Kilcher, A. Korichi, F. Le Blanc, N. Perrin, B. Roussière, J. Sauvage and H. Sergolle, Phys. Rev. **C50** (1994) 2332.
- [Dra83] G.D. Dracoulis, C. Fahlander and A.P. Byrne, Nucl. Phys. **A401** (1983) 490.
- [Dra88] G.D. Dracoulis, A.E. Stuchbery, A.O. Macchiavelli, C.W. Beausang, J. Burde, M.A. Deleplanque, R.M. Diamond and F.S. Stephens, Phys. Lett. **B208** (1988) 365.
- [Dra88a] G.D. Dracoulis, R.A. Bark, A.E. Stuchbery, A.P. Byrne, A.M. Baxter and F. Riess, Nucl. Phys. **A486** (1988) 414.
- [Dra93] G.D. Dracoulis, in *Proc. of Int. Conf. on the Future of Nuclear Spectroscopy*, 1993, Crete, (National Technical University Press, Athens)
- [Dra94] G.D. Dracoulis, Phys. Rev. **C49** (1994) 3324.
- [Dup84] P. Van Duppen, E. Coenen, K. Deneffe, M. Huyse, K. Heyde and P. Van Isacker, Phys. Rev. Lett. **52** (1984) 1974.
- [Dup85] P. Van Duppen, E. Coenen, K. Deneffe, M. Huyse and J.L. Wood, Phys. Lett. **B154** (1985) 354.
- [Dup87] P. Van Duppen, E. Coenen, K. Deneffe, M. Huyse and J.L. Wood, Phys. Rev. **C35** (1987) 1861.
- [Eji89] H. Ejiri and M.J.A. de Voigt, *Gamma-Ray and Electron Spectroscopy in Nuclear Physics*, (Clarendon Press, Oxford, 1989).

- [Fra75] S. Frauendorf and V.V. Pashkevich, Phys. Lett. **B55** (1975) 365.
- [Gav80] A.F. Gavron, Phys. Rev. **C21** (1980) 230.
- [Goe88] L. Goettig, K.B. Beard, M.W. Drigert, A. Morsad, U. Garg, I. Ahmad, R. Holzmann, R.V.F. Janssens, T.L. Khoo and W.C. Ma, in *Proc. of the Conf. on High-Spin Nuclear Structure and Novel Nuclear Shapes*, Argonne, Illinois, 1988 (ANL Report ANL-PHY-88-2), 280.
- [Gol82] G. Goldring, in *Heavy Ion Collisions*, Vol. 3, R. Bock ed., (North Holland, Amsterdam, 1982) 485.
- [Gro62] L. Grodzins, Phys. Lett. **2** (1962) 88.
- [Gut81] M. Guttormsen, Phys. Lett. **B105** (1981) 99.
- [Ham75] J.H. Hamilton, A.V. Ramayya, E.L. Bosworth, W. Lourens, J.D. Cole, B. Van Nooijen, C. Garcia-Bermudez, B. Martin, B.N. Subba Rao, H. Kawakami, L.L. Riedinger, C.R. Bingham, F. Turner, E.F. Zganjar, E.H. Spejewski, H.K. Carter, R.L. Mlekodaj, W.D. Schmidt-Ott, K.R. Baker, R.W. Fink, G.M. Gowdy, J.L. Wood, A. Xenoulis, B.D. Kern, K.J. Hofstetter, J.L. Weil, K.S. Toth, M.A. Ijaz and K.S.R. Sastry, Phys. Rev. Lett. **35** (1975) 562.
- [Han88] F. Hannachi, G. Bastin, M.G. Porquet, C. Schück, J.P. Thibaud, C. Bourgeois, L. Hildingsson, D. Jerrestam, N. Perrin, H. Sergolle, F.A. Beck, T. Byrski, J.C. Merdinger and J. Dudek, Nucl. Phys. **A481** (1988) 135.
- [Han88a] F. Hannachi, G. Bastin, M.G. Porquet, J.P. Thibaud, C. Bourgeois, L. Hildingsson, N. Perrin, H. Sergolle, F.A. Beck and J.C. Merdinger, Z. Phys. **A330** (1988) 15
- [Har65] S.E. Harris, Phys. Rev. **B138** (1965) 509.
- [Hee93] J. Heese, K.H. Maier, H. Grawe, J. Grebosz, H. Kluge, W. Meczynski, M. Schramm, R. Schubart, K. Spohr and J. Styczen, Phys. Lett. **B302** (1993) 390.
- [Hey76] K. Heyde, M. Waroquier, H. Vincx and P. van Isacker, Phys. Lett. **B64** (1976) 135; and private communication (1994).

- [Hey83] K. Heyde, P. van Isacker, M. Waroquier, J.L. Wood and R.A. Meyer, Phys. Rep. **102** (1983) 291.
- [Hüb86] H. Hübel, A.P. Byrne, S. Ogaza, A.E. Stuchbery, G.D. Dracoulis and M. Guttormsen, Nucl. Phys. **A453** (1986) 316.
- [Jam88] A.N. James, T.P. Morrison, K.Y. Ling, K.A. Connell, H.G. Price and J. Simpson, Nucl. Instr. and Methods **A267** (1988) 144.
- [Jen91] H.J. Jensen, G.B. Hagemann, P.O. Tjom, S. Frauendorf, A. Atac, M. Bergström, A. Brockstedt, H. Carlsson, P. Ekström, J.M. Espino, B. Herskind, F. Ingelbretsen, J. Jongman, S. Leoni, R.M. Lieder, T. Lönnroth, A. Maj, B. Million, A. Nordlund, J. Nyberg, M. Piiparinen, H. Ryde, M. Sugawara and A. Virtanen, Z. Phys. **A340** (1991) 351.
- [Kil89] P. Kilcher and the ISOCELE collaboration, Nucl. Instr. and Meth. in Phys. Res. **A274** (1989) 485; and in *Proc 5th Int. Conf. on Nuclei far from Stability*, Rosseau Lake, Ontario, Canada (1987) 517.
- [Kol75] D. Kolb and C.Y. Wong, Nucl. Phys. **A245** (1975) 205.
- [Kor91] M.O. Kortelahti, E.F. Zganjar, J.L. Wood, C.R. Bingham, H.K. Carter, K.S. Toth, J.H. Hamilton, J. Kormicki, L. Chaturvedi and W.B. Newbolt, Phys. Rev. **C43** (1991) 484.
- [Kra73] K.S. Krane, R.M. Steffen and R.M. Wheeler, At. Nuc. Data Tables **11** (1973) 351.
- [Krä89] A. Krämer-Flecken, T. Morek, R.M. Lieder, W. Gast, G. Hebbinghaus, H.M. Jäger and W. Urban, Nucl. Instr. and Meth. **A275** (1989) 333.
- [Kre81] A.J. Kreiner, C. Baktash, G. Garcia Bermudez and M.A.J. Mariscotti, Phys. Rev. Lett. **47** (1981) 1709.
- [Küh77] T. Kühn, P. Dabkiewicz, C. Duke, H. Fischer, H.-J. Kluge, H. Krimmeling and E.-W. Otten, Phys. Rev. Lett. **39** (1977) 180.
- [Lan91] G.J. Lane, A.P. Byrne and G.D. Dracoulis, ANU annual reports (1991-1994), ANU-P/1101, ANU-P/1118, ANU-P/1145 and ANU-P/1170, unpublished.

- [Lan94] G.J. Lane, G.D. Dracoulis, A.P. Byrne, P.M. Walker, A.M. Baxter, R.G. Henry, D. Nisius, C.N. Davids, T. Lauritsen, H. Penttila, D.J. Henderson, J.A. Sheikh and W. Nazarewicz, Phys. Lett. **B324** (1994) 14.
- [Lan95] G.J. Lane, G.D. Dracoulis, A.P. Byrne, S.S. Anderssen, P.M. Davidson, B. Fabricius, T. Kibédi, A.E. Stuchbery and A.M. Baxter, Nucl. Phys. **A**, in press.
- [Lar86] A.J. Larabee, M.P. Carpenter, L.L. Riedinger, L.H. Courtney, J.C. Waddington, V.P. Janzen, W. Nazarewicz, J.-Y. Zhang, R. Bengtsson and G.A. Leander, Phys. Lett. **B169** (1986) 21.
- [Lea78] G. Leander, in *Selected Topics in Nuclear Structure*, edited by J. Styczen and R. Kulesa (Institute of Nuclear Physics, Jagiellonian University, Krakow, 1978) 621.
- [Led78] Table of Isotopes, seventh edition, ed. C.M. Lederer and V.S. Shirley (Wiley, New York, 1978)
- [Lee87] M.A. Lee, Nuc. Data Sheets **50** (1987) 563.
- [Lee88] M.A. Lee, Nuc. Data Sheets **53** (1988) 507.
- [Lia90] Y. Liang, R. Ma, E.S. Paul, N. Xu, D.B. Fossan, J.-Y. Zhang and F. Döna, Phys. Rev. Lett. **64** (1990) 29.
- [Lia92] Y. Liang, D.B. Fossan, J.R. Hughes, D.R. LaFosse, T. Lauritsen, R. Ma, E.S. Paul, P. Vaska, M.P. Waring and N. Xu, Phys. Rev. **C45** (1992) 2177.
- [Lip60] H.J. Lipkin, Ann. of Phys. **31** (1960) 525.
- [Löb70] K.E.G. Löbner, M. Vetter and V. Hönig, Nuclear Data Tables, **A7** (1970) 495.
- [Löb75] K.E.G. Löbner, in *The Electromagnetic Interaction in Nuclear Spectroscopy*, W.D. Hamilton ed., (North Holland, Amsterdam, 1975) 141.
- [Ma84] W.C. Ma, A.V. Ramaya, J.H. Hamilton, S.J. Robinson, M.E. Barclay, K. Zhao, J.D. Cole, E.F. Zganjar and E.H. Spejewski, Phys. Lett. **B139** (1984) 276.

- [Ma86] W.C. Ma, A.V. Ramayya, J.H. Hamilton, S.J. Robinson, J.D. Cole, E.F. Zganjar, E.H. Spejewski, R. Bentsson, W. Nazarewicz and J.-Y. Zhang, Phys. Lett. **B167** (1986) 277.
- [Ma93] W.C. Ma, J.H. Hamilton, A.V. Ramayya, L. Chaturvedi, J.K. Deng, W.B. Gao, Y.R. Jiang, J. Kormicki, X.W. Zhao, N.R. Johnson, J.D. Garrett, I.Y. Lee, C. Baktash, F.K. McGowan, W. Nazarewicz and R. Wyss, Phys. Rev. **C47** (1993) R5.
- [Mac84] M.I. Macias-Marques, C. Bourgeois, P. Kilcher, B. Roussiere, J. Sauvage, M.C. Abreu and M.G. Porquet, Nucl. Phys. **A427** (1984) 205.
- [Mar69] M.A.J. Mariscotti, G. Scharff-Goldhaber and B. Buck, Phys. Rev. **178** (1969) 1864.
- [Mar91] M.J. Martin, Nuc. Data Sheets **63** (1991) 723.
- [Mat74] E. der Mateosian and A.W. Sunyar, At. Data Nuc. Data Tables **13** (1974) 391; E. der Mateosian and A.W. Sunyar, *ibid.*, **13** (1974) 407.
- [May77] F.R. May, V.V. Pashkevich and S. Frauendorf, Phys. Lett. **B68** (1977) 113.
- [Mis81] P. Misaelides, P. Tidemand-Petersson, U.J. Schrewe, I.S. Grant, R. Kirchner, O. Klepper, I.C. Malcolm, P.J. Nolan, E. Roeckl, W.-D. Schmidt-Ott and J.L. Wood, Z. Phys. **A301** (1981) 199.
- [Möl88] P. Möller and J.R. Nix, At. Data Nucl. Data Tables **39** (1988) 213.
- [Möl92] P. Möller and J.R. Nix, Nucl. Phys. **A536** (1992) 20.
- [Naz90] W. Nazarewicz, M.A. Riley and J.D. Garrett, Nucl. Phys. **A512** (1990) 61.
- [Naz93] W. Nazarewicz, Phys. Lett. **B305** (1993) 195.
- [Naz94] W. Nazarewicz and I. Ragnarsson, in *Handbook of Nuclear Properties*, Oxford University Press, to be published.
- [Nes76] A. Neskakis, R.M. Lieder, M. Müller-Veggian, H. Beuscher, W.F. Davidson and C. Mayer-Böricke, Nucl. Phys. **A261** (1976) 189.



- [New74] J.O. Newton, F.S. Stephens and R.M. Diamond, Nucl. Phys. **A236** (1974) 225.
- [New74a] J.O. Newton, in *Nuclear Spectroscopy and Reactions, Part C*, J. Cerny ed., (Academic Press, New York, 1974) 185.
- [Nil55] S.G. Nilsson, Dan. Mat. Fys. Medd. **29** (1955) No. 16.
- [Nil69] S.G. Nilsson, C.F. Tsang, A. Sobiechewski, Z. Szymanski, S. Wycech, C. Gustafson, I.-L. Lamm, P. Möller and B. Nilsson, Nucl. Phys. **A131** (1969) 1.
- [Nor70] R. Nordhagen, G. Goldring, R.M. Diamond, K. Nakai and F.S. Stephens, Nucl. Phys. **A142** (1970) 577.
- [Nyb90] J. Nyberg, A. Johnson, M.P. Carpenter, C.R. Bingham, L.H. Courtney, V.P. Janzen, S. Juutinen, A.J. Larabee, Z.-M. Liu, L.L. Riedinger, C. Baktash, M.L. Halbert, N.R. Johnson, I.Y. Lee, Y. Schutz, J.C. Waddington and D.G. Popescu, Nucl. Phys. **A511** (1990) 92.
- [Pel82] D. Pelte and D. Schwalm, in *Heavy Ion Collisions*, Vol. 3, R. Bock ed., (North Holland, Amsterdam, 1982) 1.
- [Pen87] J. Penninga, W.H.A. Hesselink, A. Balanda, A. Stolk, H. Verheul, J. van Klinken, H.J. Riezebos and M.J.A. de Voigt, Nucl. Phys. **A471** (1987) 535.
- [Por91] M.-G. Porquet, A.J. Kreiner, F. Hannachi, V. Vanin, G. Bastin, C. Bourgeois, J. Davidson, M. Debray, G. Falcone, A. Korichi, H. Mosca, N. Perrin, H. Sergolle, F.A. Beck and J.-C. Merdinger, Phys. Rev. **C44** (1991) 2445.
- [Por92] M.G. Porquet, G. Bastin, C. Bourgeois, A. Korichi, N. Perrin, H. Sergolle and F.A. Beck, J. Phys. **G18** (1992) L29.
- [Pra73] H.C. Pradhan, Y. Nogami and J. Law, Nucl. Phys. **A201** (1973) 357.
- [Pro74] D. Proetel, R.M. Diamond and F.S. Stephens, Phys. Lett. **B48** (1974) 102.
- [Pro74a] D. Proetel, D. Benson, A. Gizon, J. Gizon, M.R. Maier, R.M. Diamond and F.S. Stephens, Nucl. Phys. **A226** (1974) 237.

- [Reg95] P.H. Regan, G.D. Dracoulis, A.P. Byrne, G.J. Lane, T. Kibédi, P.M. Walker and A.M. Bruce, Phys. Rev. **C**, in press.
- [Rev92] W. Reviol, M.P. Carpenter, U. Garg, R.V.F. Janssens, I. Ahmad, I.G. Bearden, Ph. Benet, P.J. Daly, M.W. Drigert, P.B. Fernandez, T.L. Khoo, E.F. Moore, S. Pilotte and D. Ye, Nucl. Phys. **A548** (1992) 331.
- [Rev94] W. Reviol, L.L. Riedinger, J.-Y. Zhang, C.R. Bingham, W.F. Mueller, B.E. Zimmerman, R.V.F. Janssens, M.P. Carpenter, I. Ahmad, I.G. Bearden, R.G. Henry, T.L. Khoo, T. Lauritsen and Y. Liang, Phys. Rev. **C49** (1994) R587.
- [Rev95] W. Reviol, L.L. Riedinger, W.F. Mueller, J.M. Lewis, C.R. Bingham, J.-Y. Zhang and B.E. Zimmerman, Phys. Scr., in press, and private communication.
- [Rös78] F. Rösels, H.M. Fries, K. Alder and H.C. Pauli, At. Data Nucl. Data Tables **21** (1978) 291.
- [Rud73] N. Rud, D. Ward, H.R. Andrews, R.L. Graham and J.S. Geiger, Phys. Rev. Lett. **31** (1973) 1421.
- [Sch77] A.G. Schmidt, R.L. Mlekodaj, E.L. Robinson, F.T. Avignone, J. Lin, G.M. Gowdy, J.L. Wood and R.W. Fink, Phys. Lett. **B66** (1977) 133.
- [Shi95] D.T. Shi, W.C. Ma, A.V. Ramaya, J.H. Hamilton, B.R.S. Babu, J. Kormicki, L. Chaturvedi, Q.H. Lu, L.T. Brown, S.L. Tabor, M.A. Riley, J. Döring, D.E. Archer, T. Brown, S.K. Jewell, R.A. Kaye, O.J. Tekyi-Mensah and P.B. Semmes, Phys. Rev. **C51** (1995) 1720.
- [Spo94] K. Spohr, W. Meczynski, J.B. Fitzgerald, D.B. Fossan, M. Gorska, H. Grawe, J. Heese, M. Lach, K.H. Maier, A. Maj, J.C. Merdinger, M. Rejmund, R. Schubart and J. Styczen, in *Proc. of Conf. on Physics from  $\gamma$ -ray Large Detector Arrays*, Berkeley, (1994) 140.
- [Spr83] G.D. Sprouse, in *Hyperfine Interactions of Radioactive Nuclei*, J. Christiansen ed., (Springer-Verlag, Berlin, 1983) 15.
- [Ste75] F.S. Stephens, Rev. Mod. Phys. **47** (1975) 43.
- [Str67] V.M. Strutinsky, Nucl. Phys. **A95** (1967) 420.

- [Ulm86] G. Ulm, S.K. Bhattacharjee, P. Dabkiewicz, G. Huber, H.-J. Kluge, T. Kühl, H. Lochmann, E.-W. Otten, K. Wendt, S.A. Ahmad, W. Klempt, and R. Neugart, *Z. Phys.* **A325** (1986) 247.
- [Voi90] M.J.A. de Voigt, R. Kaczarowski, H.J. Riezebos, R.F. Noorman, J.C. Bacelar, M.A. Deleplanque, R.M. Diamond, F.S. Stephens, J. Sauvage and B. Roussiere, *Nucl. Phys.* **A507** (1990) 472.
- [Voi90a] M.J.A. de Voigt, R. Kaczarowski, H.J. Riezebos, R.F. Noorman, J.C. Bacelar, M.A. Deleplanque, R.M. Diamond and F.S. Stephens, *Nucl. Phys.* **A507** (1990) 447.
- [Wal89] K. Wallmeroth, G. Bollen, A. Dohn, P. Egelhof, U. Krönert, M.J.G. Borge, J. Campos, A. Rodriguez Yunta, K. Heyde, C. de Coster, J.L. Wood and H.-J. Kluge, *Nucl. Phys.* **A493** (1989) 224.
- [Wau94] J. Wauters, N. Bijmens, P. Dendooven, M. Huyse, H.-Y. Hwang, G. Reusen, J. von Shwarzenberg, P. Van Duppen, R. Kirchner and E. Roeckl, *Phys. Rev. Lett.* **72** (1994) 1329; and *Phys. Rev.* **C50** (1994) 2768.
- [Woo92] J.L. Wood, K. Heyde, W. Nazarewicz, M. Huyse and P. van Duppen, *Phys. Rep.* **215** (1992) 101.
- [Yam67] T. Yamazaki, *Nucl. Data Tables.* **A3** (1967) 1.
- [Zha87] J.-Y. Zhang, A.J. Larabee and L.L. Riedinger, *J. Phys.* **G13** (1987) L75.
- [Zho88] L. Zhou, M.P. Carpenter, C.R. Bingham, L.H. Courtney, V.P. Janzen, H.Q. Jin, W. Schmitz, C. Baktash, M.L. Halbert, N.R. Johnson, I.Y. Lee, M.N. Rao, J. Nyberg and C.D. Papanicolopoulos, *University of Tennessee Annual Report* (1988) 21, unpublished.